NUMERICAL METHODS FOR LIQUID ATOMIZATION AND APPLICATION IN DETAILED SIMULATIONS OF A DIESEL JET

By
Olivier Desjardins and Heinz Pitsch

Prepared with support from
the Department of Energy
Advanced Simulation and Computing (DOE-ASC) Program

Report No. TF-116

Flow Physics and Computational Engineering Group
Department of Mechanical Engineering
Stanford University
Stanford, CA 94305

June 2008

Numerical Methods for Liquid Atomization and Application in Detailed Simulations Of a Diesel Jet

By
Olivier Desjardins and Heinz Pitsch

Prepared with support from
the Department of Energy
Advanced Simulation and Computing (DOE-ASC) Program

Report No. TF-116

Flow Physics and Computational Engineering Group
Department of Mechanical Engineering
Stanford University
Stanford, CA 94305

June 2008

Abstract

In the context of rising environmental concerns and record-high oil prices, the need for cleaner and more efficient combustion devices becomes pressing. Because of the steady progress in computer power and computational fluid dynamics (CFD) methods, computational modeling of combustion systems emerges as a promising tool that can drive the design of future devices. In these systems, fuel is usually injected in liquid form. Atomization of the liquid fuel, or the process by which a coherent liquid flow disintegrates into droplets, represents one of the key challenges that remain to be tackled to make predictive simulations possible. Because atomization governs the size of the fuel droplets, and therefore their subsequent evaporation rate, it will have far-reaching repercussions on many aspects of the combustion process, for example pollutant formation. However, the inherent multi-physics and multi-scale nature of this process limits both experimental and numerical investigations.

For this problem to become numerically tractable, this work combines several key ingredients. Since the Reynolds number associated with atomization is generally high, numerical schemes have to be tailored for the simulation of turbulence. For this purpose, an arbitrarily high order conservative finite difference scheme for variable density, low Mach number flows is developed. Combining the second order form of this scheme with the Ghost Fluid Method (GFM), the discontinuous material properties encountered in multiphase flows can be robustly handled. Also, the surface tension force, which is singular in nature, is considered in a more accurate way. In order to represent the phase-interface geometry, two new level set

schemes are developed. First, the accurate conservative level set approach (ACLS) combines a hyperbolic tangent level set function which is transported and re-initialized using conservative schemes with a standard distance level set function for improved accuracy and robustness. This method combines good mass conservation properties with the simplicity and ease-of-use of standard level set schemes. Then, spectral refinement of a level set function is introduced. Thanks to a sub-cell polynomial reconstruction of the level set function, this approach provides great accuracy even for poorly resolved interface structures, while the use of a narrow-band formulation and semi-Lagrangian transport leads to a limited cost. The latter method is found more appropriate for simulating primary atomization because of the excellent resolution it provides.

The present approach is applied in a detailed study of the turbulent atomization process characteristic of Diesel injection. First, a temporally evolving turbulent planar jet is simulated for various Reynolds and Weber numbers. Direct visualization of the flow structures allows to lay out a clear picture of the atomization process. Early interface deformation is caused by turbulent eddies that carry enough kinetic energy to overcome surface tension forces. Then, liquid protrusions are stretched out into ligaments that rupture following Rayleigh's theory. Results suggest that aerodynamic effects contribute to both the early disruption of the liquid core and the rupture of liquid ligaments. Finally, a spatially evolving round liquid jet is simulated and qualitatively compared to recent experimental visualizations of Diesel injection.

Acknowledgments

I would like to thank my advisor Prof. Heinz Pitsch for his constant support and guidance in my research, and the members of my reading committee Prof. Sanjiva K. Lele and Prof. Gianluca Iaccarino for their time and interest in my work.

Funding by the Department of Energy under the Advanced Simulation and Computing (DOE-ASC) program is gratefully acknowledged.

Contents

List of Tables

List of Figures

Chapter 1

Introduction

1.1 Background and motivation

Atomization, or the process by which a coherent liquid disintegrates into droplets, is a fundamental topic of fluid mechanics, and has numerous engineering, environmental, as well as pharmaceutical applications. Among the many engineering applications, the atomization of liquid fuels that occurs in energy conversion devices is of great importance, since it governs the size of fuel droplets, their subsequent evaporation rate, and therefore will affect the homogeneity of the mixture. As a consequence, fuel atomization will have far-reaching repercussions on many different aspects of the combustion process, such as pollutant formation. To improve the design of energy conversion devices through computational methods, predictive models for atomization have to be provided. Figure 1.1 shows a sketch of the liquid atomization process. While models are available for the so-called secondary atomization, i.e. the break-up of small liquid drops or structures into smaller droplets, the description of primary atomization, i.e. the disintegration of a coherent liquid core into drops, is not as mature, and few models are available to describe this phenomenon. This represents one of the main bottlenecks in numerical modeling of combustion devices today.

Many reasons explain why primary atomization remains such a challenging topic. First, the complex flows associated with liquid break-up involve turbulence, surface tension effects,

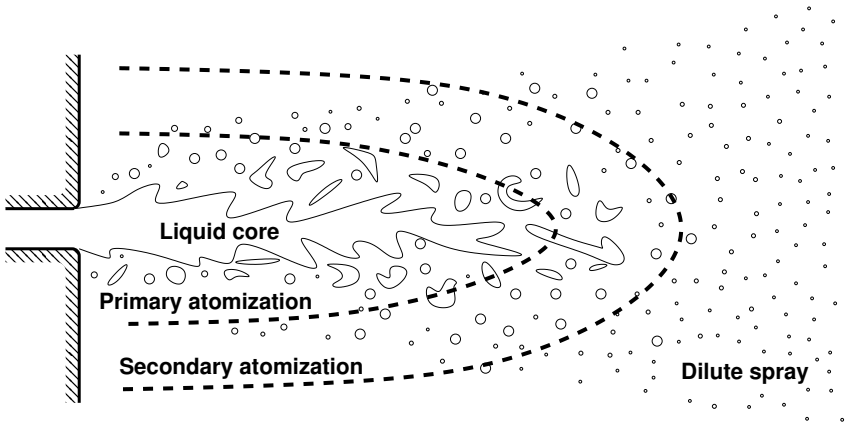

Figure 1.1: Schematics of the atomization process of a liquid jet.

and potentially large density ratios. Then, the difficulty associated with modeling is due to the importance of small liquid scales in combustion systems: modeling primary atomization means modeling a process by which mass and energy are transfered from the large liquid scales to small liquid structures. In this process, the interest is mostly in the size distribution of small liquid scales, which determines the evaporation rate. Primary atomization and the subsequent secondary breakup might not follow a cascade process, where new structures are produced only on the largest scales. Furthermore, the production of large scale structures might not be in equilibrium with small droplet evaporation, because of the long time scales involved. These observations differ greatly from standard Kolmogorov theory-based turbulence modeling.

While a consensus has been reached in identifying the mechanisms behind certain atomization problems, many fundamental aspects of primary atomization remain poorly understood to this day. Hence, numerous questions remain, such as what mechanisms govern the turbulent atomization of liquid jets in quiescent air, or whether a coherent liquid core can be found in realistic liquid injection applications. Also, it is unclear whether the classical understanding of a primary liquid breakup followed by a secondary breakup is appropriate. To all these questions, numerical simulations can provide much needed answers, provided the numerical algorithms are made sufficiently reliable.

1.2 Previous work

1.2.1 Experimental work

A large body of experimental work exists on the topic of atomization. Because numerical modeling is so limited, and because the theory behind atomization is complex, experiments have been the main means of study in this field. However, many challenges are also limiting the progress in experimental understanding of the physics of atomization. Indeed, the dispersed liquid phase limits optical access to the liquid core, and the scales involved in these flows are typically very small. As a result, experiments often aim at gathering statistical data on the droplets that result from the atomization process, instead of looking at the initial phase of the liquid breakup [101].

However, for numerous simpler two-phase flow problems, such as droplet splashing, binary drop collision, or single droplet breakup, abundant detailed experimental work has been published. For example, the issue of how a single droplet undergoes secondary breakup has been carefully analyzed by Chou and Faeth [13]. Droplet splashing and the well-known milk crown phenomenon have been studied extensively as well, see e.g. Yarin [119] for a review on the topic. Binary drop collisions have been visualized and classified for example by Ashgriz and Poo [3]. Such problems are of great interest for they are likely to play a role in the complex process of liquid atomization. However, they can be seen as secondary, since they rely on the assumption that droplets are already present in the system.

On the topic of how these droplets are initially generated, i.e. primary atomization itself, much less experimental studies are available. A specific topic on which a precise theory is available is the case of air-blast atomization, i.e. atomization caused by a fast co-flowing gas stream. In this configuration, the mechanisms leading to drop formation have been clearly identified by Hopfinger, Villermaux, and coworkers, see e.g. [53, 66, 115]. They suggested that the interface is first subject to a Kelvin-Helmholtz instability, leading to a longitudinal wave being formed on the surface of the jet. Then, as this wave grows, it undergoes a secondary instability of Rayleigh-Taylor type. This leads to the generation of bulges at the top of the wave crest. These liquid bulges are then picked up by the fast co-flowing gas,

and stretched into thin ligaments that ultimately undergo Rayleigh breakup and droplet formation. However, these investigations were limited to laminar flows, as well as high density ratio.

Concerning the issue of high speed liquid injection in a quiescent environment, experiments have yet to provide a complete picture of the atomization mechanisms. A series of studies by Faeth and coworkers [25, 97] have shone some light on the complex phenomena that take place at the surface of the liquid jet by using pulsed shadowgraphs. Their results suggest that the turbulence of the liquid field is of crucial importance in the development of the interfacial structures. Moreover, they were able to provide models for the breakup length, for the onset of turbulent breakup, and for the resulting droplet velocity. However, most of these correlations where obtained for high density ratios (on the order of 1000), in which case they observed that aerodynamics forces had little impact on the liquid structures. On the contrary, Wu and Faeth [118] suggested that for a density ratio below 500, aerodynamic effects start to influence the breakup. Since most engineering applications involve significantly smaller density ratios (on the order of 40 for Diesel injection, 100 for aircraft engines), it is expected that aerodynamic forces should be essential in the atomization process in many practical combustion devices. In this case, breakup was found to be enhanced, leading to smaller droplets, and secondary breakup was found to merge with primary atomization. Note that the idea that aerodynamic forces can contribute to the breakup of liquid jets originates from classical work on non-turbulent atomization by Levish [58] and Taylor [108].

Recently, novel techniques based on X-ray visualization have emerged, suggesting that significant progress will be made in experimental visualization of turbulent atomization. Such X-ray visualization has been employed by Wang *et al.* [116] to investigate the near-field Gasoline Direct Injection (GDI) process under realistic conditions. The assessment of the breakup mechanisms was beyond the scope of their work, however they reported observing the formation of membranes, and they related this fact to mechanisms of air-blast atomization presented by Lasheras and Hopfinger [53]. In the near future, these new techniques should allow to characterize more precisely the coherent liquid core under engine

conditions.

1.2.2 Numerical work

Because primary atomization represents a challenge for experimentalists, numerical modeling should provide a much needed alternative. However, numerical studies of primary atomization have also been very sparse. To simulate two-phase flows, various techniques have been developed, that all enjoy some benefit and suffer from limitations. Because no clear gold standard has emerged on how to conduct a numerical simulation of complex two-phase flows, the number of direct numerical studies of primary atomization remains limited. Several key issues remain, such as the discontinuous nature of the flow properties across the phase-interface, the singularity of the surface tension forces, and the very large range of scales involves in atomization. So far, all the simulations of turbulent primary atomization published have in common their severe under-resolution. De Villiers and Gosman [18] and Bianchi *et al.* [6, 5] conducted large eddy simulation (LES) of the Diesel injection, but no sub-grid scale (SGS) model for the interfacial physics was employed. It is unlikely that such an approach could provide much information on the atomization process. Ménard *et al.* [68] simulated a similar problem without SGS models, but with significantly lower Reynolds and Weber numbers. However, it is still unclear whether their simulation was properly resolved. Also, they relied on upwinded schemes and numerical dissipation to ensure the robustness of their simulations. Finally, Pan and Suga [83] simulated laminar breakup in the Rayleigh regime, but their simulations did not involve turbulent atomization.

In parallel to these efforts, several numerical studies aimed at understanding the linear stability of liquid jets through the solution of the Orr-Sommerfeld equation. Yecko *et al.* [120] and Boeck and Zaleski [8] provided some detailed analysis of the numerous instability modes, and their relative importance. Such studies are fundamental in the detailed understanding of the theory of breakup, however they are limited to the early destabilization of the liquid interface under the assumption of a parallel flow, and therefore cannot fully characterize the mechanisms of turbulent atomization.

In summary, the fully turbulent breakup of a liquid jet has been considered only rarely,

and never has it been simulated using numerical methods designed for turbulence. To successfully tackle this problem, one must carefully combine each of several key ingredients, including numerical methods capable of simulating turbulence properly, an accurate description of the gas-liquid interface, and a robust approach to handle the discontinuous material properties between the two phases.

1.2.3 Modeling work

An overview of past research on the topic of primary atomization would be incomplete without an account of conventional phenomenological models. The objective of such models is to reproduce statistically the main features of the atomization process with modest computational requirements. Many different modeling strategies have been proposed, based for example on surface instabilities [87], drop shedding [122], or cavitation [51]. However, these models replace the atomization process by the injection of round liquid blobs directly at the nozzle exit, and therefore they cannot be expected to provide accurate results close to the nozzle. In addition, such models typically assume a main atomization mechanism that might not be adequate in all situations, suggesting that fine-tuning the models against experiments might be necessary. Two novel strategies in phenomenological modeling are also of interest and should be reported here. First, Gorokhovski [34] proposed to perform stochastic modeling of primary atomization considering the liquid jet depletion as a fragmentation cascade with scaling symmetry. Second, Borghi and coworkers [111] proposed to solve a transport equation for the mean interface density in the context of Reynolds-averaged Navier-Stokes (RANS). These two approaches, along with some selected results, are reviewed in Gorokhovski and Herrmann [35], and seem promising.

1.3 Achievements

The main objective of this work is to develop a computational framework that enables the detailed study of turbulent liquid atomization. Towards this goal, several key improvements to the current state-of-the-art methods can be reported:

- An arbitrarily high order accurate, conservative finite difference scheme for variable density, low Mach number turbulent flows has been developed. Forming the core of a new structured flow solver called NGA, this scheme enables detailed simulations of complex turbulent flows. This part of the thesis is concerned with the simulation of any type of turbulent flows, such as the simulation of turbulent combustion.

- The second order form of this scheme has been modified to enable accurate and robust two-phase flow calculations using the Ghost Fluid Method (GFM) [27] to account for the surface tension term as well as the discontinuity in density, and using the Continuum Surface Force (CSF) approach [9] to account for the discontinuities in the viscous stresses. An advantage of this formulation is that a semi-implicit time integration of the equations becomes possible, which improves robustness and increases computational efficiency.

- Two novel numerical schemes for phase-interface tracking have been developed. First, the Accurate Conservative Level Set (ACLS) approach relies on a conservative formulation of the level set method, coupled to a distance function level set, to greatly reduce mass conservation errors that are known to plague level set methods, while retaining their accuracy and ease-of-use.

- Then, a Spectrally Refined Interface (SRI) approach has been formulated. This method enables sub-cell resolution of the level set function by introducing a high order pseudo-spectral reconstruction of the level set function in each flow solver grid cell. Hence, the accuracy is greatly improved, and the small scale structures that are generated in the atomization process are properly described.

- Using SRI, a detailed numerical study of turbulent Diesel-type liquid jets has been performed, and a clear picture of the atomization process has been laid out. In particular, the numerical results suggest that aerodynamic effects might play an important role in the disruption of the liquid jet. In the absence of detailed experimental data on primary atomization, statistics for velocity and liquid volume fraction are of great

interest and have therefore been reported here.

Chapter 2

Numerical methods for the simulation of turbulence

2.1 Motivation and previous work

Although numerical methods for fluid dynamics have been the subject of intense research for a number of years (see e.g. [28]), the accurate simulation of complex reactive turbulent flows remains a major challenge for any computer code. While the complexity of such flows demands highly accurate schemes for the physical phenomena to be captured adequately, their potentially large density gradients and high unsteadiness require robust numerical methods for large scale simulations to be possible. However, these two properties of accuracy and robustness are not easily combined in a single scheme. Finite difference schemes suffer from an aliasing error in the computation of the non-linear convection term of the Navier-Stokes equations, leading to an accumulation of kinetic energy in the smallest scales [52]. To reduce the impact of the resulting wiggles on the numerical solution, several strategies exist. De-aliasing can be performed in spectral space [81, 86], even though this procedure is very costly and unpractical for complex geometries or variable density flows. Lele [55] proposed the use of high order filters in physical space. However, additional work has to be performed to ensure that the filtering operation does not affect the numerical results.

Yet another strategy is to introduce upwinding in the discretization in order to stabilize the solution with numerical dissipation, but this approach has been shown to be less suited for the simulation of turbulence [71, 85]. In recent years, the most successful strategy for simulating turbulence has been to employ second order finite difference schemes on a staggered grid arrangement. This scheme, initially proposed by Harlow and Welch [38], can be shown to conserve kinetic energy discretely, therefore ensuring its robustness. In order to efficiently carry out the simulation of turbulent reactive flows, Akselvoll and Moin [1], followed by Pierce and Moin [89], adapted this scheme for variable density in cylindrical coordinates with a semi-implicit Crank-Nicolson time advancement. Similar ideas have been used successfully in other studies [109, 114, 63].

Despite its successes, this second order approach suffers from large truncation errors. Indeed, the errors obtained with a second order spatial discretization are not always negligible, and can be detrimental to the accuracy of the computed results. To illustrate this point, the convection of a Gaussian-shaped vortex can be considered. For the case shown in Fig. 2.1, a vortex was convected in diagonal direction inside a periodic unit box. With a 32×32 mesh, the vortex is represented on more than 10 points in its diameter. Such a spatial discretization per eddy is scarcely found in direct numerical simulations (DNS), and even less in large eddy simulations (LES). After two periods, when the vortex is back at the center of the domain, the second order scheme solution shows heavy distortions of the vortex shape, and secondary structures are starting to appear. On the other hand, the sixth order solution shows almost no difference with the exact solution.

In order to reduce the truncation error associated with low order numerical methods, high order finite difference compact schemes have been often employed [55, 74]. However, direct implicit time integration cannot be easily combined with these methods in the context of low Mach number flows, therefore they cannot be easily employed in cylindrical geometries, for which the CFL restrictions at the pole ($r = 0$) are highly detrimental to the stability of numerical integration. Similarly, spectral methods are extremely challenging to use in complex geometries, and their cost exceeds greatly that of finite difference methods. In more recent works, primary conservation of mass and momentum as well as

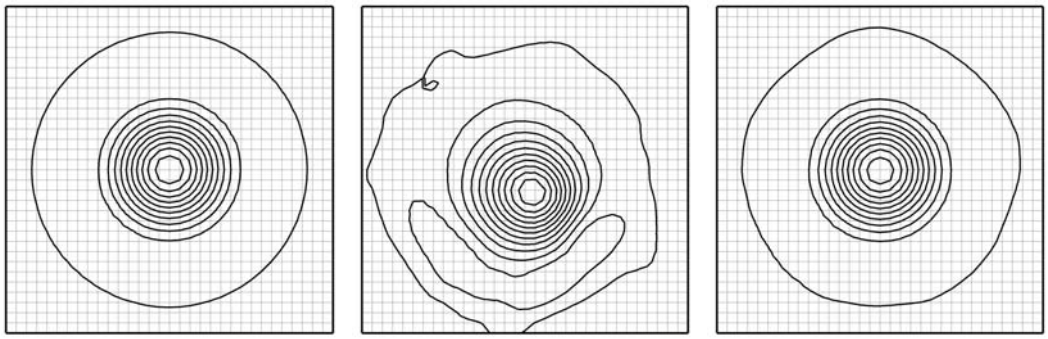

(a) Initial solution (b) Second order (c) Sixth order

Figure 2.1: Contours of vorticity norm showing the effects of the order of accuracy for the diagonal convection of a Gaussian vortex for two periods on a 32×32 mesh.

secondary conservation, i.e. conservation of kinetic energy, were combined with high order finite difference schemes for incompressible flows. In his first contribution on this subject, Morinishi *et al.* [72] proposed a set of fourth order conservative schemes for uniform cartesian coordinates on both collocated and staggered grid systems. This method was used by Nicoud [75] to describe low Mach number flows using a variable coefficient Poisson equation. Vasilyev [113] extended the incompressible fourth order conservative scheme of Morinishi *et al.* [72] to non-uniform cartesian meshes, while retaining the conservation properties. In a recent contribution, Morinishi *et al.* [73] presented a fully conservative finite difference scheme of arbitrary order of accuracy for staggered grid extended to cylindrical coordinates. Such a contribution allows for new possibilities in the simulation of turbulence, where highly accurate schemes can be employed while retaining discrete primary and secondary conservation.

2.2 Objectives

Many obstacles remain in the path towards developing a numerical tool that can simulate reactive turbulent flows with such high order conservative schemes. The objective of the

work presented in this chapter is to alleviate some of these difficulties. Towards the development of a general numerical framework for turbulent reactive DNS and LES, the following elements are addressed in the present work:

- A fully three-dimensional, variable density version of the scheme of Morinishi *et al.* [73] is presented for cartesian and cylindrical geometries.

- Adequate boundary conditions are required in order to conduct more complex simulations. A consistent approach for implementing boundary conditions is presented and tested.

- A strategy for the high order implementation of the viscous terms is proposed, along with boundary conditions.

- With these possibilities at our disposal, the question of the choice of the best order of accuracy can be raised. In order to provide some insights to this answer, several canonical flows have been simulated in order to establish best practice, and the results are discussed.

All simulations have been performed using an in-house code named NGA, for which the numerical methods presented here have been implemented in parallel using Message Passing Interface (MPI).

2.3 Governing equations

We are interested in solving the variable density, low Mach number Navier-Stokes equations. Conservation of mass reads

$$\frac{\partial \rho}{\partial t} + \nabla \cdot \rho \mathbf{u} = 0, \tag{2.1}$$

where $\mathbf{u}$ is the velocity vector and ρ the fluid density. Conservation of momentum is written as

$$\frac{\partial \rho \mathbf{u}}{\partial t} + \nabla \cdot (\rho \mathbf{u} \otimes \mathbf{u}) = -\nabla p + \nabla \cdot \boldsymbol{\sigma}, \tag{2.2}$$

where p is the pressure, and

$$\boldsymbol{\sigma} = \mu \left(\nabla \mathbf{u} + \nabla \mathbf{u}^t \right) - \frac{2}{3} \mu \nabla \cdot \mathbf{u} \, \mathbb{I}. \tag{2.3}$$

Here, μ is the dynamic viscosity and $\mathbb{I}$ is the identity tensor. The following symbolic definitions can be introduced:

$$\begin{aligned} (\text{cont}) &= \nabla \cdot \rho \mathbf{u}, & (\text{div}) &= \nabla \cdot \left(\rho \mathbf{u} \otimes \mathbf{u} \right), \\ (\text{pres}) &= \nabla p, \qquad \text{and} & (\text{visc}) &= \nabla \cdot \boldsymbol{\sigma}. \end{aligned} \tag{2.4}$$

The momentum vector will be written $\mathbf{g} = \rho \mathbf{u}$.

In this work, it will be assumed that the density is obtained through a mixing model or a combustion model that depends on flow variables and transported scalars. A typical model is to express the density as a function of a conserved scalar Z that represents the mixing between two fluids [7] and for which a transport equation is solved:

$$\frac{\partial \rho Z}{\partial t} + \nabla \cdot \left(\rho \mathbf{u} Z \right) = \nabla \cdot \left(\rho D_Z \nabla Z \right), \tag{2.5}$$

where D_Z is the diffusivity, and where $Z = 0$ for one fluid and $Z = 1$ for the other. In the remainder of this work, we will use $\rho = \hat{\rho}\left(Z\right)$ as a combustion model, keeping in mind that the actually applied model may depend on other variables. Similarly, the viscosity and diffusivity will be obtained through $\mu = \hat{\mu}\left(Z\right)$ and $D_Z = \hat{D}_Z\left(Z\right)$. The symbolic definition for scalar convection can be introduced as:

$$(\text{scal}) = \nabla \cdot \left(\rho \mathbf{u} Z \right). \tag{2.6}$$

2.4 Variable density conservative finite difference scheme

In this section, we will present the variable density version of the scheme proposed by Morinishi *et al.* [73] for cylindrical coordinates. Round and planar geometries are both of high interest. Hence, the scheme will be presented for both cylindrical and cartesian

coordinate systems.

2.4.1 Coordinate system

The physical space is described by a coordinate system $\mathbf{x} = (x_1, x_2, x_3)$ that can be cartesian, i.e. $(x_1, x_2, x_3) = (x, y, z)$ or cylindrical, i.e. $(x_1, x_2, x_3) = (x, r, \theta)$. The physical space is mapped into the uniform computational space of unity spacing $\boldsymbol{\zeta} = (\zeta_1, \zeta_2, \zeta_3)$. Associated with this mapping, scaling factors can be defined by differentiating the physical space with respect to the computational space, leading to

$$h_1 = \frac{dx_1}{d\zeta_1}, \quad h_2 = \frac{dx_2}{d\zeta_2}, \quad h_3 = \frac{dx_3}{d\zeta_3}, \tag{2.7}$$

for cartesian coordinates and

$$h_1 = \frac{dx_1}{d\zeta_1}, \quad h_2 = \frac{dx_2}{d\zeta_2}, \quad h_3 = x_2\frac{dx_3}{d\zeta_3}, \tag{2.8}$$

for cylindrical coordinates. From the scaling factors, the Jacobian can be defined by

$$J = h_1\ h_2\ h_3. \tag{2.9}$$

For the sake of generality of notation, the velocity will be written $\mathbf{u} = (u_1, u_2, u_3)^t$ where in cartesian coordinates $(u_1, u_2, u_3) = (u_x, u_y, u_z)$, while in cylindrical coordinates we write $(u_1, u_2, u_3) = (u_x, u_r, u_\theta)$. The same notation is introduced for the momentum vector $\mathbf{g} = (g_1, g_2, g_3)^t$. The variables are staggered on the computational mesh, their positions are shown in Fig. 2.2. Note that all scalar quantities (Z, ρ, μ, D_Z) are stored at the cell center like the pressure.

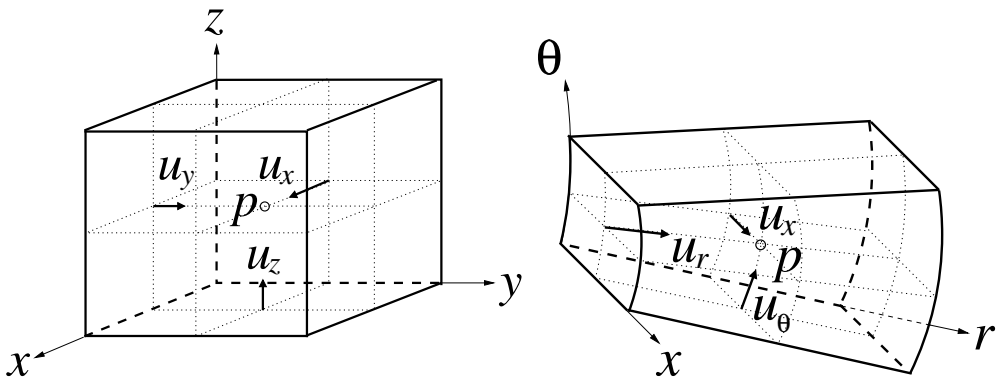

(a) Cartesian coordinates (b) Cylindrical coordinates

Figure 2.2: Staggered variable positions.

2.4.2 Discrete operators

For reference, the discrete operators defined in [73] are reintroduced here. The second order interpolation with stencil size n in the ζ_1 direction acting on a quantity ϕ is expressed as

$$\overline{\phi}^{n\,\zeta_1}(\zeta_1,\zeta_2,\zeta_3) = \frac{\phi(\zeta_1+n/2,\zeta_2,\zeta_3)+\phi(\zeta_1-n/2,\zeta_2,\zeta_3)}{2}. \tag{2.10}$$

$\overline{\phi}^{n\,\zeta_2}$ and $\overline{\phi}^{n\,\zeta_3}$ are defined in the same manner. The second order differentiation of stencil size n in the ζ_1 direction of the quantity ϕ is computed by

$$\frac{\delta_n\,\phi}{\delta_n\,\zeta_1}(\zeta_1,\zeta_2,\zeta_3) = \frac{\phi(\zeta_1+n/2,\zeta_2,\zeta_3)-\phi(\zeta_1-n/2,\zeta_2,\zeta_3)}{n}. \tag{2.11}$$

$\frac{\delta_n\,\phi}{\delta_n\,\zeta_2}$ and $\frac{\delta_n\,\phi}{\delta_n\,\zeta_3}$ are defined in the same manner. To construct the nth order accurate operators, interpolation weights α_l have to be computed by solving

$$\sum_{l=1}^{n/2}(2l-1)^{2(i-1)}\,\alpha_l = \delta_{i1}, \quad \text{for} \quad i\in[\![1,n/2]\!], \tag{2.12}$$

where δ_{ij} is the Kronecker delta. The nth order interpolation in the ζ_i direction for $i \in \{1, 2, 3\}$ is then defined by

$$\overline{\phi}^{n\text{th}\,\zeta_i} = \sum_{l=1}^{n/2} \alpha_l \, \overline{\phi}^{(2l-1)\,\zeta_i}. \tag{2.13}$$

Similarly, the nth order differentiation operator will be

$$\frac{\delta_{n\text{th}}\,\phi}{\delta_{n\text{th}}\,\zeta_i} = \sum_{l=1}^{n/2} \alpha_l \, \frac{\delta_{(2l-1)}\,\phi}{\delta_{(2l-1)}\,\zeta_i}. \tag{2.14}$$

The benefit of using these high order accurate staggered operators can be readily seen by looking at the modified wave number diagrams shown in Fig. 2.3. Here, the modified wave number has been computed for the staggered differentiation operator and for the combination of the staggered differentiation with the staggered interpolation operator, which corresponds to the collocated differentiation operator. These are typically the two types of operators which will be used in the solution of the Navier-Stokes equations. It can be observed from these graphs that regardless of the operator type, it is beneficial to use high order operators, since the dispersive errors are significantly reduced, especially at high wave numbers. Of course, the staggered operator has significantly less errors than the collocated operator. Also, dissipative errors are inexistent here since all operators are centered. In order to further analyze the *a priori* properties of these schemes, the study of aliasing errors proposed by Kravchenko and Moin [52] is extended here to include the fourth and sixth order schemes. By doing a Fourier analysis of the non-linear term computed by the different schemes, the contribution due to the aliasing effect can be extracted. This is performed on a given mesh by assuming a prescribed von Karman spectrum for the velocity, following the procedure of Kravchenko and Moin [52]. The computed aliasing error as a function of the wave number is shown in Fig. 2.4. It is clear that a non-dealiased spectral scheme will give the most errors in this case, which is what is indeed seen in Fig. 2.4. The second order scheme is less prone to these errors, followed by the fourth order and the sixth order schemes. These results suggest that the higher the order of accuracy, the more the schemes exhibit a spectral behavior.

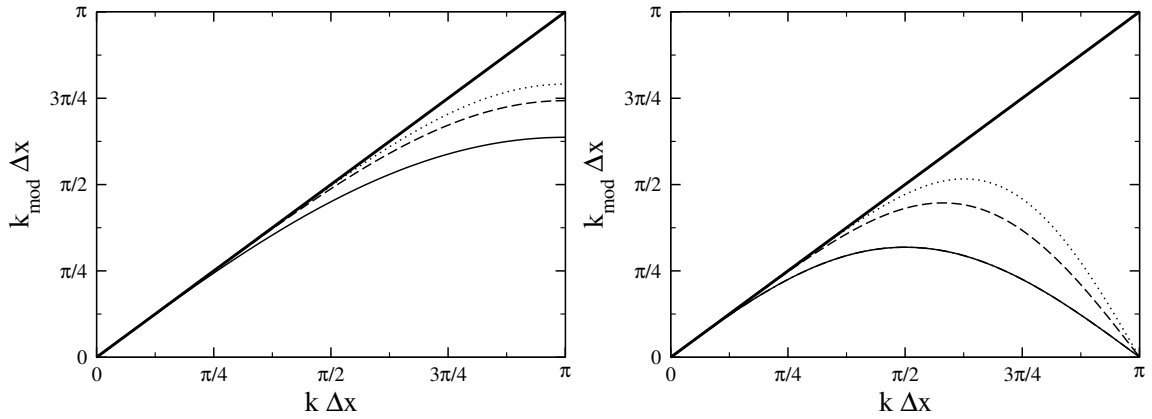

(a) Staggered operator (b) Collocated operator

Figure 2.3: Modified wave number diagram: exact (thick line); second (solid line), fourth (dashed line) and sixth (dotted line) orders.

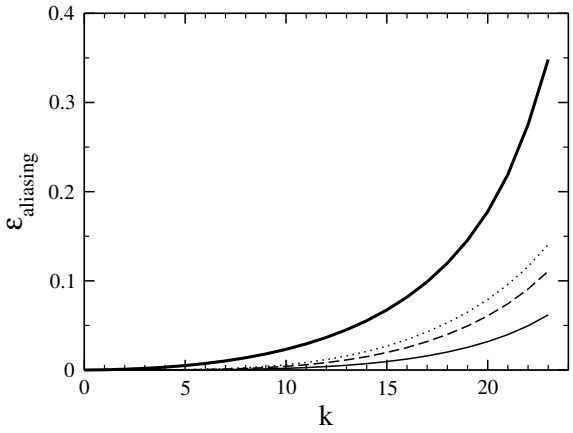

Figure 2.4: Aliasing error: spectral (thick line); second (solid line), fourth (dashed line) and sixth (dotted line) orders.

2.4.3 Numerical discretization

Using the expressions introduced above, the divergence form of the convective term of the Navier-Stokes equations transformed into computational space [73] will be written at any even order of accuracy n as

$$(\text{div-}n)_{x_1} = \sum_{i=1}^{3} \left(\frac{1}{\overline{J}^{1\,\zeta_1}} \sum_{l=1}^{n/2} \alpha_l \frac{\delta_{(2l-1)}}{\delta_{(2l-1)\,\zeta_i}} \left[\overline{\left(\frac{J}{h_i} g_i \right)}^{n\text{th}\,\zeta_1} \overline{u_1}^{(2l-1)\,\zeta_i} \right] \right), \tag{2.15}$$

$$\begin{aligned}(\text{div-}n)_{x_2} = & \sum_{i=1}^{3} \left(\frac{1}{\overline{J}^{1\,\zeta_2}} \sum_{l=1}^{n/2} \alpha_l \frac{\delta_{(2l-1)}}{\delta_{(2l-1)\,\zeta_i}} \left[\overline{\left(\frac{J}{h_i} g_i \right)}^{n\text{th}\,\zeta_2} \overline{u_2}^{(2l-1)\,\zeta_i} \right] \right) \\ & - \epsilon \frac{1}{\overline{J}^{1\,\zeta_2}} \overline{\left(\frac{J}{x_2}\, \overline{g_3}^{n\text{th}\,\zeta_3}\, \overline{u_3}^{n\text{th}\,\zeta_3} \right)}^{n\text{th}\,\zeta_2},\end{aligned} \tag{2.16}$$

$$\begin{aligned}(\text{div-}n)_{x_3} = & \sum_{i=1}^{3} \left(\frac{1}{\overline{J}^{1\,\zeta_3}} \sum_{l=1}^{n/2} \alpha_l \frac{\delta_{(2l-1)}}{\delta_{(2l-1)\,\zeta_i}} \left[\overline{\left(\frac{J}{h_i} g_i \right)}^{n\text{th}\,\zeta_3} \overline{u_3}^{(2l-1)\,\zeta_i} \right] \right) \\ & + \epsilon \frac{1}{\overline{J}^{1\,\zeta_3}} \overline{\left(\frac{J}{x_2}\, \overline{g_2}^{n\text{th}\,\zeta_2}\, \overline{u_3}^{n\text{th}\,\zeta_3} \right)}^{n\text{th}\,\zeta_3},\end{aligned} \tag{2.17}$$

where ϵ is zero in cartesian coordinates and one in cylindrical coordinates. [1]

The divergence of the momentum vector that appears in the continuity equation will be

[1] For the sake of completeness, we include here the pseudo-code that is used to calculate in the array DIVX the convective term in the ζ_1 direction defined by Eq. 2.15 at any order n:

```
for i = 1 to N_x do
  for j = 1 to N_y do
    for k = 1 to N_z do
      DIVX(i,j,k) ⇐ 0
      for st = −n/2 to n/2 − 1 do
        DIVX(i,j,k) ⇐ DIVX(i,j,k) +
          1/2 div(i,j,k,st) G1(i + st, j, k) (U1(i + 2st + 1, j, k) + U1(i,j,k))
      end for
      for st = −n/2 + 1 to n/2 do
        DIVX(i,j,k) ⇐ DIVX(i,j,k) +
          1/2 div(i,j,k,st) G2(i, j + st, k) (U1(i, j + 2st − 1, k) + U1(i,j,k))
        DIVX(i,j,k) ⇐ DIVX(i,j,k) +
          1/2 div(i,j,k,st) G3(i, j, k + st) (U1(i, j, k + 2st − 1) + U1(i,j,k))
      end for
    end for
  end for
end for
```

The array U1 contains the first component of the velocity vector, while G1, G2, and G3 are the three components of the momentum vector. The array div contains the operator defined by Eq. 2.14 divided by $\overline{J}^{1\,\zeta_1}$ at every (i,j,k) location. A schematic of the procedure can also be found in Fig. 2.9.

written

$$(\text{cont-}n) = \sum_{i=1}^{3} \left(\frac{1}{J} \frac{\delta_{n\text{th}}}{\delta_{n\text{th}}\, \zeta_i} \left[\frac{J}{h_i} g_i \right] \right). \tag{2.18}$$

Finally, the pressure gradient will be expressed as

$$(\text{pres-}n)_{x_i} = \frac{J}{\overline{J}^{1\, \zeta_i}} \frac{1}{h_i} \frac{\delta_{n\text{th}}\, p}{\delta_{n\text{th}}\, \zeta_i}. \tag{2.19}$$

The Jacobian inverse that appears in front of every term in Eqs. 2.15–2.17 and 2.19 can be evaluated by a number of methods. In our numerical tests, very little difference on the resulting order of accuracy was obtained by changing the way this term in computed. As a result, we chose to express it similarly to Morinishi *et al.* [73] by using second order interpolation.

2.4.4 Relationship between velocity and momentum

Because of the staggering of the variables in space, the velocity components and the density are not located at the same position. As a result, the ith component of the momentum vector is discretely expressed by

$$g_i = \overline{\rho}^{2\text{nd}\, x_i} u_i, \tag{2.20}$$

where the interpolation operator acting on the density is a second order interpolation in physical space that will be introduced in Section 2.7. A similar strategy is employed to compute the interpolated values of viscosity and diffusivity. Unbounded values of interpolated density are highly detrimental to the robustness of the variable density scheme. In order to avoid this issue, the density interpolation should be total variation diminishing (TVD). This is most easily achieved by limiting ourselves to a second order interpolation, regardless of the order of accuracy of the rest of the scheme. While a higher order TVD interpolation could be designed, our numerical experiments showed little effect of the second order density interpolation on the quality of the results.

Scalar scheme	Divergence order	Global accuracy	TVD property	Total stencil length
$\text{HOUC}^n_{\text{FV}}$	2	n	$\times$	$n+2$
$\text{HOUC}^n_{\text{FD}}$	m	$\min(n,m)$	$\times$	$n+m$
WENO-3	2	up to 3	✓	5
WENO-5	2	up to 5	✓	7

Table 2.1: Properties of the different scalar transport schemes used.

2.4.5 Discretization of the scalar transport equation

While not the primary objective of this work, the discretization of the scalar transport equation is included here for the sake of completeness. The advection of a scalar quantity is discretely written

$$(\text{scal-}n) = \sum_{i=1}^{3} \left(\frac{1}{J} \frac{\delta_{n\text{th}}}{\delta_{n\text{th}}\, \zeta_i} \left[\frac{J}{h_i} g_i \overline{\overline{Z}}^{\zeta_i} \right] \right), \tag{2.21}$$

where $\overline{\overline{\phi}}^{\zeta_i}$ represents the interpolation of a scalar quantity ϕ to a cell face in the ζ_i direction. This interpolation is specific to the scalar quantities, and has to be considered carefully. Indeed, the accuracy of scalar transport quantities is a critical issue in turbulent reactive simulations. The boundedness of a conserved scalar is often highly desirable for the stability of combustion models, and therefore TVD schemes such as third order or fifth order WENO [61, 45] can be considered as schemes of choice, despite the numerical diffusion they induce. While not TVD, high order upwind central schemes (HOUC) [76] of any odd order are also of great interest, since they allow to reach high order accuracy, while the slight upwinding helps obtain a smooth scalar field. Two classes of HOUC schemes have been implemented, namely a finite volume type interpolation ($\text{HOUC}^n_{\text{FV}}$) and a finite difference type interpolation ($\text{HOUC}^n_{\text{FD}}$). In both cases, n has to be odd to allow for upwinding. To obtain the nth order accuracy for the scalar advection, the $\text{HOUC}^n_{\text{FV}}$ has to be combined with a second order divergence operator, while the $\text{HOUC}^n_{\text{FD}}$ has to be combined with an mth order divergence operator, where $m > n$. These properties of the scalar transport schemes, as well as the required stencil size, are summarized in Table 2.1. Note for example that a third order

HOUC corresponds to Leonard's QUICK scheme [56].

2.4.6 Temporal integration

The Navier-Stokes equations are solved using the second order semi-implicit Crank-Nicolson scheme of Pierce and Moin [89]. Inspired by the classical fractional step approach [48], this iterative time advancement scheme uses staggering in time between the momentum field and the scalar and density fields. The scalars are advanced first, the density field is updated, and the momentum equations are then advanced. The pressure Poisson equation is then solved to enforce continuity using a combination of spectral methods, Krylov-based methods [112], and multi-grid methods [26], depending on the geometry of the problem. In order to relax the CFL conditions that can limit very severely the time step size in cylindrical coordinates, an implicit correction is computed for the scalar and momentum equations, using an approximate factorization technique similar to the one used by Choi and Moin [11]. This implicit correction requires the solution of a poly-diagonal system in parallel for each velocity component and for each spatial direction that is treated implicitly. The number of diagonals in the linear problem depends on the order of the scheme. For example, the second order formulation leads to a tri-diagonal system, while the fourth order formulation leads to an hepta-diagonal problem. This semi-implicit approach combines the benefit of conserving kinetic energy discretely in time in the case of constant density, as discussed in Ham *et al.* [37], and of allowing to run with greatly relaxed CFL restrictions. It should however be noted that in the case of variable density, this methodology fails to discretely conserve kinetic energy. Indeed, Pierce and Moin [89] showed that a second order temporal error that is proportional to the time derivative of density is introduced.

2.4.7 Conservation properties

For all terms written in divergence form, it has been noted that conservation is achieved *a priori* [73]. As a result, quantities such as mass, momentum, or fuel mass fraction solved using a scalar transport equation are conserved discretely. However, to prove discrete energy

conservation, a transport equation for the kinetic energy should be written. As for its analytical counterpart, this transport equation is based on the continuity and momentum equations. If all terms in the kinetic energy equation can be written in the form of a divergence, then kinetic energy is discretely conserved.

As already pointed out by Morinishi *et al.* [72] and Vasilyev [113], local kinetic energy is ambiguous to define in a staggered grid arrangement, as the velocity components are found at different locations. The square of the velocity components can be evaluated at the center of each of the faces and then interpolated back at the cell center. This way, the discrete kinetic energy should be defined as

$$K = \frac{1}{2J} \sum_{i=1}^{3} \overline{\overline{J}^{1\,\zeta_i} g_i u_i}, \tag{2.22}$$

where $\overline{\phi}$ represents a cell-centered value of ϕ obtained by any interpolation technique. As the mesh is non-uniform, the Jacobians have to be reintroduced to account for stretching. The discrete transport equation for the kinetic energy will be deduced from the discrete transport equations for the velocity components, by combining the approaches introduced by Morinishi *et al.* [72, 73]. For instance, after multiplying the convective term for the first component of the velocity vector by the first velocity component, we shall obtain

$$\begin{aligned} \overline{J}^{1\,\zeta_1} u_1 \left(\text{div-}n\right)_{x_1} = \sum_{i=1}^{3} \left(\sum_{l=1}^{n/2} \alpha_l \frac{\delta_{(2l-1)}}{\delta_{(2l-1)\,\zeta_i}} \left[\overline{\left(\frac{J}{h_i} g_i \right)}^{n\text{th}\,\zeta_1} \widetilde{u_1 u_1}^{(2l-1)\,\zeta_i} \right] \right) \\ + \frac{1}{2} u_1^2 \, \overline{\left(\text{cont-}n\right)}^{n\text{th}\,\zeta_1}, \end{aligned} \tag{2.23}$$

where a new interpolation operator has been introduced, which is defined as

$$\begin{aligned} \widetilde{\phi\psi}^{n\,\zeta_1} \left(\zeta_1, \zeta_2, \zeta_3\right) = \frac{1}{2} \phi \left(\zeta_1 + n/2, \zeta_2, \zeta_3\right) \psi \left(\zeta_1 - n/2, \zeta_2, \zeta_3\right) \\ + \frac{1}{2} \phi \left(\zeta_1 - n/2, \zeta_2, \zeta_3\right) \psi \left(\zeta_1 + n/2, \zeta_2, \zeta_3\right). \end{aligned} \tag{2.24}$$

As in the case of constant density, the convective term of the momentum equation will discretely conserve kinetic energy only if the continuity equation is exactly satisfied.

On the other hand, the pressure term differs significantly from the case of constant density and further analysis is required. Morinishi *et al.* [72] introduced an interpolation scheme in order to rewrite the pressure term

$$\overline{\overline{J}^{1\,\zeta_1} u_i \,(\text{pres-}n)_{x_i}} = \sum_{l=1}^{n/2} \alpha_l \; \overline{u_i \; \frac{\delta_{(2l-1)} p}{\delta_{(2l-1)} \zeta_i}}^{(2l-1)\,\zeta_i} \tag{2.25}$$

$$= \sum_{l=1}^{n/2} \alpha_l \; \frac{\delta_{(2l-1)}}{\delta_{(2l-1)} \zeta_i} \left(u_i \overline{p}^{(2l-1)\,\zeta_i} \right) - p \; \frac{\delta_{n\text{th}}}{\delta_{n\text{th}}\,\zeta_i} \left[\frac{J}{h_i} u_i \right]. \tag{2.26}$$

With this new interpolation operator, it is straighforward to see that the pressure term conserves kinetic energy in the case of constant density. However, in the case of variable density, the last term is not zero as the continuity equation does not imply a divergence free velocity field. This pressure-dilatation term ($-p \, \nabla \cdot \mathbf{u}$) is of course physical, since it exists also in the continuous transport equation for kinetic energy. It represents the energy transfer between the kinetic energy and the internal energy through the work of pressure in the presence of dilatation. It should be noted however that no equation is solved for the internal energy, therefore there exists no counterpart to the pressure-dilatation term. As a result, numerical errors in kinetic energy may be able to accumulate through this term. This phenomenon, referred to as spurious heat release [89], is caused by the discrete discrepancy that exists between the continuity equation (Eq. 2.1) and the scalar transport equation (Eq. 2.5), as will be discussed in further details in Section 2.4.8. This issue is caused by the combined effects of the high order formulation and the variable density aspect of the flows considered.

2.4.8 Test cases

Numerical tests are conducted to check that adequate order of accuracy as well as conservation properties are obtained.

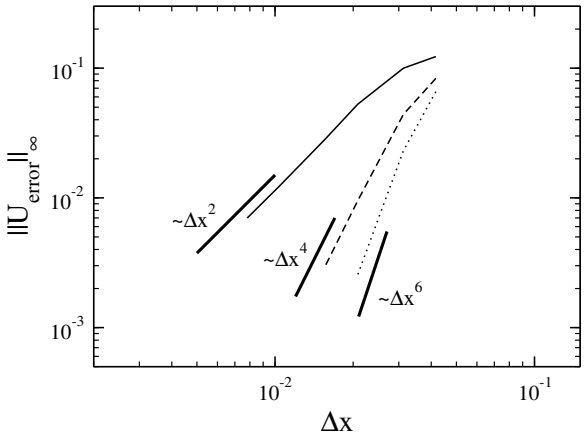

Figure 2.5: Accuracy check for the inviscid convection of a circular vortex: second order (solid line); fourth order (dashed line); sixth order (dotted line).

High order accuracy

In order to verify the correct behavior of the numerical scheme, the order of accuracy is evaluated by convecting a circular vortex inside a two-dimensional unit box $[-0.5, 0.5] \times [-0.5, 0.5]$ with periodic boundary conditions. The initial velocity field is given by

$$\mathbf{u}\,(x, y) = \begin{pmatrix} 1 - \frac{y}{2} e^{-\left(x^2+y^2\right)/a^2} \\ \frac{x}{2} e^{-\left(x^2+y^2\right)/a^2} \end{pmatrix}, \tag{2.27}$$

where the value of a is set to 0.2. The mesh is uniform in the y direction, but has stretching in the x direction. The mesh is given as $x = x_0 + s_x \sin(2\pi x_0)$, where x_0 is uniform in $[-0.5, 0.5]$. The value of s_x is set to 0.15, leading to very strong stretching. The simulation is performed at a constant CFL number of 0.01 for one time unit, when the vortex should be back at its original location, and the L_∞ norm of the error between the computed axial velocity and the exact solution is evaluated. The results of this test case are shown in Fig. 2.5, demonstrating that the expected orders of accuracy are recovered.

Constant density energy conservation

It has already been shown that mass and momentum conservation are obtained in the case of periodic boundary conditions. Furthermore, it has been shown that the kinetic energy in the system even for non-uniform meshes should be discretely conserved as long as the continuity equation is satisfied. In order to verify this for the presented scheme, a three-dimensional computation is performed in a unit box discretized on a 16^3 mesh, stretched in a similar way as for the vortex convection problem. The velocity field is initialized with uniform random numbers between -1 and 1, and projected to satisfy the divergence-free constraint. The time step size is set to $\Delta t = 0.002$. The evolution of the kinetic energy in the system is shown for two different time integration schemes, namely a second order explicit Runge-Kutta scheme and the semi-implicit second order Crank-Nicolson scheme presented in Section 2.4.6. Figure 2.6 shows that the Crank-Nicolson scheme conserves kinetic energy, as expected. Interestingly, it can be observed that the higher the spatial order of accuracy, the faster the energy growth in time for the case of the second order Runge-Kutta scheme. As the spatial discretization already conserves kinetic energy, it appears important to use a time discretization that preserves this property to ensure a correct long time behavior of the solution even for high orders of accuracy. As a consequence, the Crank-Nicolson time advancement will be used in all the following test cases.

Variable density energy conservation

The discrete conservation of kinetic energy should also be satisfied even in the case of variable density. To verify this property, additional computations are performed in a unit box discretized on a 32^3 mesh. A turbulent velocity field with a Taylor microscale Reynolds number of about 33 is achieved by a linear forcing procedure [64]. The initial eddy turn-over time is $\tau_0 = 6.1$. A mixture fraction (Z) scalar field is initialized between 0 and 1 according to the procedure proposed by Eswaran and Pope [24]. Finally the density field is computed from the mixture fraction field using an equation of state corresponding to two miscible

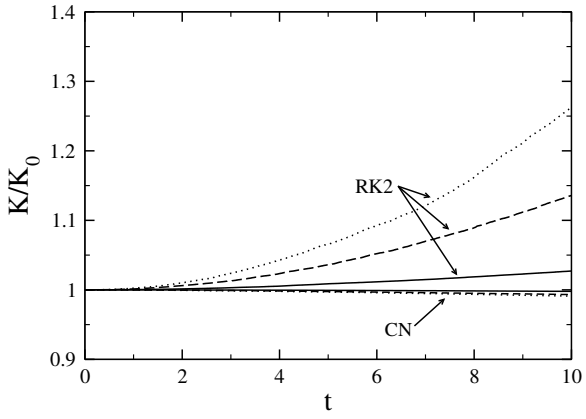

Figure 2.6: Temporal evolution of the kinetic energy in the case of constant density: second order (solid line); fourth order (dashed line); sixth order (dotted line).

fluids

$$\rho(Z) = \frac{1}{aZ + b}. \tag{2.28}$$

The simulations were performed with a density ratio of 10 ($a = 9$, $b = 1$), a second order discretization for the convective and viscous part of the momentum equation, and a fifth order WENO scheme for the scalar transport equation. This first simulation is performed with both kinematic viscosity and diffusivity kept constant (Pr = 1). Figure 2.7 shows the time evolution of the kinetic energy in the domain. As expected, the kinetic energy follows a power law decay in time. The computation is restarted from $t = 5$ without viscosity and diffusivity to characterize the conservation properties of the different spatial discretizations. The variation in the total kinetic energy shown in Fig. 2.7(a) and in Fig. 2.7(b) is small when compared to its decay in the presence of viscosity and diffusivity. The remaining variations may come from two contributions, namely the time integration errors or the pressure-dilatation term. In the latter case, the difference should correspond to an energy exchange with the internal energy. To quantify this energy transfer, an additional equation for the total internal energy is solved by

$$\frac{dE_{int}}{dt} = p \; \nabla \cdot \mathbf{u}, \tag{2.29}$$

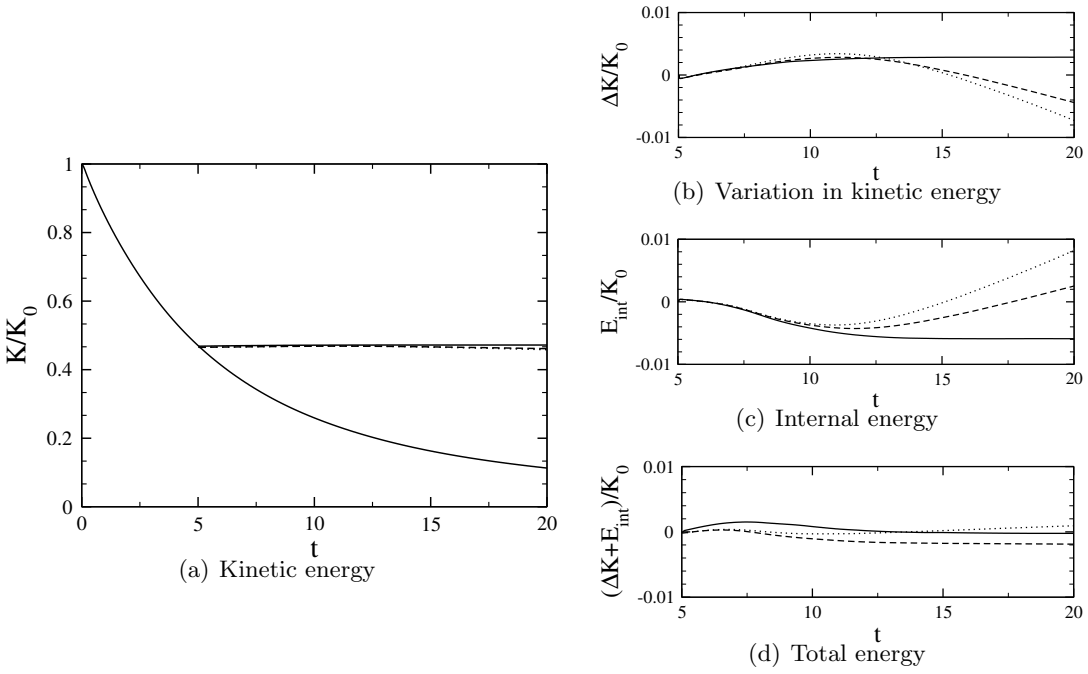

(a) Kinetic energy

(b) Variation in kinetic energy

(c) Internal energy

(d) Total energy

Figure 2.7: Temporal evolution of the kinetic and internal energies in the case of variable density: second order (solid line); fourth order (dashed line); sixth order (dotted line).

and the resulting reconstructed change in internal energy is presented in Fig. 2.7(c). As observed in Fig. 2.7(d), the total energy defined as the sum of kinetic energy (K) and internal energy (E_{int}) is nearly constant throughout the simulations for the three orders of accuracy (second, fourth, and sixth) tested. It can thus be inferred that the contribution from the temporal errors is very small, and that most of the kinetic energy variation can be explained by the effect of the pressure-dilatation term.

However, in this particular case, the pressure dilatation term arises only in the discrete equations. Indeed, in the absence of scalar diffusion, the scalar transport equation reads

$$\frac{\partial \rho Z}{\partial t} + \nabla \cdot (\rho \mathbf{u} Z) = 0. \tag{2.30}$$

Together with the continuity equation (Eq. 2.1) and the equation of state (Eq. 2.28), one can show that

$$\nabla \cdot \mathbf{u} = 0. \tag{2.31}$$

As a result, under these circumstances, the total kinetic energy should remain constant and there should be no energy transfer to internal energy through the pressure-dilatation term. Nevertheless, as the discrete forms of the continuity equation and the scalar transport equation are different, Eq. 2.31 will not be satisfied discretely. This discrete discrepancy comes from using different operators for the divergence in the continuity and scalar transport equations, as well as different operators for the interpolation of the scalar and the density. This can be observed in the fact that the transfer to internal energy is larger for sixth and fourth order than it is for second order, as the discrete divergence operators corresponding to these orders of accuracy differ more strongly from the second order divergence operator used in conjunction with WENO-5. As a result, to limit the contribution from this spurious heat release, one should choose the scalar transport scheme such that the same divergence operator is used for the continuity and for the scalar transport equation. This conclusion could suggest that full finite difference schemes (such as $\text{HOUC}^n_{\text{FD}}$) are better suited for high order variable density simulations. However, as presented in Table 2.1, their global stencil size is larger, and it is more challenging to achieve boundedness of the scalar with

such schemes. Considering that the spurious heat release observed in this case is very small, schemes such as third and fifth order WENO and $\text{HOUC}^n_{\text{FV}}$ will be preferred.

2.5 Boundary conditions treatment

2.5.1 Global conservation

In the case of non-periodic boundary conditions, local conservation does not imply global conservation, and therefore global conservation properties need to be redefined. With local conservation already satisfied, Morinishi *et al.* [72] defined global conservation through the relation

$$\sum_{k=1,}^{N_i} (h_i)_k \left.\frac{\delta\phi}{\delta x_i}\right|_k = \phi_{N_i+1/2} - \phi_{1/2}, \tag{2.32}$$

where N_i is the number of points in the ith direction. This property is the discrete equivalent to Green's theorem, and this condition is the basis of the boundary condition treatment proposed here.

Only boundary conditions corresponding to walls (slip and no-slip) as well as other Dirichlet conditions, such as inflow and convective outflow conditions [80, 1], are treated in this paper. The different operators for interpolation and differentiation will be modified to account for boundaries in such a way that quantities outside the physical domain are never used. Primary conservation of mass and momentum will be discussed next.

2.5.2 Mass conservation

In a low-Mach number formulation, the pressure field is computed as the solution of a Poisson equation. The best boundary condition for the pressure is the application of zero normal gradients [98]. As a consequence, the volumetric integral of the pressure Laplacian is analytically zero

$$\int_V \Delta P dV = \oint_{\delta V} \nabla P \cdot \mathbf{dS} = 0. \tag{2.33}$$

To ensure that the equation solved for the pressure has a solution, its right hand side should verify the same condition. For instance, in a fractional step formulation, the Poisson equation is

$$\Delta\left(\delta P\right) = \frac{1}{\Delta t}\left(\text{cont-}n\right). \tag{2.34}$$

As a consequence, the volumetric integral of the continuity equation has to be analytically zero. The discrete form of this condition,

$$\sum_{x_1,x_2,x_3} J\left(\text{cont-}n\right) = 0, \tag{2.35}$$

ensures global mass conservation and is mandatory for low-Mach number formulations. This aspect is fundamental: if Eq. 2.35 is not satisfied, the Poisson equation for the pressure has no mathematical solution, since its right hand side is not in the image of the Laplacian operator. This and Eq. 2.32 define the necessary conditions that the divergence operator of the continuity equation has to satisfy.

While these properties are inherent to the second order formulation, a special treatment has to be derived for higher order formulations. As long as a divergence operator requires a velocity value outside the domain, Eq. 2.32 is not satisfied. For instance, a fourth-order divergence operator requires information about one point outside the domain and a sixth order formulation requires two values, which is shown in Fig. 2.8. To alleviate the problem arising in the fourth order formulation, Morinishi *et al.* [73] have proposed to compute the value for this outside point by using linear extrapolation with points inside the domain. They have shown that this discretely conserves mass. However, this approach cannot be easily extended to order higher than four.

Here, we propose a more general approach which can be derived for any order of accuracy. The differentiation operator given by Eq. 2.18 is expressed as a weighted linear combination of values at different grid points. In fact, Eq. 2.32 states that these weights add up to zero at every grid point in the domain except for the boundaries where their sums are either equal to $+1$ or -1, as shown in Fig. 2.8. This condition alone ensures discrete mass conservation.

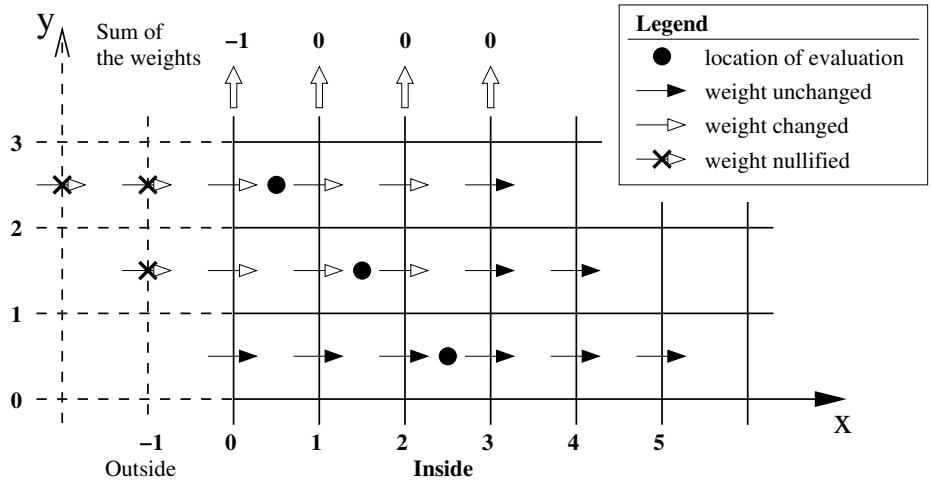

Figure 2.8: Definition of the procedure to update the divergence operator to ensure mass conservation (illustrated for sixth order).

Following this observation, the weights of the divergence operator corresponding to points outside the domain will be nullified, while the weights inside the domain will be adjusted to verify Eq. 2.32. Figure 2.8 illustrates this procedure for the case of sixth order. If n is the order of the formulation, one can show that $n/2$ weights would have to be changed for $n/2-1$ divergence operators. As the condition derived from Eq. 2.32 only specifies $n/2$ independent constraints (one for each grid point), the determination of the updated weights is not unique. The weights are then chosen so as to optimize the order of accuracy of the divergence operators. This method is applied in such a way that the order of accuracy of the gradient normal to the wall increases with distance to the wall. The weights for the divergence operator have been precomputed for fourth and sixth order discretization and are available in Table 2.2 with the order of accuracy corresponding to the evaluation of the different quantities. Only the case of a boundary on one side is presented. It is straightforward to derive the divergence operators for the other side. Also, note that the multi-dimensional extension of this stencil treatment is trivial, since directions are naturally uncoupled. It should be observed that in the case of fourth order discretization, the current procedure recovers the result proposed by Morinishi *et al.* [73].

n	Weights								Effective order
	Outside		Inside						
4	·	0	$-\alpha_1 - \frac{2}{3}\alpha_2$	$\alpha_1 + \frac{1}{3}\alpha_2$	$\frac{1}{3}\alpha_2$	·	·	·	1
4	·	·	$-\frac{1}{3}\alpha_2$	$-\alpha_1$	α_1	$\frac{1}{3}\alpha_2$	·	·	4
6	0	0	$-\alpha_1 - \frac{2}{3}\alpha_2 - \frac{1}{5}\alpha_3$	$\alpha_1 + \frac{1}{3}\alpha_2 - \frac{2}{5}\alpha_3$	$\frac{1}{3}\alpha_2 + \frac{2}{5}\alpha_3$	$\frac{1}{5}\alpha_3$	·	·	1
6	·	0	$-\frac{1}{3}\alpha_2 - \frac{3}{5}\alpha_3$	$-\alpha_1 + \frac{3}{5}\alpha_3$	$\alpha_1 - \frac{1}{5}\alpha_3$	$\frac{1}{3}\alpha_2$	$\frac{1}{5}\alpha_3$	·	2
6	·	·	$-\frac{1}{5}\alpha_3$	$-\frac{1}{3}\alpha_2$	$-\alpha_1$	α_1	$\frac{1}{3}\alpha_2$	$\frac{1}{3}\alpha_3$	6

Table 2.2: Weights for the mass conserving nth order interpolations.

As the normal velocity at a wall is zero, Eq. 2.35 is already satisfied. In the case of inflow/outflow conditions, the total mass flux leaving the domain should be exactly equal to the total mass flux entering the domain. For example, this could be done by adjusting the mean velocity at the outlet before solving the Poisson equation [36].

2.5.3 Momentum conservation

While global mass conservation is mandatory for low-Mach number formulations, global conservation of momentum might be relaxed. In fact, one might just use a simple procedure where velocities outside the domain are set to zero in the case of walls and to their corresponding values in case of inflow/outflow Dirichlet conditions. However, this procedure would not be very accurate. Furthermore, if exact conservation of momentum is preferred, a new procedure has to be derived. Morinishi *et al.* [72] proposed a method that discretely conserves momentum for fourth order accurate formulations by prescribing the flux at the single point outside of the physical domain. However, this approach cannot be easily extended to higher than fourth order, as different evaluations of the fluxes are required at the same point for higher order schemes.

To ensure that Eq. 2.32 is verified, the divergence and interpolation operators that appear in the momentum equation (Eq. 2.2) have to be changed. The procedure will be outlined for the fourth order accurate discretization of the term $d(\rho u_x u_y)/dx$ for the u_y velocity component (Fig. 2.9). A similar procedure would be used for the treatment of the other convective terms. In the discretization of the momentum equation (Eq. 2.16), the fluxes are constructed as the product of a full order interpolation of the momentum

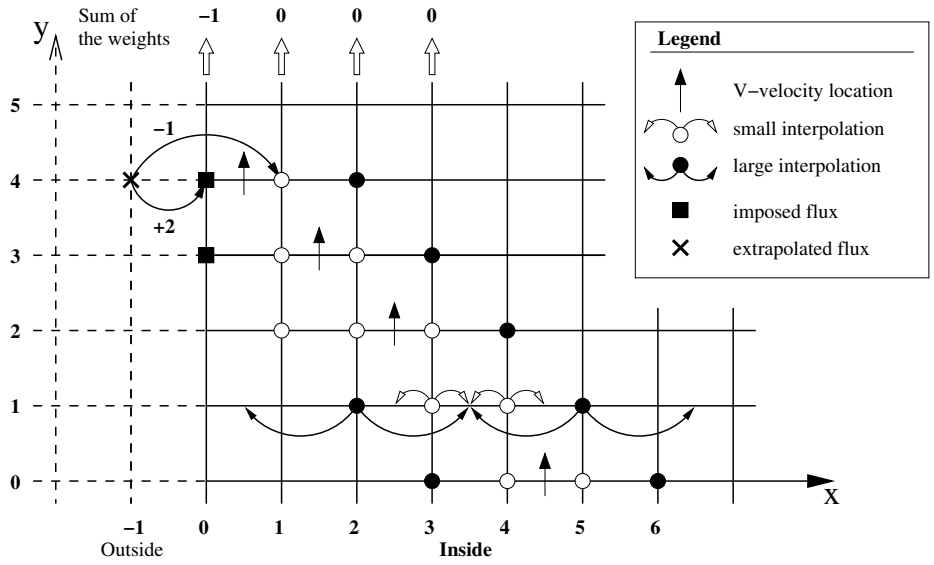

Figure 2.9: Definition of the procedure to update the divergence operator to ensure momentum conservation (illustrated for fourth order).

$(\overline{\left(\frac{J}{h_x}g_x\right)}^{4\text{th}\,\zeta_y})$ and a second order interpolation of the velocities with variable stencil sizes $(\overline{u_y}^{(2l-1)\,\zeta_x})$. The procedure to ensure global conservation of momentum can be decomposed as follows:

- First, the size of the stencil used for the second order interpolations is changed to avoid looking for a value outside of the physical domain. In Fig. 2.9, this is done for the flux evaluated at the point $(x, y) = (1, 2)$ for which the interpolation $\overline{u_y}^{3\,\zeta_x}$ is replaced by $\overline{u_y}^{1\,\zeta_x}$.

- Second, the momentum values used in the interpolation are set to zero for values outside the physical domain, as the normal velocity to the wall is always zero.

- Finally, the fluxes outside the domain are evaluated using second order extrapolation from values at the wall and inside the domain. For instance, the flux at the point

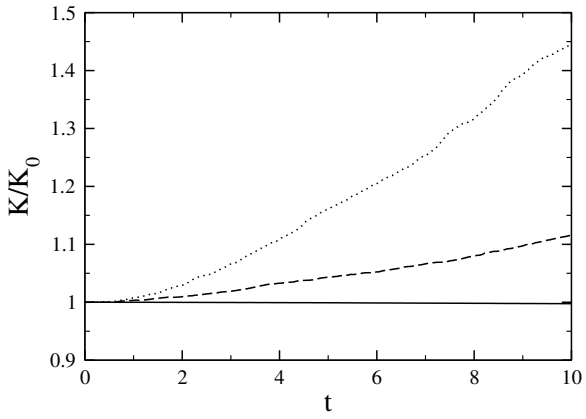

Figure 2.10: Temporal evolution of the kinetic energy for a domain with walls: second order (solid line); fourth order (dashed line); sixth order (dotted line).

$(x, y) = (-1, 4)$ would be written as

$$f|_{(-1,4)} = 2 \cdot \overline{\left(\frac{J}{h_x} g_x\right)}^{n\text{th}\,\zeta_y}\Big|_{(0,4)} \cdot u_y^{bc} - \overline{\left(\frac{J}{h_x} g_x\right)}^{n\text{th}\,\zeta_y}\Big|_{(1,4)} \cdot \overline{u_y}^{1\,\zeta_x}\big|_{(1,4)}, \qquad (2.36)$$

where u_y^{bc} would be zero for a wall.

The treatment of the pressure gradient is simpler because of its linear nature. In fact, the same procedure previously proposed for the divergence operator of the continuity equation is applied to the differentiation operator used for the pressure gradient (Table 2.2). Furthermore, a zero normal pressure gradient is enforced when evaluated at the boundary interface.

2.5.4 Energy conservation in an inviscid channel

The proposed boundary conditions were developed to ensure exact primary conservation (mass and momentum). To analyze their impact on the conservation of energy, the simulation of Section 2.4.8 is repeated with no-slip walls in the y direction. The same stretched mesh is used for the simulation. Figure 2.10 compares the temporal evolution of the total kinetic energy for different orders of accuracy. The second order formulation recovers the

energy conservation obtained in Section 2.4.8. On the other hand, the total kinetic energy increases for the fourth and sixth order formulations. However, this energy increase remains limited, and is found to be of the same order than the second order temporal errors obtained in Fig. 2.6 with the Runge-Kutta time integration scheme. Furthermore, in the presence of viscosity, the velocities at the wall would be zero, thus reducing even further the energy increase due to the proposed boundary treatment. In realistic configurations, such an increase in kinetic energy is expected to have very little effect on the overall solution, as will be shown for several wall-bounded flows in Section 2.8.

2.6 Centerline treatment

2.6.1 Singularity at the axis

In cylindrical coordinates, the Navier-Stokes equations present a singularity at the axis ($r = 0$) as the inverse of the radius appears in some of the terms of the continuity and momentum equations. Morinishi *et al.* [73] have already shown that this singularity is not physical, but rather originates from the coordinate system. For instance, the equation for the radial component of the velocity on the axis can be transformed to remove the singularity. For an inviscid flow, this would yield:

$$\frac{\partial \rho u_r}{\partial t} + \frac{\partial \rho u_x u_r}{\partial x} + \frac{\partial}{\partial r}\left(2\rho u_r u_r + \frac{\partial \rho u_r u_\theta}{\partial \theta} - \rho u_\theta u_\theta\right) + \frac{\partial p}{\partial r} = 0. \tag{2.37}$$

Furthermore, because of the coordinate transformation, the evaluation at the axis of some of the quantities is single-valued, while others are multi-valued. For example, the radial and azimuthal velocities are multivalued at the axis since

$$u_r(x, 0, \theta) = u_y(x, 0)\cos\theta + u_z(x, 0)\sin\theta, \tag{2.38}$$

$$u_\theta(x, 0, \theta) = -u_y(x, 0)\sin\theta + u_z(x, 0)\cos\theta, \tag{2.39}$$

where u_y and u_z represent the two components of the velocity vector in a cartesian frame of reference. Any discrete formulation should ensure that both equations are satisfied.

2.6.2 Radial velocity on the axis

Because of the staggering arrangement of the components of the velocity vector inherent to the discrete formulation presented in Section 2.4, only the radial velocity is located exactly on the axis. To avoid the resulting singularity, several treatments have been proposed where the radial velocity at the axis is reconstructed from some off-axis values of velocity components [22, 30, 73]. All of these treatments are based on an equation equivalent to Eq. 2.38 and assume that the multivalued radial component of the velocity vector can be expressed as

$$u_r(x, 0, \theta_{k+1/2}) = \overline{u_y}(x, 0) \cos\theta_{k+1/2} + \overline{u_z}(x, 0) \sin\theta_{k+1/2}. \tag{2.40}$$

Several expressions have been formulated for $\overline{u_y}$ and $\overline{u_z}$ as averages over the θ direction of the radial velocity or the azimuthal velocity or a combination of both. As the value of the radial velocity at the axis only appears in the convective and the viscous terms of the equations for the radial velocity, the formulation proposed by Morinishi *et al.* [73] is retained:

$$\overline{u_y}(x, 0) = \frac{2}{N_\theta} \sum_{k=0}^{N_\theta - 1} u_r(x, r_1, \theta_{k+1/2}) \cos\theta_{k+1/2}, \tag{2.41}$$

$$\overline{u_z}(x, 0) = \frac{2}{N_\theta} \sum_{k=0}^{N_\theta - 1} u_r(x, r_1, \theta_{k+1/2}) \sin\theta_{k+1/2}, \tag{2.42}$$

where r_1 is the radius of the first off axis radial velocity. Using the series expansion at the axis proposed by Constantinescu and Lele [16] for the radial velocity, one can show that the velocity thus resconstructed is second order accurate in the radial direction. However, since the value for the velocity is obtained by interpolation of other velocities, strict conservation of energy cannot be shown. In fact, Morinishi *et al.* [73] have already shown that the kinetic energy increases for purely inviscid flows.

Recently, Morinishi *et al.* [73] have formulated a discrete equation for the radial velocity

at the axis, which discretely conserves kinetic energy. As for the velocity reconstruction, this equation is also second order accurate in the radial direction.

2.6.3 On the other side of the axis

The original discrete formulation of the Navier-Stokes equations by Morinishi *et al.* [73] was only second order accurate in the radial direction. As for simple pipe or jet flows most velocity gradients are found in this direction, it is worth considering increasing the order of accuracy in this direction. However, as the order of accuracy increases, the length of the stencil increases, and more and more points on the other side of the axis will have to be used. The concept of using information on the other side of the axis was proposed in the context of second order schemes by Eggels *et al.* [22], and used also for example by Verzicco and Orlandi [114].

Constantinescu and Lele [16] have already shown that necessary values at negative radius can be expressed as simple functions of values found at positive radius. For instance, they pointed out that:

$$\begin{aligned} u_x(x,-r,\theta) &= \ u_x(x,r,\theta+\pi) \\ u_r(x,-r,\theta) &= -u_r(x,r,\theta+\pi) \\ u_\theta(x,-r,\theta) &= -u_\theta(x,r,\theta+\pi) \end{aligned} \tag{2.43}$$

In the discrete formulation presented in Section 2.4, other quantities are also required for points across the axis. Following the same methodology, one can show that the scaling factors as well as the Jacobian satisfy similar symmetry or anti-symmetry conditions:

$$\begin{aligned} h_x(x,-r,\theta) = \Delta x &= h_x(x,r,\theta+\pi), \\ h_r(x,-r,\theta) = \Delta r &= h_r(x,r,\theta+\pi), \\ h_\theta(x,-r,\theta) = -r\Delta\theta &= -h_\theta(x,r,\theta+\pi), \\ J(x,-r,\theta) = -r\Delta r\Delta x\Delta\theta &= -J(x,r,\theta+\pi). \end{aligned} \tag{2.44}$$

The last relation is different from the relation used by Morinishi *et al.* [73] in their derivation of the equation for the radial velocity at the axis, where the Jacobian was given

as

$$J(x, -r, \theta) = J(x, r, \theta + \pi). \tag{2.45}$$

However, the expression for the Jacobian in Eq. 2.45 cannot be used for higher order formulations of the terms in the radial directions, as it would introduce numerical errors in the divergence of the velocity field close to the axis. This can be clearly illustrated with the example of a uniform flow of unity velocity magnitude characterized by

$$\begin{aligned} u_r(x, r, \theta) &= +\cos\theta \\ u_\theta(x, r, \theta) &= -\sin\theta. \end{aligned} \tag{2.46}$$

With Eq. 2.44, the fourth order accurate evaluation of the continuity equation (Eq. 2.18) at the center of the first off-axis cell $(x, r_{1/2}, \theta)$ takes the form

$$(\text{cont-}n\text{-antisym}) = \frac{1}{r_{1/2}} \left(\alpha_1 + \alpha_2 - 1 + O\left(\Delta\theta^4\right)\right) \cos\theta, \tag{2.47}$$

which is indeed fourth order accurate since $\alpha_1 + \alpha_2 = 1$ (Eq. 2.12). On the other hand, with Eq. 2.45, the continuity equation becomes

$$(\text{cont-}n\text{-sym}) = \frac{1}{r_{1/2}} \left(\alpha_1 + \frac{\alpha_2}{3} - 1 + O\left(\Delta\theta^4\right)\right) \cos\theta, \tag{2.48}$$

which introduces a constant error in the continuity equation.

2.6.4 Test case

To assess the stability and accuracy of the possible treatments of the axis as well as the higher order formulations, a Lamb vortex [67] is convected in a cylindrical configuration across the axis. This configuration, which corresponds to a dipole vortex inside a circle of unity radius surrounded by a potential flow, was first presented by Verzicco and Orlandi [114]. The two dimensional configuration consists of a disk with radius $R = 2.5$ with an initial vortex centered around $(r, \theta) = (1, 0)$. For a vortex centered on the axis, the

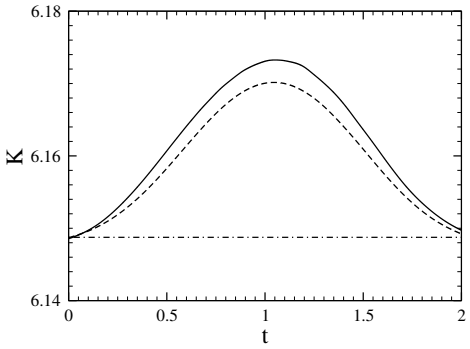

Figure 2.11: Temporal evolution of the kinetic energy for the convection of a Lamb vortex for different pole treatments in cylindrical coordinates: second order (solid line) and fourth order (dashed line) with second order velocity reconstruction; second order with the axis equation of Morinishi *et al.* [73] (dash-dotted line).

velocity components are given by the expressions

$$u_r = \begin{cases} U\left(C\frac{J_1(a_1 r)}{a_1 r} - 1\right)\cos\theta & \text{for } r < 1 \\ -\frac{U}{r^2}\cos\theta & \text{for } r > 1, \end{cases} \tag{2.49}$$

$$u_\theta = \begin{cases} U\left(1 - C\left(J_0(a_1 r) - \frac{J_1(a_1 r)}{a_1 r}\right)\right)\sin\theta & \text{for } r < 1 \\ -\frac{U}{r^2}\sin\theta & \text{for } r > 1, \end{cases} \tag{2.50}$$

where $C = \frac{2}{J_0(a_1)}$, with $J_0(r)$ and $J_1(r)$ the Bessel functions of the first kind and a_1 the first root of the Bessel function ($J_1(a_1) = 0$). The vortex advects itself at the speed U. The expressions for an off axis vortex can easily be derived.

A first simulation is performed on a uniform mesh with resolution $N_x \times N_r \times N_\theta = 1\times64\times64$ to assess the conservation properties as well as the overall accuracy of the schemes. The timestep used for those simulations is taken to be $\Delta t = 5.10^{-4}$, which corresponds to a maximum convective CFL condition in the azimuthal direction of 0.48, and which is small enough to avoid temporal errors. Figure 2.11 shows the time history of the kinetic energy in the domain for various pole treatments and scheme orders. As expected, the solution of the equation for the radial velocity at the axis proposed by Morinishi *et al.* [73] assures

perfect discrete conservation of kinetic energy, while a reconstruction of the radial velocity by interpolation does not ensure strict conservation of kinetic energy. It is also to be noted that in this particular case, the kinetic energy fluctuations are smaller for higher order discretization. To better analyze the accuracy of the different pole treatments, contours of the vorticity magnitude are created as the vortex crosses the axis (Fig. 2.12). While the velocity reconstruction method does not conserve kinetic energy, it still shows good accuracy when compared to the exact solution. Increasing the order of accuracy leads to a small improvement of the results as the first order errors are mostly produced by the centerline treatment. The comparison has also been done for the pole treatment proposed by Morinishi *et al.* [73]. The solution of the discrete equation for the radial velocity at the axis introduces some disturbances upstream of the vortex and alter significantly the vorticity contours at the pole. By using a Taylor expansion in the radial direction, it can be shown that the discrete equation solved at the axis has the following limit:

$$\frac{\partial \rho u_r}{\partial t} + \frac{\partial \rho u_x u_r}{\partial x} + \frac{\partial}{\partial r}\left(\rho u_r u_r + \rho u_r \frac{\partial u_\theta}{\partial \theta} - \rho u_\theta u_\theta\right) + u_r \frac{\partial \rho u_r}{\partial r} + \frac{\partial p}{\partial r} = 0. \tag{2.51}$$

This equation differs significantly from Eq. 2.37 which should be the analytical equivalent for any equations for the radial velocity at the axis. These errors produced in a very small region of the domain might not affect the overall accuracy of the formulation in fully turbulent flows. However, it is preferable to ensure at least first order convergence everywhere in the domain in order to obtain that the numerical errors decrease with the mesh size. As a result, the choice was made to use the second order velocity reconstruction at the axis instead of enforcing strict energy conservation by solving the equation proposed by Morinishi *et al.* [73].

Finally a more thourough accuracy analysis has been performed by varying the mesh size. First, a solution is computed on a very fine mesh with $N_x \times N_r \times N_\theta = 1 \times 512 \times 512$. This solution is assumed to represent adequately the exact solution. Several runs are then performed with the second order accurate formulation with varying mesh sizes. Because of the semi-implicit nature of the time integration scheme, the computations are conducted

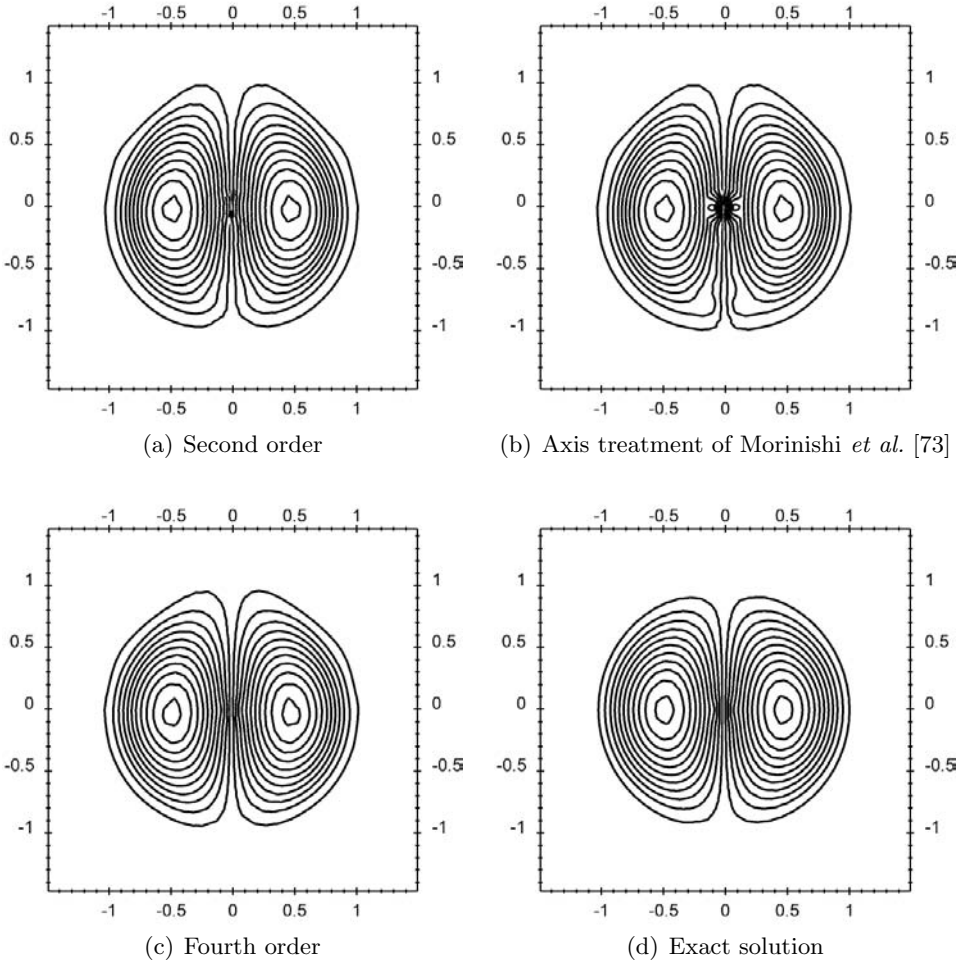

(a) Second order (b) Axis treatment of Morinishi *et al.* [73]

(c) Fourth order (d) Exact solution

Figure 2.12: Contours of vorticity magnitude for the convection of a Lamb vortex in cylindrical coordinates.

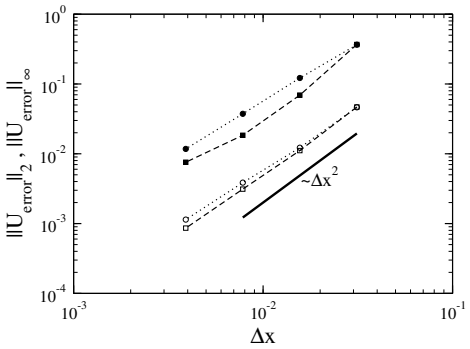

Figure 2.13: Accuracy check for the inviscid convection of a Lamb vortex in cylindrical coordinates: L_2-norm (open symbols) and L_∞-norm (closed symbols) for radial velocity (dotted line) and azimuthal velocity (dashed line).

with a maximum CFL condition in the azimuthal direction of 5. Figure 2.13 shows the L_2 and L_∞ norms for the radial and the azimuthal velocities. Both norms for both components show nearly perfect second order accuracy for the simulation. Since the axis treatment is only second order accurate, and the test case puts the emphasis on the centerline itself, the higher order accurate formulations will not display better than second order accuracy. However, in realistic cases where the centerline does not play such a major role, we do not expect the limited accuracy at the axis to degrade the quality of the solution significantly, and therefore we should be able to fully benefit from the high order accuracy.

2.7 Viscous formulation

In order to consistently reduce the spatial discretization errors when solving the Navier-Stokes equations, the order of accuracy of the viscous terms should also be increased. However, no aliasing errors will be generated by these terms, since they are linear in velocity. Moreover, because of its dissipative nature, the viscous part of the Navier-Stokes equation does not typically lead to stability issues, and therefore it is more easily discretized than the convective part. Thus, a straightforward methodology for computing high order accurate viscous terms based on Lagrange polynomials will be presented here.

2.7.1 Numerical discretization

To consistently obtain high order accuracy on non-uniform meshes, we introduce a different set of discrete operators than for the convective terms, based on a local Lagrange polynomial representation of the quantity on which the operators have to be applied. In order to obtain an nth order accurate interpolation or differentiation of a quantity ϕ at a location x in the direction x_i, an $(n-1)$th order Lagrange polynomial P is fitted through the n data points available in the stencil. This operation is centered in computational space, meaning that the interpolation or differentiation of ϕ is computed with as many stencil points on one side of the evaluation point than on the other. The interpolation is written

$$\overline{\phi}^{n\text{th}\,x_i} = P(x), \tag{2.52}$$

while the differentiation is expressed by

$$\frac{\delta_{n\text{th}}\phi}{\delta_{n\text{th}}x_i} = P'(x). \tag{2.53}$$

Note that we use the physical space in the notations, to differentiate these operators from the convective operators. Since all calculations are performed in physical space directly, high order accuracy is ensured even on non-uniform meshes. These operators are all linear in ϕ, meaning that they can be pre-computed initially and stored at every mesh location in order to save computational time. With these operators defined, the divergence of the velocity vector based on the viscous metrics can be introduced as

$$(\text{visc-div-}n) = \frac{\delta_{n\text{th}}u_1}{\delta_{n\text{th}}x_1} + \frac{1}{\beta}\frac{\delta_{n\text{th}}(\beta u_2)}{\delta_{n\text{th}}x_2} + \frac{1}{\beta}\frac{\delta_{n\text{th}}u_3}{\delta_{n\text{th}}x_3}, \tag{2.54}$$

where β is one in cartesian coordinates and x_2 in cylindrical coordinates. The viscous term in the Navier-Stokes equation is then written

$$\begin{aligned}(\text{visc-}n)_{x_1} = &\frac{\delta_{n\text{th}}}{\delta_{n\text{th}}x_1}\left[2\mu\left(\frac{\delta_{n\text{th}}u_1}{\delta_{n\text{th}}x_1} - \frac{1}{3}(\text{visc-div-}n)\right)\right] \\ &+ \frac{1}{\beta}\frac{\delta_{n\text{th}}}{\delta_{n\text{th}}x_2}\left[\beta\overline{\overline{\mu}^{2\text{nd }x_1}}^{2\text{nd }x_2}\left(\frac{\delta_{n\text{th}}u_1}{\delta_{n\text{th}}x_2} + \frac{\delta_{n\text{th}}u_2}{\delta_{n\text{th}}x_1}\right)\right] \\ &+ \frac{1}{\beta}\frac{\delta_{n\text{th}}}{\delta_{n\text{th}}x_3}\left[\overline{\overline{\mu}^{2\text{nd }x_1}}^{2\text{nd }x_3}\left(\frac{1}{\beta}\frac{\delta_{n\text{th}}u_1}{\delta_{n\text{th}}x_3} + \frac{\delta_{n\text{th}}u_3}{\delta_{n\text{th}}x_1}\right)\right],\end{aligned} \tag{2.55}$$

$$\begin{aligned}(\text{visc-}n)_{x_2} = &\frac{\delta_{n\text{th}}}{\delta_{n\text{th}}x_1}\left[\overline{\overline{\mu}^{2\text{nd }x_1}}^{2\text{nd }x_2}\left(\frac{\delta_{n\text{th}}u_2}{\delta_{n\text{th}}x_1} + \frac{\delta_{n\text{th}}u_1}{\delta_{n\text{th}}x_2}\right)\right] \\ &+ \frac{1}{\beta}\frac{\delta_{n\text{th}}}{\delta_{n\text{th}}x_2}\left[2\beta\mu\left(\frac{\delta_{n\text{th}}u_2}{\delta_{n\text{th}}x_2} - \frac{1}{3}(\text{visc-div-}n)\right)\right] \\ &+ \frac{1}{\beta}\frac{\delta_{n\text{th}}}{\delta_{n\text{th}}x_3}\left[\overline{\overline{\mu}^{2\text{nd }x_2}}^{2\text{nd }x_3}\left(\frac{1}{\beta}\frac{\delta_{n\text{th}}u_2}{\delta_{n\text{th}}x_3} + \frac{\delta_{n\text{th}}u_3}{\delta_{n\text{th}}x_2} - \epsilon\frac{1}{\beta}\overline{u_3}^{n\text{th }x_2}\right)\right] \\ &- \epsilon\frac{1}{\beta}\overline{\left[2\mu\left(\frac{1}{\beta}\frac{\delta_{n\text{th}}u_3}{\delta_{n\text{th}}x_3} - \frac{1}{3}(\text{visc-div-}n) + \epsilon\frac{1}{\beta}\overline{u_2}^{n\text{th }x_2}\right)\right]}^{n\text{th }x_2},\end{aligned} \tag{2.56}$$

$$\begin{aligned}(\text{visc-}n)_{x_3} = &\frac{\delta_{n\text{th}}}{\delta_{n\text{th}}x_1}\left[\overline{\overline{\mu}^{2\text{nd }x_1}}^{2\text{nd }x_3}\left(\frac{\delta_{n\text{th}}u_3}{\delta_{n\text{th}}x_1} + \frac{1}{\beta}\frac{\delta_{n\text{th}}u_1}{\delta_{n\text{th}}x_3}\right)\right] \\ &+ \frac{1}{\beta}\frac{\delta_{n\text{th}}}{\delta_{n\text{th}}x_2}\left[\beta\overline{\overline{\mu}^{2\text{nd }x_2}}^{2\text{nd }x_3}\left(\frac{\delta_{n\text{th}}u_3}{\delta_{n\text{th}}x_2} + \frac{1}{\beta}\frac{\delta_{n\text{th}}u_2}{\delta_{n\text{th}}x_3} - \epsilon\frac{1}{\beta}\overline{u_3}^{n\text{th }x_2}\right)\right] \\ &+ \frac{1}{\beta}\frac{\delta_{n\text{th}}}{\delta_{n\text{th}}x_3}\left[2\mu\left(\frac{1}{\beta}\frac{\delta_{n\text{th}}u_3}{\delta_{n\text{th}}x_3} - \frac{1}{3}(\text{visc-div-}n) + \epsilon\frac{1}{\beta}\overline{u_2}^{n\text{th }x_2}\right)\right] \\ &+ \epsilon\frac{1}{\beta}\overline{\left[\beta\overline{\overline{\mu}^{2\text{nd }x_2}}^{2\text{nd }x_3}\left(\frac{\delta_{n\text{th}}u_3}{\delta_{n\text{th}}x_2} + \frac{1}{\beta}\frac{\delta_{n\text{th}}u_2}{\delta_{n\text{th}}x_3} - \epsilon\frac{1}{\beta}\overline{u_3}^{n\text{th }x_2}\right)\right]}^{n\text{th }x_2}.\end{aligned} \tag{2.57}$$

2.7.2 Centerline treatment

The β coefficient equals x_2 in cylindrical coordinates, meaning that a singularity arises in the discretization of the viscous term when $1/r$ is evaluated at the centerline. In Eq. 2.55, this is never the case, since $1/r$ always appears off-axis as a result of the staggered variable arrangement. Similarly, in Eq. 2.56 the situation does not arise because the u_r velocity at the axis is obtained through a different procedure, as explained in Section 2.6. On the other hand, in Eq. 2.57, $\frac{1}{r}\frac{\delta_{n\text{th}}u_r}{\delta_{n\text{th}}\theta} - \frac{1}{r}\overline{u_\theta}^{n\text{th }r}$ is evaluated twice on the axis. However, on the

centerline, the u_r and u_θ velocity components are related by

$$\frac{1}{r}\frac{\partial u_r}{\partial \theta} = \frac{u_\theta}{r}, \tag{2.58}$$

meaning that

$$\frac{1}{r}\frac{\delta_{n\text{th}} u_r}{\delta_{n\text{th}}\theta} - \frac{1}{r}\overline{u_\theta}^{n\text{th}\,r} = 0. \tag{2.59}$$

With this property, the singularity at the centerline can thus be removed by ensuring that when $r = 0$, $1/\beta$ is set to zero explicitly.

2.7.3 Boundary conditions

The strategy that was chosen to handle viscous boundary conditions differs significantly from that of the convective terms. In order to maximize the order of accuracy close to the boundaries, the operators that were introduced for the viscous terms are upwinded to ensure that no point outside the physical domain is reached. The overall strategy is therefore to discard all stencil points that are outside the physical domain, and to construct upwinded operators from a Lagrange polynomial of the highest possible order given the available stencil points. For instance, as illustrated in Fig. 2.14 for fourth order, the evaluation of the polynomials (Eq. 2.52 and Eq. 2.53) at the point $(x, y) = (0, 3)$ is using two values inside the domain in addition to the boundary value itself whenever available. This methodology allows for an optimal accuracy close to the boundary, while ensuring that no outside value is ever used, which greatly simplifies the implementation of three-dimensional complex walls.

2.7.4 Decay of a Taylor-Green vortex

In order to verify the correct behavior of the proposed scheme for the viscous terms of the Navier-Stokes equations, the viscous dissipation of a two-dimensional Taylor-Green vortex inside a periodic box of size 2π has been simulated. The initial velocity is given by

$$\mathbf{u}\,(x, y) = \begin{pmatrix} \cos(x)\sin(y) \\ -\sin(x)\cos(y) \end{pmatrix}. \tag{2.60}$$

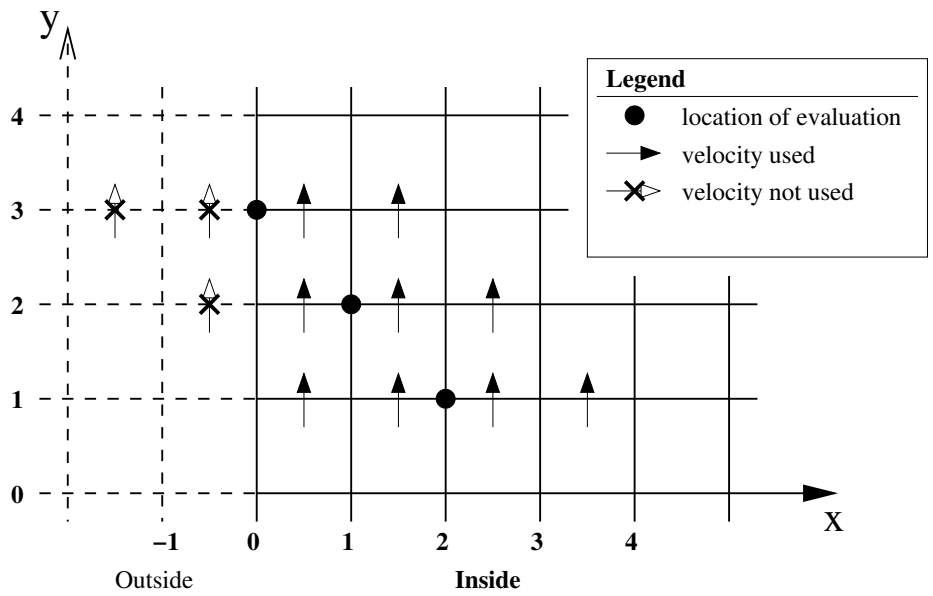

Figure 2.14: Definition of the procedure to compute the differentiation/interpolation operators close to boundaries (illustrated for fourth order).

The mesh is uniform in the y direction, but has stretching in the x direction. If x_0 is uniform in $[0, 2\pi]$, the mesh is defined as $x = x_0 + s_x \sin(x_0)$. The value of s_x is set to 0.5, leading to very strong stretching. The viscosity is set to $\mu = 1 \times 10^6$ to make sure that the numerical errors due to the convective terms are negligible in comparison to the viscous errors. In order to ensure that the numerical errors due to the time integration remain low, a time step size of $\Delta t = 5 \times 10^{-10}$ is chosen, leading to a viscous CFL number consistently below 0.2. The ratio Γ_N between the kinetic energy in the system at time $t = 5 \times 10^{-8}$ and the initial kinetic energy is compared to its analytical value Γ_A and the error is plotted in Fig. 2.15. Two different cases have been tested, namely the full viscous formulation presented in the beginning of Section 2.7, shown in Fig. 2.15(a), and a similar formulation where the definition of the divergence operator used in the continuity equation (Eq. 2.18) has been modified to match the divergence operator used in Eq. 2.54, shown in Fig. 2.15(b).

While the modified formulation displays the expected order of accuracy, the formulation

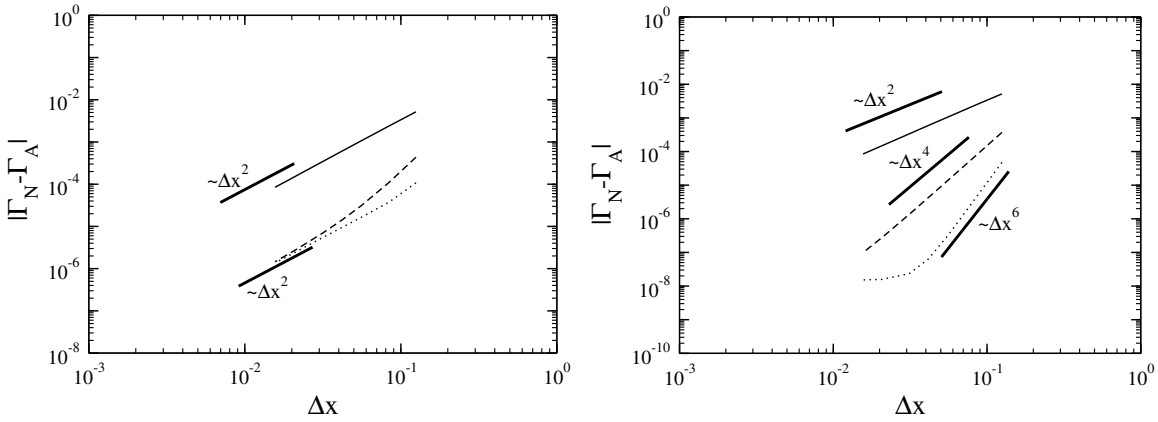

(a) (visc-div-n) from Eq. 2.54.

(b) $\sum_{i=1}^{3}\left(\frac{1}{J}\frac{\delta_{nth}}{\delta_{nth}\,\zeta_i}\left(\frac{J}{h_i}u_i\right)\right)$ replaced by (visc-div-n).

Figure 2.15: Accuracy check for the viscous term for a Taylor-Green vortex flow: second order (solid line); fourth order (dashed line); sixth order (dotted line).

with the unmodified divergence remains second order accurate, although the errors are greatly reduced by increasing the order of accuracy. This second order error is introduced when the dilatational part of the velocity gradient tensor is removed with a divergence operator that does not match the one used to enforce continuity. For an incompressible flow, we expect that $\nabla \cdot \mathbf{u} = 0$ discretely, however (visc-div-n) obtained by Eq. 2.54 will not be discretely zero. While this specific issue is interesting to notice, it is not expected to affect the quality of the results, since a significant reduction of two orders of magnitude is still obtained for the spatial discretization errors with the proposed formulation. Note also that in the absence of mesh stretching, the two divergence operators are discretely similar, therefore this problem does not arise.

2.8 Simulations of canonical flows

In this section, the arbitrarily high order accurate methods presented before are employed to simulate a range of canonical flows. The focus is mainly to study the influence of the order of the numerical schemes on the solution. This influence will be evaluated by considering

the classical quantities characterizing the flow statistics.

2.8.1 Homogeneous isotropic turbulence

For the first case, homogeneous isotropic turbulence is simulated by means of DNS and LES, conducted using the second, fourth, and sixth order schemes. The first simulation is for homogeneous isotropic turbulence forced linearly by the method proposed by Lundgren [64]. The Taylor Reynolds number is approximately 50, and the turbulence is resolved with $k_{max}\eta > 1.5$, where k_{max} is the highest resolved wavenumber and η is the Kolmogorov scale, as suggested by Yeung and Pope [121]. Note that this is the DNS case 3c performed by Rosales and Meneveau [95]. Figure 2.16(a) shows the nondimensional energy spectra obtained with the three numerical schemes used. It can be observed that for the three schemes the spectra are in excellent agreement with the results obtained by Rosales and Meneveau [95] with a spectral code. It seems however that the dispersive errors at the smallest resolved scale for the second order lead to a weak over-prediction of the energy at these scales. In the context of DNS, this does not appear to be a significant issue, since most of the energy dissipation occurs at larger scales.

The LES case is for decaying isotropic turbulence simulated on a 32^3 mesh using a classical dynamic subgrid-scale model [31, 59]. Note that for all the simulations in this paper, the evaluation of the velocity gradient tensor for the sub-grid scale model is performed with a second order accurate method, regardless of the order of accuracy used for the convective and viscous terms. The physical parameters are chosen to match the experiment of Comte-Bellot and Corrsin [15], and the initial field is constructed to have the three-dimensional energy spectrum of the experimental measurements at the first of the three measured times. The energy spectrum at these three times is plotted in Fig. 2.16(b) for second, fourth, and sixth order. It can be observed that at the smallest resolved scales, which are much more energetic in the case of LES than for DNS, the numerical errors become noticeable. Indeed, the spectra in the second order case slightly over-predicts the energy on a significant part of the inertial sub-range. This would suggest that one should avoid using the second order accurate formulation for testing sub-grid scale models. These results are in agreement with

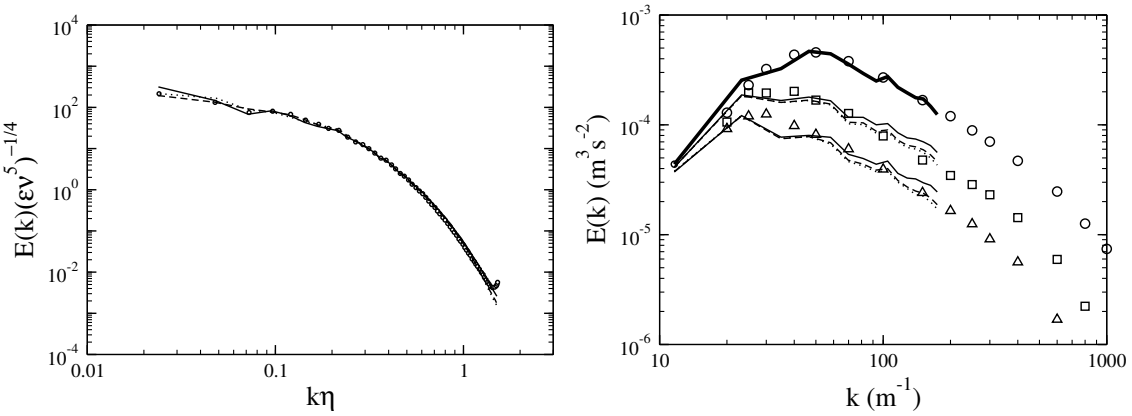

(a) DNS case (b) LES case

Figure 2.16: Kinetic energy spectra for homogeneous isotropic turbulence simulations: second order (solid line); fourth order (dashed line); sixth order (dotted line); spectral simulation [95] (symbols in left figure); experimental spectra [15] (symbols in right figure); spectrum of initial field (thick line in right figure).

the observations of Ghosal [32] and Chow and Moin [14]. Note that, even though there are noticeable differences between second and fourth order, results from sixth and fourth order are very close to each other. In our numerical experiments, we also observed that contributions from viscous and convective errors were of the same order.

2.8.2 Vortex ring colliding with a wall

To evaluate the impact of the proposed boundary conditions on the overall accuracy of the scheme, a vortex ring colliding with a wall is simulated. Following the numerical test of Verzicco and Orlandi [114], this simulation is performed in cylindrical coordinates using a two-dimensional axisymmetric domain of size $L_x \times L_r = 4 \times 4$, closed at $x = 0$ by a wall. Slip boundary conditions are applied at $x = 4$ and $r = 4$. A thin ring of initial Gaussian vorticity is placed at a height $x_0 = 2$ from the wall. The toroidal radius of the ring is set to $r_0 = 1$, leading to the following expression for the initial velocity field:

$$\mathbf{u}\,(x,r) = \begin{pmatrix} u_x \\ u_r \end{pmatrix} = \frac{1}{\pi s^2}\left(1 - e^{-s^2/a^2}\right)\begin{pmatrix} r - r_0 \\ x_0 - x \end{pmatrix}, \tag{2.61}$$

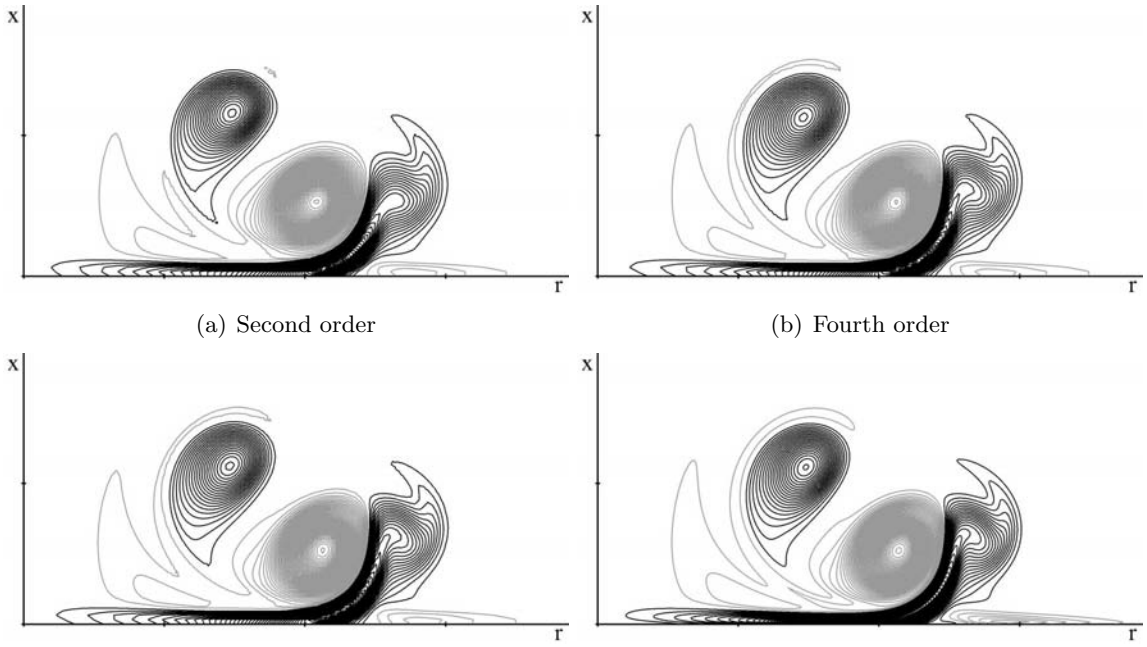

(a) Second order (b) Fourth order

(c) Sixth order (d) Second order, fine mesh

Figure 2.17: Azimuthal vorticity contours of a vortex ring colliding with a wall at $t = 30$.

where $s = \sqrt{(x - x_0)^2 + (r - r_0)^2}$ is the distance from the center of the ring core. As in [114], we set $a = 0.4131$ and the viscosity to 3.45×10^{-4}, leading to a Reynolds number of 2895. The simulation is run with a time step size $\Delta t = 0.03$ until $t = 30$, when the main vortex ring has generated both a secondary and a tertiary ring. The azimuthal vorticity contours are shown in Fig. 2.17 at the final time for second, fourth, and sixth order on a 128^2 mesh, as well as for second order on a 512^2 mesh. While the second order solution on the coarse mesh is already satisfactory, as pointed out by Verzicco and Orlandi [114], the solution converges towards the fine mesh solution as the order of accuracy is increased. To quantify this convergence, the azimuthal vorticity is plotted as a function of r at $x = 0.75$ for all four cases in Fig. 2.18. It clearly appears that the second order solution is not able to fully capture the peak in vorticity at $r = 2.75$, while the fourth order solution follows very accurately the fine mesh solution. Interestingly, very small differences are observed between the fourth order solution and the sixth order solution, indicating that for the given mesh,

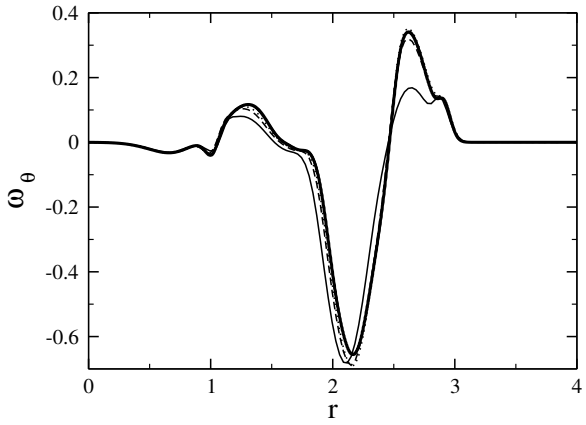

Figure 2.18: Azimuthal vorticity as a function of r at $x = 0.75$ and $t = 30$: second order (solid line); fourth order (dashed line); sixth order (dotted line); second order on the fine mesh (thick line).

convergence in the order of the scheme has almost been achieved. It can be noted that it was observed for this case that the convective order of accuracy was the most important. In our numerical tests, little improvement was obtained by increasing the order of accuracy of the viscous term.

2.8.3 Rayleigh-Taylor instability

The two-dimensional Rayleigh-Taylor instability problem is considered to check the ability of the method to simulate variable density flows accurately. The configuration consists of two miscible fluids separated by a horizontal perturbed interface. The heavy fluid (with unity density) is above the light fluid (with density 0.1). The mean interface is located at $y = 0$ in a domain size of $[-0.5, 0.5] \times [-0.5, 0.5]$. The exact location of the interface is given by

$$y_{int}(x) = -\alpha \sum_{k=1}^{7} \cos(\omega_k \pi x), \tag{2.62}$$

where the amplitude of the sinusoidal waves is $\alpha = 0.001$ and the wave numbers are $\omega_k = 4, 14, 23, 28, 33, 42, 51, 59,$ following the test case of Nourgaliev and Theofanous [76]. A

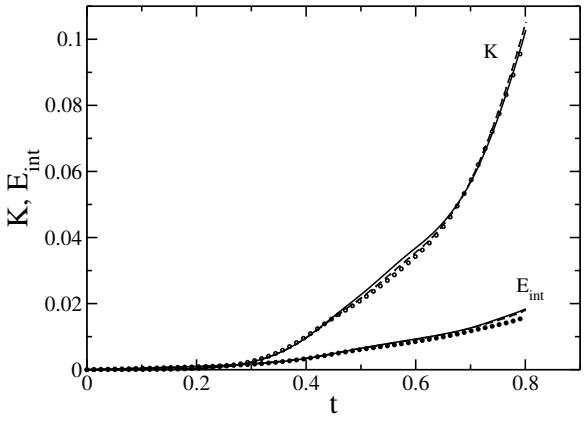

Figure 2.19: Temporal evolution of kinetic and internal energies of the Rayleigh-Taylor instability: second order (solid line), fourth order (dashed line), and sixth order (dotted line); second order on the fine mesh (symbols).

mixture fraction scalar field is constructed as

$$Z(x,y) = \frac{1}{2}\left(1 + \tanh\left(\frac{y_{int}(x) - y}{2\delta}\right)\right), \tag{2.63}$$

where the thickness of the interface is $\delta = 0.002$. Finally, the density is evaluated from the mixture fraction using the same equation of state as previously used in Section 2.4.8. The two fluids have identical kinematic viscosity $\nu = 0.001$ and kinematic diffusivity $D_Z = 0.0005$. The value for the gravity acceleration is $g = 9$ so that the Reynolds number is $Re = \sqrt{gL_y}L_x/\nu = 3000$. Simulations have been performed on two different meshes. A coarse mesh of $N_x \times N_y = 128 \times 128$ has been used for simulations with second, fourth, and sixth order accurate formulations, while a solution has been obtained on a finer grid of $N_x \times N_y = 512 \times 512$ mesh points with the second order formulation. The time step size is $\Delta t = 0.001$ for the coarse mesh and $\Delta t = 0.00025$ for the fine mesh.

Figure 2.19 shows the time evolution of the kinetic energy and the internal energy defined by Eq. 2.29 for the four simulations. While the fourth order formulation shows some differences compared to the second order, the sixth order shows little improvement over fourth order. As previously explained in Section 2.4.8, the energy transfer to internal

energy is caused by the discrepancy between the continuity and scalar transport equations. In the present simulations, there are two reasons for this discrepancy. The first contribution has already been described and comes from the numerical discretization. It is grid dependent and its effect decreases as the grid is refined. The amplitude of this contribution can be assessed by comparing the internal energy on the coarse and on the fine mesh. The second contribution comes from the scalar diffusion term. It appears clearly that the transfer to internal energy due to the numerical discretization is very small in comparison to the contribution due to the scalar diffusion.

Contour plots of the density are extracted at $t = 0.75$ for the four simulations (Fig. 2.20). While the second order formulation predicts the overall features of the instability, the fourth and sixth order formulations compare more favorably to the solution on the finer mesh. To further quantify these differences, the density profile at $y = 0$ is plotted in Fig. 2.21. The second order formulation, while capturing the overall shape of the density profile, is unable to correctly predict the dip in density at $x = \pm 0.1$. Increasing the order of accuracy from second to fourth and then to sixth leads to quantitatively better predictions of the density profile.

2.8.4 Turbulent pipe

To further analyze the influence of higher order discretization on turbulent simulations in the presence of mean gradients, a turbulent pipe flow is simulated by means of DNS. The configuration was originally investigated experimentally and numerically by Eggels *et al.* [22]. The Reynolds number, based on the radius and the friction velocity, was $\mathrm{Re}_\tau = 180$ for the DNS and in the range $\mathrm{Re}_\tau = 183 - 190$ for the experimental setup. For the DNS, Eggels *et al.* [22] used a domain of size $L_x \times L_r \times L_\theta = 10R \times R \times 2\pi$ and a grid resolution of $N_x \times N_r \times N_\theta = 256 \times 96 \times 128$ points. Further numerical analysis has been performed by Fukagata and Kasagi [30] with the same grid resolution but a different numerical discretization. The same grid resolution has been used for the present simulations, but with different orders of accuracy. The results are compared with the latest DNS results by Fukagata and Kasagi [30] and the experimental measurements of Eggels *et al.* [22] in

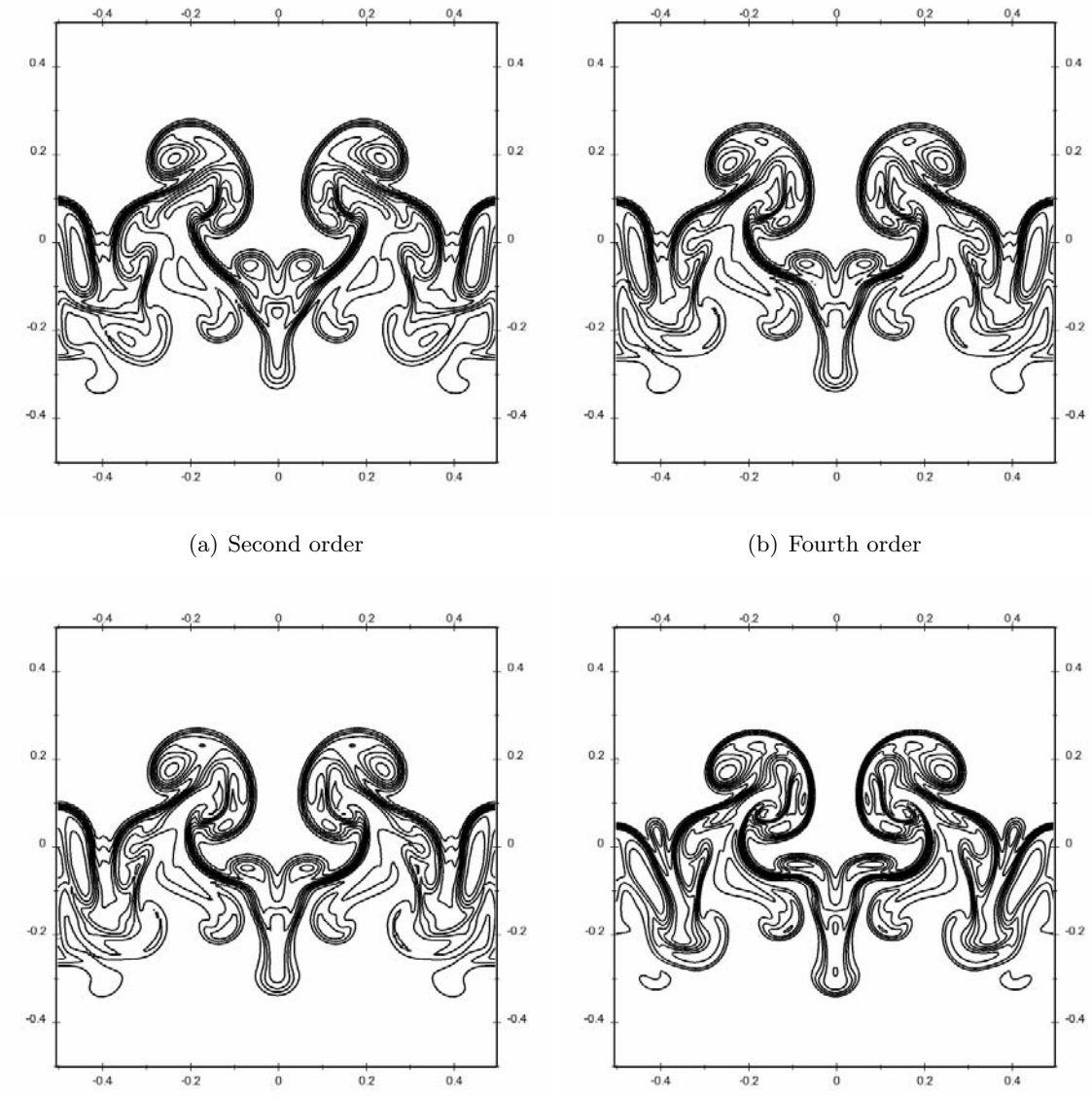

(a) Second order

(b) Fourth order

(c) Sixth order

(d) Second order, fine mesh

Figure 2.20: Density contours of Rayleigh-Taylor instability at $t = 0.75$.

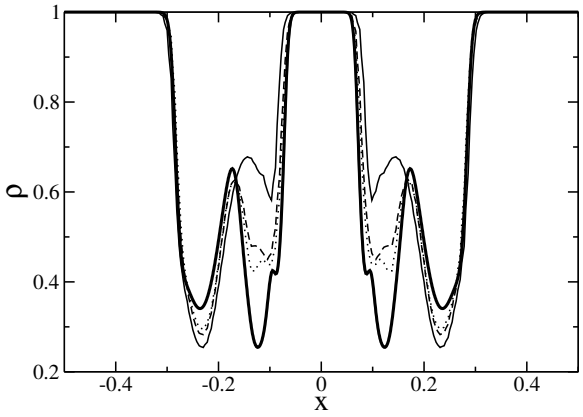

Figure 2.21: Density as a function of x at $y = 0.20$ and $t = 0.75$: second order (solid line); fourth order (dashed line); sixth order (dotted line); second order on the fine mesh (thick line).

Figs. 2.22(a), 2.22(c) and 2.22(e). The Reynolds number based on the radius and the bulk velocity is $\mathrm{Re}_b = 2655$. For all plots, $u_\tau = \mathrm{Re}_\tau/\mathrm{Re}_b$ is used to non-dimensionalize the statistical results.

The mean and the fluctuations of the velocities obtained with both the second and fourth order formulations compare extremely well with the DNS data of Fukagata and Kasagi [30]. The comparison of the fluctuations of the velocities shows only very little differences for the radial and azimuthal velocities. Also the skewness profiles of the radial and the axial velocities agree well with the experiments for the fourth order scheme, while the second order shows some minor deviations, especially in the viscous sub-layer where a slight over-prediction can be noticed. This over-prediction can also be observed in the second order accurate DNS results of Fukagata and Kasagi [30]. The skewness of the axial velocity in the log-layer is predicted to be nearly constant (around -0.5) by the second and fourth order formulations in agreement with the experimental measurements. On the other hand, the DNS data of Fukagata and Kasagi [30] predicts significantly lower values.

The importance of higher order accuracy is also investigated in the framework of LES. Because of the low Reynolds number, when simulated on a relatively coarse grid and with low order of accuracy, the flow can relaminarize [73]. Morinishi *et al.* [73] have already

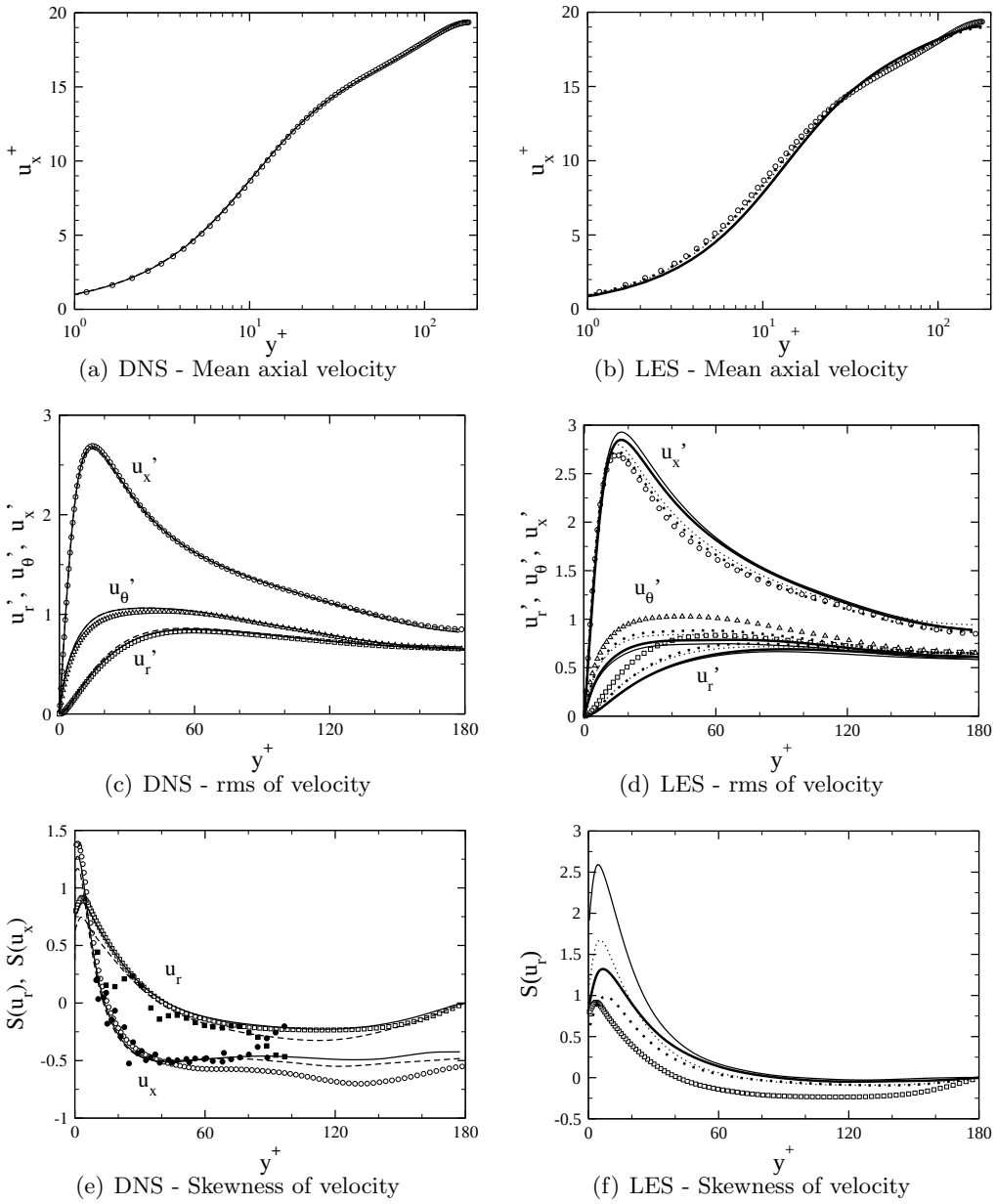

(a) DNS - Mean axial velocity

(b) LES - Mean axial velocity

(c) DNS - rms of velocity

(d) LES - rms of velocity

(e) DNS - Skewness of velocity

(f) LES - Skewness of velocity

Figure 2.22: Statistics of a pipe flow for the DNS and the LES cases: second order (solid line); fourth order (dashed line); sixth order (dotted line); DNS of Fukagata and Kasagi [30] (open symbols); experimental measurements of Eggels *et al.* [22] (closed symbols); dynamic Smagorinksy model (thin lines); Lagrangian dynamic model (thick lines).

performed several simulations with different orders of accuracy for the convective terms in the axial and azimuthal directions. However, the convective term in the radial direction as well as all diffusion terms remained second order accurate. In the present work, we intend to analyze the effects of higher order formulations for all convective and viscous terms. Two LES (second order and sixth order accurate) were performed using the grid employed by Morinishi *et al.* [73] with a resolution of $N_x \times N_r \times N_\theta = 48 \times 64 \times 48$ points. Two sub-grid scale models have been tested, namely a standard dynamic Smagorinsky model [31, 59] and the Lagrangian dynamic sub-grid scale model by Meneveau *et al.* [69].

Figures 2.22(b), 2.22(d), and 2.22(f) show the results obtained for the four simulations performed in comparison with the DNS results of Fukagata and Kasagi [30]. As expected, the sixth order formulation predicts significantly more accurately the mean and fluctuations of the velocities. The skewness of the radial velocity is greatly improved by changing the order of accuracy from second to sixth order. These results clearly show that increasing the order of accuracy of the convective terms in the radial direction as well as all the viscous terms has a significant impact on the quality of the LES predictions. It should also be noted that the impact of changing the order of accuracy appears far greater than that of changing the sub-grid scale model. For the given mesh, the Lagrangian model was found to consistently predict the flow with better accuracy than the standard dynamic procedure [31, 59]. However, the improvement that can be obtained by changing the sub-grid scale model is limited in comparison with the effect of increasing the order of accuracy of the numerical schemes, except for the skewness prediction, where the Lagrangian model performs surprisingly well. To analyze the performance of sub-grid scale models, the numerical errors due to the spatial discretization should be sufficiently small [32, 14], therefore it appears that the second order formulation should not be used in this case to develop and analyze models.

2.8.5 Round jet

Finally, the higher order formulations are applied in an LES of a variable density turbulent jet (Fig. 2.23). The configuration, studied experimentally by Amielh *et al.* [2] and Djeridane *et al.* [19], corresponds to an axisymmetric jet at ambient pressure and temperature. Pure

Figure 2.23: Volumetric rendering of the mixture fraction of helium for the variable density jet.

helium is injected through a pipe of diameter $D_j = 26\,\text{mm}$ at a bulk velocity of $\overline{U}_j = 25\,\text{m/s}$. A slow surrounding co-flow of air is supplied at a bulk velocity of $U_e = 0.9\,\text{m/s}$. The entire configuration is enclosed in a cylindrical vessel of internal diameter $D_e = 285\,\text{mm}$. The Reynolds number based on the diameter of the helium pipe and the average velocity on the axis ($U_j = 32\,\text{m/s}$) is $\text{Re}_j = 6890$. The density ratio between helium and air is about 7.2. The LES is performed on a grid with a resolution of $N_x \times N_r \times N_\theta = 128 \times 76 \times 64$ points. The lip that separates the helium jet from the air co-flow is represented as a wall of thickness $8 \times 10^{-4}\,\text{m}$ that extends over $2D_j$ into the computational domain. The sub-grid scale model used for the current simulations is the Lagrangian dynamic subgrid-scale model by Meneveau *et al.* [69] and extended for variable density and to include the modeling of the turbulent eddy diffusivity by Réveillon and Vervisch [94]. The fluid properties, such as the molecular viscosity and the molecular diffusivity, as well as the equation of state, are precomputed and tabulated as a function of mixture fraction. In order to generate the inflow conditions, a periodic cylindrical pipe is first computed. The turbulent velocity field at an x position is stored as a function of time in order to be re-injected at the entrance of the jet simulation. The computations are performed using the second and fourth order accurate formulations, and compared to the experimental results in Fig. 2.24. The rms

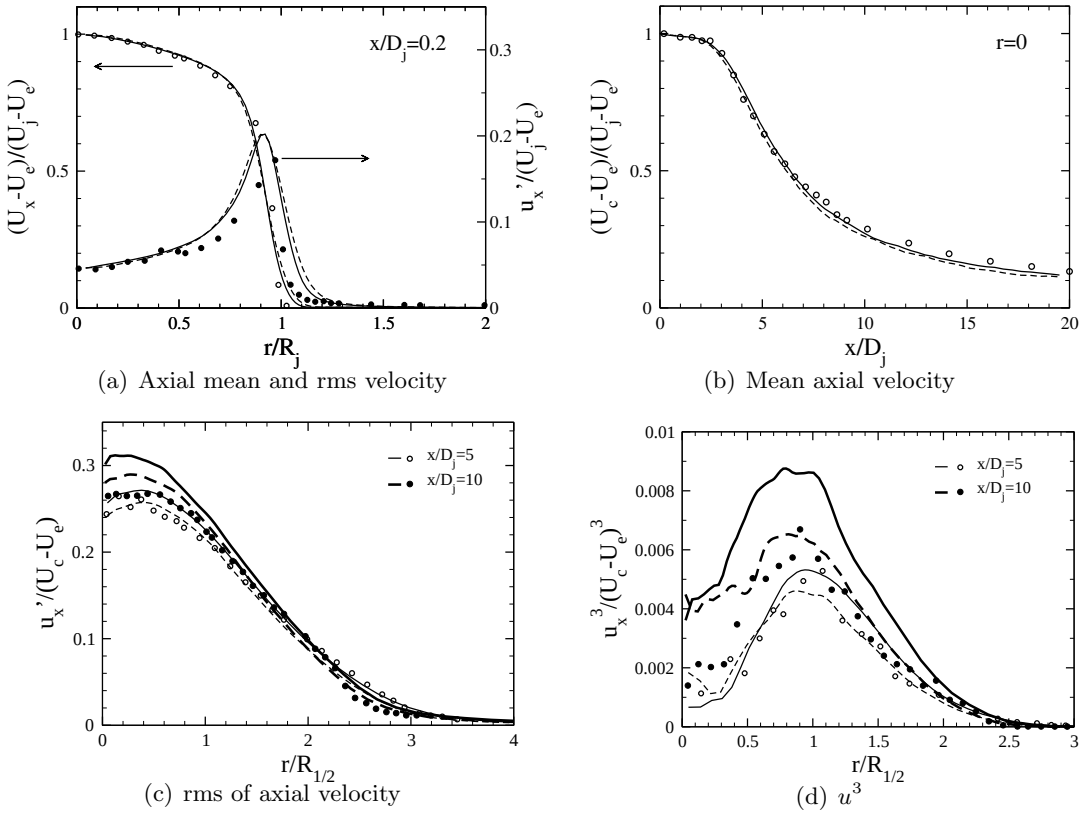

Figure 2.24: Statistics of the LES of the turbulent variable density jet: second order (solid line); fourth order (dashed line); experimental measurements [19, 2] (symbols).

values of the velocities are non-dimensionalized by using the velocity on the axis (U_c). The radii are non-dimensionalized by using the velocity half width radius ($R_{1/2}$).

Figure 2.24(a) shows that for both second and fourth order, the statistics at the first measurement station ($x/D_j = 0.2$) are in excellent agreement with the experimental results. The mean axial velocity on the axis shown in Fig. 2.24(b) is predicted with excellent accuracy by both the second order and the fourth order formulations. The length of the potential core as well as the decay of the mean velocity in the self similar region of the jet are well captured. However, differences between the two formulations start to appear when looking at higher order statistics. Figure 2.24(c) shows the rms of the velocity at two locations

Order	Turbulent pipe		Rayleigh-Taylor		Vortex ring		Isotropic turbulence	
	Time	Ratio	Time	Ratio	Time	Ratio	Time	Ratio
2	3.33	-	1.17	-	0.84	-	1.20	-
4	5.62	1.69	2.54	2.17	2.23	2.65	1.84	1.53
6	8.57	1.52	4.75	1.87	3.55	1.60	3.00	1.63

Table 2.3: Timing of different runs at various orders. Times are per time step, in seconds.

in the jet at $x/D_j = 5$ and $x/D_j = 10$. The second order formulation consistently over-predicts the velocity rms close to the center of the jet, while the fourth order formulation performs slightly better. The same conclusion can be obtained by looking at the third order statistics shown in Fig. 2.24(d). Again, the second order formulation consistently leads to an over-prediction, while the fourth order results follow more accurately the experimental profiles. Overall, both the second and fourth order formulations predict with good accuracy the mean quantities. However, higher order statistics are better predicted with higher order formulations. It can be noted that the improvement obtained by increasing the order of accuracy is not as impressive as for the turbulent pipe case. This can be attributed to the use of a very coarse mesh, on which one can expect that the sub-grid scale modeling errors might be more dominant.

2.8.6 Cost

The improved accuracy that can be obtained by running with higher order schemes comes at a price: indeed, the size of the stencils involved in the computations is significantly increased, and therefore the number of operations is expected to increase as well when using higher order schemes. As a consequence, one may wonder what is most efficient: retaining a low order accurate scheme and increasing the size of the mesh, or increasing the accuracy of the numerical schemes. Clearly, this is a difficult question, for the answer will strongly depend on the problem considered. However, it is possible to investigate this issue for a few simple test cases, where the error and the cost can be properly evaluated.

First, it is interesting to report here the average cost per time step for some of the test cases presented before, using different orders of accuracy. Table 2.3 summarizes this

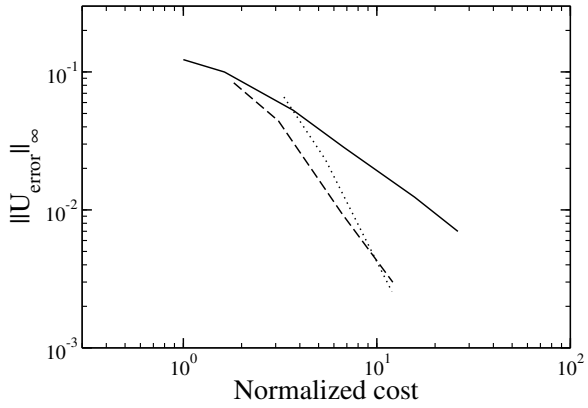

Figure 2.25: Error as a function of cost per time step when increasing mesh size for the inviscid convection of a circular vortex: second order (solid line); fourth order (dashed line); sixth order (dotted line).

information. On average, going from second to fourth order accuracy leads to doubling the cost of the simulation, while going from fourth to sixth order slightly less than doubles the simulation cost. Considering the improvement on the quality of the predictions that was observed for the different test cases, it appears that the fourth order accurate formulation could be very beneficial. For instance, in the case of the inviscid convection of a circular vortex presented in Section 2.4.8, one only has to use half the mesh points in each direction with the fourth order formulation to obtain the same error level as the second order scheme. At constant CFL, this would translate to a factor 4 reduction in CPU time for two-dimensional simulations and a factor 8 for three-dimensional simulations. A more rigorous assessment of this is shown in Fig. 2.25, where the L_∞ norm of the error between the computed axial velocity and the exact solution for various mesh sizes is plotted as a function of the cost for one time step, normalized by the cost of one time step on a 24×24 mesh with second order accuracy. This test clearly shows that there is a range of errors for which it is more efficient to use fourth order accuracy instead of second order accuracy. However, for most of the error range tested, sixth order accuracy is too expensive to be of interest, except if very small errors are necessary. These results are obviously for the considered case, but they suggest in general that for different ranges of errors, different

Order	$24 \times 32 \times 24$		$32 \times 48 \times 32$		$48 \times 64 \times 48$	
	Cost	Error	Cost	Error	Cost	Error
2	0.230	0.278	0.627	0.166	2.120	0.085
4	0.358	0.169	0.989	0.097	3.184	0.030
6	0.517	0.135	1.453	0.089	4.456	0.026

Table 2.4: Time per time steps, in seconds, and relative errors between LES and DNS at $y^+ = 10$, for different order of accuracy and different meshes for the turbulent pipe LES.

schemes might be more efficient.

A more realistic problem is the LES of a turbulent pipe presented before. For this problem, the mesh has been varied, and the mean axial velocity is compared to DNS. Three meshes are considered, namely a $24 \times 32 \times 24$ mesh, a $32 \times 48 \times 32$ mesh, and a $48 \times 64 \times 48$ mesh. We are interested in comparing the relative cost of increasing the mesh size or increasing the order of accuracy, as well as the quality of the predicted axial velocity profile. Figure 2.26 shows the mean axial velocity with second order accuracy for the three different meshes, and the mean axial velocity for various orders of accuracy for the coarsest mesh. It is interesting to note that the fourth order results on the $24 \times 32 \times 24$ mesh are very similar to the second order results on a $32 \times 48 \times 32$ mesh. Table 2.4 shows the cost per time step of the different computations, as well as the relative errors between the LES mean axial velocity predictions and the DNS results at $y^+ = 10$. Here, it can be observed that the fourth order computation on the coarse mesh is about half the cost of the second order computation on the medium mesh, while these two simulations lead to similar errors. The same remark applies to the fourth order computation on the medium mesh compared to the second order computation on the fine mesh. Note also that these comparisons do not account for the fact that the time step size increases as the mesh is coarsened. Here again, the fourth order method seems beneficial for this case. However, the added cost of using the sixth order scheme is not justified by the increase in accuracy, which is very limited between fourth and sixth order. Indeed, it is expected that the LES modeling errors will very quickly dominate the computation, and that further improvement in the quality of the predictions will require first to improve the model.

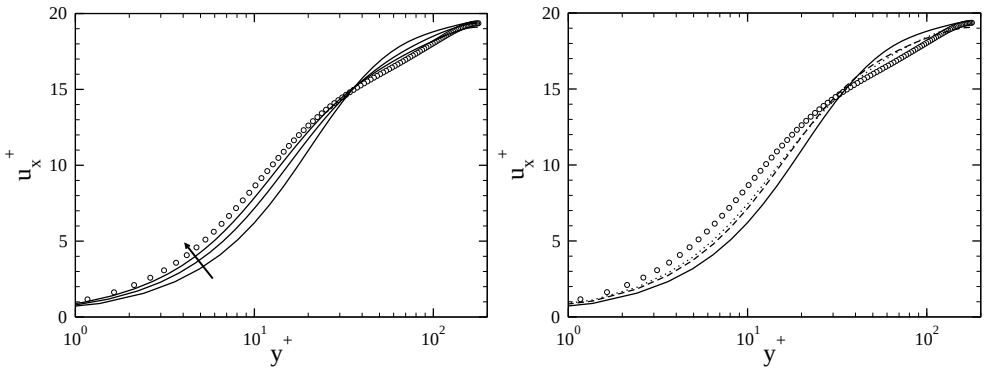

(a) Second order accuracy, increasing mesh size

(b) $24 \times 32 \times 24$ mesh, increasing order of accuracy

Figure 2.26: Mean axial velocity for the LES of a pipe flow: second order (solid line); fourth order (dashed line); sixth order (dotted line); DNS of Fukagata and Kasagi [30] (open symbols); increasing mesh size is indicated by the arrow.

2.9 Summary

A variable density, conservative, arbitrarily high order finite difference method for variable density low Mach number flows has been presented and tested, including an specific treatment of the boundary conditions. This technique has been applied in a range of test problems, including laminar and turbulent flows, constant and variable density flows, as well as LES and DNS. It has been observed that increasing the spatial order of accuracy consistently improves the quality of the results obtained, suggesting that the use of such high order schemes can be beneficial. The increase in computational effort, however, is not negligible when using higher order schemes, and an investigation of the error to cost ratio has been performed. This suggests that the order of the most efficient scheme will depend on the level of error that is acceptable for a given simulation. However, for the test problems considered, namely the inviscid convection of a vortex and the LES of a turbulent pipe flow, fourth order accuracy was found more efficient that second order accuracy. Sixth order accuracy was found to be excessively expensive. However, note that for the two DNS performed, namely the computation of homogeneous isotropic turbulence and the computation of a turbulent pipe, limited improvement on the low order statistics was obtained by

increasing the order of accuracy. This can be attributed to the fact that in DNS, most flow structures are properly resolved, meaning that truncation errors have a limited impact on the results. In the context of DNS of multiphase flows, for which the small scale interfacial structures may reach smaller sizes than the Kolmogorov size, the mesh will have to be fine enough to resolve the interface properly. Consequently, the smallest turbulent eddies should be well resolved, and second order accuracy should be sufficient. In the following, the second order version of the NGA code will be used to simulate primary atomization. A description of the techniques used for this purpose will be next.

Chapter 3

Accurate conservative level set method

3.1 Motivation and challenges

In most propulsion devices, the fuel is introduced in liquid form in a combustion chamber, where it undergoes atomization, evaporation, mixing with air, and chemical reactions in the combustion process. Since the atomization process governs the liquid droplet diameter distribution, it strongly affects both the subsequent evaporation and combustion. Consequently, full predictive capabilities for numerical tools will only be achieved once the atomization is accurately modeled. However, no satisfying models exist to this date, mostly because of the high complexity of the physics involved. Surface instabilities, ligament formation, ligament stretching and fragmentation, and droplet coalescence, all interact with turbulence to transform large scale coherent liquid structures into small scale droplets. Such a problem has scarcely been studied numerically, because it poses several great challenges.

The first challenge lies in the fact that the material properties, such as density and viscosity, are different in the two phases. Hence, a flow solver needs to be capable of handling large density ratios, of the order of 40 for Diesel engines, up to several hundreds for aircraft engines. Second, one of the characteristics of liquid-gas flows is the presence of a surface

tension force, which exists only at the interface between the liquid and the gas. The singular nature of this force leads to a difficult discretization. High robustness is therefore required from the flow solver. A third challenge lies in the interface localization and transport. While many approaches have been developed, they all suffer from various limitations, so that no clear gold standard exists today. Prerequisites for such methods include high accuracy, robustness, and the capability of accurately extracting the interface normals and curvature. Moreover, in the case of incompressible flows, the interface transport and localization should ensure that the volume of each phase is exactly conserved. Another challenge comes from the small scales that the atomization process produces. The formation of always smaller liquid structures leads to a multi-scale problem that requires high resolution to tackle, and that will generally generate liquid structures at the limit of numerical resolution.

3.2 Previous work

Among the available strategies to numerically transport an interface, the volume-of-fluid (VOF) method [99] is one of the most popular. Because it relies on a liquid volume fraction scalar to represent the interface, this method ensures discrete mass conservation. However, since the VOF scalar is discontinuous across the interface, a specific geometric advection scheme is required, which puts constraints on both the accuracy of the method and the time step size. Additionally, accessing quantities such as the interface normals or curvature can prove challenging.

The front-tracking approach was introduced by Unverdi and Tryggvason [110]. It consists of discretizing the interface using an unstructured moving mesh that is transported in a Lagrangian fashion. While enjoying the benefit of a purely Lagrangian transport, this method requires frequent mesh rearrangements that affect the conservation of the liquid volume. Moreover, the parallelization of such a method is very challenging. The main limitation of this approach is the lack of automatic topology modification. Any interface merging or break-up events have to be handled manually, which can be a complex procedure, especially for three-dimensional simulations. Since topology changes are extremely

frequent in primary atomization, front-tracking methods seem unadapted.

The level set method [82, 100] aims at representing the interface implicitely by an iso-level of a smooth function. This smooth function is preserved with a re-initialization process. Simple Eulerian scalar transport schemes can be used to transport this function, and therefore highly accurate methods are available. Moreover, parallelization is straightforward and highly efficient, and the smoothness of the level set function makes the interface normals and curvature readily available. However, level set methods are typically plagued by mass conservation issues, since no inherent conservation property of the level set function exists. This represents a severe drawback to level set methods, considering that inaccuracies in the liquid mass of fuel in a reactive simulation could lead to large errors in quantities such as temperature, or pollutant mass fractions.

In order to improve the mass conservation property of the level set method, several hybrid approaches have been proposed. Enright *et al.* [23] proposed a particle level set method (PLS), where Lagrangian markers are employed to correct the front location predicted by Eulerian transport. Sussman *et al.* [104] proposed to couple a level set method with the VOF technique (CLSVOF), hence benefiting from both the good mass conservation property of the VOF approach and the smooth interface description of the level set method. While both these methods have been quite successful, they suffer from additional problems. Their cost is typically much greater than the cost of a simple level set method, because many particles per cell are required for an accurate solution for the PLS approach, and because of the time step size restrictions for the geometric transport of the VOF scalar for the CLSVOF method. Moreover, the complexity of these techniques is significantly greater than that of a classical level set method.

Another attempt to alleviate the mass conservation issue of level set methods has been to refine the mesh locally in order to decrease the numerical errors associated with level set transport and re-initialization. This refinement can be used for the level set equation only, such as in the case of the refined level set grid (RLSG) method of Herrmann [41], or it can be a standard arbitrary mesh refinement (AMR) approach, where the Navier-Stokes equations are also solved on the refined mesh [76]. While this approach ensures a good

resolution of all structures, it remains both challenging to implement on parallel systems and significantly more expensive than classical methods. Moreover, the time step size in the case of strong local refinement is likely to be extremely restrictive.

Recently, Olsson *et al.* [78, 79] proposed a simple modification to the level set method in order to reduce mass conservation errors while retaining the simplicity of the original method. By replacing the usual signed distance function of the classical level set approach by a hyperbolic tangent profile that is transported and re-initialized using conservative equations, they showed in Olsson and Kreiss [78] that the mass conservation errors could be reduced by an order of magnitude in comparison with the results obtained with a signed distance function. In Olsson *et al.* [79], they improved their re-initialization equation, and further studied their approach in the context of finite elements. The work presented here is based on the conservative level set method with the improved re-initialization equation from Olsson *et al.* [79]. However the choice was made to remain in the context of finite difference methods. Starting from the observation that the conservative level set approach is difficult to use in the context of complex turbulent flows, several key modifications to this approach are introduced, resulting in both improved accuracy and robustness.

3.3 Mathematical formulation

3.3.1 Incompressible Navier-Stokes equations

In order to describe two-phase flows, the incompressible form of the Navier-Stokes equations is introduced,

$$\frac{\partial \mathbf{u}}{\partial t} + \mathbf{u} \cdot \nabla \mathbf{u} = -\frac{1}{\rho} \nabla p + \frac{1}{\rho} \nabla \cdot \left(\mu \left[\nabla \mathbf{u} + \nabla \mathbf{u}^t \right] \right) + \mathbf{g}, \tag{3.1}$$

where $\mathbf{u}$ is the velocity field, ρ is the density, p is the pressure, $\mathbf{g}$ is the gravitational acceleration, and μ is the dynamic viscosity. The continuity equation can be written in terms of the incompressibility constraint

$$\frac{\partial \rho}{\partial t} + \nabla \cdot (\rho \mathbf{u}) = \frac{\partial \rho}{\partial t} + \mathbf{u} \cdot \nabla \rho = 0. \tag{3.2}$$

The interface Γ separates the liquid from the gaseous phase. In each phase, the material properties are constant, allowing us to write $\rho = \rho_l$ in the liquid phase, while $\rho = \rho_g$ in the gas phase. Similarly, $\mu = \mu_l$ in the liquid and $\mu = \mu_g$ in the gas. At the interface, the material properties are subject to a jump that is written $[\rho]_\Gamma = \rho_l - \rho_g$ and $[\mu]_\Gamma = \mu_l - \mu_g$ for the density and the viscosity, respectively. The velocity field is continuous across the interface, $[\mathbf{u}]_\Gamma = 0$. However, the pressure is not continuous between the two phases, and we can write

$$[p]_\Gamma = \sigma\kappa + 2\,[\mu]_\Gamma\,\mathbf{n}^t \cdot \nabla\mathbf{u} \cdot \mathbf{n}, \tag{3.3}$$

where σ is the surface tension, κ is the interface curvature, and $\mathbf{n}$ is the interface normal.

3.3.2 Level set equation

In the level set approach, the interface is defined implicitly as an iso-surface of a smooth function. This approach benefits from many advantages, including automatic handling of topology changes, efficient parallelization, as well as easy and accurate access to the interface normals and curvature. Before proposing a new accurate and mass-conserving method, here we will first introduce two of the different level set formulations that can be found in the literature, and which, in modified form, form the basis of our new approach. These methods are the popular distance function proposed by Chopp [12] and the hyperbolic tangent function that was used by Olsson and Kreiss [78] in the context of their conservative level set method.

Distance level set

The classical level set technique relies on representing the interface implicitly as the zero level set of a smooth function ϕ chosen to be the signed distance from the interface, i.e.

$$|\phi\,(\mathbf{x}, t)| = |\mathbf{x} - \mathbf{x}_\Gamma|\,, \tag{3.4}$$

where $\mathbf{x}_\Gamma$ corresponds to the closest point on the interface from $\mathbf{x}$, and $\phi(\mathbf{x},t) > 0$ on one side of the interface, and $\phi(\mathbf{x},t) < 0$ on the other side. With this definition of the level set function, the interface itself corresponds to the $\phi(\mathbf{x},t) = 0$ iso-surface. This choice leads to a very smooth ϕ-field, which can be adequately transported and differentiated to compute the normal vector $\mathbf{n}$ and the curvature κ of the interface defined as

$$\mathbf{n} = \frac{\nabla\phi}{|\nabla\phi|} \tag{3.5}$$

and

$$\kappa = -\nabla \cdot \mathbf{n}. \tag{3.6}$$

The transport of the interface can simply be described by

$$\frac{\partial\phi}{\partial t} + \mathbf{u} \cdot \nabla\phi = 0. \tag{3.7}$$

However, transporting the interface using Eq. 3.7 will distort the level set function, and the smoothness of ϕ will be lost, leading to numerical problems. In order to ensure that ϕ remains smooth, an additional treatment is introduced to reshape ϕ into a distance function. This re-initialization of the distance profile can be performed using different procedures. The most common method is to solve a Hamilton-Jacobi equation [105],

$$\frac{\partial\phi}{\partial\tau} + S\left(|\nabla\phi| - 1\right) = 0, \tag{3.8}$$

where S is a modified sign function as in [88], and τ represents a pseudo-time. This equation can be discretized with high accuracy, therefore leading to an accurate reconstruction of the distance profile. However, it suffers from CFL limitations, making it prohibitively expensive in complex situations such as highly stretched meshes or cylindrical coordinates. In order to circumvent these limitations, Sethian [100] proposed a fast marching approach for the distance re-initialization based on solving locally $|\nabla\phi| = 1$ while employing only points closer to the interface in the numerical stencil. Using a heap sort algorithm, this procedure

can be made highly efficient, even on parallel systems [39]. However, the accuracy of this approach is limited, and the re-distancing of the points closest to the interface induces a displacement of the front.

One of the main limitations of the distance function level set approach in the context of multiphase flows is that neither the level set transport nor the re-initialization inherently conserve the volume of the region enclosed by the zero level set. For liquid/gas flows, for example, this can lead to gains or losses in the mass of the liquid, which can lead to substantial errors in many applications.

Hyperbolic tangent level set

Instead of a signed distance function, Olsson and Kreiss [78, 79] employed a hyperbolic tangent function ψ defined as

$$\psi(\mathbf{x}, t) = \frac{1}{2}\left(\tanh\left(\frac{\phi(\mathbf{x}, t)}{2\epsilon}\right) + 1\right), \tag{3.9}$$

where ϵ is a parameter that sets the thickness of the profile. Rather than defining the interface location by the iso-surface $\phi = 0$, it is now defined by the location of the $\psi = 0.5$ iso-surface. The transport of the interface can still be performed by solving the same equation as Eq. 3.7 for ψ. However, it can also be written in conservative form provided the velocity field $\mathbf{u}$ is solenoidal, i.e. $\nabla \cdot \mathbf{u} = 0$, namely

$$\frac{\partial \psi}{\partial t} + \nabla \cdot (\mathbf{u}\psi) = 0. \tag{3.10}$$

With the level set transport equation written in conservative form, and the given definition of ψ, it is clear that the scalar ψ should be a conserved quantity. As in the case of the level set function ϕ, nothing insures that solving Eq. 3.10 will preserve the form of the hyperbolic tangent profile ψ. As a result, an additional re-initialization equation needs to

be introduced to re-establish the shape of the profile. As in [79], this equation is written

$$\frac{\partial \psi}{\partial \tau} + \nabla \cdot (\psi (1-\psi) \mathbf{n}) = \nabla \cdot (\epsilon (\nabla \psi \cdot \mathbf{n}) \mathbf{n}) . \tag{3.11}$$

This equation is advanced in pseudo-time τ, it consists of a compression term on the left hand side that aims at sharpening the profile, and of a diffusion term on the right hand size ensuring that the profile remains of characteristic thickness ϵ, and is therefore resolvable on a given mesh. It should be noted that this equation is also written in conservative form. As a result, solving successively for Eq. 3.10 and 3.11 should accomplish the transport of the $\psi = 0.5$ iso-surface, preserve the shape of the hyperbolic tangent profile, and ensure the conservation of ψ.

For the sake of simplicity, the following symbolic definitions can be introduced:

$$\begin{aligned} (\text{scal}) &= \nabla \cdot (\mathbf{u}\psi) , \\ (\text{comp}) &= \nabla \cdot (\psi (1-\psi) \mathbf{n}) , \\ \text{and} \quad (\text{diff}) &= \nabla \cdot (\epsilon (\nabla \psi \cdot \mathbf{n}) \mathbf{n}) . \end{aligned} \tag{3.12}$$

3.4 Accurate conservative level set (ACLS) method

3.4.1 Original conservative level set method

The conservative level set method of Olsson *et al.* [78, 79] aims at reducing the mass conservation errors by exploiting the discrete conservation of the ψ-scalar. In the limit where the thickness ϵ of the hyperbolic tangent profile ψ goes to zero, the volume integral of the ψ-function approaches the volume enclosed in the $\psi = 0.5$ iso-surface, namely

$$\lim_{\epsilon \to 0} \int_V \psi (\mathbf{x}; t) \, d\mathbf{x} = \int_V H (\psi (\mathbf{x}; t) - 0.5) \, d\mathbf{x}, \tag{3.13}$$

where H is the Heaviside function and V is a volume. Since all the equations that need to be solved for ψ are conservative, discrete conservation of the volume enclosed in the interface becomes possible. Clearly, for a given numerical mesh with a spacing Δx, taking $\epsilon \ll \Delta x$

would lead to strong under-resolution of the hyperbolic tangent profile, and hence the numerical transport and re-initialization of ψ would suffer from severe numerical problems. In order to sufficiently resolve ψ, Olsson and Kreiss [78] proposed to use $\epsilon = \Delta x/2$, which leads to a hyperbolic tangent profile represented on two to three mesh points. With such a discretization of the profile, discretely solving Eqs. 3.10 and 3.11 becomes possible. However, the volumetric integral of ψ does not exactly correspond to the volume enclosed in the $\psi = 0.5$ iso-surface. Consequently, the volume enclosed in the $\psi = 0.5$ iso-surface will not be discretely conserved. Olsson and Kreiss [78] observed however that such an approach greatly reduced the conservation errors. The underlying conservation of ψ provides an anchor to the $\psi = 0.5$ iso-surface, preventing the accumulation of transport and re-initialization inaccuracies leading to large mass conservation errors. In their numerical tests, Olsson and Kreiss [78] obtained very encouraging results where discrete conservation errors were reduced by an order of magnitude in comparison to classical level set approaches.

3.4.2 Computation of the interface normals

In Olsson and Kreiss [78], it was mentioned that the choice of numerical method for the transport of the ψ-quantity was based on three considerations. First, the discrete conservation of the transport should be ensured. Second, no spurious oscillations should be introduced, and third, the thickness of the hyperbolic tangent profile should be kept constant. The first point is straightforward, and satisfied by most numerical methods. Similarly, the third point can be ensured by solving the re-initialization equation for the hyperbolic tangent profile, Eq. 3.11. However, the second point is difficult to enforce in general, and it requires non-oscillatory transport schemes, which are typically expensive. Indeed, the cost of total variation diminishing (TVD) or total variation bounded (TVB) schemes is typically more than the cost of simple non-TVD(B) transport schemes. Note that this cost could be significantly reduced by using low order TVD schemes away from the interface, such as a first order upwind scheme. In addition, achieving the TVD(B) property constitutes a challenge, especially for high order schemes. For example, WENO-type schemes [61, 45] are not TVD: most likely they are at best only TVB when combined with a TVD Runge-Kutta

time integration [82]. Moreover, the effectiveness of non-oscillatory schemes is strongly conditioned on the divergence-free quality of the velocity field. In complex, realistic turbulence simulations, ensuring that the velocity field is discretely divergence free to machine accuracy is a challenge. As a result, we can say that avoiding spurious oscillations, although desirable, is simply impossible to achieve in general. Consequently, the robustness of the method should not be based on this property.

A convenient method to compute the normal vectors is to write

$$\mathbf{n} = \frac{\nabla\psi}{|\nabla\psi|}, \tag{3.14}$$

as in Olsson *et al.* [78, 79]. However, this approach is strongly sensitive to spurious oscillations in the ψ-field. Indeed, an oscillation in ψ will appear as a large change in direction of the normal vector. As a result, the normals obtained by Eq. 3.14 are not appropriate to use in the re-initialization equation, Eq. 3.11. As this equation contains a compression term that moves the level set scalar ψ along the directions defined by the normal vectors in order to re-form a hyperbolic tangent function, we can expect that having normals that point in the wrong direction will lead to severe numerical difficulties. More precisely, (comp) will create an accumulation of ψ where the normal vectors are facing each other. In the presence of parasitic oscillations of the normal vectors, this means that spots of the scalar ψ will form spuriously in the domain, leading to an unphysical displacement of the liquid mass, similar to jetsam/flotsam problems of some VOF methods [99]. To illustrate this point, a few steps of Zalesak's disk [123] problem are computed. This test case, for which the detailed parameters will be given in Section 3.4.7, is often employed to assess the accuracy of level set methods. No re-initialization is used, the level set function is simply transported using a non-TVD(B) scheme. It can be observed in Fig. 3.1(a) that the resulting normal vectors are alternating direction, as can be expected from taking the gradient of a field with spurious oscillations. The consequences of this, including the formation of jetsam/flotsam, are severe and will be shown in Section 3.4.7.

In order to remedy this problem, we propose to first recompute ϕ from the ψ-function

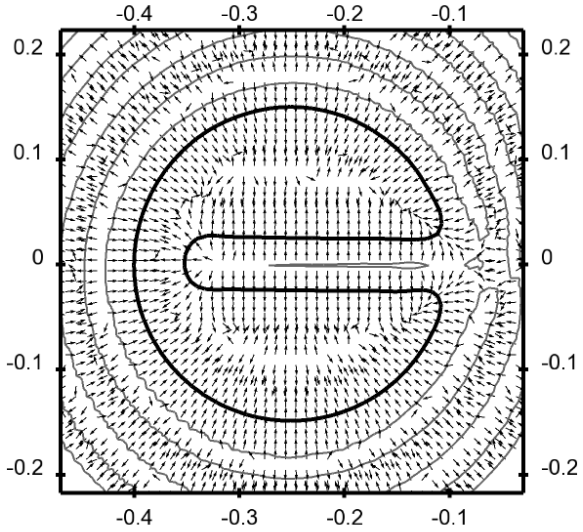

(a) Normals from ψ. Interface location (black line), and iso-contours of ψ (grey lines).

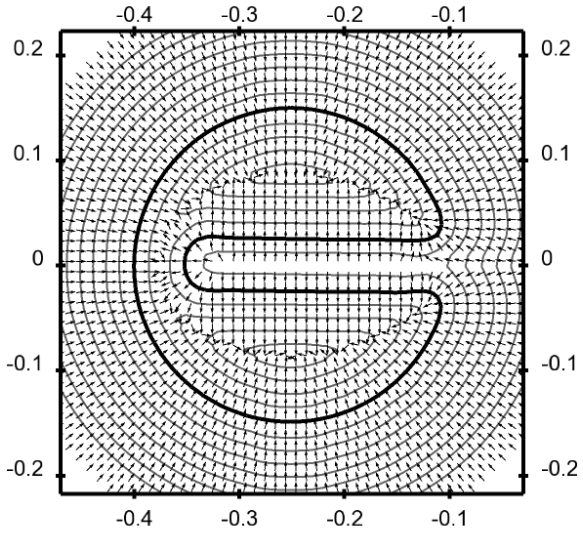

(b) Normals from ϕ. Interface location (black line), and iso-contours of ϕ (grey lines).

Figure 3.1: Computation of interface normals in the presence of spurious oscillations in ψ.

using a standard re-distancing algorithm, then to use Eq. 3.5 to compute the normal from the smooth, reconstructed distance function ϕ. This distance reconstruction can be performed efficiently using a fast marching method (FMM), therefore it does not affect the overall cost of the method significantly. The specific cost increase due to the FMM will be discussed in comparison with the cost of a non-oscillatory scheme in the following section. Moreover, the distance ϕ for the points closest to the interface can simply be obtained by inverting the hyperbolic tangent function, meaning that no spurious displacement of the interface will be induced by this operation. It is then straightforward to access the interface normals by Eq. 3.5. It can be seen in Fig. 3.1(b) that the resulting normals are smooth, and that they are perfectly useable to perform the re-initialization.

3.4.3 High order level set transport

Having modified the way the normal vectors are computed, the non-oscillatory property of the level set transport becomes unnecessary. Therefore, we can take advantage of fast, high order, non-TVD(B) scalar transport schemes. A commonly used approach is the High Order Upstream Central (HOUC-n, where n is the order of the scheme) class of schemes, employed for example in [76] for level set transport. These schemes are implemented in the context of the numerical code developed in Chapter 2 for accurate simulations of turbulent reactive flows, NGA. Following the notations used in Chapter 2, the nth order level set transport scheme can be written as

$$(\text{scal-}n) = \sum_{i=1}^{3} \left(\frac{1}{J} \frac{\delta_{2\text{nd}}}{\delta_{2\text{nd}}\, \zeta_i} \left[\frac{J}{h_i} u_i \overline{\overline{\psi}}^{\zeta_i} \right] \right), \tag{3.15}$$

where u_i is the ith component of the velocity vector, ζ_i represents the computational space, which is related to physical space x_i through $h_i = dx_i/d\zeta_i$ and $J = \prod_{i=1}^{3} h_i$. The second order interpolation operator is defined for a variable α by

$$\overline{\alpha}^{2\text{nd}\,\zeta_1}(\zeta_1, \zeta_2, \zeta_3) = \frac{\alpha(\zeta_1 + 1/2, \zeta_2, \zeta_3) + \alpha(\zeta_1 - 1/2, \zeta_2, \zeta_3)}{2}, \tag{3.16}$$

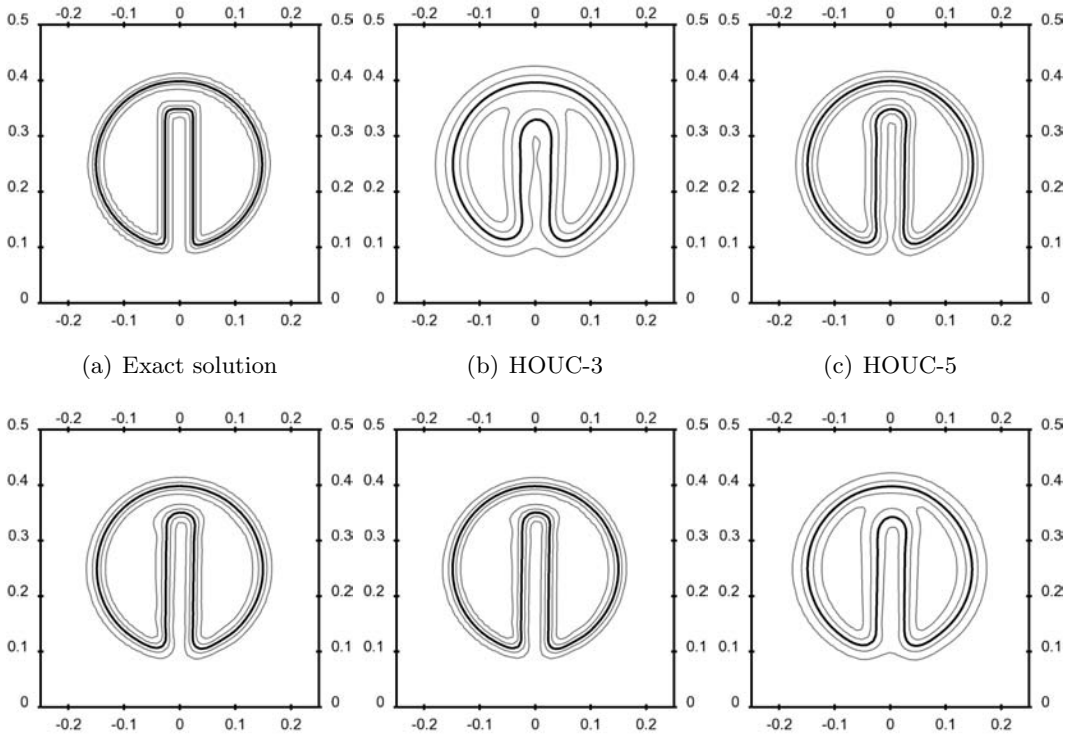

(a) Exact solution (b) HOUC-3 (c) HOUC-5

(d) HOUC-7 (e) HOUC-9 (f) WENO-5

Figure 3.2: Contours of ψ for the transport without re-initialization of Zalesak's disk.

and the second order differentiation operator is defined by

$$\frac{\delta_{2\text{nd}}\alpha}{\delta_{2\text{nd}}\,\zeta_1}\left(\zeta_1,\zeta_2,\zeta_3\right)=\frac{\alpha\left(\zeta_1+1/2,\zeta_2,\zeta_3\right)-\alpha\left(\zeta_1-1/2,\zeta_2,\zeta_3\right)}{2}. \tag{3.17}$$

$\overline{\overline{\psi}}^{\zeta_i}$ is an nth order interpolation of the ψ variable to the i-direction cell face, which can be based on a HOUC approach or a WENO-type scheme [61, 45]. In Fig. 3.2, the importance of using accurate transport schemes can be assessed by comparing the quality of the rotated Zalesak's disk on a 100×100 mesh. As expected, the accuracy of the transported ψ increases as the order of accuracy of the chosen scheme increases. Despite the fact that none of the HOUC schemes used are non-oscillatory, the solution after one rotation remains acceptable, without being noticeably affected by spurious oscillations. Moreover, the sharpness of the

Scalar scheme	Time (seconds per time step)
HOUC-3	0.0440
HOUC-5	0.0607
HOUC-7	0.0798
HOUC-9	0.0997
WENO-5	0.1177

Table 3.1: Cost of the different scalar schemes tested for the transport of Zalesak's disk.

profile is much better preserved when the order of accuracy of the transport scheme is higher, and when non-TVD(B) schemes are preferred to a TVB scheme such as WENO-5. Having a more accurate transport scheme will allow to rely much less on the re-initialization equation. Instead of spreading out the profile due to transport inaccuracies, and then re-sharpen it using the re-initialization equation, it is highly beneficial to try to keep the profile as close to the original hyperbolic tangent as possible. In order to find the right compromise, it is instructive to compare the computational cost associated with the individual transport schemes. The cost of the different schemes used in Fig. 3.2 is compared in Table 3.1. It can be seen that the non-oscillatory scheme is by far the most expensive scheme, even though its actual accuracy should theoretically be between third and fifth order. On the other hand, if one accepts to use other non-TVD(B) schemes, a ninth order HOUC can be used for notably less cost than the fifth order WENO scheme.

It is also interesting to compare the actual cost of the entire procedure, including the cost of the FMM that is used prior to computing the normal vectors. Table 3.2 shows that the additional cost of the FMM remains low, as long as a banded approach is used, in the case where the 5th order HOUC is used for scalar transport. As a conclusion, even though an additional step has to be performed compared to the classical conservative level set method, the cost of the full proposed approach is still lower than that of using a lower order non-oscillatory scheme. It is also more accurate, and much more robust, since it can be argued that even a non-oscillatory scheme will lead to spurious oscillations in the presence of a complex, turbulent field that is not discretely divergence free.

Scalar scheme	Time (seconds per time step)	Increase in cost (%)
HOUC-5	0.0607	–
HOUC-5 + FMM(5)	0.0645	6.3%
HOUC-5 + FMM(10)	0.0712	17.3%
HOUC-5 + FMM(20)	0.0839	38.2%

Table 3.2: Additional cost of the fast marching method performed on n bands (FMM(n)) for Zalesak's disk.

3.4.4 Conservative re-initialization

Now that we have established how to transport the level set function ψ, and how to extract the normal vectors $\mathbf{n}$ from it, the actual discretization of the re-initialization step can be discussed. The re-initialization equation for the hyperbolic tangent level set given in Eq. 3.11 is not the exact same form that was employed by Olsson and Kreiss [78], and Olsson *et al.* [79] performed this discretization in the context of finite elements. For finite differences, we observed that this step requires specific attention in order to avoid using overly large stencils, that would be detrimental to the robustness and accuracy of the solution. The values of the level set functions ϕ and ψ are stored at the cell centers, but the compressive flux $\mathbf{F}_C = \psi\,(1-\psi)\,\mathbf{n}$ and the diffusive flux $\mathbf{F}_D = \epsilon\,(\nabla\psi \cdot \mathbf{n})\,\mathbf{n}$ need to be computed at the cell faces, in order to obtain cell centered residuals when taking the divergence of the fluxes. Consequently, if a standard centered differencing approach is used to compute $\mathbf{n}$ from ϕ, as shown in Fig. 3.3(a), computing $\mathbf{F}_C$ and $\mathbf{F}_D$ will require one additional interpolation, leading to an effective 5-points stencil in one dimension. This was found to be a poor discretization strategy subject to spurious oscillations. In order to ensure the compactness of the discretization stencils, the concept of face normals was introduced instead. These face normal vectors can be computed using more compact stencils, as shown in Fig. 3.3. Using the notations employed in Chapter 2, the x_j-component of the x_i-face gradient of a

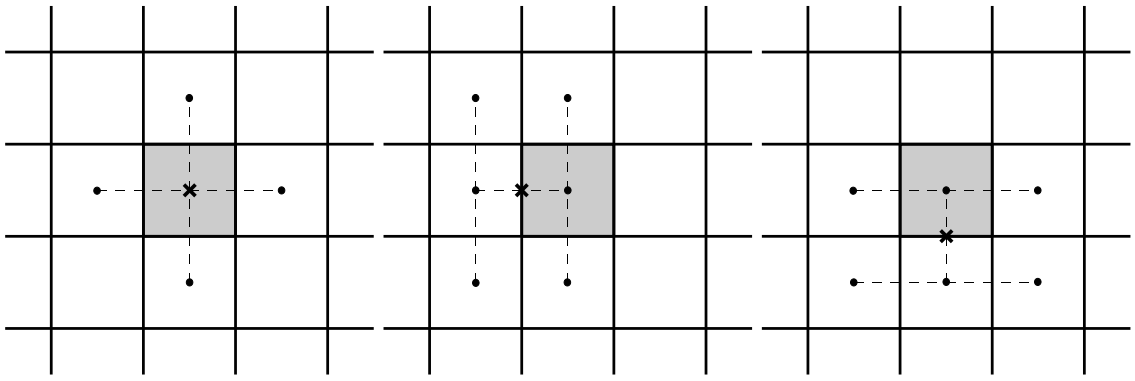

(a) Centered differencing stencil (b) x-face normal vector stencil (c) y-face normal vector stencil

Figure 3.3: Discretization of the normals.

scalar quantity a can be written as

$$(\nabla^{x_i} a)_{x_j} = \begin{cases} \frac{\delta_{2\text{nd}}\, a}{\delta_{2\text{nd}}\, x_i} & \text{for } i = j, \\ \\ \overline{\frac{\delta_{2\text{nd}}\, a}{\delta_{2\text{nd}}\, x_j}}^{2\text{nd}\, x_i} & \text{for } i \neq j, \end{cases} \tag{3.18}$$

where $\delta_{2\text{nd}}\, a/\delta_{2\text{nd}}\, x_i$ is a second order differentiation of variable a in physical space, and $\overline{a}^{2\text{nd}\, x_i}$ is the second order interpolation of a in physical space. These face gradients are used to compute the normals from ϕ as well as the $\nabla\psi$ term in the (diff) term of Eq. 3.11. The x_i-face normal vector can then be defined by

$$\mathbf{n}^{x_i} = \frac{\nabla^{x_i} a}{|\nabla^{x_i} a|}. \tag{3.19}$$

The compression term of Eq. 3.11 is discretized with second order accuracy in computational space, so as to ensure the discrete equivalence of the divergence operator used for the continuity equation and the one used for the re-initialization equation. The discrete version

of (comp) reads

$$\text{(comp-2)} = \sum_{i=1}^{3} \left(\frac{1}{J} \frac{\delta_{2\text{nd}}}{\delta_{2\text{nd}}\, \zeta_i} \left[\frac{J}{h_i} \mathbf{n}_i^{x_i} \overline{\psi\,(1-\psi)}^{2\text{nd}\,\zeta_i} \right] \right). \tag{3.20}$$

The diffusive term of Eq. 3.11 is discretized similarly by writing

$$\text{(diff-2)} = \sum_{i=1}^{3} \left(\frac{1}{J} \frac{\delta_{2\text{nd}}}{\delta_{2\text{nd}}\, \zeta_i} \left[\frac{J}{h_i} \epsilon\, \mathbf{n}_i^{x_i} \left(\mathbf{n}^{x_i} \cdot \nabla^{x_i} \psi \right) \right] \right). \tag{3.21}$$

With this approach, a compact scheme can be used to discretize the full conservative re-initialization equation: 3 points are used in one dimension, 9 in two dimensions, and 27 points in three dimensions. This scheme is discretely conservative, second order accurate, and has been found to be robust in our test cases.

It should be noted that this conservative re-initialization converges very fast. Indeed, as noticed by Olsson *et al.* [79], with a choice of parameters following $\Delta x \sim \Delta t \sim \epsilon$, one or two time steps are enough to reach steady state. The spreading of the hyperbolic tangent induced by one time step of transport (Eq. 3.10) occurs on a length scale which can be expressed as $l_{\text{conv}} \approx \alpha_{\text{conv}}\, \Delta x$, where α_{conv} represents the convective CFL number. Similarly, the compression term (comp) of the conservative re-initialization (Eq. 3.11) for p time steps $\Delta\tau$ will displace the ψ-scalar over a length scale $l_{\text{comp}} \approx \alpha_{\text{comp}}\, p\, \Delta x$, where α_{comp} represents the compressive CFL number for the conservative re-initialization. To ensure that the displaced ψ-scalar is properly reshaped into a hyperbolic tangent function, it is desirable to have $l_{\text{comp}} \approx l_{\text{conv}}$, which leads to $p\, \alpha_{\text{comp}} \approx \alpha_{\text{conv}}$. For the sake of simplicity, the choice is made to always use $p = 2$, and $\alpha_{\text{comp}} \approx \alpha_{\text{conv}}/2$, instead of checking the convergence of the re-initialization equation at each step. This approach has been found to be sufficient to ensure the proper behavior of the re-initialization equation, as demonstrated by the examples discussed below.

Mesh	Error
8×8	0.17772
16×16	0.09200
32×32	0.15270
64×64	0.12575

Table 3.3: Evolution of the finite difference curvature error with mesh spacing.

3.4.5 Curvature computation

In order to accurately predict surface tension forces, it is of fundamental importance to have a converging curvature computation. The curvature could be directly computed from the hyperbolic tangent level set function ψ, but following the previous discussions about the presence of spurious oscillations in ψ, it is clear that differentiating the hyperbolic tangent level set should be avoided, and that the curvature should be computed from ϕ. However, since the distance level set field ϕ is recomputed at every step from an FMM, inaccuracies in the distance field are also expected. Since two successive levels of differentiation are applied to the ϕ-field to obtain the curvature, it is to be expected that a ϕ-field computed through the FMM with at best second order accuracy will provide first order normals, and a curvature that will not converge under mesh refinement. In order to verify this property, the curvature has been computed by taking a second order divergence of the face normals. Such a scheme gives a compact curvature computation, using 27 points in three dimensions, which only differs from the standard, second order, compact curvature computation [100] by the way the normalization is done. This scheme was tested by computing the curvature from an FMM-reconstructed distance, for a circle of radius 0.5 centered in a squared domain of size $[0, 2] \times [0, 2]$. The L_2 error is shown in Table 3.3. Clearly, no convergence is obtained under mesh refinement.

In order to remedy this problem, a least squares approach was introduced. While the finite difference approach proposed above uses a 27 point stencil in three dimensions, a second order polynomial reconstruction of ϕ only requires 10 points to be obtained. If the same 27 point stencil is used to perform the least squares reconstruction instead of only

Mesh	Error
8×8	0.28207
16×16	0.17276
32×32	0.08279
64×64	0.04737

Table 3.4: Evolution of the least squares curvature error with mesh spacing.

the 10 necessary points, the size of the statistical sample will be rather large, and it can be expected that the numerical errors due the inaccuracy of the FMM will be smeared out. This approach was proposed recently by Marchandise *et al.* [65], and succesfully employed to obtain converging curvatures from a discontinuous Galerkin scalar field. The results for the test case used above, but with the least squares curvature computation are shown in Table 3.4. It can indeed be observed that first order convergence is recovered.

3.4.6 ACLS solution procedure

A brief summary of the ACLS solution procedure is given here:

- Using a semi-implicit Crank-Nicolson time integration, advance the ψ field by solving Eq. 3.10. Unless specified otherwise, HOUC-5 will be used for this step.
- Use FMM to efficiently reconstruct ϕ from ψ.
- Compute the face normals from ϕ.
- Compute the least squares curvature from ϕ.
- Perform the conservative re-initialization step: Using a semi-implicit Crank-Nicolson time integration, Eq. 3.11 is advanced.

3.4.7 Level set transport tests

Long time conservation of an under-resolved sphere

In order to evaluate the capability of the proposed ACLS method to conserve the mass at low resolution, a poorly resolved sphere of diameter D is transported in a uniform velocity field

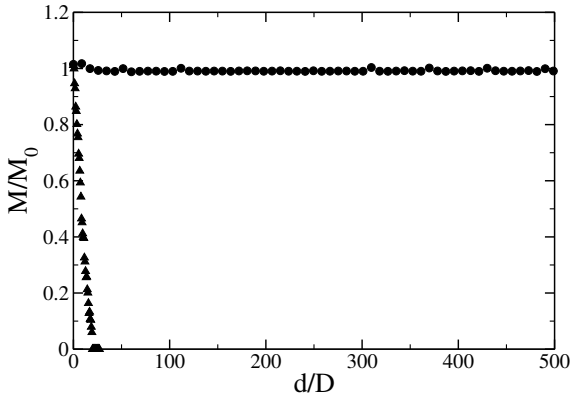

Figure 3.4: Evolution of the mass in an under-resolved droplet as a function of the distance traveled; standard distance level set approach (triangles) and ACLS (circles).

with a CFL number of 0.5. For comparison, the same test is conducted with a standard distance function level set using WENO-5 for the transport and FMM for the distance re-initialization, which is performed every 10 time steps. With only five mesh points in the diameter, we observe in Fig. 3.4 that the standard distance level set method looses all the mass in the sphere in less than $50D$, even with the low re-initialization frequency. However, we can see that the ACLS approach maintains the mass indefinitely. After being transported for a distance larger than $500D$, the mass is still adequately maintained. Only very limited oscillations in the mass can be observed, which can be attributed to the very poor discretization of the sphere.

Zalesak's disk

In order to assess the capability of the ACLS method to adequately transport thin structures and sharp corners, the solid body rotation of a notched circle is simulated. The circle is 0.15 in radius, with a notch of width 0.05 and height 0.25. It is centered initially at $(0.5, 0.75)$ in a $[-0.5, 0.5] \times [-0.5, 0.5]$ domain, discretized on a 100×100 mesh. The solid body rotation is applied to this shape until one revolution is completed. The time integration of the full revolution is performed using a semi-implicit Crank-Nicolson in 500 time steps, leading to a CFL number of 0.6.

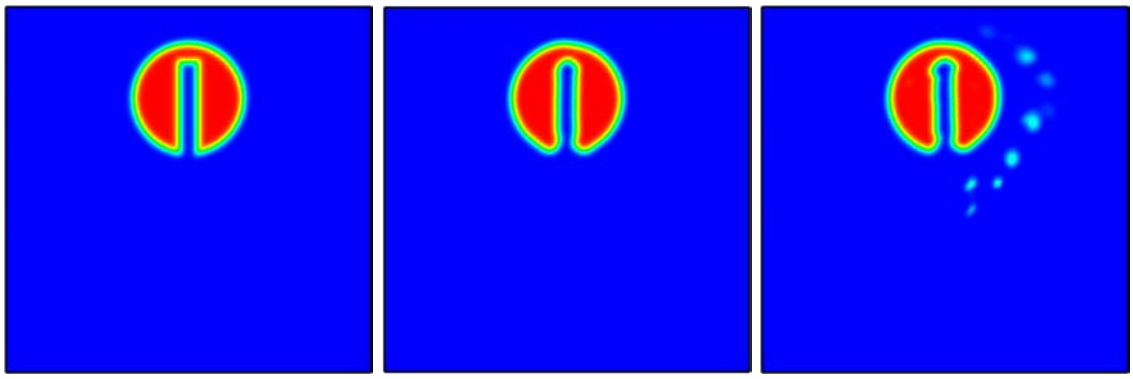

(a) Exact solution (b) ACLS method (c) Normals from ψ

Figure 3.5: ψ-scalar for Zalesak's disk problem with ACLS or by computing the normals from ψ, after a full rotation. Color map is from $\psi = 0$ to $\psi = 1$.

First, the full ACLS procedure is tested and compared to the approach where the normal vectors are directly obtained from ψ. For both methods, HOUC-5 is used for the transport equation, Eq. 3.10. Figure 3.5 compares the transported ψ-field with the exact solution for both cases. Clearly, the ACLS method leads to very satisfactory results, with a properly maintained hyperbolic tangent thickness, while the method where the normals are obtained from the ψ-field shows many regions of accumulated ψ-scalar away from the notched disk. While this is not a major problem for this case, it is clear that it will become critical to the stability of the method for realistic problems.

In Fig. 3.6, the notched circle shape is compared with the exact solution using different level set transport schemes to discretize Eq. 3.10, namely HOUC-5 and WENO-5. While both results are very satisfactory, it is clear that HOUC-5 leads to a more accurate solution due to both the increased accuracy of HOUC in comparison to WENO and because the HOUC scheme will rely much less on the conservative re-initialization. These results confirm that it is beneficial to avoid spreading of the ψ profile, and also that the HOUC-5 solution behaves adequately despite the absence of any non-oscillatory property.

As a third test case, the influence of the conservative re-initialization frequency is analyzed. Figure 3.7 compares the results obtained by re-initializing at each time step and re-initializing every 10 time steps. Clearly, very little differences can be observed in the results,

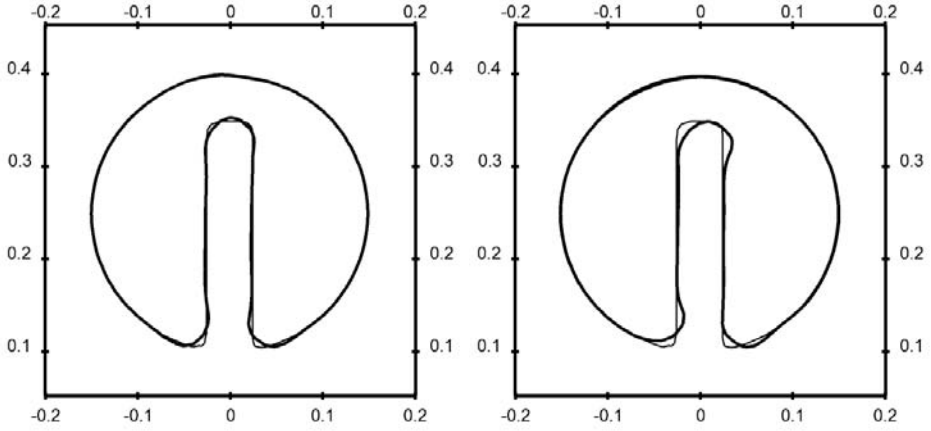

(a) HOUC-5 transport (b) WENO-5 transport

Figure 3.6: Effect of the transport scheme on Zalesak's disk after a full rotation with ACLS: computed interface location (thick line) and exact interface location (thin line).

suggesting that the accuracy of the ACLS approach is not affected by the re-initialization frequency. This appears as a strong advantage compared to classical level set approaches, for which more re-initialization usually means less accurate results.

Finally, a more detailed mesh convergence analysis is performed using both a 50×50 mesh and a 200×200 mesh in addition to the 100×100 mesh introduced before. The CFL number is kept constant for the different cases. Figure 3.8 compares the results after one rotation for the three meshes employed. The computed interface converges toward the exact solution in a satisfactory manner. Figure 3.9 shows the time evolution of the normalized area enclosed in the interface for the three different meshes. Even with the coarsest mesh, the conservation errors remain very limited, and these errors are significantly reduced by going to finer meshes. Table 3.5 summarizes the maximum area conservation errors for the three meshes. Between the 50×50 mesh and the 100×100 mesh, the error is strongly reduced. This can be attributed to the fact that numerical errors lead to the closure of the notch for the coarsest mesh simulation. Between the medium and the fine simulation, second order convergence of area conservation errors is observed.

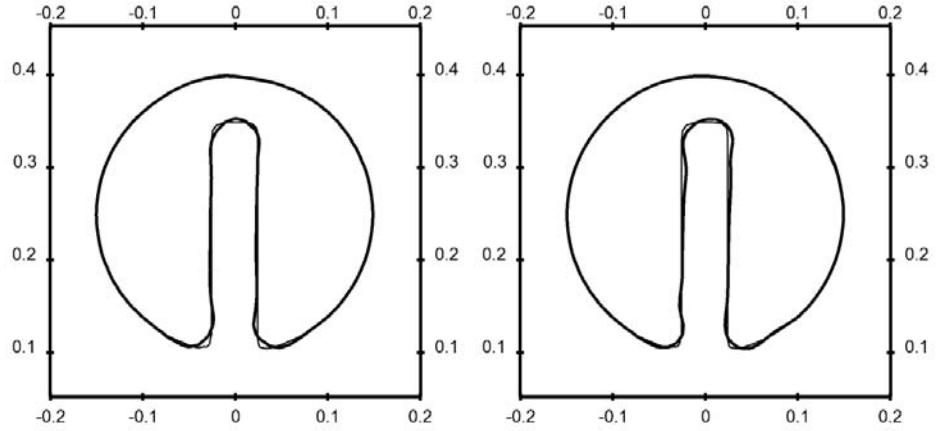

(a) Conservative re-initialization every step (b) Conservative re-initialization every 10 steps

Figure 3.7: Effect of the re-initialization frequency on Zalesak's disk after a full rotation with ACLS: computed interface location (thick line) and exact interface location (thin line).

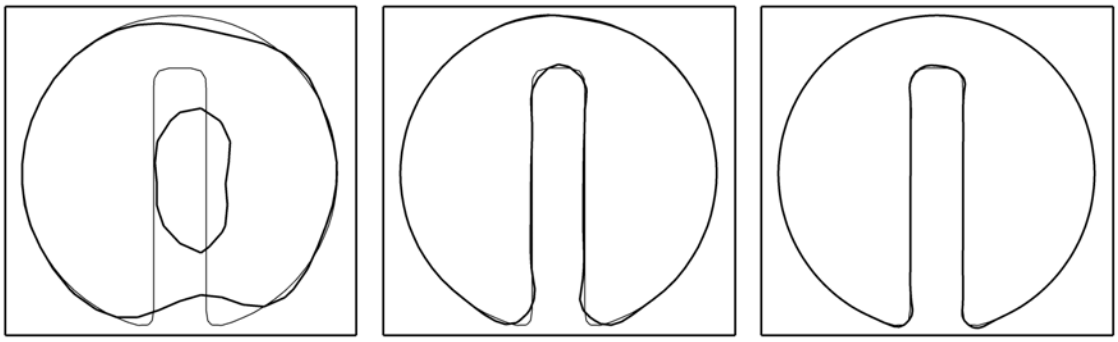

(a) 50×50 mesh (b) 100×100 mesh (c) 200×200 mesh

Figure 3.8: Effect of the mesh spacing on Zalesak's disk after a full rotation with ACLS: computed interface location (thick line) and exact interface location (thin line).

Mesh	Error (%)
50×50	0.7167
100×100	0.0352
200×200	0.0085

Table 3.5: Evolution of the maximum area conservation error with mesh spacing for Zalesak's disk.

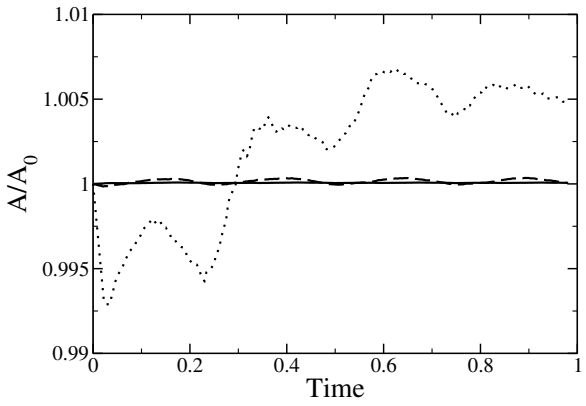

Figure 3.9: Temporal evolution of the normalized area enclosed in the interface for Zalesak's disk using the ACLS method on different meshes: 50×50 mesh (dotted line), 100×100 mesh (dash line), and 200×200 mesh (solid line).

Circle in a deformation field

The deformation of a circle by a single vortex has been considered to assess the ability of numerical methods to resolve thin filaments, e.g. see [23]. In a $[0,1] \times [0,1]$ domain, a circle of radius 0.15 is initially centered at $(0.5, 0.75)$. The velocity field is obtained from the stream function

$$\Psi(\mathbf{x}, t) = \frac{1}{\pi} \sin^2(\pi x) \cos^2(\pi y) \cos(\pi t/T), \tag{3.22}$$

where T is set to 8. At $t = T/2$, the deformation will be maximum, then the process is inverted until $t = T$, at which point the circle should be back to its initial shape and location. The simulation is conducted on two meshes, namely a 128×128 and a 256×256 mesh. For the coarse run, the time step size is set to $\Delta t = 0.01$, leading to a maximum CFL number of 1.28. For the finer mesh, the time step size is divided by two. Figure 3.10 shows the result of both runs at $t = T/2$. Clearly, at this time, the width of the trailing ligament should fall below the resolution of the 128×128 mesh, meaning that the numerically correct solution should be to loose the corresponding area. However, because of the conservative re-inititialization step, the ACLS method attempts to maintain this area on the mesh, which leads to the formation of drops of the size of one or two grid cells. When the velocity field

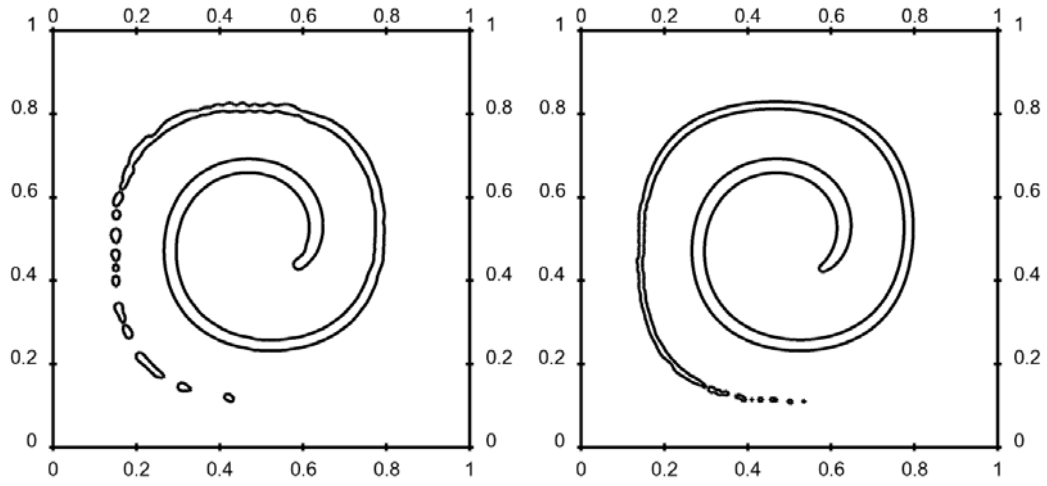

(a) 128×128 mesh (b) 256×256 mesh

Figure 3.10: Interface location for the circle in a deformation field test case at $t = T/2$ for different mesh sizes.

is reversed, this area is recovered. In Fig. 3.11, it can be observed that the circle at $t = T$ displays some deformation because of the droplets that have been created. However, going to a finer mesh greatly improves these results. Finally, Fig. 3.12 shows the evolution of the normalized area with time for the two meshes. Note that even on the coarse mesh, the error at maximum stretching remains below 4%, while the fine mesh shows a maximum error below 0.5%. At $t = T$, most of the area is recovered, leading to an error of less than 0.1% on the coarse mesh, and less than 0.01% for the fine mesh. In comparison, Herrmann [41] reported for a standard level set technique an area conservation error at $t = T$ of more than 30% on a 128×128 mesh, and more than 4% on a 256×256 mesh.

3.5 Solution of the Navier-Stokes equations

This section describes the coupling with the flow solver NGA introduced in Chapter 2. NGA solves the variable density, low Mach number Navier-Stokes equations using high order conservative finite difference methods that are staggered in time and space. Such methods have

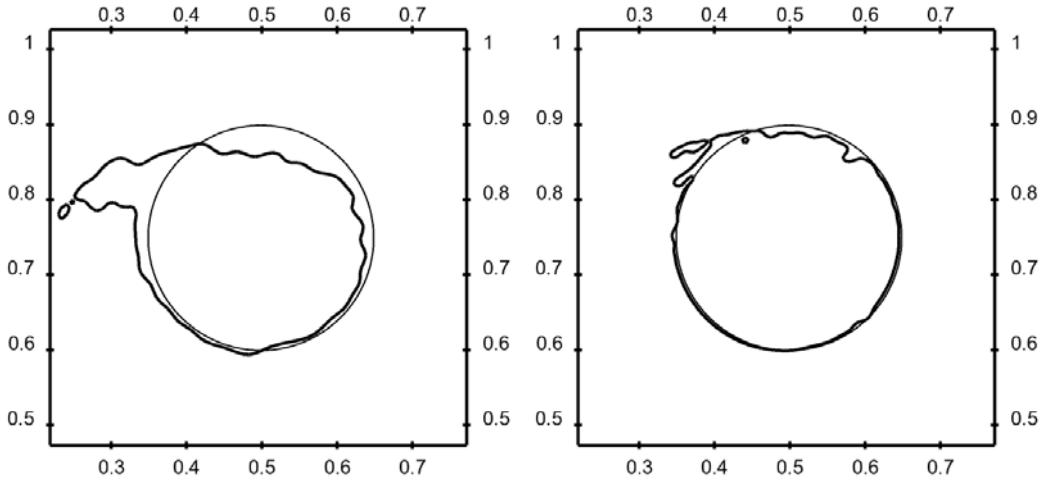

(a) 128×128 mesh (b) 256×256 mesh

Figure 3.11: Interface location for the circle in a deformation field test case at $t = T$ for different mesh sizes: computed interface (thick line) and exact solution (thin line).

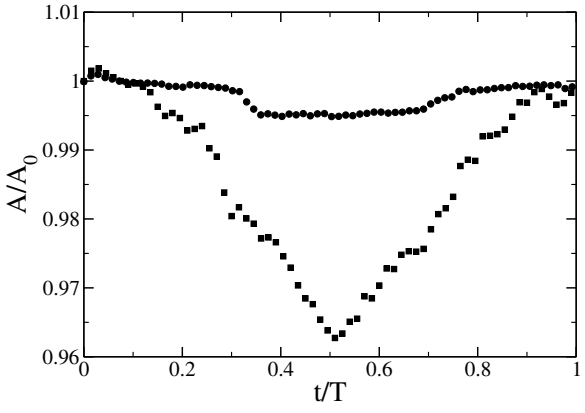

Figure 3.12: Temporal evolution of the normalized area for the circle in a deformation field test case for different mesh sizes: 128×128 mesh (squares) and 256×256 mesh (circles).

been shown earlier to be highly suited for turbulence simulations, and therefore are expected to be highly beneficial for ensuring the accuracy of turbulent multiphase simulations.

3.5.1 Approach

Different strategies have been developed to handle the large density ratio and the surface tension force in a flow solver. The continuum surface force approach (CSF) [9] spreads out both the density jump and the surface tension force over a few cells surrounding the interface in order to facilitate the numerical discretization. Consequently, this approach tends to misrepresent the smallest front structures. In the context of finite differences, the ghost fluid method (GFM) [27] provides a very attractive way of handling discontinuities by using generalized Taylor series expansions that directly include these discontinuities. Because GFM explicitly deals with the density jump, the resulting discretization is not affected by the density ratio. Similarly, the surface tension force can be included directly in the form of a pressure jump, providing an adequate sharp numerical treatment of this singular term.

In this work, we will use GFM for the surface tension term as well as for the density jump in the pressure term. However, the discretization of the viscous terms using GFM is rather complex, and is challenging to implement implicitly. In order to alleviate this issue, we will use the CSF approach to discretize the viscous terms. For a turbulent flow where the viscous contribution is small in comparison with the convective terms, we do not expect this to significantly affect the quality of the solution. However, it allows us to use implicit solvers to robustly handle the viscous terms.

3.5.2 Ghost fluid methodology

One of the central issues with two-phase flow simulations lies in the numerical discretization of the pressure gradient term. Indeed, this term contains the density, which exhibits a jump at the interface, and the pressure itself is discontinuous at the interface because of both the surface tension force and the viscous jump, as seen in Eq. 3.3. An efficient discretization of

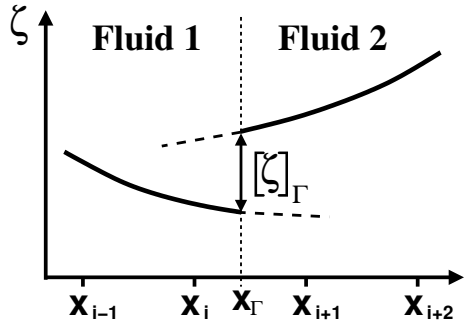

Figure 3.13: Illustration of the ghost fluid approach for a variable ζ which displays a discontinuity at x_Γ. The dashed lines represent Taylor series expansions across the interface Γ.

this term requires a specific treatment. The ghost fluid method is used here to account for the pressure jump caused by surface tension, while the jump caused by the discontinuous viscous stress is handled by the continuum surface force technique. GFM relies on the assumption that all the jump conditions for a given variable $[\zeta]_\Gamma$ and its spatial derivatives $[\partial\zeta/\partial x]_\Gamma$, $[\partial^2\zeta/\partial x^2]_\Gamma$, ... are known at the interface Γ. First, the Taylor series expansion of ζ_l in the gas is written as

$$\zeta_l(x) = \zeta_l(x_\Gamma) + (x - x_\Gamma)\frac{\partial \zeta_l}{\partial x}(x_\Gamma) + \frac{1}{2}(x - x_\Gamma)^2\frac{\partial^2 \zeta_l}{\partial x^2}(x_\Gamma) + \mathcal{O}((x - x_\Gamma)^3)\,, \tag{3.23}$$

and the expansion of ζ_g in the liquid is written as

$$\zeta_g(x) = \zeta_g(x_\Gamma) + (x - x_\Gamma)\frac{\partial \zeta_g}{\partial x}(x_\Gamma) + \frac{1}{2}(x - x_\Gamma)^2\frac{\partial^2 \zeta_g}{\partial x^2}(x_\Gamma) + \mathcal{O}((x - x_\Gamma)^3)\,, \tag{3.24}$$

as is illustrated in Fig. 3.13. Subtracting these two equations provides a similar expansion for the jump of ζ, $[\zeta]$, in the neighborhood of the interface:

$$[\zeta] = [\zeta]_\Gamma + (x - x_\Gamma)\left[\frac{\partial \zeta}{\partial x}\right]_\Gamma + \frac{1}{2}(x - x_\Gamma)^2\left[\frac{\partial^2 \zeta}{\partial x^2}\right]_\Gamma + \mathcal{O}((x - x_\Gamma)^3)\,. \tag{3.25}$$

Then, spatial derivatives may be expressed using only values in the same phase. If the

interface Γ is located somewhere between x_{i-1} and x_{i+1}, the first derivative may be written:

$$\begin{aligned}\left.\frac{\partial \zeta}{\partial x}\right|_{g,i} &= \frac{\zeta_{g,i+1} - \zeta_{g,i-1}}{2\Delta x} + \mathcal{O}(\Delta x^2)\,, \\ &= \frac{\zeta_{l,i+1} - [\zeta]_{i+1} - \zeta_{g,i-1}}{2\Delta x} + \mathcal{O}(\Delta x^2)\,,\end{aligned} \tag{3.26}$$

where

$$[\zeta]_{i+1} = [\zeta]_\Gamma + (x_{i+1} - x_\Gamma)\left[\frac{\partial \zeta}{\partial x}\right]_\Gamma + \mathcal{O}((x_{i+1} - x_\Gamma)^2)\,. \tag{3.27}$$

This methodology may be used to discretize the pressure Laplacian for an interface located between x_i and x_{i+1} with $x - x_\Gamma > 0$ corresponding to the liquid phase:

$$\left.\frac{\partial}{\partial x}\left(\frac{1}{\rho}\frac{\partial P}{\partial x}\right)\right|_{g,i} = \frac{1}{\rho_g}\frac{P_{g,i+1} - 2P_{g,i} + P_{g,i-1}}{\Delta x^2} + \mathcal{O}(\Delta x^2)\,, \tag{3.28}$$

$$= \frac{1}{\rho_g}\frac{P_{l,i+1} - [P]_{i+1} - 2P_{g,i} + P_{g,i-1}}{\Delta x^2} + \mathcal{O}(\Delta x^2)\,, \tag{3.29}$$

where

$$[P]_{i+1} = [P]_\Gamma + (x_{i+1} - x_\Gamma)\left[\frac{\partial P}{\partial x}\right]_\Gamma + \mathcal{O}((x_{i+1} - x_\Gamma)^2)\,. \tag{3.30}$$

These equations cannot be used in this form, because unlike the pressure jump at the interface, which is a known quantity that depends on local surface tension, the pressure gradient jump at the interface $[\partial P/\partial x]_\Gamma$ is not known *a priori* and has to be derived. With the assumption that the velocity is continuous across the interface, the pressure gradient divided by the density that appears on the RHS of the momentum equation also has to be continuous:

$$\left[\frac{1}{\rho}\frac{\partial P}{\partial x}\right]_\Gamma = 0\,. \tag{3.31}$$

This equation allows to evaluate the pressure gradient jump across the interface from the

pressure gradient in the gas or in the liquid:

$$\begin{aligned}\left[\frac{\partial P}{\partial x}\right]_\Gamma &= -\rho_l \left[\frac{1}{\rho}\right] \left.\frac{\partial P}{\partial x}\right|_{g,\Gamma}, \\ &= -\rho_g \left[\frac{1}{\rho}\right] \left.\frac{\partial P}{\partial x}\right|_{l,\Gamma}.\end{aligned} \tag{3.32}$$

By using the Taylor series expansion of the pressure gradient in the gas or in the liquid from the interface, the pressure jump can be taken equal to the pressure gradient at $i+1/2$:

$$\left.\frac{\partial P}{\partial x}\right|_{g,\Gamma} = \left.\frac{\partial P}{\partial x}\right|_{g,i+1/2} + \mathcal{O}(x_{i+1/2} - x_\Gamma), \tag{3.33}$$

and

$$[P]_{i+1} \simeq [P]_\Gamma - (x_{i+1} - x_\Gamma)\rho_l \left[\frac{1}{\rho}\right] \left.\frac{\partial P}{\partial x}\right|_{g,i+1/2}, \tag{3.34}$$

$$\simeq [P]_\Gamma - (x_{i+1} - x_\Gamma)\rho_l \left[\frac{1}{\rho}\right] \frac{P_{g,i+1} - P_{g,i}}{\Delta x}, \tag{3.35}$$

$$\simeq [P]_\Gamma - (x_{i+1} - x_\Gamma)\rho_l \left[\frac{1}{\rho}\right] \frac{P_{l,i+1} - [P]_{i+1} - P_{g,i}}{\Delta x}. \tag{3.36}$$

The last equation has to be inverted to obtain $[P]_{i+1}$. Then, introducing the index $\theta = (x_\Gamma - x_i)/\Delta x$ and a modified density $\rho^\star = \rho_g\theta + \rho_l(1-\theta)$, the pressure jump at x_{i+1} reads:

$$[P]_{i+1} \simeq \frac{\rho_g}{\rho^\star}[P]_\Gamma + \left(1 - \frac{\rho_g}{\rho^\star}\right)(P_{l,i+1} - P_{g,i}). \tag{3.37}$$

Finally, the pressure jump at x_{i+1} may be replaced in Eq. 3.29, leading to the following discretization of the Laplacian:

$$\left.\frac{\partial}{\partial x}\left(\frac{1}{\rho}\frac{\partial P}{\partial x}\right)\right|_{g,i} = \frac{\frac{1}{\rho^\star}(P_{l,i+1} - P_{g,i}) - \frac{1}{\rho_g}(P_{g,i} - P_{g,i-1})}{\Delta x^2} - \frac{[P]_\Gamma}{\rho^\star \Delta x^2}. \tag{3.38}$$

The extension of this expression to two or three dimensions is straightforward. This result for the pressure equation was obtained by Kang *et al.* [46] and Liu *et al.* [60]. Not using discrete operators to differentiate or interpolate quantities that vary by several orders

of magnitude across the interface is likely to reduce the numerical discretization errors, and therefore the GFM is expected to provide improved accuracy. One additional benefit of using GFM is that because the surface tension force is embedded in the pressure gradient, the discrete balance of pressure forces and surface tension forces is guaranteed, whereas several other methods require an explicit treatment to obtain this property [41, 29].

3.5.3 Viscous formulation

Although advantageous, the GFM is challenging to apply in the presence of the viscous term. While formulations have been proposed [46], they are not easy to implement, and an implicit formulation has proven challenging to develop. Consequently, in the present method the continuum surface force (CSF) approach by Brackbill *et al.* [9] is used for the viscous terms. Considering that we are interested in turbulent problems, the viscous terms are expected to be significant only at the smallest scales, which do not contain much energy, and therefore this choice is not likely to influence significantly the quality of the results. In place of using a smeared-out Heaviside function to compute the density and viscosity, as in Olsson and Kreiss [78], we directly use ψ:

$$\begin{aligned} \rho(\mathbf{x},t) &= \rho_g + (\rho_l - \rho_g)\,\psi\,(\mathbf{x},t)\,, \\ \mu(\mathbf{x},t) &= \mu_g + (\mu_l - \mu_g)\,\psi\,(\mathbf{x},t)\,. \end{aligned} \tag{3.39}$$

Using this approach, an implicit time integration is straightforward, and therefore the time step size is not limited by the viscous CFL condition.

3.5.4 Time integration

Following the approach described in Chapter 2, we make use of an iterative temporal advancement with staggering in time between the velocity field and the scalar and density fields. In the context of multiphase flow simulations, the level set field is advanced first from $t^{n-1/2}$ to $t^{n+1/2}$ using the velocity at t^n. A semi-implicit Crank-Nicolson approach is used here, but it should be noted that the sub-iterations concern only the level set field

advancement, and are not related to the velocity sub-iterations, since the velocity field at time t^n is known. The velocity field is then advanced from t^n to t^{n+1}, and the level set information is used at $t^{n+1/2}$ to solve the Poisson equation for pressure. This variable-coefficient, elliptic equation is solved using a combination of Krylov-based methods [112] preconditioned using a multi-grid solver [26].

3.5.5 Full solution procedure

The full solution procedure is here summarized:

- Using the ACLS methodology, advance the interface implicitly from $t^{n-1/2}$ to $t^{n+1/2}$ using the velocity at t^n.
- Advance the velocity field implicitly from t^n to t^{n+1} by solving Eq. 3.1 without pressure gradient.
- Project the velocity field by solving the Poisson equation making use of GFM. The solution of the pressure equation is computed using a Krylov-based method, preconditioned by a multi-grid solver.
- Correct the velocity at t^{n+1} using the pressure gradient, again using GFM.

3.6 Applications

In order to assess the capability of the proposed method to tackle a wide range of multiphase problems, several test cases involving surface tension, topology changes, and high density ratios, are investigated. For all these problems, the minimum number of points required to obtain a good description of the physics is discussed. The proposed methodology is then used to compute then turbulent atomization of a liquid Diesel jet.

3.6.1 Parasitic currents

The errors in curvature computation will lead to discrete errors in the surface tension force, ultimately generating spurious velocities at the interface between the two phases. To assess

La	12	120	1200	12000	120000	1200000
Ca	4.54×10^{-5}	3.67×10^{-5}	3.62×10^{-5}	4.15×10^{-5}	3.75×10^{-5}	8.19×10^{-6}

Table 3.6: Dependence of the magnitude of parasitic currents with the Laplace number for a static droplet with surface tension on a 32×32 mesh.

Mesh	8×8	16×16	32×32	64×64	128×128
Ca	1.61×10^{-4}	8.95×10^{-5}	4.15×10^{-5}	2.24×10^{-5}	1.16×10^{-5}

Table 3.7: Dependence of the magnitude of parasitic currents with mesh spacing for a static droplet with surface tension with La = 12000.

the importance of these parasitic currents, a static two dimensional drop with a diameter of $D = 0.4$, placed at the center of a unit box, is computed. The viscosity of both fluids is set to $\mu = 0.1$, the surface tension coefficient to $\sigma = 1$, and the density ratio to unity. By changing the density ρ of both fluids, the Laplace number $\mathrm{La} = 1/\mathrm{Oh}^2 = \sigma\rho D/\mu^2$ can be varied. The capillary number $\mathrm{Ca} = |u_{\max}|\,\mu/\sigma$ is computed at a non-dimensional time of $t\sigma/(\mu D) = 250$. The results for a 32×32 mesh, presented in Table 3.6, show that the capillary number remains small independently of the Laplace number.

To assess mesh convergence of the parasitic currents, the Laplace number is fixed to 12000, while mesh spacing is varied. Table 3.7 shows the resulting capillary numbers, that display first order convergence.

While these values are slightly larger than those obtained by previous studies that benefited from higher order curvature computations [41, 106, 90], they remain very small, and have not been found to affect the accuracy of the computed solutions in an unreasonable way.

3.6.2 Standing wave

Next, the viscous damping of a surface wave is investigated. This test case will help assess the capability of the proposed method to accurately simulate problems where viscosity and surface tension forces interact. In a two dimensional domain of size $[0, 2\pi] \times [0, 2\pi]$, two superimposed fluids with density ρ_1 and ρ_2 are initially separated by a flat interface, slightly

perturbed by a sine wave profile, namely

$$\phi(x,y) = \pi - y + A_0 \cos(2\pi x/\lambda), \tag{3.40}$$

where the wavelength of the perturbation λ is set to 2π, and the initial amplitude of the wave is $A_0 = 0.01\lambda$. Periodic boundary conditions are used for the x-direction, and slip walls are used in the y-direction. In the case where both fluids have the same kinematic viscosity ν, Properetti [91] employed initial value theory to derive an analytical expression to the evolution of the wave amplitude with time. The reader is referred to Prosperetti [91] for the details of these analytical results. We simply recall here the inviscid oscillation frequency $\omega_0 = \sqrt{\frac{\sigma}{\rho_1+\rho_2}}$ that is used to non-dimensionalize the computational time.

Following the case study presented by Herrmann [41], we investigate a first case with unity density ratio, and a second with a density ratio of 1000. For both cases, three different meshes are tested, namely an 8×8 mesh, a 16×16 mesh, and a 32×32 mesh. The simulations are performed up to a time of $\omega_0 t = 20$, leading to approximately three full oscillation periods. During these simulations, we ensure that the conservative re-initialization is called at least once. Moreover, the FMM is employed at each iteration in order to reconstruct ϕ from ψ, as described in Section 3.4.2.

For the first case, the non-dimensional surface tension coefficient is set to $\sigma = 2$, and the non-dimensional kinematic viscosity in both fluids is set to $\nu = 0.064720863$. Both fluid densities are set to unity. The time step size is taken to be $\Delta t = 0.01$, regardless of the mesh size. The time evolution of the wave amplitude for the different meshes as well as for the theoretical results are shown for this first case in Fig. 3.14(a). The error between the exact solution and the computed solution, normalized by A_0, is shown in Fig. 3.14(b). It can be observed that even with a mesh as coarse as 8×8, adequate results are obtained. However, a slight discrepancy in the oscillation period leads to a significant error on this mesh. As expected, increasing the mesh size to 16×16 or 32×32 gives much more accurate results. The RMS values of the error in amplitude for the three meshes employed are summarized in Table 3.8. Second order convergence is observed.

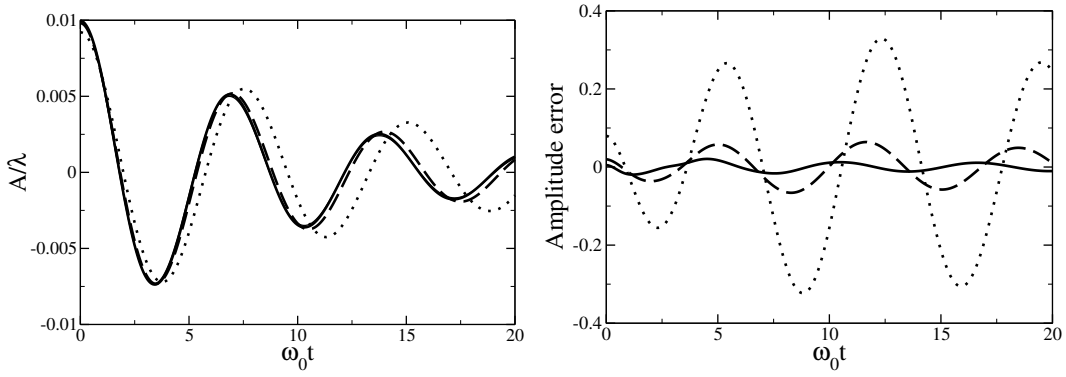

(a) Time evolution of the wave amplitude (b) Time evolution of the amplitude error

Figure 3.14: Damped surface wave problem with unity density ratio. 8×8 mesh (dotted line), 16×16 mesh (dashed line), 32×32 mesh (solid line), and theory (thin line).

Mesh	Error
8×8	0.1996610
16×16	0.0395346
32×32	0.0103786

Table 3.8: RMS value of the amplitude error for the standing wave with unity density ratio.

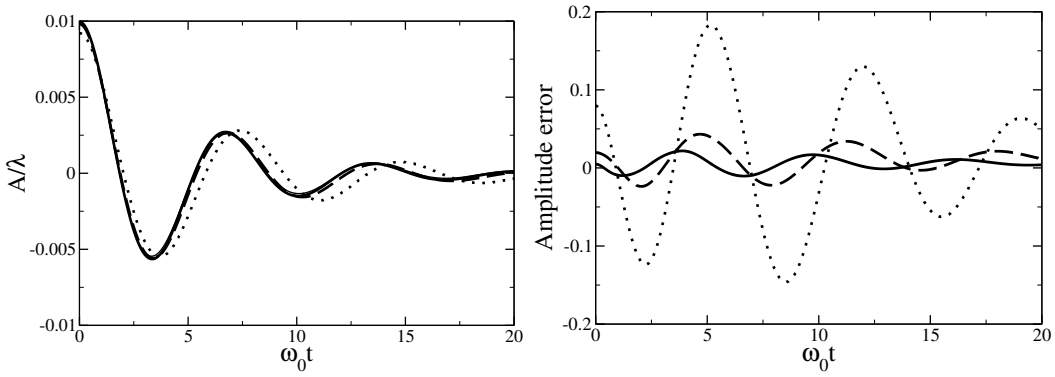

(a) Time evolution of the wave amplitude (b) Time evolution of the amplitude error

Figure 3.15: Damped surface wave problem with density ratio 1 : 1000. 8×8 mesh (dotted line), 16×16 mesh (dashed line), 32×32 mesh (solid line), and theory (thin line).

Mesh	Error
8×8	0.0892302
16×16	0.02043
32×32	0.00971

Table 3.9: RMS value of the amplitude error for the standing wave with density ratio 1 : 1000.

These results are comparable to previous work [41, 90], and suggest that about ten mesh points per wavelength are necessary to capture the physics accurately.

The next case involves a high density ratio, obtained by setting $\rho_1 = 1$ and $\rho_2 = 1000$. The kinematic viscosity of both fluids is set to $\nu = 0.0064720863$. Again the results are compared to the work of Prosperetti [91], and we can see in Fig. 3.15 that good agreement is obtained, even with the coarsest mesh. Table 3.9 summarizes the RMS of the errors in amplitude, and we can see that at least first order convergence is obtained. This slow convergence rate has also been reported by Herrmann [41]. These results suggest again that about ten points per wavelength are sufficient to accurately describe the physics of this problem, even with large density ratios.

3.6.3 Capillary instability

The computation of a Rayleigh instability is performed in order to assess in details the capability of the proposed approach to simulate surface tension-driven instabilities. This test case follows the work of Ménard *et al.* [68], where the dispersion relation was computed, and completes it by investigating mesh convergence. Following Ménard *et al.* [68], the capillary instability of a stationary water column in air is computed on a two dimensional axisymmetric domain of size $[0, \lambda] \times [0, 3r_0]$, where r_0 is the mean column radius, which is set to $r_0 = 1/3 \times 10^{-3}$ m, and the initial perturbation wavelength is λ. The initial level set field therefore reads

$$\phi(x, y) = r_0 - y + A_0 \cos(2\pi x/\lambda), \tag{3.41}$$

where A_0 is the initial disturbance amplitude set to $A_0 = 10^{-4}\Delta y$, where Δy is the mesh spacing in the y-direction. The computational domain has periodic conditions in the x-direction, and a slip wall in the y-direction. Whereas Ménard *et al.* [68] used 61 grid points in the y-direction, we choose to decrease this number to only 24. Keeping $\Delta x = \Delta y$, the number of points in the x-direction is varied in order to change the disturbance wavelength λ. We then compute the non-dimensional growth rate β/β_0 of the disturbance, where $\beta_0 = \sqrt{\sigma/\left(\rho_l r_0^3\right)}$, as a function of its non-dimensional wavenumber $\xi = 2\pi r_0/\lambda$, and compare it to the linear theory due to Weber [117]. The results, shown in Fig. 3.16, are very satisfactory, and suggest that the proposed methodology succeeds at capturing this capillary instability with as little as 8 points per column radius.

As a second step, we propose to compare the results for $\lambda = 12r_0$ obtained with three different meshes, namely a 32×8 mesh, a 64×16 mesh, and a 128×32 mesh. Figure 3.17 shows the time evolution of the interface location for the different meshes. It can be observed that the medium and the fine mesh solution are very close to each other, while the coarse mesh solution is significantly different, and underpredicts the growth rate of the instability. Table 3.10 compares the errors for both the velocity and the level set, assuming the fine mesh solution is the exact solution, both before break-up and after break-up. The order of convergence that is obtained for the L_1-norm of the errors for u, v, and ψ is between first

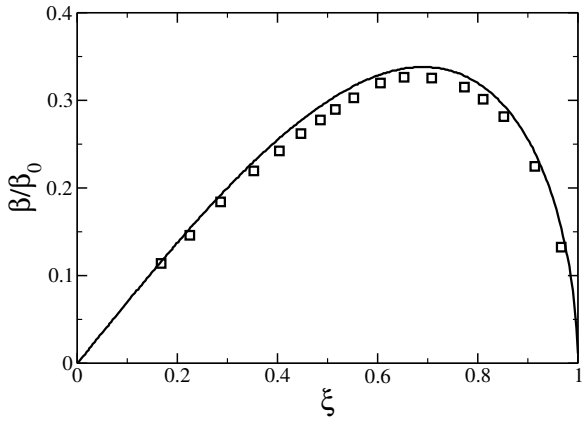

Figure 3.16: Growth rate of the disturbance as a function of its wavelength for the capillary instability. Simulation with 24 points in the radial direction (symbols), and linear theory by Weber [117] (line).

Quantity	$t = 5 \times 10^{-3}$ s	$t = 1 \times 10^{-2}$ s	$t = 1.5 \times 10^{-2}$ s
u	1.06	1.27	0.79
v	1.05	1.52	1.09
ψ	1.42	2.24	2.04

Table 3.10: Convergence rates of the L_1-errors of different quantities, at different times, for the capillary instability test case.

and second order, even during and after the break-up of the column. Again, these results suggest that the medium mesh is sufficient to obtain an accurate description of the physics, and therefore it can be concluded that about 10 grid points in the column are necessary to appropriately predict capillary break-up.

3.6.4 Turbulent atomization of a liquid Diesel jet

All cases performed until now are very limited in terms of complexity, because they cover only low Reynolds number flows, or flows governed by surface tension and viscous effects. In order to assess the performance of the proposed approach in the presence of fully developed turbulence, the simulation of a turbulent liquid jet in quiescent air is conducted. The properties for the simulation are inspired by liquid Diesel injection systems, although both

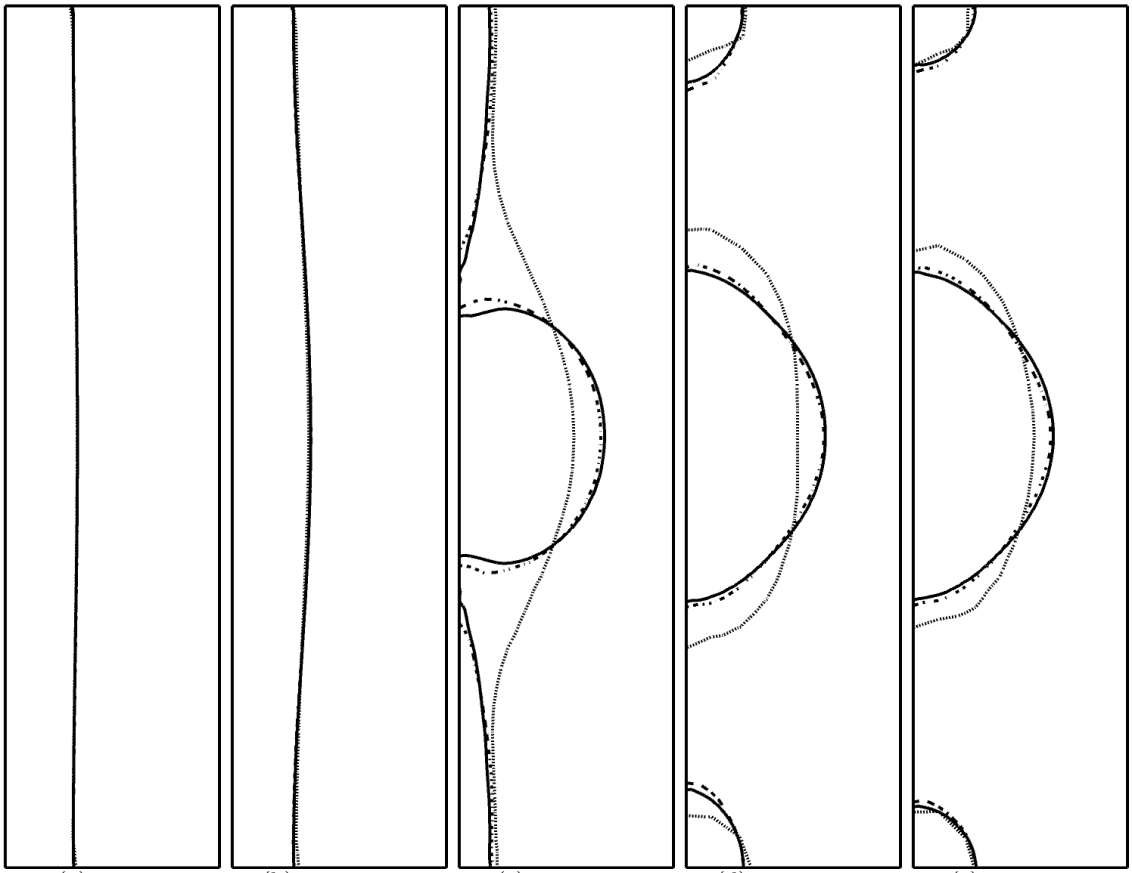

(a) $t = 0\,\mathrm{s}$ (b) $t = 0.005\,\mathrm{s}$ (c) $t = 0.01\,\mathrm{s}$ (d) $t = 0.015\,\mathrm{s}$ (e) $t = 0.02\,\mathrm{s}$

Figure 3.17: Interface shape for the capillary instability where $\lambda = 12r_0$, computed with three different meshes: a 32×8 mesh (dotted line), a 64×16 mesh (dashed line), and a 128×32 mesh (solid line).

ρ_l/ρ_g	μ_l/μ_g	Re_l	We_l
40	40	3000	10000

Table 3.11: Physics parameters for the liquid jet atomization test case.

the Reynolds number and Weber number have been reduced to make the simulation possible. The parameters employed are summarized in Table 3.11.

No sub-grid scale model is employed for this simulation, even though it seems likely that the smallest structures are not fully resolved. This simulation can provide some much needed insights, both on the resolution requirements to simulate turbulent atomization, and on the performance of the present method in the context of turbulent flows. The computation is performed on a domain of size $24D \times 3D \times 3D$, where D is the jet diameter, discretized on a $1024 \times 128 \times 128$ mesh. The inflow conditions are obtained by first simulating a turbulent pipe using the liquid properties, and storing the time-dependent velocity information. This information is then re-injected in the computational domain.

Instantaneous snapshots of the interface at different times are presented in Fig. 3.18. The interface displays a complex, turbulent behavior, as the liquid jet undergoes turbulent atomization. Many complex phenomena interact, leading to a fast break-up of the liquid core into ligaments and sheets, then droplets. It is interesting to note that by the end of the computational domain, the liquid core has fully disintegrated. The ψ-field as well as the magnitude of the vorticity field are presented in several two dimensional cuts in Fig. 3.19. The fully developed nature of the turbulence appears clearly, along with the chaotic nature of the interface. Even for such a complex, turbulent, three-dimensional flow, the proposed multiphase method appears robust.

Finally, we compare the mass enclosed in the $\psi = 0.5$ iso-contour with the expected liquid mass as a function of time in Fig. 3.20. With a maximum of 3% mass loss, the method appears very satisfactory in terms of mass conservation, even in a complex turbulent case.

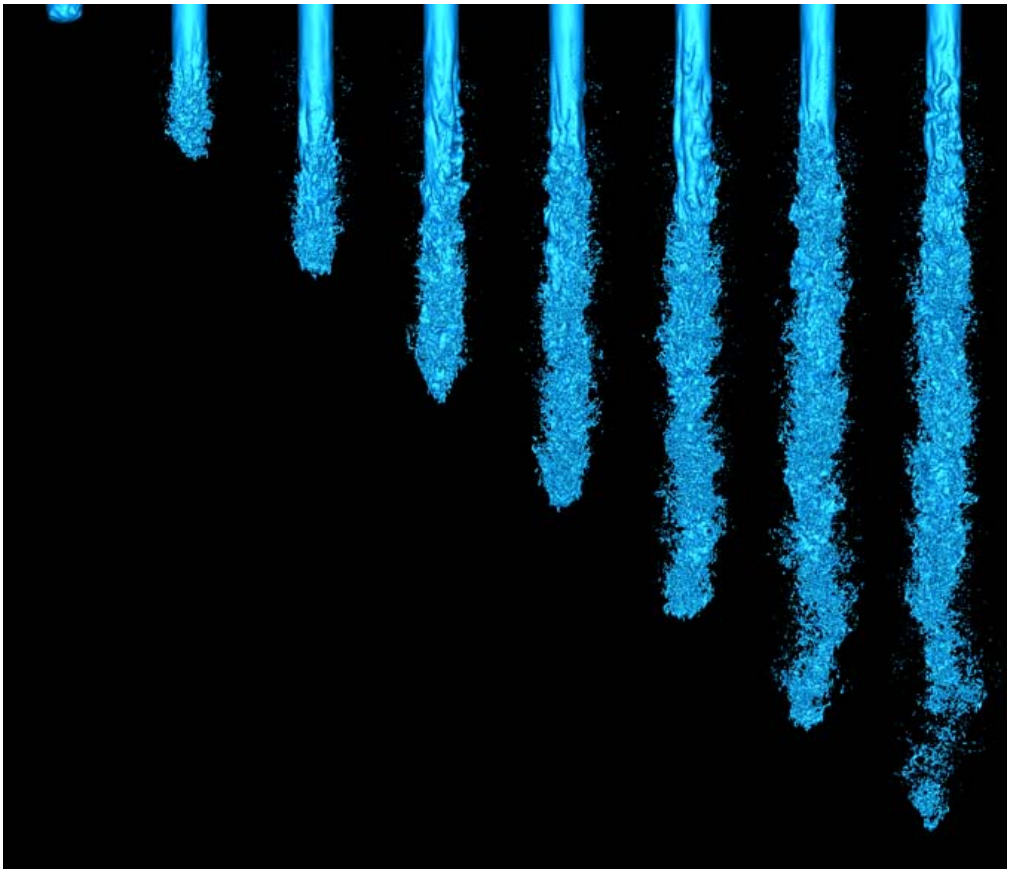

Figure 3.18: Turbulent atomization of a liquid Diesel jet. $\Delta t = 2.5$ between each image.

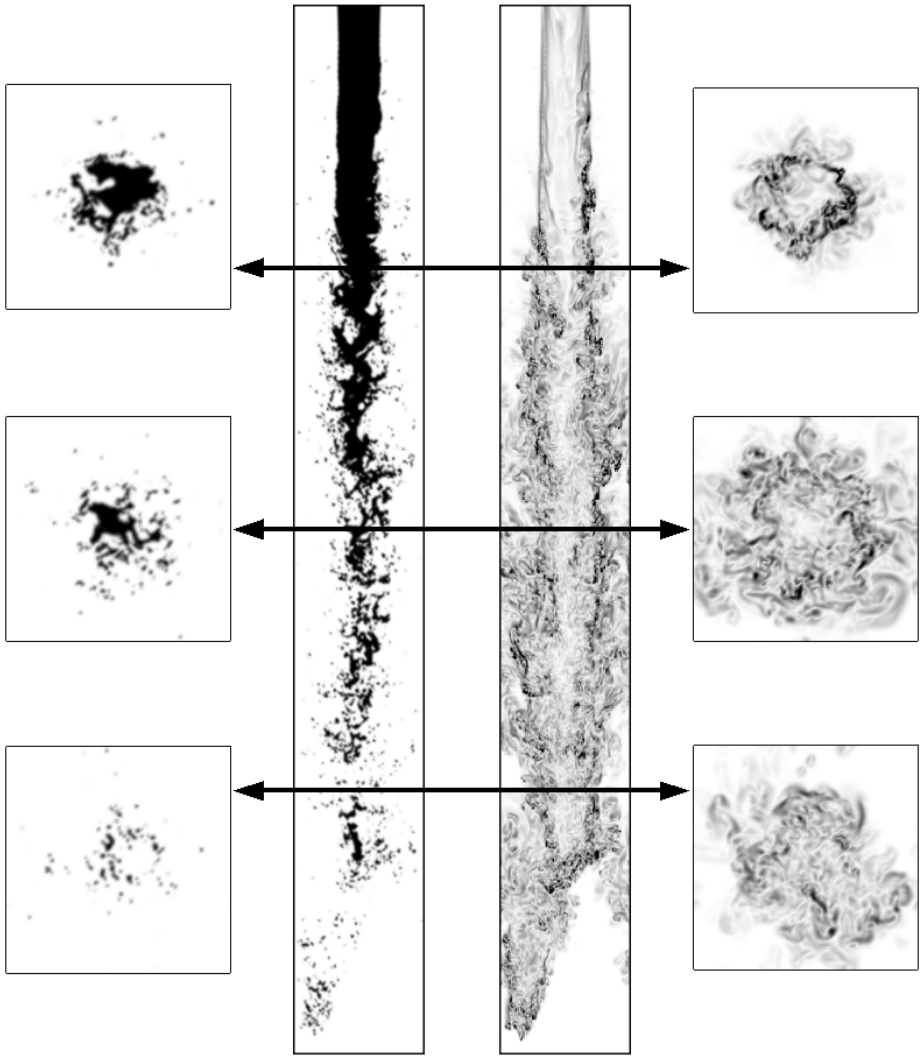

Figure 3.19: ψ-field (left) and magnitude of the vorticity (right) on two dimensional axial and lateral cuts at $t = 22.8$ for the turbulent liquid jet case.

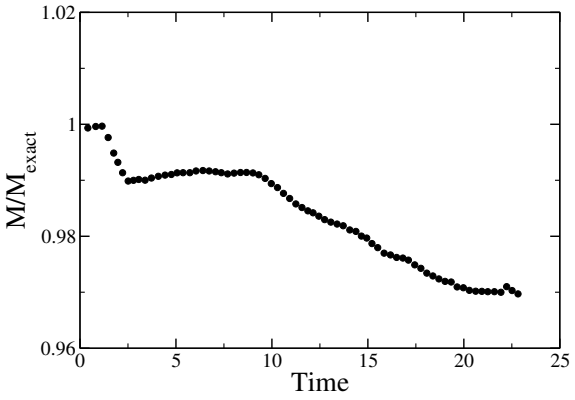

Figure 3.20: Mass conservation errors for the turbulent liquid jet case.

3.7 Summary

The ACLS methodology provides accurate and robust interface transport with good mass conservation properties. The combination of a converging curvature, implicit time advancement, and good mass conservation makes this approach very well suited for many complex multiphase problems. Even for the complex problem of turbulent atomization of a liquid jet, the method is robust and mass conservation errors are shown to remain small. However, the close examination of Fig. 3.10 suggests that this level set method can lead to numerical breakup. This can be observed when the stretching of the ligament in the deformation field leads to the generation of drops at the scale of the cell size. Since this case should technically lead to the loss of part of the area enclosed in the interface, trying to enforce the conservation of this area will be detrimental to the accuracy of the method. The mechanism by which the conservative re-initialization equation works can be related to an additional, numerically induced, surface tension force. This numerical capillary effect will effectively induce a cut-off in the scales that can be generated in the simulation, such that all structures should always remain properly resolved. This is not surprising, and this analysis can be generalized to all mass-conserving approaches to interface transport, such as VOF or CLSVOF. However, this remark can lead to questions on the ability of the ACLS approach and other mass-conserving schemes to handle properly the smallest scale structures. We

have seen already this tendency of transforming ligaments into drops, and similarly we can expect a natural tendency of replacing sheets by ligaments. As a consequence, it is of great interest to investigate a different level set approach that could improve the representation of the smallest scale structures. This is done in the following through the introduction of sub-cell resolution.

Chapter 4

Spectrally refined interface

4.1 Objectives

To simulate primary atomization, it is clear that accurately predicting the smallest scales is fundamental. Having realized that most numerical methods become inaccurate at the smallest resolved scales, the idea of introducing sub-cell resolution for the level set function becomes natural. In this chapter, the choice is made to improve the sub-cell representation of a level set function through a pseudo-spectral approach. In each cell, a polynomial reconstruction of the level set function is created, leading to highly improved accuracy of the transport at the smallest scales. By maintaining a Eulerian-type description of the interface, topology changes and characteristics crossings are handled automatically. Such a strategy is not new, and has been employed before [103, 65]. However, all the previous work relied on a fully pseudo-spectral description of all the equations. Because of the cost associated with high order pseudo-spectral schemes, the order of the pseudo-spectral method presented by Marchandise *et al.* [65] remained limited. In Sussman and Hussaini [103], only level set transport tests were performed, without the coupling to the Navier-Stokes equations. Here, in a similar spirit as in the RLSG method [41], the pseudo-spectral description is used only for the level set, with the objective to introduce sub-cell interface resolution. Because of the potentially high order polynomial description, the frequent re-initialization

step that is characteristic to level set methods becomes superfluous, since the increased accuracy handles both small and large gradients adequately. In order to allow for very fine resolution without affecting the time step size, the interface transport is performed using a semi-Lagrangian approach. Finally, a method to extract the curvature is proposed that computes a converging curvature at the scale of the flow solver grid, therefore removing all possible coupling with sub-cell fluctuations.

4.2 Spectrally Refined Interface (SRI) approach

4.2.1 Pseudo-spectral collocation-based sub-cell reconstruction

Consider any level set function G. The transport equation for this function is written

$$\frac{\partial G}{\partial t} + \boldsymbol{u} \cdot \nabla G = 0. \tag{4.1}$$

In order to enable sub-cell resolution, a polynomial reconstruction of the level set function is generated in each cell by introducing a set of quadrature points. These points correspond to the locations where the nodal values of the level set function are specified. Several considerations have to be taken into account while choosing the quadrature points, such as the accuracy of the resulting reconstruction. For example, a uniform distribution of quadrature points inside each cell is expected to lead to the Runge phenomenon, which will strongly limit the accuracy of the polynomial reconstruction [43, 10]. To avoid this issue, the most logical approach is to employ Gauss quadrature. Here, the choice is made to use Gauss-Lobatto quadrature, such that some quadrature points are located on the cell faces. This property will be used to improve the continuity of the level set function across cells. The Gauss-Lobatto quadrature points can be based on any suitable family of orthogonal polynomials, such as Legendre or Chebyshev. Figure 4.1 shows an example of quadrature points for different numbers of unknowns p. The multi-dimensional extension of this approach is straightforward for the structured cartesian mesh considered here. However, it is also possible for complex unstructured meshes by using linear transformations [62].

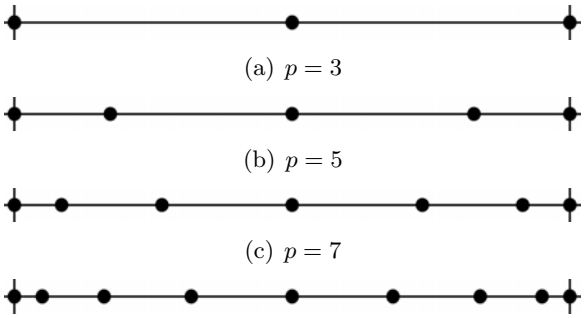

Figure 4.1: Location of the Gauss-Lobatto quadrature nodes based on the Legendre polynomials in one dimension for various numbers of unknowns p.

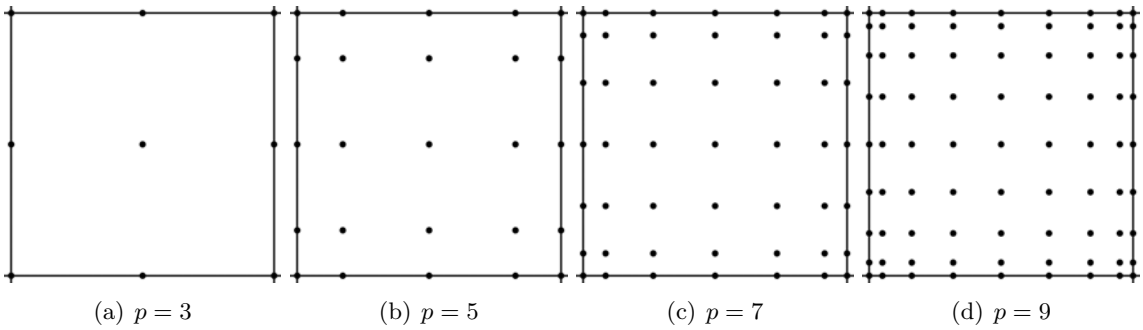

Figure 4.2: Location of the Gauss-Lobatto quadrature nodes based on the Legendre polynomials in two dimensions for various numbers of unknowns p^2.

Sample two-dimensional sets of quadrature nodes in a cell are shown in Fig. 4.2. In each flow solver cell, the quadrature points located on the right, top, and far face are considered as ghost nodes, whose G values are equal to those of the neighboring cells. For example, in the x-direction, the values of the quadrature nodes located at the right face of cell i are not stored, but considered to be equal to the G values of the quadrature nodes located at the left face of cell $i + 1$. This is illustrated in Fig. 4.3 for a two dimensional configuration. This approach avoids any redundancy in computing face points, and naturally improves the continuity of the polynomials across cell faces.

Because of the structured environment which is considered here, one index will be used per direction to describe the computational space. Let the G value of the quadrature point

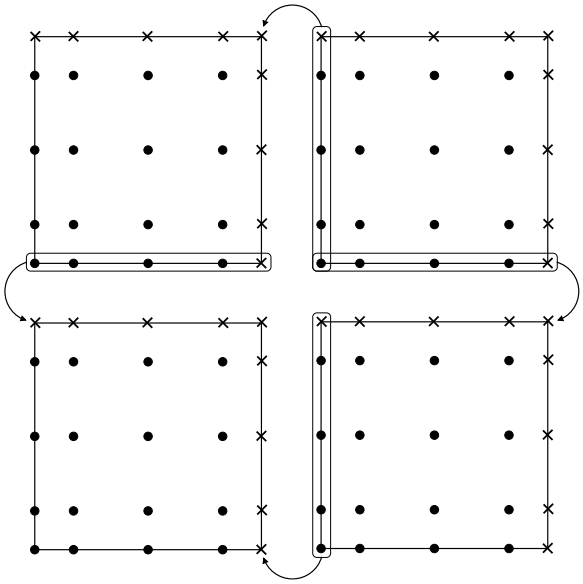

Figure 4.3: Ghost quadrature point locations (crosses), normal quadrature points (circles), and inter-cell communication patterns (arrows).

(l, m, n) of the flow solver cell (i, j, k) be denoted $G_{i,j,k}^{l,m,n}$, and its position vector $\boldsymbol{x}_{i,j,k}^{l,m,n}$. Consider the number of quadrature points per direction to be p. For the sake of simplicity of notation, this number of points will be considered equal for each direction. Using the cardinal functions for algebraic interpolation $L^{\alpha}(\boldsymbol{x})$ for $\alpha \in [\![1, p]\!]$, the level set function reconstruction within cell (i, j, k) will be written

$$G_{i,j,k}(\boldsymbol{x}) = \sum_{l=1}^{p} \sum_{m=1}^{p} \sum_{n=1}^{p} L^{l}(\boldsymbol{x}) L^{m}(\boldsymbol{x}) L^{n}(\boldsymbol{x}) G_{i,j,k}^{l,m,n}. \tag{4.2}$$

Note that this reconstruction is of order $p - 1$. This expression can be further simplified to account for the independence of the directions and the simple form of L^{α}. Consider a cell of unit size in one direction and let r_l with $l \in [\![1, p]\!]$ represent the position of the l^{th} quadrature point in that direction, for which then $r_1 = 0$ and $r_p = 1$. Similarly, let the flow solver mesh be defined by the location of the lower, left, proximal corner (x_i, y_j, z_k) for each

cell (i, j, k). The basis polynomials are then written

$$L^{\alpha}(r) = \frac{\prod_{\beta=1,\beta\neq\alpha}^{p}(r - r_{\beta})}{\prod_{\beta=1,\beta\neq\alpha}^{p}(r_{\alpha} - r_{\beta})}. \tag{4.3}$$

The polynomial reconstruction of the level set function for cell (i, j, k) will then be expressed directly as

$$G_{i,j,k}(x, y, z) = \sum_{l=1}^{p} L^{l}\left(\frac{x - x_i}{x_{i+1} - x_i}\right) \sum_{m=1}^{p} L^{m}\left(\frac{y - y_j}{y_{j+1} - y_j}\right) \sum_{n=1}^{p} L^{n}\left(\frac{z - z_k}{z_{k+1} - z_k}\right) G_{i,j,k}^{l,m,n}. \tag{4.4}$$

The computational cost of this approach remains limited, since some of the quantities related to the polynomial reconstruction can be pre-computed for a unit cell and stored. The one dimensional equivalent to Eq. 4.4 is

$$G_i(x) = \sum_{l=1}^{p} L^{l}\left(\frac{x - x_i}{x_{i+1} - x_i}\right) G_i^{l}. \tag{4.5}$$

This expression can be expanded into

$$G_i(x) = \sum_{l=1}^{p} \frac{\prod_{\beta=1,\beta\neq l}^{p}\left(\left(\frac{x-x_i}{x_{i+1}-x_i}\right) - r_{\beta}\right)}{\prod_{\beta=1,\beta\neq l}^{p}(r_l - r_{\beta})} G_i^{l}, \tag{4.6}$$

which can be re-written as

$$G_i(x) = P\left(\frac{x - x_i}{x_{i+1} - x_i}\right) \sum_{l=1}^{p} \frac{G_i^{l}}{\left(\frac{x-x_i}{x_{i+1}-x_i} - r_l\right) Q_l}, \tag{4.7}$$

where

$$P(r) = \prod_{\alpha=1}^{p}(r - r_{\alpha}) \quad \text{and} \quad Q_l = \prod_{\alpha=1,\alpha\neq l}^{p}(r_l - r_{\alpha}). \tag{4.8}$$

For $l \in [\![1, p]\!]$, the quantity Q_l can be pre-computed and stored, making the polynomial evaluation at any point in space efficient. In order to further reduce the computational cost associated with this sub-cell polynomial reconstruction, these polynomials are created only

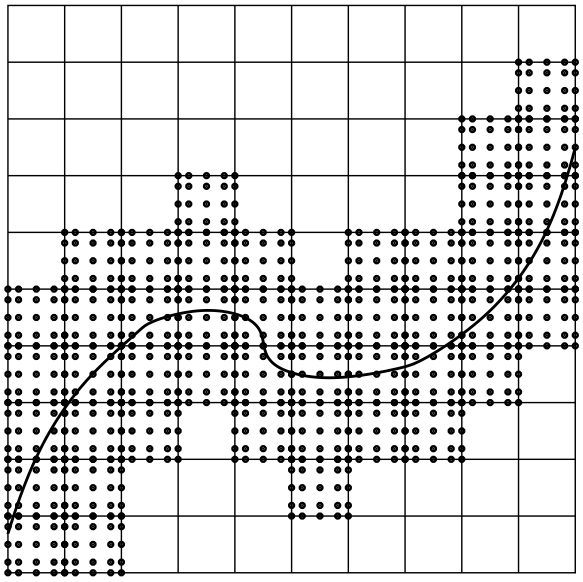

Figure 4.4: Narrow band spectral refinement around the G_0 iso-contour of the level set function G (thick line).

in a narrow band around the front, i.e. around the G_0 value of the level set function, as illustrated by Fig. 4.4.

4.2.2 Semi-Lagrangian transport

Having a sub-cell polynomial reconstruction of the level set function G in each cell is only the first step. An efficient and accurate transport scheme must now be devised. Classically, pseudo-spectral methods have been used to solve conservation laws by computing fluxes from the polynomials directly. This approach is spectrally accurate, but it leads to very strong time step size restrictions. Indeed, as can be seen in Fig. 4.1, the smallest distance between two quadrature nodes decreases faster for Gauss-type quadratures than for a uniform distribution as p increases, leading rapidly to very severe CFL restrictions. More precisely, it can be shown that the time step size should vary as p^{-2}. This makes this approach unsuited in the case where $p > 3$. As a consequence, a different approach has to be followed that allows to circumvent the time step restriction associated with sub-cell

refinement.

Semi-Lagrangian (SL) transport naturally emerges as an attractive alternative. Instead of discretizing Eq. 4.1, SL transport consists of observing that G should be constant along the trajectory of material points evolving at velocity $\boldsymbol{u}$. Therefore, the trajectory that passes through $\boldsymbol{x}^{n+1}$ at time t^{n+1} can be followed backward in time to $t^n = t^{n+1} - \Delta t$ to obtain the old location $\boldsymbol{x}^n$. The value of the level set function G^{n+1} at $\boldsymbol{x}^{n+1}$ can simply be obtained by noting that $G^{n+1}\left(\boldsymbol{x}^{n+1}\right) = G^n\left(\boldsymbol{x}^n\right)$. Because of the Lagrangian nature of this method, larger time step sizes can be used. The only requirement is the computation of $\boldsymbol{x}^n$ from $\boldsymbol{x}^{n+1}$, which involves solving an ordinary differential equation. Moreover, this approach is efficient and easy to implement. These advantages make SL transport seemingly a beneficial method for the discretization of any advection term. But the method is typically avoided for conserved quantities, since it does not have any conservation property. This limitation is not a problem in the case of level set, where the transport equation (Eq. 4.1) is already written in non-conservative form. Another commonly accepted limitation of SL transport is its tendency to be overly diffusive [84]. This is due to the interpolation step that has to be performed to compute $G^n\left(\boldsymbol{x}^n\right)$, since $\boldsymbol{x}^n$ is unlikely to coincide with the locations where G^n is known. However, in the framework of SRI, a polynomial reconstruction of order $p-1$ is readily available in each cell. Hence, this polynomial can simply be evaluated at the old location $\boldsymbol{x}^n$, and high accuracy can be expected from the SL transport. It is therefore expected that numerical diffusion will not be an issue. Figure 4.5 illustrates the transport procedure. Each quadrature point is advected backwards in time (Figs. 4.5(a) and 4.5(b)) using a Runge-Kutta scheme. The order of the time integration can be varied between first and fourth order. The effect of the temporal order of accuracy will be discussed at the end of this section. To construct the velocity vector in the RK algorithm, a tri-linear interpolation from the 8 closest points is used. At the old location, the polynomial reconstruction of G is evaluated (Fig. 4.5(c)), leading to the new G value at the new quadrature point location $\boldsymbol{x}^{n+1}$ (Fig. 4.5(d)). Note that this procedure is applicable only when the old location $\boldsymbol{x}^n$ lies within the narrow band where the polynomial reconstruction of G is available. In the case where $\boldsymbol{x}^n$ falls outside the refined region, the procedure is modified to use either a boundary

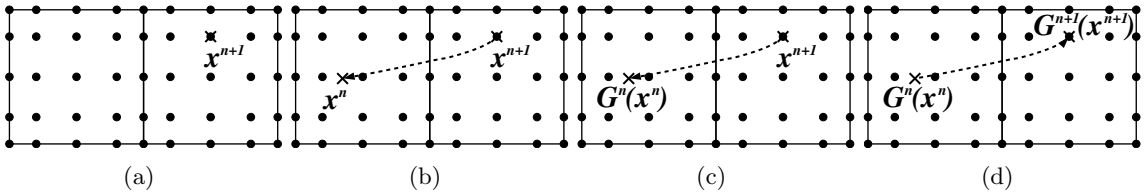

Figure 4.5: Semi-Lagrangian transport of the spectrally refined level set function G.

condition value for the level set function or to revert back to unrefined level set values that can be transported using a classical scalar transport scheme. As an example, if the level set function is taken to be a signed distance function, i.e.

$$|\phi(\boldsymbol{x},t)| = |\boldsymbol{x} - \boldsymbol{x}_\Gamma|, \tag{4.9}$$

where $\boldsymbol{x}_\Gamma$ corresponds to the point on the interface that is closest to $\boldsymbol{x}$, and $\phi(\boldsymbol{x},t) > 0$ on one side of the interface, and $\phi(\boldsymbol{x},t) < 0$ on the other side, then the values of the level set function need to be provided outside of the narrow band. This can be done either by transporting the level set using a classical approach, preferably using fast, low-order accurate methods, or by extending the distance function from the narrow band to a larger band using a standard re-initialization technique. If the choice is made to use a sharp hyperbolic tangent function, i.e.

$$\psi(\boldsymbol{x},t) = \frac{1}{2}\left(\tanh\left(\frac{\phi(\boldsymbol{x},t)}{2\epsilon}\right) + 1\right), \tag{4.10}$$

where ϵ is the thickness of the function, then, as long as ϵ is small enough, its values outside the refined narrow band can be approximated by 0 or 1, depending on which side of the interface is considered.

4.2.3 Stabilization technique

Ensuring the stability of the numerical method is fundamental. In multi-domain spectral methods, the stability is ensured by using a Riemann solver that introduces diffusion in

the treatment of the fluxes at the cell faces [62, 43]. Because SL transport is used here, this approach is not applicable. As a consequence, the stability of the proposed approach could be an issue. In order to alleviate this potential problem, two methods have been employed. The first method has already been described, and consists of reducing the cell to cell oscillations of the polynomials by enforcing that the face quadrature nodes share the same values. While not discretely ensuring the continuity of the polynomials across cells, this greatly reduces the oscillations between each sub-cell reconstruction. The other method that is employed here to ensure the robustness of the SRI approach is to revert back to local tri-linear interpolations between quadrature nodes when the polynomial is found to oscillate, as shown in Fig. 4.6. Very simple and straightforward to implement, the idea behind this approach is to check that each polynomial evaluation lies between the level set values of the 8 closest quadrature points. If it is indeed the case, then the polynomial evaluation is considered valid, and therefore trusted. If it is not the case, then it means that locally the polynomial reconstruction is oscillating, and therefore it is replaced by the use of tri-linear interpolation. This was found to be sufficient to remove all oscillations from the computed solutions. Moreover, it was also found that it is only rarely necessary to revert to tri-linear interpolation, and therefore it is expected to have little impact on the accuracy of the method. For example, in the solid body rotation of a notched circle test case presented below, the tri-linear interpolation was used only 8.2% of the time, and for the circle in a deformation field test case, it was used 10.6% of the time. In addition, note that the second order error introduced in this tri-linear interpolation step is at the sub-cell level, therefore of order $O\left((\Delta x/p)^2\right)$.

4.2.4 Curvature computation

A central element of multiphase models is the computation of the interface curvature. Indeed, this term governs the surface tension force, which itself is fundamental to capturing accurately two-phase flow phenomena. However, extracting a curvature that converges under mesh refinement from the sub-cell information that is available through SRI can be challenging, since it is likely that sub-cell structures will appear, that should not be seen by

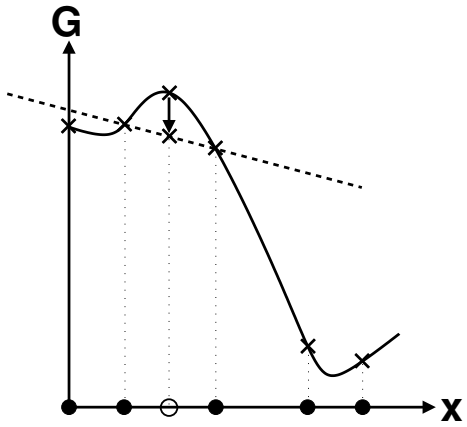

Figure 4.6: One dimensional illustration of the stabilization approach for SRI: when evaluating the polynomial function (solid line) at a new location (open circle) outside the quadrature points (filled circles), the resulting value is replaced by a linear interpolation between the closest neighbors (dashed line) if the polynomial evaluation does not lie between the values of the closest neighbors.

the momentum solver mesh. Two pathological cases are presented in Fig. 4.7. Figure 4.7(a) illustrates the case when the interface is flat over each cell. This case would lead to a zero sub-cell curvature, while the curvature on the flow solver mesh is clearly non-zero. The opposite situation is shown in Fig. 4.7(b), where small sub-cell oscillations in front position are present. In this case, the sub-cell curvature is difficult to compute, and many different formulations are possible. Herrmann [41] chooses to compute local sub-cell curvatures, and then evaluates surface-averages. It is unclear whether such an approach will provide an adequate curvature, since the surface-averaged quantity can be polluted by sub-cell oscillations.

This suggests that the curvature should be computed from information resolvable by the flow solver mesh. In other words, since the length scales below $2\Delta x$ are not resolved by the flow solver, and therefore might not correspond to physical phenomena, these should be filtered out of the interface before the curvature is computed. In order to do this, two steps are introduced:

- *Reconstruction of a signed distance to the interface on the flow solver mesh.* This

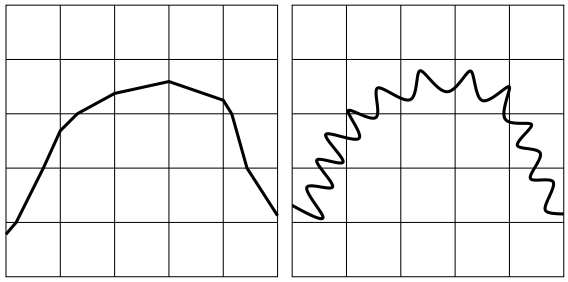

Figure 4.7: Pathological cases for sub-cell curvature computation.

operation is done by combining a marching cubes (MC) algorithm with a parallel fast marching method (FMM) [100, 39], leading to a very fast and efficient algorithm. Only the narrow band of flow solver cells that are required in the computation of the curvature needs to possess the distance information. The initial distance to the interface is measured explicitly using a second order approach illustrated in Fig. 4.8. From the sub-cell interface information, an algorithm similar to MC is used to triangulate the interface. Each closest flow solver cell is then explicitly projected onto the triangulated interface, providing both the normal vector $\boldsymbol{n}$ and the distance to the interface. This information is then extended over a few cells using FMM. Because both MC and FMM are at best only second order accurate, the detection of the interface crossings shown in Fig 4.8(b) is performed using linear interpolation.

- *Least squares computation of curvature from the reconstructed distance function.* Following Marchandise *et al.* [65], a third order least squares algorithm is used to approximate the distance function resulting from the previous step. This approach is found to provide a mesh converging curvature, because of the tendency of the least squares method to smear out some of the numerical errors on the distance field. This is shown by evaluating the curvature of a circle of diameter $D = 1$ centered in a $[0, 2] \times [0, 2]$ domain discretized with various meshes, for which the errors are summarized in Table 4.1. At least first order convergence of the curvature is recovered, and the curvature is found to converge faster for poorly resolved structures.

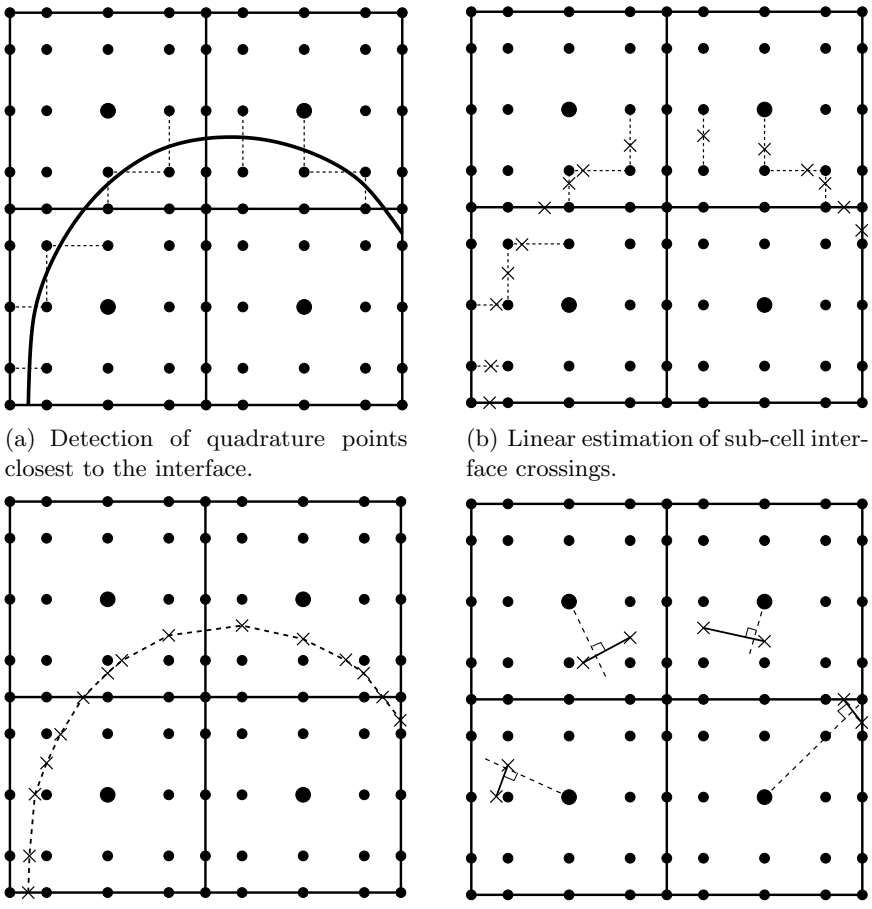

(a) Detection of quadrature points closest to the interface.

(b) Linear estimation of sub-cell interface crossings.

(c) Triangulation of the sub-cell interface.

(d) Geometric projection of the flow solver centroids on the closest triangles.

Figure 4.8: Second order distance reconstruction on the flow solver mesh.

Mesh	$D/\Delta x$	Error
8×8	4	0.62297
16×16	8	0.11251
32×32	16	0.06577
64×64	32	0.03378

Table 4.1: Convergence of the L_2 error of least squares curvature with mesh spacing.

4.2.5 Re-initialization

Similar to the discontinuous Galerkin method of Marchandise *et al.* [65], the re-initialization of the level set function is found to be mostly superfluous when using the SRI method. Only when the gradient of the level set function becomes overly small or large, the need to re-initialize the G-field arises, since the triangulation of the sub-cell interface can then become inaccurate. As a result, a re-initialization step is necessary, however it is performed only rarely, typically for every 100 time steps. Two re-initialization strategies have been employed and compared. The first consists simply of interpolating on the quadrature points the distance field that is reconstructed on the flow solver mesh. While being very inexpensive, this approach removes all the sub-cell information that was stored on the quadrature points, and therefore can introduce significant errors, i.e. of the same order as what is expected from a classical re-initialization step on the flow solver mesh. However, since this re-initialization needs to be performed only rarely, it is not expected to affect the quality of the simulations. The second approach tested here uses the triangulated interface to explicitly re-evaluate the distance of each quadrature point to the interface. This is much more accurate since the errors are second order, based on the sub-cell mesh. Obviously, the cost of this re-initialization step is much greater, since all quadrature points need to be explicitly projected onto the triangulated interface so that their distance can be evaluated. In realistic cases, this operation was found to have the cost of several flow solver time steps. Consequently, the first re-initialization strategy is preferred.

4.2.6 Solid body rotation of a notched disk

Having described the SRI approach in detail, numerical tests are now presented in order to assess the capability of the method to accurately represent small scale interface transport. The default SRI formulation employed in these test cases uses $p = 5$ Gauss-Lobatto quadrature nodes based on Legendre polynomials, and a second order Runge-Kutta time integration. The effect of varying these parameters will be evaluated throughout this section.

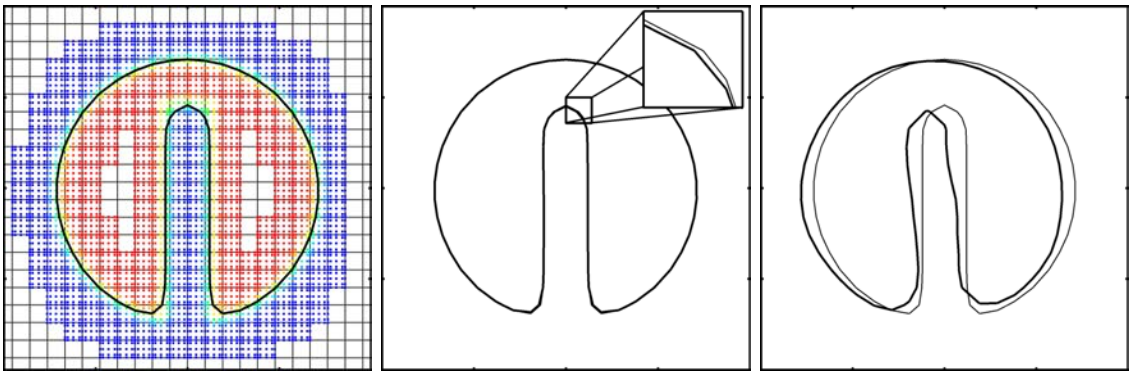

(a) (b) (c)

Figure 4.9: Solid body rotation of Zalesak's disk with second order Runge-Kutta for the SL transport, and $p = 5$. (a) Exact interface location (thick line), quadrature nodes colored by the level set function, and flow solver mesh. (b) Solution after one rotation: exact solution (thin line) and SRI solution (thick line). (c) Solution after 50 rotations: exact solution (thin line) and SRI solution (thick line).

The solid body rotation of a notched circle has often been used to assess the quality of interface transport. In a $[-0.5, 0.5] \times [-0.5, 0.5]$ domain, a circle of radius 0.15 with a notch of height 0.25 and width 0.05, initially centered at $(0, 0.25)$, undergoes a solid body rotation at angular velocity 2π. A 50^2 flow solver grid is used, and the time step size is set to $1/200$, meaning that 200 time steps are necessary to perform one full rotation of the circle. This leads to a CFL number close to 0.77. The level set function is taken to be a hyperbolic tangent function of thickness $\epsilon = \Delta x/p$. Figure 4.9 compares the exact solution with the computed solution after one rotation and after 50 rotations. Even though the mesh used for this simulation is very coarse and resolves the notch on only two cells, the SRI solution appears excellent after one rotation, and it remains very satisfactory even after 50 rotations. This first result suggests that the SRI concept enables a highly accurate description of small interfacial features, even for long time transport.

Effect of temporal accuracy

In order to understand the effect of the order of accuracy of the Runge-Kutta scheme in the SL transport, the same notched circle is now transported using fourth order Runge-Kutta.

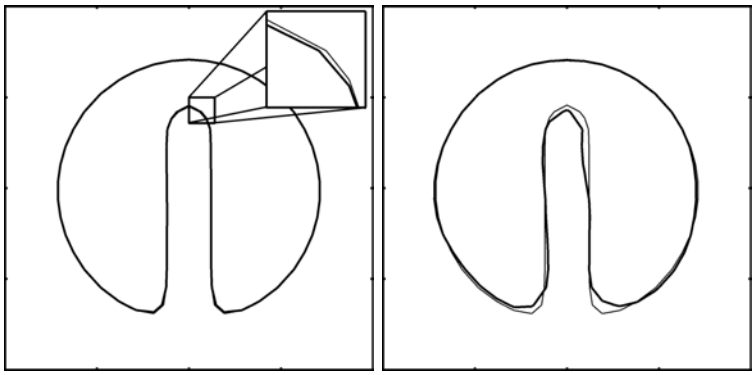

(a) (b)

Figure 4.10: Solid body rotation of Zalesak's disk with fourth order Runge-Kutta for the SL transport, and $p = 5$. (a) Solution after one rotation: exact solution (thin line) and SRI solution (thick line). (b) Solution after 50 rotations: exact solution (thin line) and SRI solution (thick line).

Figure 4.10 presents the transported solution after one rotation and after 50 rotations. While the solution after one rotation shows very little difference compared to the interface location computed using second order Runge-Kutta, the solution after 50 rotations is greatly improved by using fourth order Runge-Kutta temporal integration, and compares very well with the exact solution.

Effect of polynomial order

The impact of the number of quadrature points per cell on the accuracy of the interfacial transport is now assessed. The previous test clearly showed that the temporal errors become dominant with 50 iterations, therefore the following tests will be performed with the fourth order Runge-Kutta. Figure 4.11 shows the performance of SRI with $p = 3$. While the solution after one rotation remains satisfactory, although slightly distorted, the interface rapidly deteriorates. Already after 10 rotations, the notch has disappeared. The poor accuracy of the polynomial reconstruction strongly limits the capability of transporting the small-scale notch, but also the capability of accurately representing the circle itself for a long time. Figure 4.12 shows the same test case with $p = 9$. As expected, the accuracy is

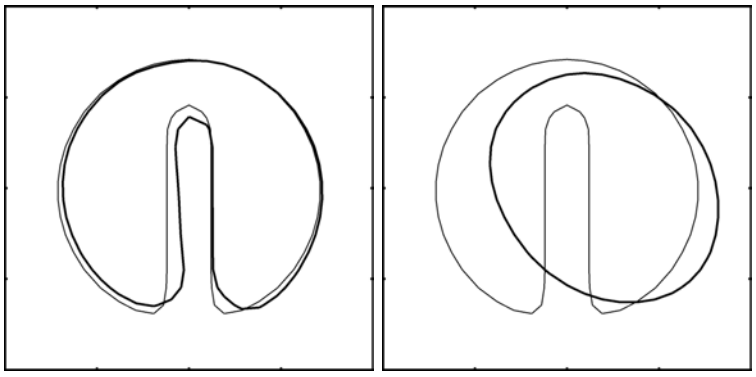

(a) (b)

Figure 4.11: Solid body rotation of Zalesak's disk with fourth order Runge-Kutta for the SL transport, and $p = 3$. (a) Solution after one rotation: exact solution (thin line) and SRI solution (thick line). (b) Solution after 10 rotations: exact solution (thin line) and SRI solution (thick line).

very satisfactory, and even after 50 iterations the computed interface location follows very accurately the exact solution. For the case of the solid body rotation of Zalesak's disk, these results suggest that $p = 5$ is enough to obtain a good solution, but that p could be increased in cases where spatial accuracy is more important. The temporal accuracy of the Runge-Kutta integration has an impact for long time transport, and fourth order seems desirable. However, it can be expected that for a less trivial problem, temporal accuracy may not play such an important role.

Effect of quadrature points

Finally, the impact of the distribution of quadrature points in the cells is discussed. Figure 4.13 presents results for the Zalesak's disk problem solved using Gauss-Lobatto quadrature based on Chebychev polynomials and Fig. 4.14 shows results obtained with a uniform distribution of quadrature nodes. The results obtained with the Chebychev-based quadrature are similar to those computed with the Legendre-based quadrature, although they seem slightly less accurate. Indeed, after 50 rotations, the notch does not appear to be as well preserved when using Chebychev-based Gauss-Lobatto quadrature. However, these

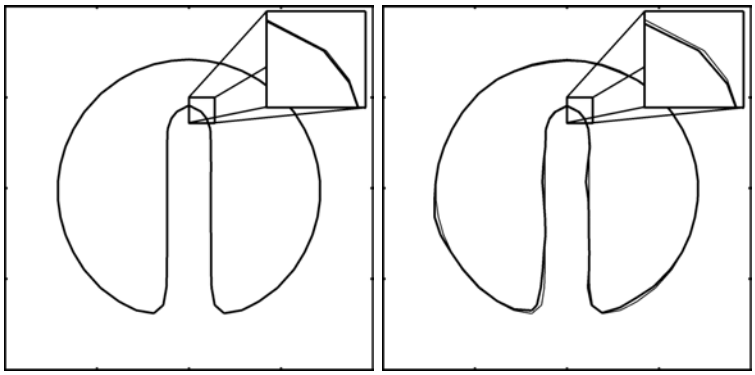

(a) (b)

Figure 4.12: Solid body rotation of Zalesak's disk with fourth order Runge-Kutta for the SL transport, and $p = 9$. (a) Solution after one rotation: exact solution (thin line) and SRI solution (thick line). (b) Solution after 50 rotations: exact solution (thin line) and SRI solution (thick line).

differences are small and suggest that the accuracy of SRI is only weakly dependent on the choice of polynomials used in the Gauss-Lobatto quadrature. The uniform distribution, on the other hand, gives very distorted solutions even for the first rotation, and most features of the notched circle are lost after 50 rotations. These poor results are expected, since the accuracy of the polynomial reconstruction is known to be much better when using Gaussian quadrature.

All these parametric tests suggest that:

- Gauss-Lobatto quadrature based on Legendre polynomials performs best,
- $p = 5$ is sufficient to accurately represent the notch, even on two grid cells,
- the accuracy of the Runge-Kutta integration becomes important for long-time transport.

The area conservation errors for different parameters are given in Table 4.2. Because the errors at the top and at the bottom of the notch tend to compensate, this measure does not represent the overall accuracy of the shape of the disk and might be misleading on its own. However, it provides some clues on the conservation property of SRI. The error values

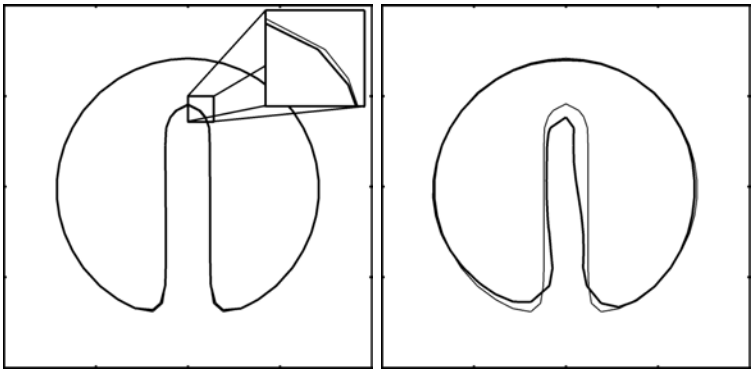

(a) (b)

Figure 4.13: Solid body rotation of Zalesak's disk with fourth order Runge-Kutta for the SL transport, and $p = 5$, using Gauss-Lobatto quadrature points based on the Chebychev polynomials. (a) Solution after one rotation: exact solution (thin line) and SRI solution (thick line). (b) Solution after 50 rotations: exact solution (thin line) and SRI solution (thick line).

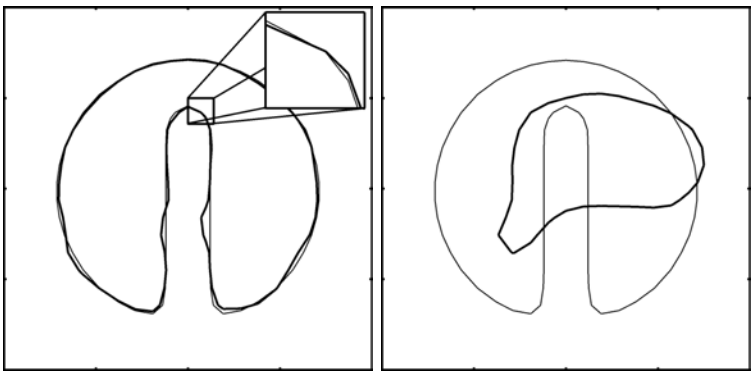

(a) (b)

Figure 4.14: Solid body rotation of Zalesak's disk with fourth order Runge-Kutta for the SL transport, and $p = 5$, using uniformly distributed quadrature points. (a) Solution after one rotation: exact solution (thin line) and SRI solution (thick line). (b) Solution after 50 rotations: exact solution (thin line) and SRI solution (thick line).

p	Temporal order	% Area loss after one rotation	% Area loss after 50 rotations
5	2	0.366	1.100
5	4	0.366	0.595
9	4	0.488	0.899

Table 4.2: Area conservation errors for Zalesak's disk problem with different parameters.

obtained are typically below one percent, even after 50 rotations, which is well below what was observed on the same mesh with the particle level set (PLS) method [23].

4.2.7 Sphere in a deformation field

The velocity field for the previous case was linear, meaning that a tri-linear interpolation of the velocity to the quadrature points location will be exact. In general, this will not be the case, and therefore it is interesting to assess the accuracy of SRI for non-linear velocities. As an example of such a test case, the deformation of a three-dimensional sphere proposed by LeVeque [57] can be used. A sphere of radius 0.15 is placed at $(0.35, 0.35, 0.35)$ in a unit box, discretized by a 100^3 mesh. The velocity field is set to

$$\begin{aligned} u\left(x,y,z,t\right) &= 2\cos\left(\pi t/T\right)\sin^2\left(\pi x\right)\sin\left(2\pi y\right)\sin\left(2\pi z\right), \\ v\left(x,y,z,t\right) &= -\cos\left(\pi t/T\right)\sin\left(2\pi x\right)\sin^2\left(\pi y\right)\sin\left(2\pi z\right), \\ w\left(x,y,z,t\right) &= -\cos\left(\pi t/T\right)\sin\left(2\pi x\right)\sin\left(2\pi y\right)\sin^2\left(\pi z\right), \end{aligned} \tag{4.11}$$

where $T = 3$. The time step size is set to 0.005, and the second order Runge-Kutta scheme is used for the temporal integration. Snapshots of the interface as resolved on the flow solver mesh at $t = 0, 0.3, 0.6, 1.0, 1.5, 2.0, 2.5, 3.0$ are shown in Fig. 4.15. The geometrical features of the interface are very similar to the results of Enright *et al.* [23], where the thin sheet that is formed at $t = T/2$ is starting to disappear from the flow solver mesh, but the sphere at $t = T$ is still properly recovered. The sub-cell interface reconstruction provided by the marching cubes algorithm is shown in Fig. 4.16, where it appears clearly that even at $t = T/2$, where the stretching is maximum, the sub-cell polynomial reconstruction is

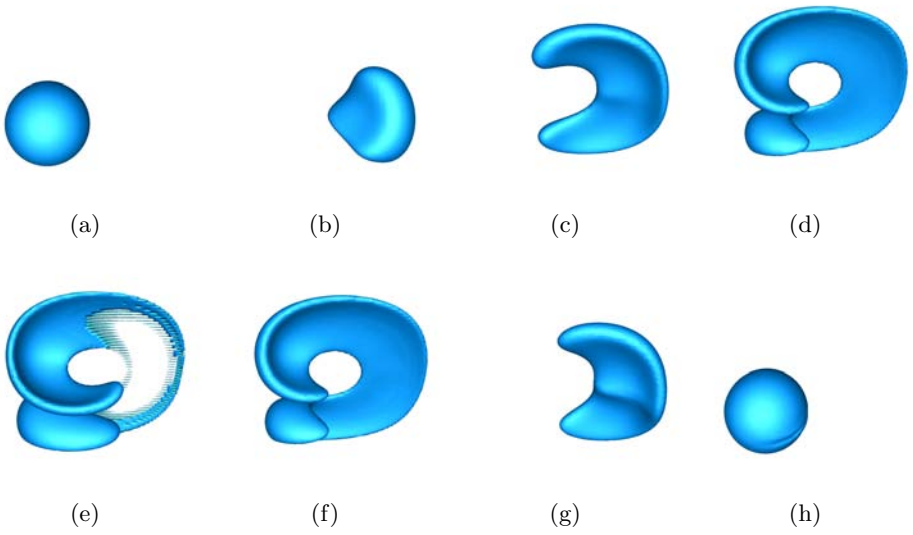

Figure 4.15: Sphere in a three-dimensional deformation velocity field. Evolution of the location of the interface at the flow solver level as a function of time.

capable of retaining the thin sheet. Because this sheet is still properly resolved, it is fully recovered on the flow solver mesh when the flow is inverted. The evolution of the volumetric error as a function of time is shown in Fig. 4.17. Even at $t = T/2$, the error remains very small, and is comparable to the results of Enright *et al.* [23]. At the end of the simulation, the volume conservation error is back to less that 0.1%, which is more than an order of magnitude smaller than what was obtained by Enright *et al.* [23]. It is interesting to note that these good results are obtained with $p = 5$, where each cell of the refined band has to transport $(5-1)^3 = 64$ quadrature points, which is similar to the number of particles that were transported by Enright *et al.* [23].

4.2.8 Comparison with ACLS method

To assess the suitability of the SRI approach to simulate primary atomization, the circle in a deformation field test case that was initially presented in Chapter 3 is reproduced here. The goal is to compare the behavior of the two methods at our disposal in the transport of very thin ligaments. The same initial conditions are used, with a circle of radius 0.15 that is

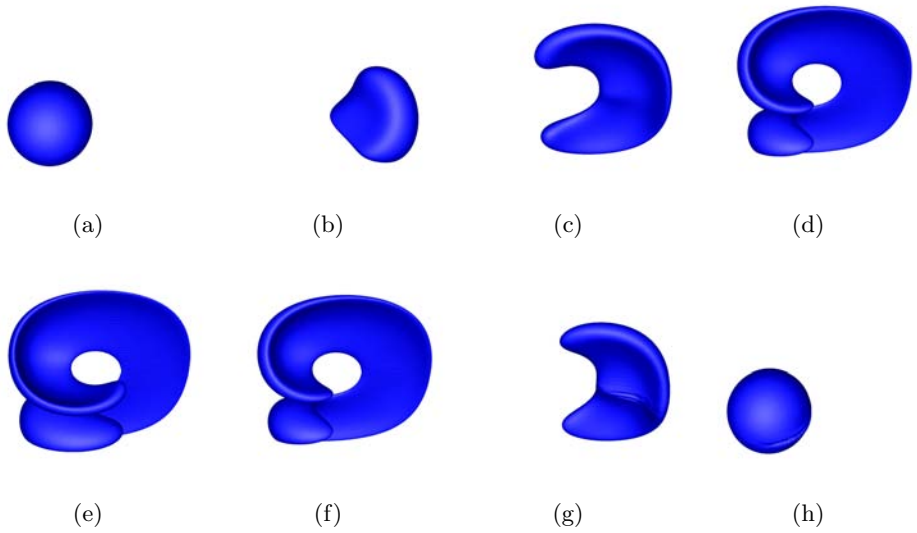

Figure 4.16: Sphere in a three-dimensional deformation velocity field. Evolution of the location of the interface at the sub-cell level as a function of time.

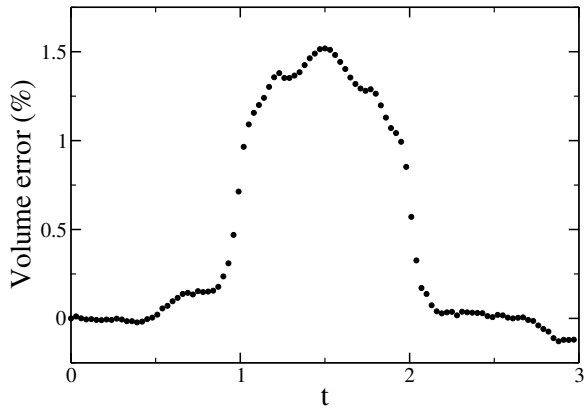

Figure 4.17: Volume error as a function of time for the sphere in a three-dimensional deformation velocity field with the SRI approach.

centered at $(0.5, 0.75)$ in a unit-sized box, and the velocity field is obtained from the stream function described by Eq. 3.22, where the period T is set to 8. SRI and ACLS are compared for a 128×128 mesh at $t = T/2$, when the stretching is maximum. Figure 4.18 shows the two solutions, as well as a fine solution computed on a 1024×1024 mesh using the SRI approach. This fine solution will be regarded as the reference solution. Because the ACLS method attempts to conserve all the mass on the 128×128 mesh, it tends to rupture the ligament into small resolved droplets. On the other hand, the SRI method does not display spurious numerical breakup of the ligament. Therefore, this observation confirms that the SRI approach is better suited to simulate atomization problems than the ACLS method. Figure 4.19 compares the time evolution of the normalized area contained in the interface for the two methods. Note that for both approaches, the conservation errors remain small. The ACLS approach leads to a maximum error below 4%, and the error for the SRI method remains below 2%. In conclusion, the two schemes give excellent results in terms of mass conservation, but the way they achieve this good conservation is fundamentally different: the ACLS approach tends to filter out the smallest, under-resolved scales that are likely to be lost, while the SRI approach keeps on tracking the smallest scales even when they fall below the flow solver mesh size. In the process of filtering out the smallest scales, the ACLS method induces a displacement of the interface that does not occur with the SRI concept, making the ACLS method more likely to produce spurious ligament breakup than the SRI method.

4.3 Validation and numerical results

Several two-phase flow test cases are now presented in order to assess the behavior of the SRI approach. The first case of a two-dimensional drop demonstrates that the spurious currents generated by curvature errors remain sufficiently small. Then, a standing wave is computed in order to verify the accurate description of surface tension and viscous forces. To assess the convergence of the method on a more complex two-phase flow problem, a Rayleigh-Taylor instability is computed. Finally, a turbulent two-phase shear layer simulation is presented,

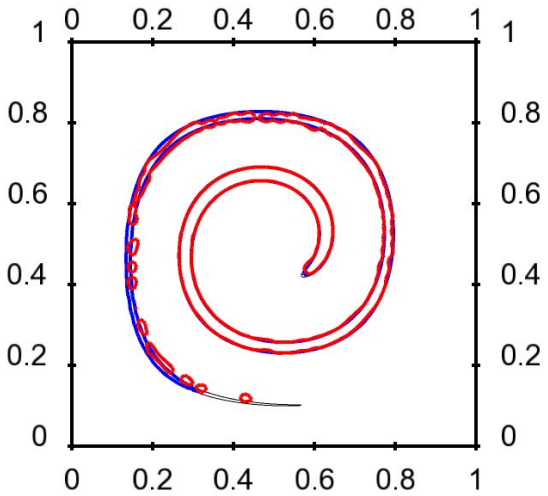

Figure 4.18: Interface location for the circle in a deformation field test case at $t = T/2$ with a 128×128 mesh for the different schemes: SRI method (blue line), ACLS method (red line), and SRI method on a 1024×1024 mesh (thin black line).

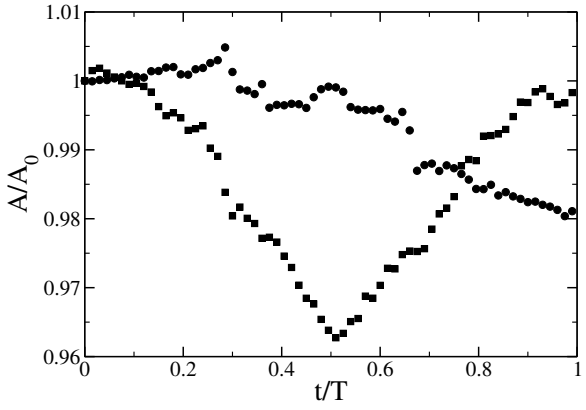

Figure 4.19: Temporal evolution of the normalized area for the circle in a deformation field test case with a 128×128 mesh for the different schemes: SRI method (circles) and ACLS method (squares).

ρ	0.3	3	30	300	3000	30000
La	12	120	1200	12000	120000	1200000
Δt	0.0006	0.002	0.006	0.02	0.06	0.2
Ca	1.10×10^{-5}	0.90×10^{-5}	2.93×10^{-5}	2.09×10^{-5}	7.46×10^{-5}	3.77×10^{-5}

Table 4.3: Dependence of the magnitude of parasitic currents with the Laplace number for a static droplet with surface tension on a 32×32 mesh.

displaying the capability of the method to handle turbulent atomization problems.

4.3.1 Spurious currents

First, a two dimensional drop of diameter $D = 0.4$ is placed in the center of unit size box. Initially, the velocity field is zero, but because of inaccuracies in the computation of interfacial curvature, a spurious flow will be generated. The two fluids have the same density ρ and the same viscosity $\mu = 0.1$, the surface tension coefficient σ is unity. In order to consider various importance of surface tension versus viscous forces, the Laplace number $\mathrm{La} = 1/\mathrm{Oh}^2 = \sigma\rho D/\mu^2$ is varied by changing the densities of both fluids, where Oh is the Ohnesorge number. To assess the intensity of the spurious currents, the Capillary number $\mathrm{Ca} = |u_{\max}|\mu/\sigma$ is computed at a non-dimensional time $t\sigma/(\mu D) = 250$. The simulations are performed on a 32×32 mesh, and the time step size is varied to satisfy the capillary CFL restriction. Detailed parameters and results are reported in Table 4.3. The resulting capillary numbers show little dependence on the Laplace number, and the values of Ca remain very small. Therefore, it is expected that the spurious currents should not affect two-phase flow simulations based on the SRI method.

4.3.2 Standing wave

Next, the interaction of surface tension forces with viscous effects is assessed by simulating the viscous decay of a two-dimensional standing wave with various density ratios. In a $[0, 2\pi] \times [0, 2\pi]$ domain, two fluids are initially separated by an interface defined by the zero

Mesh	Error
8×8	0.27082
16×16	0.08356
32×32	0.02808
64×64	0.01346

Table 4.4: RMS value of the amplitude error for the standing wave problem with unity density ratio.

iso-contour of

$$\phi\left(x, y\right) = \pi - y + A_0 \cos\left(2\pi x/\lambda\right), \tag{4.12}$$

where λ is set to 2π and A_0 is set to 0.01λ. In the x-direction, periodic boundary conditions are employed, while the y-direction assumes top and bottom symmetry. The surface tension coefficient is set to $\sigma = 2$, and the kinematic viscosity ν of both fluids is set to be equal. In the case of similar kinematic viscosities, Prosperetti [91] provides a theoretical solution to the evolution of the wave amplitude, which we will use to compare our results. The time is non-dimensionalized using the inviscid oscillation frequency $\omega_0 = \sqrt{\frac{\sigma}{\rho_1+\rho_2}}$, where ρ_1 and ρ_2 are the densities in each fluid. Following the numerical study of Herrmann [41], two cases are considered. The first one assumes $\rho_1 = \rho_2 = 1$ and $\nu = 0.064720863$. The simulations are performed on various meshes, from 8×8 to 64×64, until $\omega_0 t = 20$ is reached. Figure 4.20 presents both the evolution of the wave amplitude with time for the different meshes in comparison to the theory, and the time evolution of the error in amplitude. The rms value of the error is then summarized in Table 4.4. Figure 4.21 shows that close to second order convergence is obtained for this problem. Moreover, while the 8×8 mesh predicts an incorrect frequency, leading to large errors in amplitude, the 16×16 mesh leads to very satisfactory results.

The second case considers a density ratio of $\rho_2/\rho_1 = 1000$, and $\nu = 0.0064720863$. Figure 4.22 shows the results for this case, and Table 4.5 summarizes the rms of the amplitude error. Again the convergence shown in Fig. 4.23 is between first and second order, and the 16×16 solution is already very satisfactory. This confirms that the proposed approach is capable of accurately predicting this flow, even with a relatively small number of points per

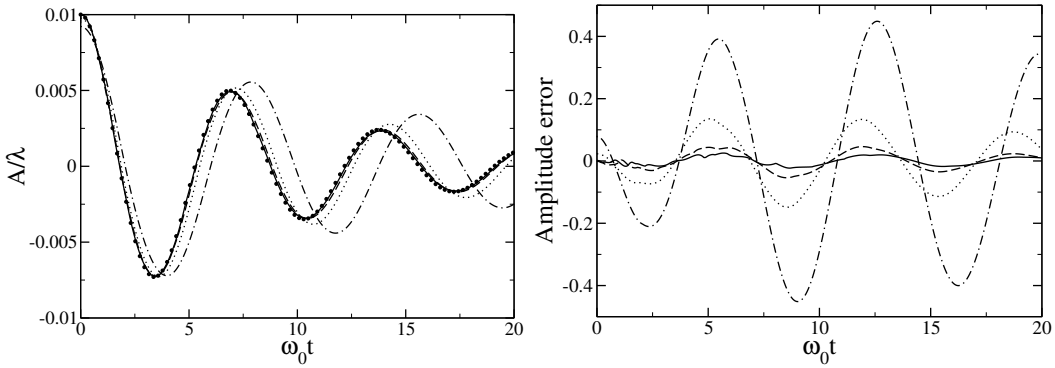

(a) Time evolution of the wave amplitude (b) Time evolution of the amplitude error

Figure 4.20: Damped surface wave problem with unity density ratio. 8×8 mesh (dash-dotted line), 16×16 mesh (dotted line), 32×32 mesh (dashed line), 64×64 mesh (solid line), and theory (symbols).

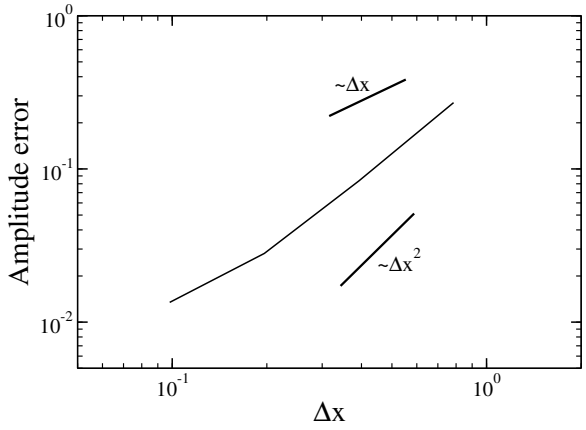

Figure 4.21: Convergence of the amplitude error for the standing wave problem with unity density ratio.

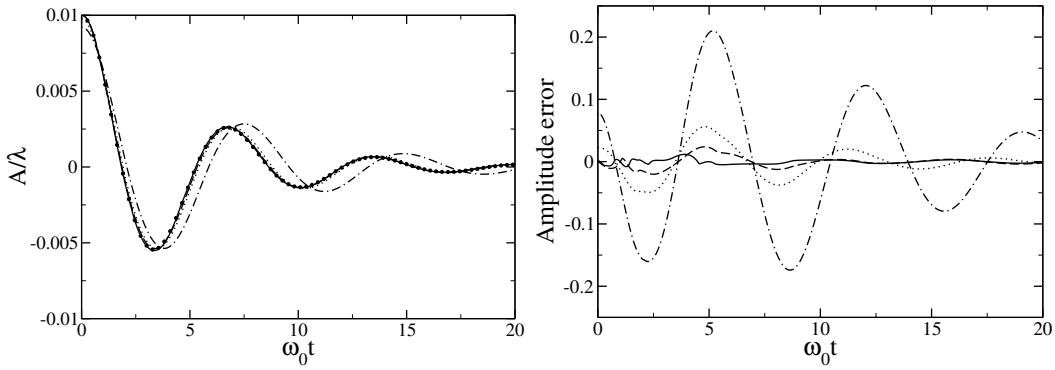

(a) Time evolution of the wave amplitude (b) Time evolution of the amplitude error

Figure 4.22: Damped surface wave problem with density ratio 1 : 1000. 8×8 mesh (dash-dotted line), 16×16 mesh (dotted line), 32×32 mesh (dashed line), 64×64 mesh (solid line), and theory (symbols).

Mesh	Error
8×8	0.10127
16×16	0.02421
32×32	0.00887
64×64	0.00353

Table 4.5: RMS value of the amplitude error for the standing wave problem with density ratio 1 : 1000.

wavelength.

4.3.3 Rayleigh-Taylor instability

The SRI approach is now employed to simulate the growth of a two-dimensional Rayleigh-Taylor instability. Numerous studies have used this problem to characterize the quality of interface transport methods, see e.g. [41]. However, many of these do not consider surface tension effects. The case studied here follows the simulation of Gomez *et al.* [33], which includes surface tension forces. In a $[1 \times 4]$ domain, two fluids are initially on top of each other, separated by an interface defined by the zero iso-contour of

$$\phi(x, y) = y + A_0 \cos(2\pi x), \tag{4.13}$$

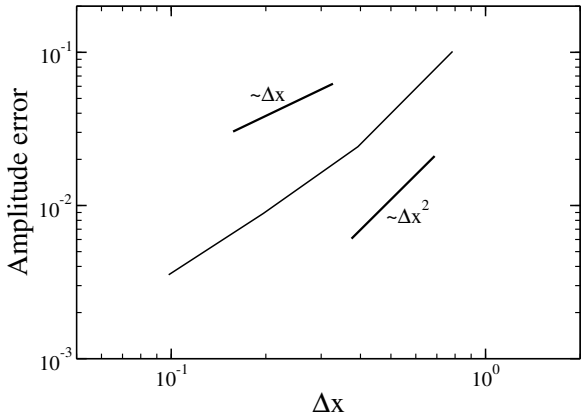

Figure 4.23: Convergence of the amplitude error for the standing wave problem with density ratio 1 : 1000.

where A_0 is taken to be 0.05. The top fluid has a density $\rho_1 = 1.225$, while the density of the bottom fluid is set to $\rho_2 = 0.1694$. Both fluids have the same dynamic viscosity, $\mu_1 = \mu_2 = 0.00313$, and the surface tension coefficient is set to $\sigma = 0.1337$. Five different meshes are considered, ranging from 32×128 to 512×2048. Figure 4.24 presents the temporal evolution of the interface location for the finest mesh. These results are in good agreement with the simulations of Gomez *et al.* [33], and show the expected formation and growth of a spike of heavy fluid, while a bubble of light fluid rises. When comparing the solution between the various meshes for different times, as shown in Fig. 4.25, it can be seen that the mesh convergence is rather slow. A more quantitative evaluation of the rate of convergence of the solution is performed in Table 4.6, where the error in the maximum depth of the spike with the different meshes is reported at $t = 1.0$, 1.1 and 1.2, considering the finest solution as the reference solution. The error in spike penetration is then plotted as a function of the mesh size in Fig. 4.26. The resulting error initially converges slowly, but reaches second order convergence rapidly. However, if one considers more complex features of the flow that involve larger curvatures, such as the extremities of the mushroom cap shape at the end of the spike, it is clear that slower convergence is achieved.

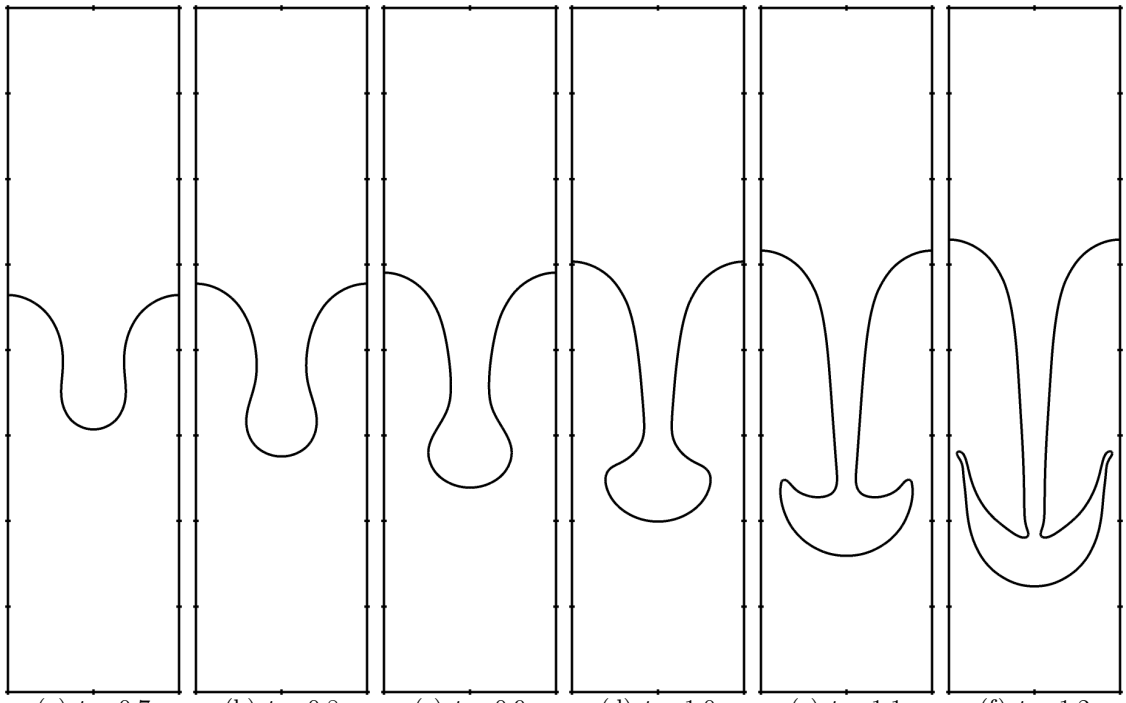

(a) $t = 0.7$ (b) $t = 0.8$ (c) $t = 0.9$ (d) $t = 1.0$ (e) $t = 1.1$ (f) $t = 1.2$

Figure 4.24: Phase-interface shape as a function of time for the Rayleigh-Taylor instability problem on a 512×2048 mesh.

Mesh	$t = 1.0$	$t = 1.1$	$t = 1.2$
32×128	0.09408	0.08566	0.05987
64×256	0.04300	0.03841	0.02306
128×512	0.01569	0.01318	0.00678
256×1024	0.00328	0.00270	0.00151

Table 4.6: Error in maximum penetration of the spike of heavy fluid compared to the finest simulation for the Rayleigh-Taylor instability problem, at different times for different meshes.

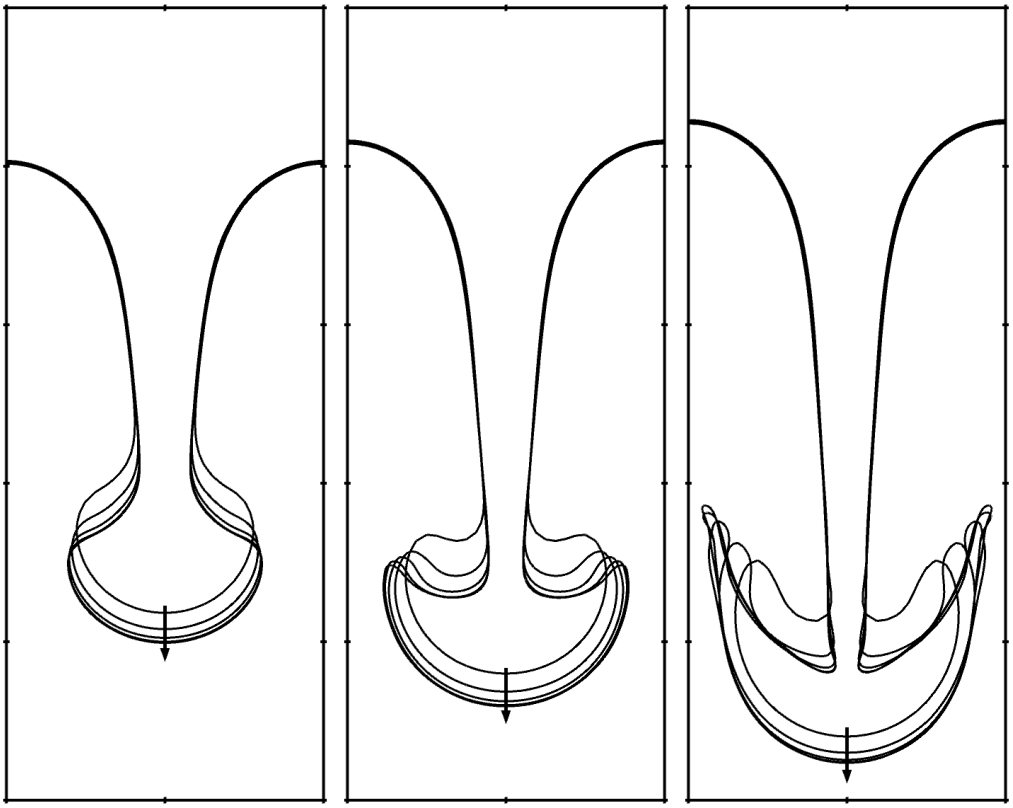

(a) $t = 1.0$ (b) $t = 1.1$ (c) $t = 1.2$

Figure 4.25: Phase-interface shapes as a function of time for the Rayleigh-Taylor instability problem. Arrow indicates increasing mesh sizes (32×128, 64×256, 128×512, 256×1024, and 512×2048).

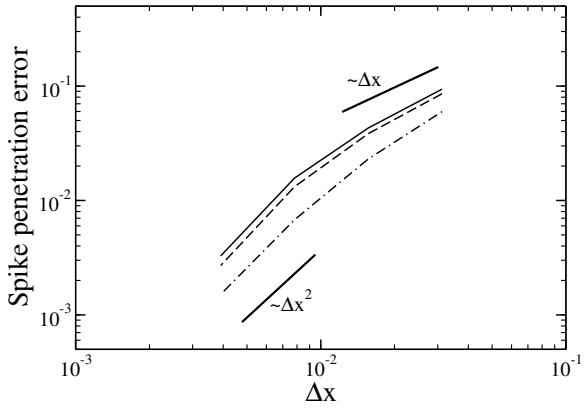

Figure 4.26: Convergence of the error in spike penetration for the Rayleigh-Taylor instability problem at different times: $t = 1.0$ (solid line), $t = 1.1$ (dashed line), and $t = 1.2$ (dot-dash line).

4.3.4 Two-phase shear layer

Finally, the SRI approach is employed in a complex realistic two-phase flow problem, namely the simulation of a three-dimensional turbulent shear-layer. The computation is based on the experimental work of Ben Rayana [4]. The simulation is run on a $512 \times 128 \times 256$ mesh. Figure 4.27 illustrates the setup of the shear layer, with water flowing on a flat surface, while air is injected at higher velocity above the water surface. The two flows are separated at injection by a lip of thickness $e = 2.2$ mm, and their velocity profiles at injection are taken from the experimental measurements. The properties of both fluids, including the surface tension coefficient, are those of water and air, with the exception that the water density has been reduced to $\rho_l = 50$ kg/m^3. As in the experiment, the momentum flux ratio is set to $M = 16$, with a bulk air velocity of $U_g = 20$ m/s and a bulk water velocity of $U_l = 0.7746$ m/s, for a height of the water layer of 10 cm.

Figure 4.28 shows a top view of the interface in a region of about 9 cm $\times$ 7 cm right after the lip, both for the experiment and the simulation. From a qualitative point of view, the simulated interface corresponds to the experimental results. The first large Kelvin-Helmholtz–type structure is properly recovered, including some lateral wrinkling of the interface within the wave. Secondary lateral instabilities then follow, leading to fingering of

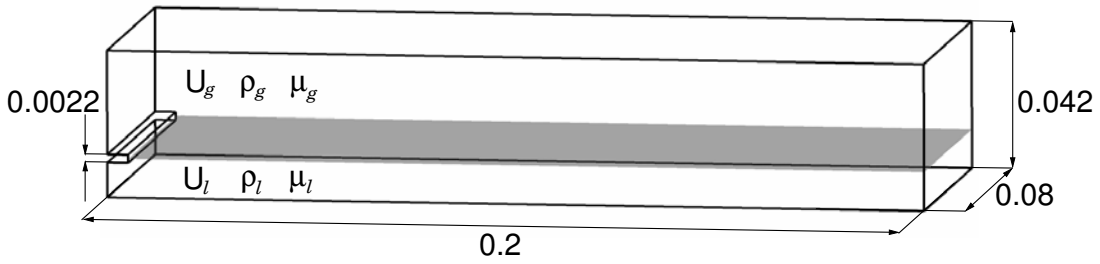

Figure 4.27: Schematics of the computational setup for the two-phase shear layer flow. Dimensions are given in meters.

the interface, and to the generation of droplets. While the experimental picture shown here does not display any ligament but only a few droplets, both were observed experimentally. Note that the difference in density ratio could explain the tendency of the simulation to generate more ligaments, potentially because of aerodynamic forces. The SRI approach appears robust even in the presence of a complex turbulent flow.

Finally, Fig. 4.29 presents the relative cost of the different components of the NGA code during the course of the shear layer simulation. Only the three main elements, namely the SRI solver, the pressure solver, and the velocity solver are included here. Note that the sum of these three components corresponds to almost 100% of the cost of the full NGA code. SRI is found to correspond to the third of the cost of the full code, well behind the pressure solver, which accounts for almost 50% of the simulation cost. This confirms that even for a realistic parallel simulation with complex topology, the SRI approach remains affordable, with a cost well below that of the pressure solver.

4.4 Summary

A spectral refinement approach for the description of interfacial flows has been proposed. This method introduces quadrature nodes in each cell to enable the construction of high order polynomials to represent a level set function with improved accuracy. The results of basic transport tests are excellent, and suggest that even at the smallest scales, the

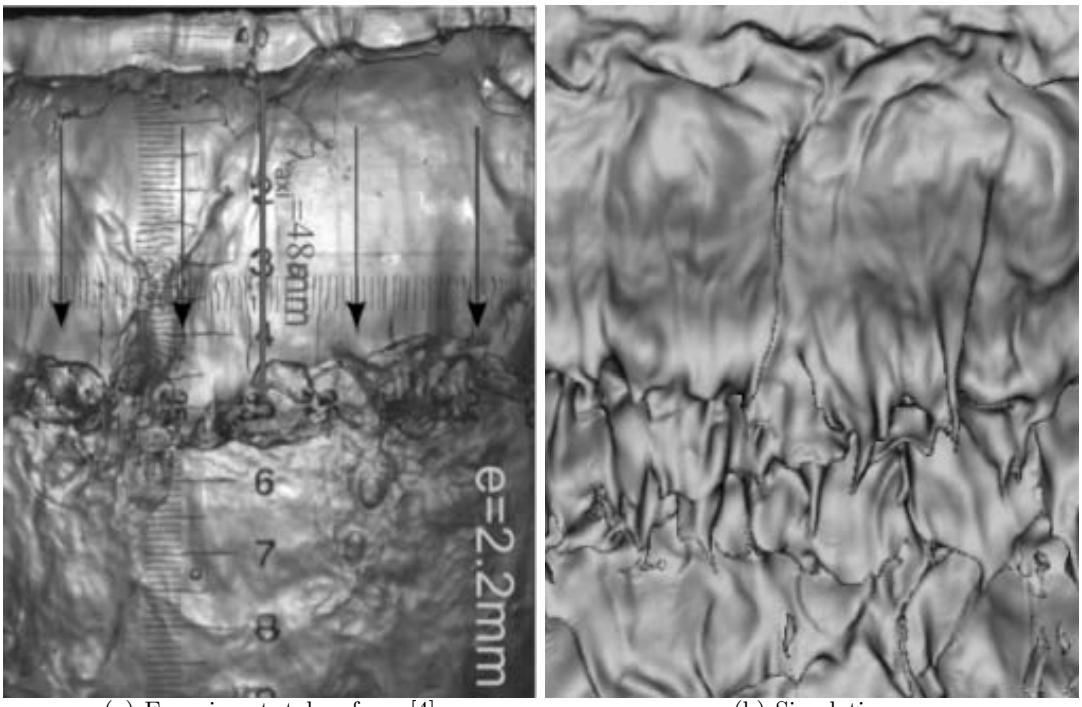

(a) Experiment, taken from [4] (b) Simulation

Figure 4.28: Top view of the phase-interface in the shear layer flow. Flow direction is from top to bottom.

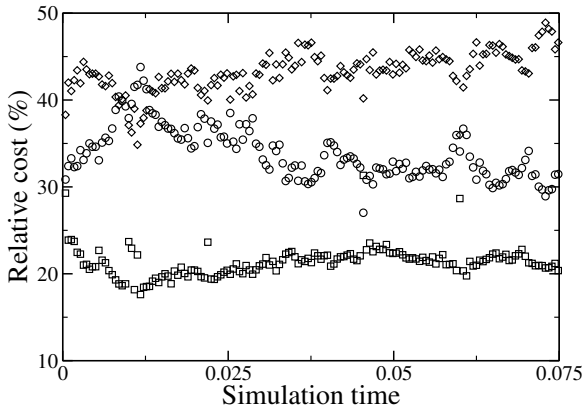

Figure 4.29: Relative cost of the different components of the NGA code during the course of the shear layer simulation: SRI solver (circles), velocity solver (squares), and pressure solver (diamonds).

interfacial representation remains accurate. The full method has finally been employed for the simulation of a two-phase shear layer. Despite the complexity of the flow structures, the SRI approach was found to remain robust, and to predict an interface shape that agrees qualitatively with the experimental results. As a consequence, SRI appears as the level set method of choice for detailed numerical simulations of primary atomization, and it will therefore be employed in the next chapter to investigate turbulent atomization of liquid jets.

Chapter 5

Detailed simulation of Diesel-type jets

5.1 Objectives

Now that adequate numerical methods have been designed, detailed numerical simulations of turbulent atomization can be performed. The work in this section has several objectives:

- Establish numerical simulations as a realistic means to study turbulent atomization.
- Investigate and report the statistics of a turbulent liquid jet.
- Visualize primary atomization of a turbulent liquid jet, and compare the computed results to available experimental observations.
- Identify key atomization mechanisms.
- Analyze the effect of the jet Reynolds number.
- Analyze the effect of the jet Weber number.

This work is considered a first step towards realistic applications. The density ratio employed is similar to that of Diesel injection. The Reynolds number is slightly reduced compared to realistic injectors, but still of the right order of magnitude. The Weber number is

strongly reduced in order to make the liquid structures tractable.

5.2 Turbulent planar jet

5.2.1 Flow configuration

The flow considered in this section consists of a temporally evolving planar liquid jet in quiescent air. Figure 5.1 shows a sketch of the flow configuration. The liquid jet is initially of height H, and its bulk velocity is U_0. The computational domain is periodic in the streamwise and spanwise directions, x and z respectively, while in the y direction, a symmetry condition is employed. The $4H \times 6H \times 4H$ domain is discretized on a $256 \times 384 \times 256$ uniform mesh, leading to $\Delta x = \Delta y = \Delta z = H/64$. The initial velocity is obtained from a precursor simulation of a periodic channel flow. This precursor simulation is conducted in a $4H \times H \times 4H$ domain, discretized on a $256 \times 192 \times 256$ mesh, using the liquid material properties. Once the flow is established, i.e. once the friction coefficient reaches a constant value, the simulation is stopped and the velocity field is recorded. This field is then interpolated on the jet mesh to initialize the velocity in the region $-H/2 < y < H/2$, while the velocity outside of this region is set to zero. Even though the initial co-existence between a turbulent liquid and a still gas is a greatly simplified representation of turbulent liquid injection, the presence of realistic turbulence ensures that the planar jet destabilizes and develops rapidly. Throughout this work, time $t^\star$ will be non-dimensionalized using $t = t^\star U_0/H$.

The parameters used for the simulations are summarized in Table 5.1. The density ratio is set to $\rho_l/\rho_g = 40$, which corresponds to what is typically observed in Diesel engines, and which is sufficiently low to avoid any numerical difficulties. The choice is made to take $\mu_l/\mu_g = 40$, leading to $\nu_l = \nu_g$. Both the Reynolds number, $\mathrm{Re} = \rho_l U_0 H/\mu_l$, and the Weber number, $\mathrm{We} = \rho_l U_0^2 H/\sigma$, are varied such that both the effect of turbulence and the effect of surface tension forces can be studied. The Ohnesorge number, $\mathrm{Oh} = \mu_l/\left(\rho_l H \sigma\right)^{1/2}$, is also reported in Table 5.1 for the various cases. Clearly, the Ohnesorge number remains small for all cases, meaning that the liquid viscosity should not play any significant role

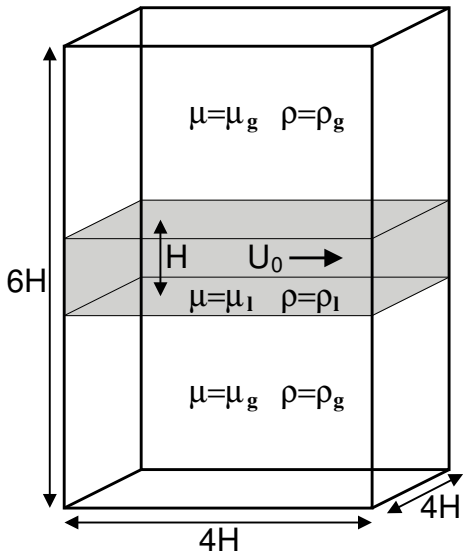

Figure 5.1: Schematics of the temporally evolving planar jet.

throughout the atomization process, which is expected to be the case for Diesel injection. Figure 5.2 places the different cases studied on the Ohnesorge chart, first introduced by Ohnesorge [77], then improved by Reitz [93], Lefebvre [54], and Miesse [70]. Note that all the cases considered here lie within the so-called second wind induced breakup regime. However, as noted by [54], a fully turbulent liquid jet will be immediately disrupted because of the non-zero vertical velocity component, leading to a global turbulent disintegration of the liquid. As a result, it is expected that the cases studied here will all undergo turbulent atomization.

5.2.2 Resolution considerations

In order to ensure the adequate resolution of the flow for the various simulation parameters, several issues have to be considered. Obviously, the smallest turbulent scales need to be properly resolved by the flow solver mesh. In addition, the liquid structures have to be resolved as well, which might lead to an even more restricting constraint on the mesh size. Indeed, small ligaments and droplets are expected to form, as well as potentially extremely thin sheets. Strictly speaking, the only true cut-off scale for the liquid structures is the

Case	ρ_l/ρ_g	μ_l/μ_g	Re	We	Oh
$TPa1$	40	40	3000	500	0.007454
$TPa2$	40	40	2000	500	0.011180
$TPb1$	40	40	3000	1000	0.010541
$TPb2$	40	40	2000	1000	0.015811
$TPc1$	40	40	3000	2000	0.014907
$TPc2$	40	40	2000	2000	0.022361

Table 5.1: Flow parameters for the various planar jet simulations.

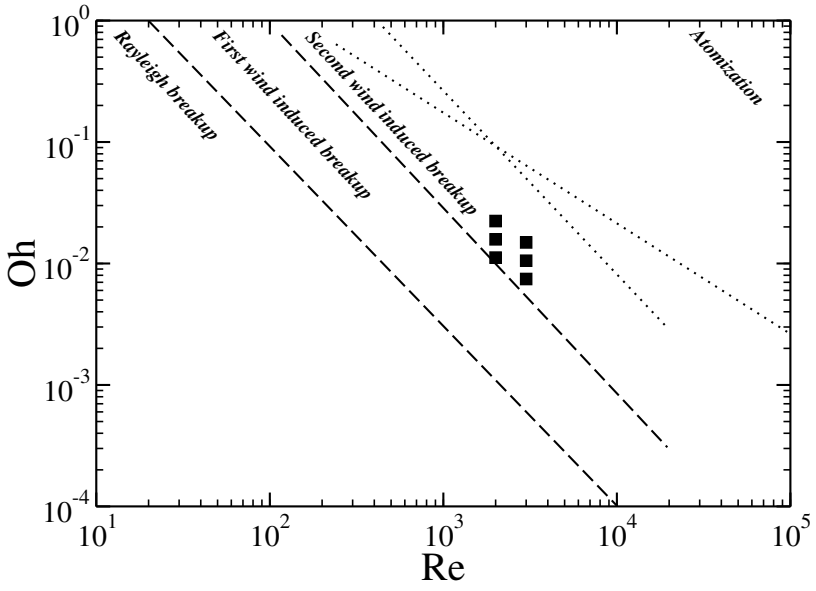

Figure 5.2: Cases considered in this work (symbols, see Table 5.1 for details) placed on the Ohnesorge chart for liquid jet breakup.

actual phase-interface thickness, which is clearly too small to be resolvable by the approach followed here. This specific aspect of multiphase flows represents a difficult challenge, and current state-of-the-art methods in two-phase flow modeling remain far from being able to tackle problems such as the formation of small satellite droplets, bag breakup of liquid sheets, or drainage of gas layers between two liquid structures before collision. However, all these phenomena are expected to occur regularly during the turbulent atomization of a liquid jet. As a consequence, the notion of direct numerical simulations (DNS) of multiphase flows remains controversial. The assumption behind the work presented here is that the main features of turbulent atomization can be simulated with reasonable accuracy, without accounting for the extremely small scales associated with two-phase flows, provided that most scales are properly resolved. While this assumption is typically valid for turbulence simulations, where the fluctuating energy decreases as smaller scales are considered, it might not be adequate for two-phase flows, where small liquid structures can carry a lot of momentum, and small scale phenomena can govern the outcome of large scale events, as in the case of binary drop collision. Even with these limitations in mind, the present work can provide valuable insights on the physics of primary atomization, as well as on the capability of sharp level set based methods to predict turbulent breakup.

The resolution of the turbulence is related to the number of grid points per jet height H, 64 in the present work, as well as the Reynold number Re, 2000 or 3000 here. This is comparable to numerous previous studies of temporal and spatial jets. Stanley *et al.* [102] performed a DNS of a spatial jet at $\mathrm{Re} = 3000$ using 30 mesh points within the jet height, and found the smallest value for the Kolmogorov scale, defined by $\eta = \left(\nu^3/\epsilon\right)^{1/4}$ where ϵ is the dissipation, to be $\eta \approx \Delta x/3$. Da Silva and Pereira [17] computed a temporally evolving planar jet at $\mathrm{Re} = 3000$, using 48 mesh points inside the jet height, and reported finding $\Delta x/\eta \approx 3$. Assuming a classical scaling for the number of points across the jet height proportional to $\mathrm{Re}^{3/4}$, these previous studies suggest that even the cases at $\mathrm{Re} = 5000$ should be properly resolved with 64 points per H. While this analysis is valid for single phase jets, it is yet unclear whether similar scalings apply in presence of two phases. As a consequence, we limit ourselves to a Reynolds number of 3000 to ensure proper resolution

of the turbulence.

The resolution of the liquid scales will be assessed following the consideration of Ménard *et al.* [68], who proposed to introduce a grid-based Weber number defined by $\mathrm{We}_{\Delta x} = \rho_l U_0^2 \Delta x/\sigma$. This corresponds to the Weber number of the smallest resolvable liquid structure, assuming that such a structure is of the order of the mesh size Δx. Ménard *et al.* [68] suggested that if $\mathrm{We}_{\Delta x}$ is smaller than about 10, then no further breakup is expected from a liquid structure of the size of the mesh. This limit of 10 for the Weber number matches the experimental observations of Hsiang and Faeth [42]. While this is a convincing argument for a droplet or a ligament, it does not apply easily to a liquid sheet, for which breakup could still obviously occur. This brings us back to the previous part of the discussion on what can realistically be resolved in complex two-phase flow simulations. In our case, because the SRI approach provides sub-cell interfacial resolution, structures as small as $\Delta x/p$, where p is the order of the polynomials used in the level set function reconstruction, should become tractable, at least in the sense that they should be maintained and transported, even though the flow around them might not be properly captured. This suggests that another Weber number, $\mathrm{We}_{\Delta x/p} = \rho_l U_0^2 \Delta x/(p\sigma)$, should be defined as well. For the different Weber numbers We considered in this study, Table 5.2 presents these two mesh-based Weber numbers, considering that p is set to 5. For all cases, the sub-cell Weber number is well below 10, suggesting that most liquid scales should remain tractable throughout the simulations. In addition, the grid-based Weber number remains low, which should be sufficient to ensure the accuracy of the flow around most liquid structures. This can be further assessed by directly evaluating the liquid mass conservation errors as a function of time, as shown in Fig. 5.3. Small mass loss should suggest that indeed most liquid structures are properly resolved at all times. For all three Re = 3000 cases, which are expected to be the most challenging simulations in terms of resolution, the mass conservation errors are found to remain below 2% for $t < 30$. This value is considered here to be sufficiently small to confirm that the chosen numerical parameters lead to a properly resolved flow. Finally, the temporal evolution of the normalized streamwise momentum is shown in Fig. 5.4. Note that momentum conservation errors are larger than mass conservation errors, which can be

We	$We_{\Delta x}$	$We_{\Delta x/p}$
500	7.8125	1.5625
1000	15.625	3.1250
2000	31.250	6.2500

Table 5.2: Grid-based Weber numbers for the different cases simulated.

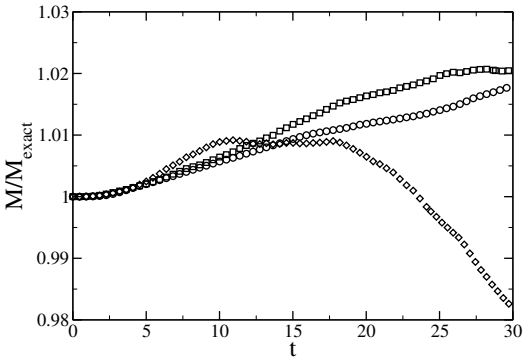

Figure 5.3: Temporal evolution of the liquid mass normalized by the exact liquid mass in the domain for Re = 3000: We = 500 (circles), We = 1000 (squares), and We = 2000 (diamonds).

explained by the fact that the liquid structures that become under-resolved and disappear from the flow solver mesh often carry a lot of momentum. An illustration for this is the case of a single liquid droplet moving in quiescent gas. If this droplet disappears, the momentum associated with it, which corresponds to most of the momentum contained in the system, is also lost. Yet, the momentum conservation errors remain limited, of the order of 5% for We = 500, 10% for We = 1000, and 15% for We = 2000.

5.3 Statistical results

First, statistical results will be analyzed. While we are interested in the detailed mechanisms of breakup, which should be easier to analyze and understand from instantaneous results, averaged data on multiphase jet have almost never been reported, and therefore are of great interest.

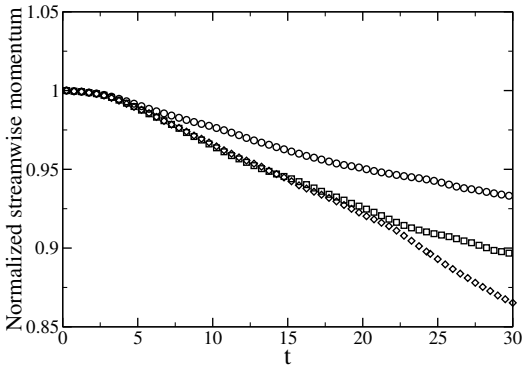

Figure 5.4: Temporal evolution of the streamwise momentum normalized by the initial streamwise momentum in the domain for Re = 3000: We = 500 (circles), We = 1000 (squares), and We = 2000 (diamonds).

5.3.1 Jet growth

First, the jet half-width based on the longitudinal velocity is plotted in Fig. 5.5. The width of the jets is expressed as the half-width δ_U, defined as the distance from the jet centerline to the point at which the mean streamwise velocity excess is half of the centerline velocity. It can be seen that after $t \approx 5$, the growth rate of all jets is close to linear, although some deviation is clearly visible. These fluctuations in the jet half-width can be attributed to several aspects of the present simulations, such as the lateral confinement leading to a small statistical sample size, and to the low Reynolds numbers. Also, note that surface tension effects are expected to affect the development of the jets. This can be seen by comparing the growth rate of the jets for different Weber numbers. High Weber number jets grow faster, while low Weber number jets tend to have a slower growth, which suggests that surface tension forces tend to stabilize the jets. It can be observed that the growth rates of the jets decrease when the half-widths reach $2H$, which suggests that confinement in the y-direction prevents further development of the fluid structures. As a result, further analysis will be limited to $t < 30$, for which we can expect the y boundaries to remain sufficiently far from the jets.

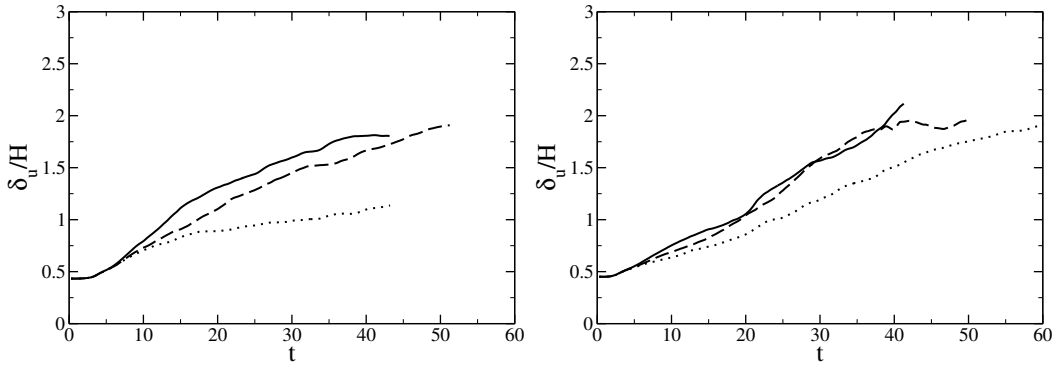

(a) Re = 2000 (b) Re = 3000

Figure 5.5: Time evolution of jet half-width: We = 500 (dotted line), We = 1000 (dash line), and We = 2000 (solid line).

5.3.2 Volume fraction statistics

Figure 5.6 shows the temporal evolution of the mean liquid volume fraction in the Re = 3000 jets. Again, the stabilizing effect of surface tension forces appears clearly, since the spreading of the volume fraction profiles is significantly reduced for lower Weber numbers. In all cases, at $t = 30$ the mean liquid volume fraction at the center of the jet is approximately 0.5, suggesting that as much gas as liquid is present in the core of the jet at this time. Note that for larger Weber numbers, the liquid occupies almost the entire computational domain at $t = 30$, which confirms that vertical confinement effects could become important after this time. Figure 5.7 shows the RMS profiles of the liquid volume fraction. For all cases, at later times, it can be noted that the RMS becomes large within the jet core itself, which is in part due to the existence of gas bubbles that have been entrapped in the liquid. Later in the higher Weber number simulations the growth of liquid protrusions leads to the formation of holes in the liquid core, when the interface from both sides of the jet merges. On the gas side, the large RMS values are due initially to the presence of numerous protrusions, then to the development of ligaments.

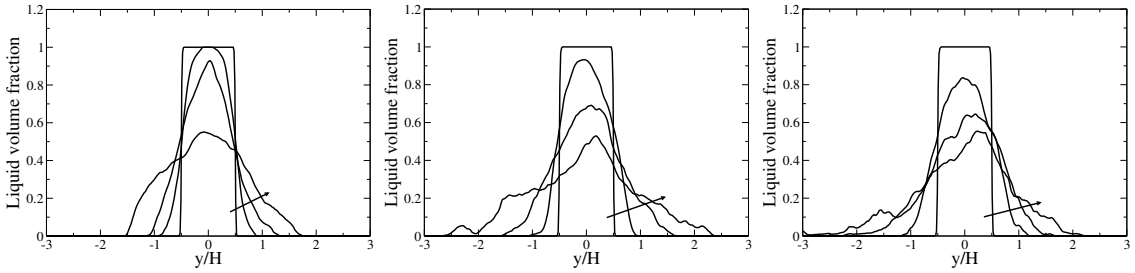

(a) We = 500 (b) We = 1000 (c) We = 2000

Figure 5.6: Mean profiles of liquid volume fraction for the planar jets at different times for Re = 3000 and various Weber numbers. Arrows indicate increasing time ($t = 1, 10, 20, 30$).

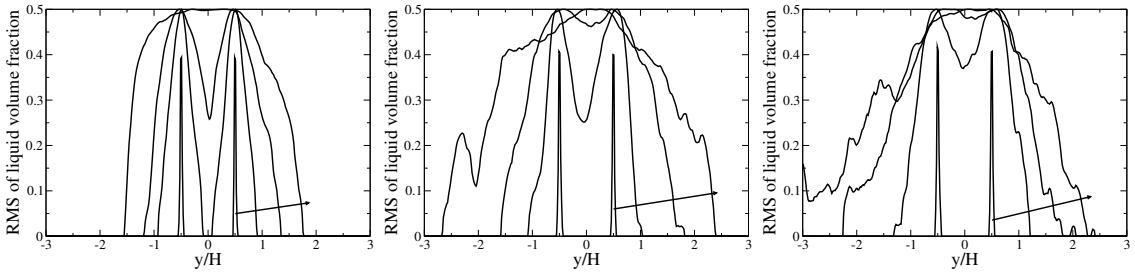

(a) We = 500 (b) We = 1000 (c) We = 2000

Figure 5.7: RMS profiles of liquid volume fraction for the planar jets at different times for Re = 3000 and various Weber numbers. Arrows indicate increasing time ($t = 1, 10, 20, 30$).

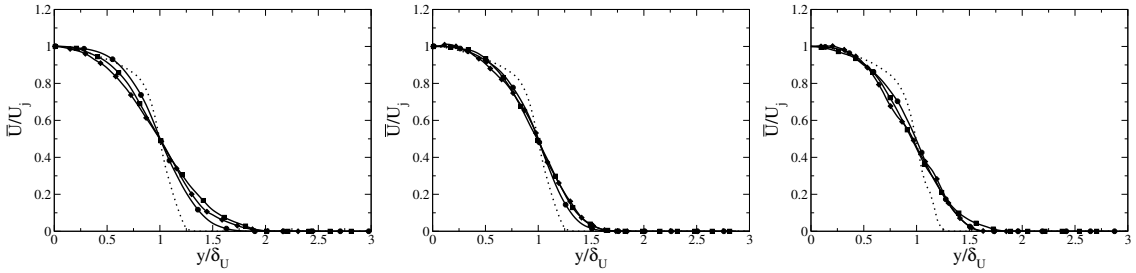

(a) We = 500 (b) We = 1000 (c) We = 2000

Figure 5.8: Mean profiles of streamwise velocity of the planar jets at different times for Re = 3000 and various Weber numbers: $t = 1$ (dotted line), $t = 10$ (circles), $t = 20$ (squares), and $t = 30$ (diamonds).

5.3.3 Velocity statistics

The mean longitudinal velocity is plotted at four different times for Re = 3000 and for various Weber numbers in Fig. 5.8. The velocity is normalized by the centerline velocity, and the y-coordinate is normalized by the jet half-width. With this normalization, a similar single-phase jet would show self-similar behavior in the time interval where a linear growth rate is observed. Here, it can be noted that the collapse of normalized profiles at different times is not perfect, especially for the low Weber number case, for which surface tension effects are stronger. However, for high Weber numbers, it appears that the velocity profiles collapse rather well, which suggests that two-phase jets display a self-similar nature when surface tension forces are not dominating.

In order to investigate the mean flow field in more details, the mean streamwise velocity conditioned on the phase is shown in Fig. 5.9 for Re = 3000 and for various Weber numbers. A clear difference can be observed between the liquid velocity and the gas velocity, regardless of the Weber number. In all cases, the liquid is associated with a larger mean velocity than the gas. This is expected, since initially all the momentum is carried by the liquid. As the jets undergo breakup, the liquid ligaments and droplets tend to retain a larger velocity than the surrounding gas. It should be noted that this effect is more pronounced with the lowest Weber number jet, for which the mean axial liquid velocity is 75%

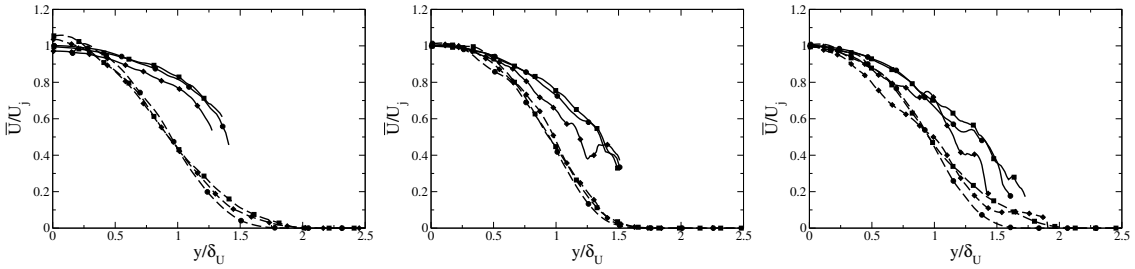

(a) We = 500 (b) We = 1000 (c) We = 2000

Figure 5.9: Phase-conditioned mean profiles of streamwise velocity of the planar jets at different times for Re = 3000 and various Weber numbers: liquid phase (solid lines) and gas phase (dash lines) at $t = 10$ (circles), $t = 20$ (squares), and $t = 30$ (diamonds).

larger than the mean gas velocity at the jet half-width. This can be attributed to the fact that this jet undergoes little disruption because of the larger surface tension forces. As a result, momentum exchange between phases tends to remain limited. For the largest Weber number, the mean axial liquid velocity is less than 40% larger than the mean gas velocity at the jet half-width, indicating that momentum exchange between the phases is enhanced by the intense disruption of the jet.

Figure 5.10 shows the RMS profiles of the axial velocity for the same cases. Regardless of the Weber number, these profiles show a large peak around the jet half-width. Such strong maxima in streamwise velocity fluctuations are not observed in single phase jets [102], and are likely due to the interaction of the turbulent eddies with the phase-interface, as well as with the surface tension force. Indeed, the amplitude of these peaks decreases with increasing Weber number.

Finally, Fig. 5.11 shows the longitudinal energy spectrum E_{11} as a function of the wave number k for case $TPb1$ at three different times during the course of the simulation. These spectra are computed at $y = \delta_U$. Note that we recover almost a decade with a $k^{-5/3}$ slope, indicating that this jet is fully turbulent. As time increases, the turbulent kinetic energy decreases slowly because of viscous dissipation.

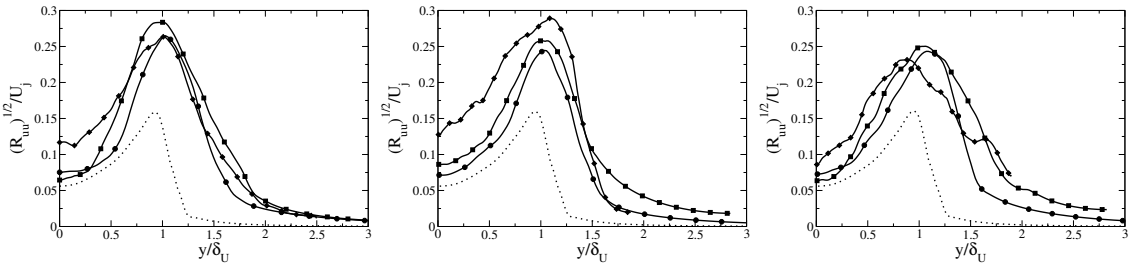

(a) We = 500 (b) We = 1000 (c) We = 2000

Figure 5.10: RMS profiles of streamwise velocity of the planar jets at different times for Re = 3000 and various Weber numbers: $t = 1$ (dotted line), $t = 10$ (circles), $t = 20$ (squares), and $t = 30$ (diamonds).

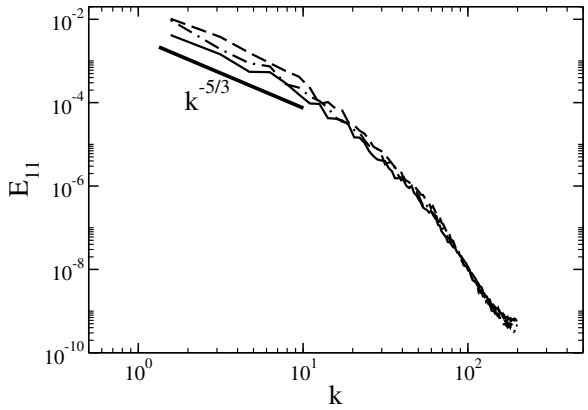

Figure 5.11: Streamwise energy spectrum at $y = \delta_U$ for planar jet $TPb1$ at different times: $t = 10$ (dash line), $t = 20$ (dash-dot line), and $t = 30$ (solid line).

5.4 Instantaneous results

5.4.1 Global description of the flow

In this section, the global features of the flow for jet $TPb1$ are first described. Figure 5.12 presents a three-dimensional view of the phase-interface at different times during the development of the liquid jet. As expected, because of the initially turbulent liquid, the interface starts wrinkling immediately after the beginning of the run. These corrugations then grow and complex phenomena become apparent, such as the entrapment of air bubbles within the liquid jet, or the wrapping of liquid sheets around eddies. As the interfacial structures become larger, individual ligaments are being stretched. Typically, they are found to be oriented in the $(-x)$-direction. These ligaments eventually rupture and form droplets. It should be noted that the disruption of the jet as well as the formation of droplets is dominated by these ligaments. The disruption of the jet does not display a cascade nature, where the jet would first breakup in big structures, then in smaller structures. The fact that most droplets are generated through the rupture of pre-existing ligaments is essential to the atomization process, and has been recurrently observed and documented [115]. From the results of these simulations, a clear picture of the atomization already emerges that can be summarized in three essential steps:

- Initial corrugation of the interface,
- Formation and stretching of liquid ligaments, and
- Rupture of these ligaments, leading to droplet formation.

It is interesting to note that Kelvin-Helmholtz (KH) instabilities are not observed at early times, and therefore, should not contribute to the first part of the jet development at $t < 10$. Yet, numerous droplets have already been generated. This suggests that the liquid turbulence plays an important role in the generation of the first droplets. As the jet keeps developing, a large scale KH type wave becomes visible, and greatly enhances the generation of ligaments, sheets, and droplets. However, this wave appears late in the simulation, and

it might be caused by the confinement of the liquid jet, both in the streamwise and the lateral directions. The numerous liquid ligaments, crests, and droplets observed in the simulation results are qualitatively in good agreement with experimental observations by Faeth *et al.* [25].

Figure 5.13 shows an iso-surface of the Q-criterion, which is the second invariant of the velocity gradient tensor. This quantity has been widely used to help visualize coherent vortical structures [44, 20]. The iso-surface at $Q = 5$ is shown, since it allows to visualize the main structures of the flow while retaining the clarity of the figure. This value will be used for all Q-criterion iso-surfaces in this chapter. Between the two first images, the nature of the flow structures changes strongly. At $t = 2.5$, both vortex streaks, expected from wall-bounded flows, and flat vortices that are aligned in the streamwise direction are found. The nature of these structures will be examined more closely below. At $t = 7.5$ and later on, the vortices resemble the worm-like structures expected for well-developed jet turbulence. The size of the largest structures increases with time, as turbulence develops. From the first three pictures, no KH-type wave can be identified. However, it becomes noticeable at later times that a KH longitudinal fluctuation is present. The full turbulent nature of this flow appears clearly, and a wide range of structure sizes interact within each shear layer at first, then between the two shear layers at later times.

Comparing the simulation results with experimental observations that have been reported in the literature, two main differences can be noted. First, Sallam *et al.* [96] reported that the ligaments they observed in their jets were randomly oriented, rather than preferentially oriented in the $(-x)$-direction. They attributed this fact to the small importance of aerodynamic forces in relationship with the large density ratio they were using. Here, because the density ratio is much lower, aerodynamic forces on the liquid structures are expected to be significant. The aerodynamic forces acting on the protruding liquid ligaments cause them to be deflected towards the $(-x)$-direction, which was experimentally observed for a density ratio of the order of 100 by Wu and Faeth [118]. These differences are of great interest, since liquid atomization in many combustion devices, such as Diesel engines and gas turbines, involves such small density ratios. The present results might therefore

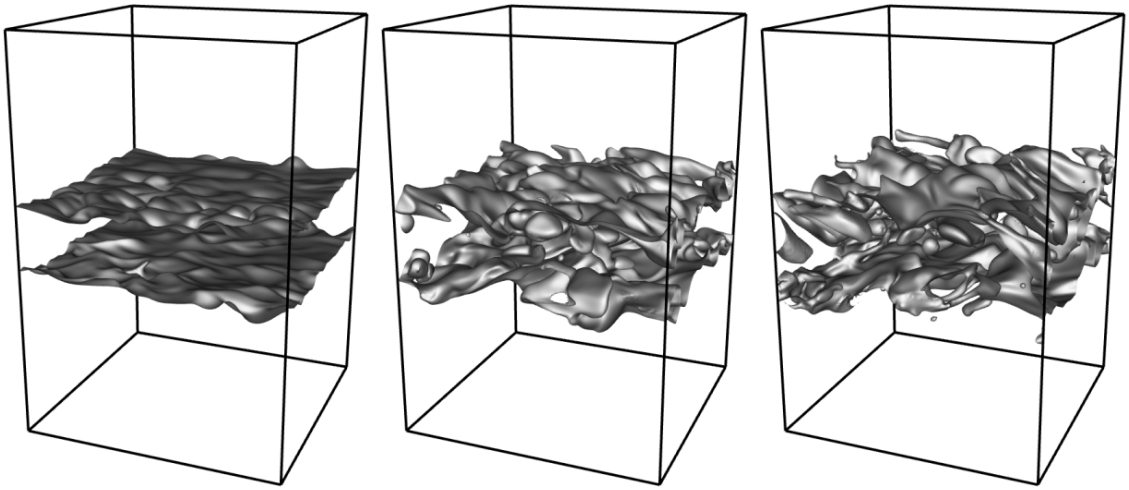

(a) $t = 2.5$ (b) $t = 7.5$ (c) $t = 12.5$

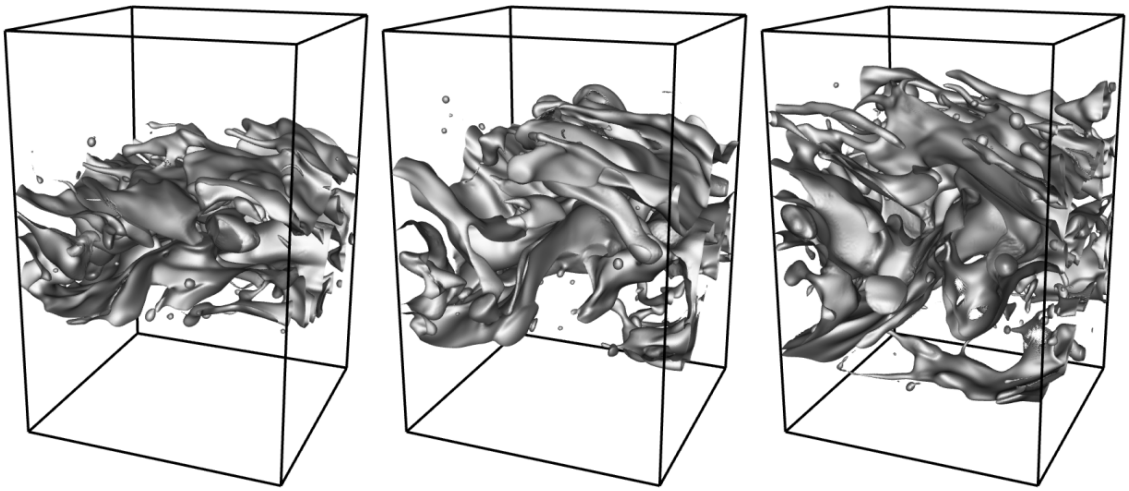

(d) $t = 17.5$ (e) $t = 22.5$ (f) $t = 27.5$

Figure 5.12: Instantaneous phase-interface location at different times for case $TPb1$.

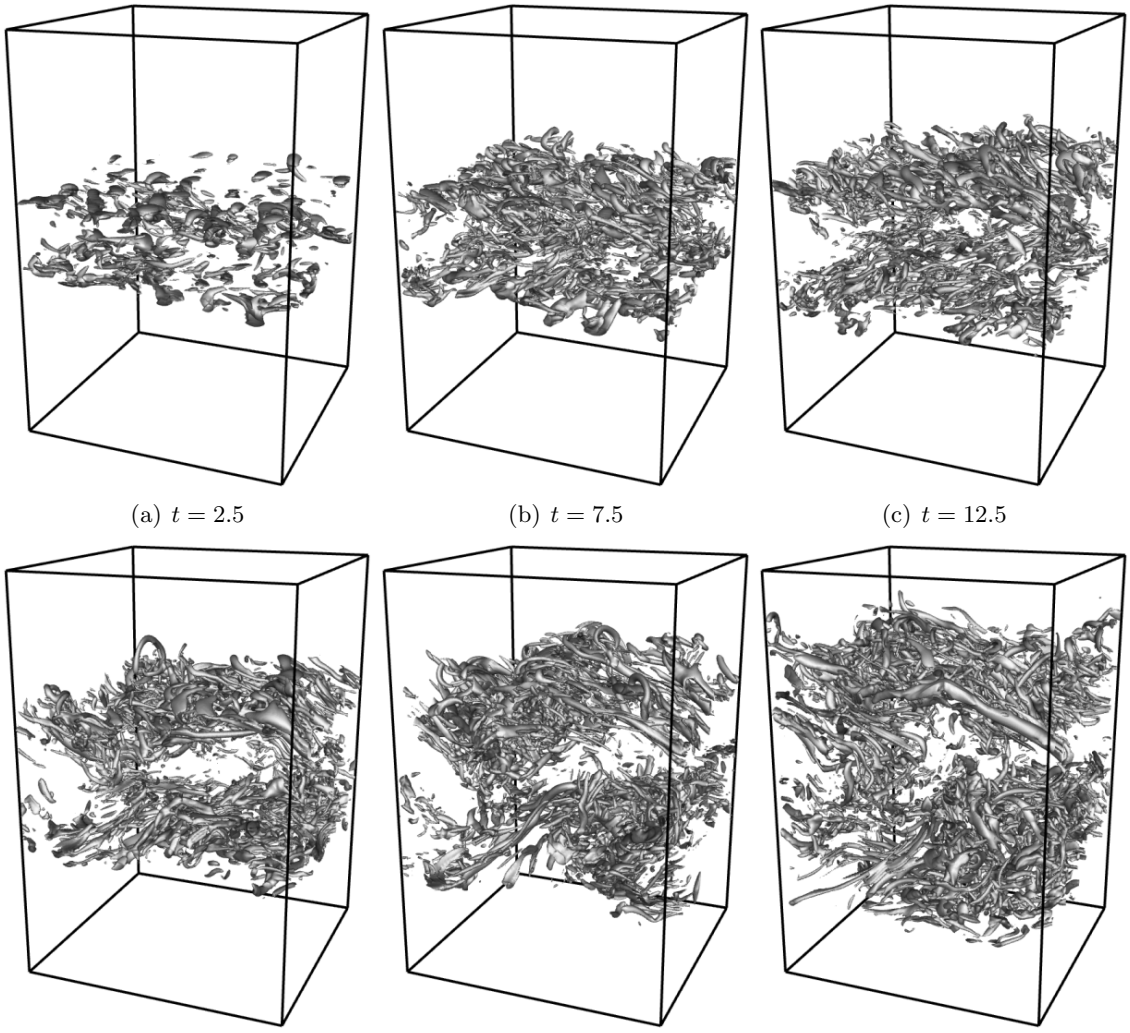

(a) $t = 2.5$ (b) $t = 7.5$ (c) $t = 12.5$

(d) $t = 17.5$ (e) $t = 22.5$ (f) $t = 27.5$

Figure 5.13: Instantaneous normalized Q-criterion at different times for case $TPb2$: $Q = 5$ iso-surface is shown.

be more relevant for these applications. Second, Sallam *et al.* [96] reported not observing any bubble in the region where the interface was sufficiently undisturbed to allow for direct visualization. In contrast the present simulations show gas bubbles trapped in the liquid. Again, this difference is likely to be caused by the importance of aerodynamic effects in the simulations, which will be shown below to greatly enhance the interface deformation.

5.4.2 Effect of the Weber number

The effect of the surface tension forces is discussed by comparing a top view ($+y$) of the interface at different Weber numbers. Cases $TPa1$, $TPb1$, and $TPc1$ are considered for this purpose. Figure 5.14 shows this top view at the times $t = 5$, 15, and 25. For the earliest time, a significant difference between the three interfacial shapes can be noted for the different Weber numbers. The interface roughness is much lower for We = 500 than for We = 2000, which is expected since surface tension forces work against the deformation of the interface. Clearly, at this time, the large scale structures are still very similar for the three different cases, indicating that the large scale turbulent eddies carry enough energy to induce interfacial deformation despite surface tension forces. Smaller scales become much more apparent for high Weber numbers, which suggests that surface tension forces act as a cut-off in interfacial structure length-scales. For high Weber number, even small turbulent scales, which carry less kinetic energy, can deform the interface, while for low Weber number, only energetic scales are able to disrupt the interface. The observation of the interfaces at later times confirms this analysis, and in general the low Weber number interface remains much less disturbed than the high Weber number interface. Note that similarities between the structures for various Weber numbers have mostly disappeared at $t = 15$. Regardless of the Weber number considered, droplets are generated through the creation and stretching of liquid ligaments. Ligaments are longer, thinner, and more numerous as the Weber number is increased. The same remark can be made concerning droplets, which tend to be smaller and more abundant for the high Weber number case than for the low Weber number. Finally, it should be noted that the sizes of ligaments and droplets become larger at later times in all cases, which has been observed also by Sallam *et al.* [96], and can be attributed to the

dissipation of the small turbulent scales.

5.4.3 Effect of the Reynolds number

In order to assess the effect of the Reynolds number on the interface disruption, two different Reynolds numbers have been considered. While it is unclear whether many lasting differences will emerge between Re = 2000 and Re = 3000, the difference in the level of turbulence should at least impact the early deformation of the interface. Figure 5.15 compares the interface for cases $TPb1$ and $TPb2$ at different times throughout the simulations. Clearly, the later development of the various liquid structures is very similar between the two Reynolds numbers. The resulting ligaments appear to be of the same size, and the droplets seem similar in size and number. This observation suggests that the processes by which ligaments are stretched out and ruptured are not significantly affected by changing the Reynolds number. Of course, the range of scales found in Re = 2000 turbulence and Re = 3000 turbulence is rather limited, therefore it is possible that changing the Reynolds number more significantly could have a stronger effect. Note that Sallam *et al.* [96] reported that increasing the injection velocity, i.e. increasing both the Reynolds number and the Weber number at the same time, led to little consequences on the largest liquid structures, while smaller and more numerous small scales were obtained. The main difference between the two simulations can be found in the earliest interface visualization, where the corrugation length scales appear larger for the low Reynolds number case. This is to be expected, considering that less energy is contained in small eddies for the low Reynolds number case compared to the larger Reynolds number case. Consequently, the early deformation on the smaller scales of the interface is more likely to take place on relatively larger length scales as the Reynolds number is reduced.

5.4.4 Onset of atomization

The early destabilization of the phase-interface is now discussed in more details. Figure 5.16 shows the temporal evolution of both interface location and iso-surface of Q-criterion for

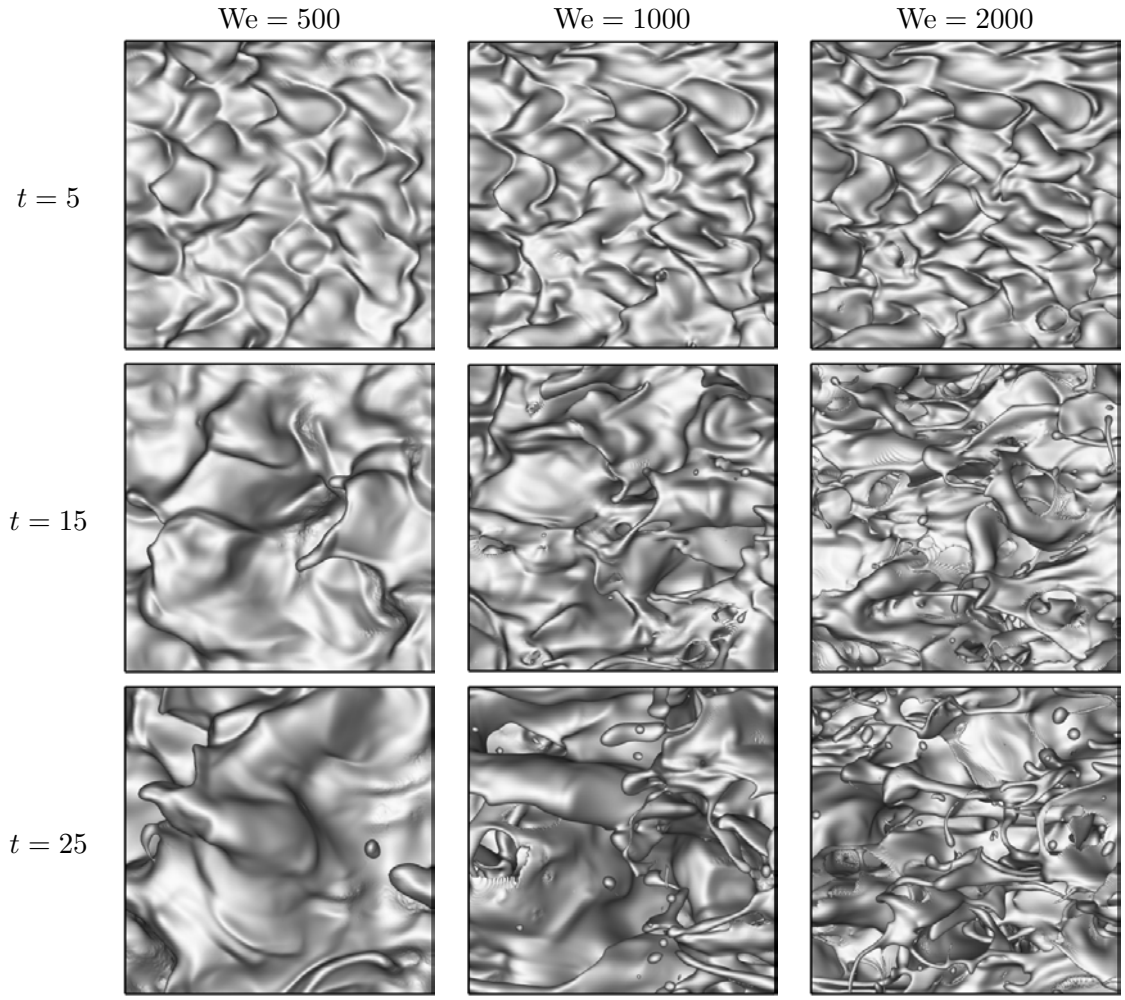

Figure 5.14: Top view of the interface for Re = 3000 as a function of time and Weber number.

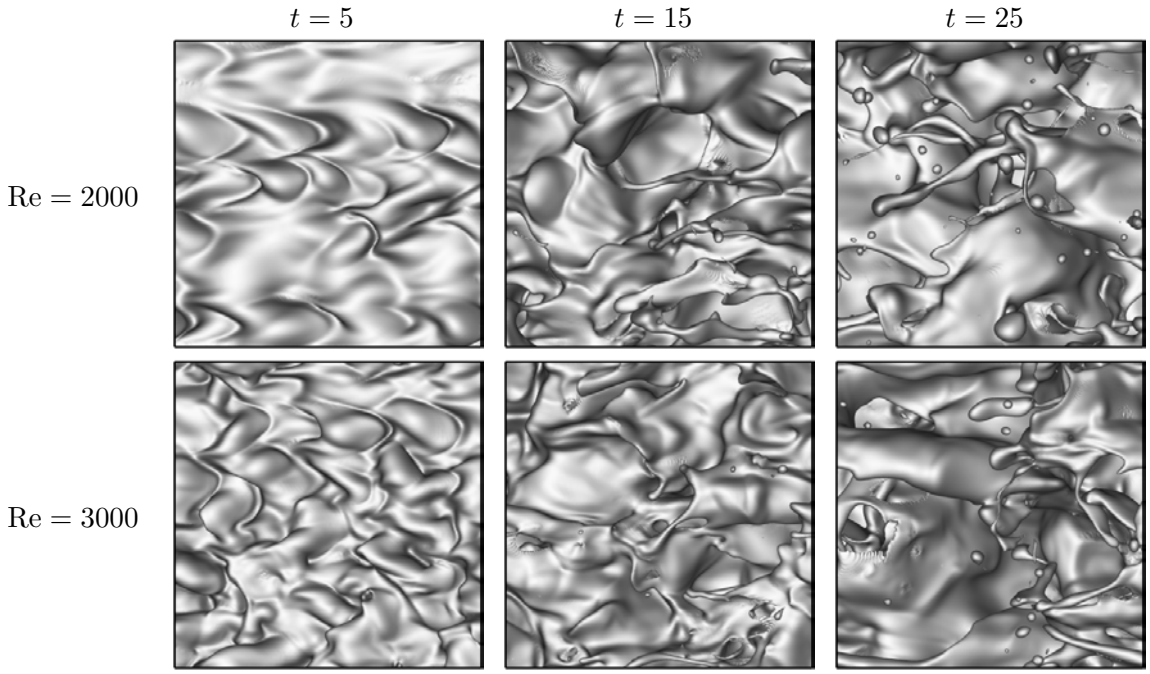

Figure 5.15: Top view of the interface for We = 1000 as a function of time and Reynolds number.

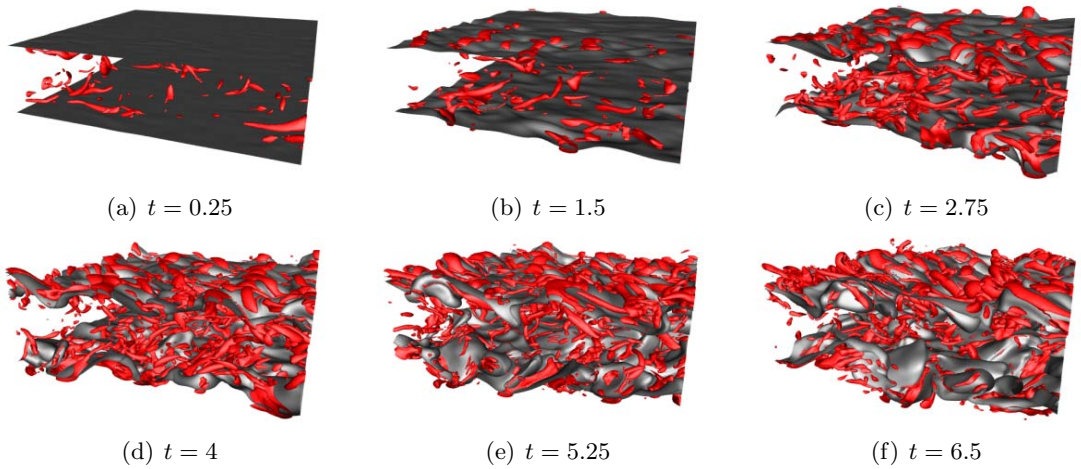

(a) $t = 0.25$ (b) $t = 1.5$ (c) $t = 2.75$

(d) $t = 4$ (e) $t = 5.25$ (f) $t = 6.5$

Figure 5.16: Time evolution of phase-interface (grey) and iso-surface of Q-criterion (red) for Re = 3000 and We = 1000 for early times.

case $TPb1$, at early times. At $t = 0.25$, the interface has barely started to deform, and the turbulent structures clearly resemble wall-bounded turbulence, with the characteristic vortex tubes inclined at approximately 45° from the interface, where the wall used to be [47, 49, 50]. As the simulation progresses and reaches $t = 1.5$, the interface begins to display some corrugations. While the liquid flow structures remain very similar to wall-bounded turbulence, the occurrence of flat structures in the gas should be noted. These structures appear at the phase-interface surface, mostly aligned in the spanwise direction. At $t = 2.75$, these gas structures become more pronounced. From a close examination of the interface, it can be noted that these spanwise structures are always found where the interface displays a hump towards the gas. At this time, the turbulence within the liquid layer has evolved significantly from wall-bounded turbulence, with more numerous structures, and increased complexity in their shape and alignment. This can be attributed to the interactions that start to take place with the interfacial corrugations, which have reached a significant size. In order to better understand the nature of the spanwise-aligned structures found in the gas stream, Fig. 5.17 shows a vertical view of the interface and of an iso-surface of Q-criterion, colored by the axial component of the vorticity, both from the liquid side and from the gas

side. The difference between the structures on the liquid side and on the gas side appears clearly. The liquid side contains small tubular vortices that resemble wall-bounded flow structures. They are mostly aligned with the flow direction, and display either a positive or a negative axial vorticity, which implies that they rotate about the x-axis, in one direction or the other. On the contrary, the gas structures are mostly flat eddies slightly stretched in the spanwise direction, and they show small levels of axial vorticity. This suggests that these structures are recirculation regions formed on top of the protruding interface, therefore containing mostly spanwise vorticity. This observation can be related to the aerodynamic effects discussed earlier. As the vertical component of the velocity field leads to interfacial corrugations, the gas phase is required to flow around the protruding liquid eddies. This process will form an area of low pressure, and generate lift on the liquid eddy. As the liquid obstacle rises even higher, local recirculation regions are likely to form in the gas phase. At later times, Fig. 5.16 shows that as this lift effect accentuates the interfacial deformation, more complex structures are formed, both in the liquid phase and in the gas phase. The description of aerodynamic effects at the onset of turbulent atomization was first proposed through phenomenological analysis in Wu and Faeth [118] in order to provide an explanation for the fact that smaller droplets were obtained when lower density ratios were used in atomization experiments. In the present simulations, this theory is clearly validated, and stands out as a central element of turbulent primary breakup. Figure 5.18 shows two sketches that illustrate the initial deformation of the interface and the mechanism through which lift enhances interfacial disruption. In this figure, L is the turbulent eddy size, v'_L the associated turbulent vertical velocity, and it is assumed that the liquid structure moves at the bulk jet velocity U_0. Estimates for the scaling of the different effects interacting here were first used in Wu and Faeth [118] to relate the expected drop diameter to the Weber number, and is reiterated here for the sake of completeness. Per unit volume, the following can be written:

- *Kinetic energy of the liquid structure:* $E_K \sim \rho_l {v'_L}^2$.
- *Energy added through aerodynamic lift:* $E_L \sim \rho_g {U_0}^2$.

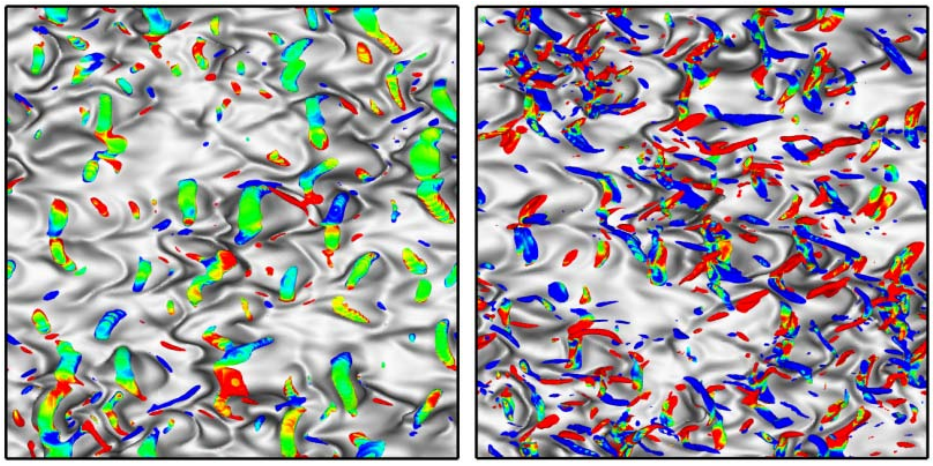

(a) From gas side. (b) From liquid size.

Figure 5.17: Time evolution of phase-interface (grey) and iso-surface of Q-criterion (red) for Re = 3000 and We = 1000 for early times.

- *Energy associated with surface tension:* $E_{ST} \sim \sigma/L$.

E_L and E_K need to overcome E_{ST} in order to lead to breakup. If the density ratio is large, it seems safe to neglect aerodynamic lift. The important effects are then the turbulent kinetic energy in the vertical direction, versus the stabilizing effect of surface tension. Clearly, if v'_L is such that $E_K > E_{ST}$, then the interface is expected to deform. In the inertial sub-range, ${v'_L}^3/L \sim \epsilon$, therefore E_K can be expressed as $E_K \sim \rho_l \epsilon^{2/3} L^{2/3}$. For smaller values of L, E_{ST} will increase while E_K will decrease, meaning that surface tension forces will act as a cut-off in the interfacial perturbation length scales by preventing small eddies that carry little energy to deform the interface. If the density ratio is smaller, then E_L will contribute to the destabilization of the interface, enabling smaller structures to deform the interface.

On the topic of early ligament formation, it should be noted that the actual shape of the liquid structures that are removed from the central liquid core depends on the form of the turbulent eddy that initiated its development. Also, this shape is affected by the surrounding turbulent structures, leading to a very complex behavior. Because of the three dimensionality of the initial wall-bounded turbulent flow, the interface tends to initially form compact humps that protrude in the gas, leading to ligaments. However, wider liquid

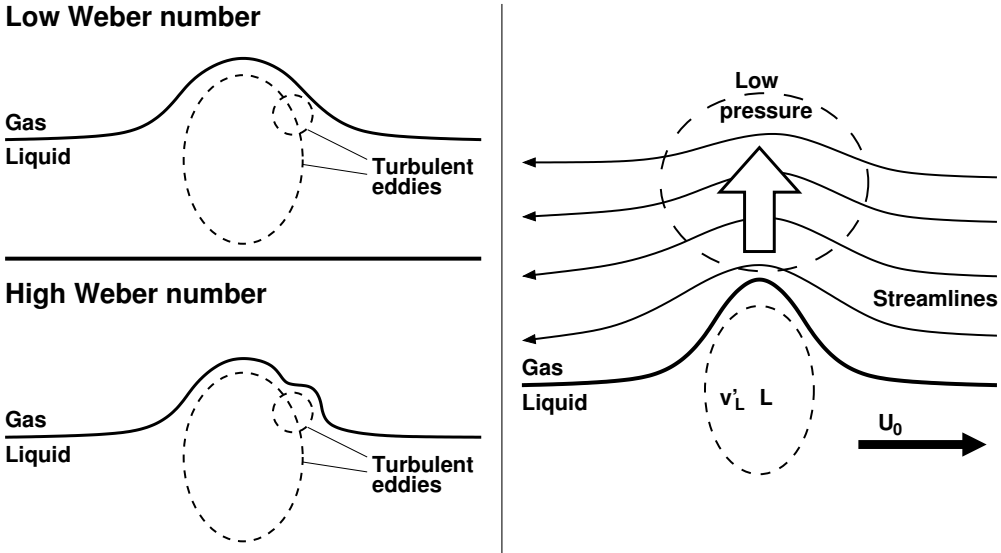

(a) Early interfacial deformation

(b) Aerodynamic breakup enhancement

Figure 5.18: Schematics of the mechanisms leading to turbulent breakup: early deformation of the interface due to vertical turbulent velocity (left), and aerodynamic enhancement of breakup through lift effect (right).

structures are also formed, leading to liquid crests. These crests often produce several ligaments, but occasionally generate thin sheets. These sheets have very complex dynamics, that warrant further investigation. Note that they seem to be more strongly affected by aerodynamic effects, and that their rupture leads to the recovery of one or several ligaments. It seems unlikely that these sheets are properly resolved in the present simulations, therefore drawing any conclusions on their physics is difficult. However, their existence can probably be related to bag breakup events that have been observed experimentally [97].

5.4.5 Ligament rupture

Having analyzed the mechanisms through which ligaments are generated, the rupture of these ligaments should now be characterized more precisely. Two potential processes are competing to break the ligaments and form droplets, namely the classical Rayleigh breakup, i.e. the capillary breakup of a liquid cylinder, and aerodynamic forces acting on the ligaments, i.e. secondary atomization. The idea that primary and secondary breakup merge and interact together for low density ratios has been introduced previously, see e.g. [25]. Ranger and Nicholls [92] and Hsiang and Faeth [42] presented the mechanisms by which a droplet undergoes secondary atomization, and Wu and Faeth [118] suggested that this process could affect liquid structures during primary atomization itself. It has already been clearly established that the cases considered here are strongly affected by aerodynamic forces, therefore it is likely that these forces will contribute to the rupture of the ligaments that they helped forming. Wu and Faeth [118] provided a phenomenological formula for the ratio of the Rayleigh breakup time scale τ_R to the aerodynamic breakup time scale τ_A that is based on the distance from the injection and the local turbulent Weber number. Following the work of Hsiang and Faeth [42], the timescale associated with aerodynamic breakup of a liquid structure of size L moving at U_0 in still gas can be expressed as $\tau_A = \sqrt{\rho_l/\rho_g}L/U_0$. Similarly, Rayleigh breakup can classically be characterized by $\tau_R = \sqrt{\rho_l L^3/\sigma}$. The smallest time scale should correspond to the main mechanism by which ligament breakup occurs. The ratio of these time scales can be expressed by $\tau_A/\tau_R = \mathrm{We}_{L,g}^{-1/2}$, where $\mathrm{We}_{L,g} = \rho_g U_0^2 L/\sigma$ is a Weber number based on the gas density and the liquid protrusion size. Two conclusions

can be drawn from this time scale analysis: the higher the surface tension force is, the more likely it is for breakup to be due to capillary instabilities, and the larger the liquid structures are, the more likely it is for breakup to originate from aerodynamic forces. Recall that in the present simulations liquid structures tend to become larger with time. This observation can be related to the time it takes to develop larger corrugations, and also to the increase of the turbulent scales with time. Consequently, it can be expected that Rayleigh breakup should dominate early on, while at later times aerodynamic effects could lead to merged primary/secondary breakup, especially for high Weber number cases. Case $TPb1$ displays the two types of ligament breakup. Figure 5.19(a) shows classical Rayleigh breakup of a ligament early in the simulation, leading to the formation of three droplets. Figure 5.19(b) shows the breakup of a ligament aligned in the spanwise direction. In this case, it is unclear what the main mechanism for breakup is, since aerodynamic forces acting on a ligament misaligned with the mean flow direction should be intense. Finally, Fig. 5.19(c) shows a clear aerodynamic stripping of a large ligament, leading to the creation of secondary bulges and ligaments.

5.4.6 Detailed liquid structures

- *Bubble entrapment.* Early in the simulations, the wall-bounded nature of the turbulent flow leads to frequent entrapment of air bubbles. In wall-bounded flows, two counter-rotating vortex streaks close to each other lead to a local sweep effect, followed by an ejection phenomenon where fluid is rapidly displaced away from the wall [50, 47, 49]. A similar process is encountered here, except that the phase-interface is being deformed in the process. Figure 5.20 illustrates this process by showing the phase-interface as well as an iso-surface of Q-criterion colored by the axial vorticity. Streaks that are formed in the nozzle flow survive during the early times of the jet development. The interface is pinched between these two counter-rotating vortices, eventually forming an air pocket in the liquid. This process is similar to the ejections in wall-bounded flows, except that in the presence of a deformable interface, the streaks tend to engulf the gas in the liquid, which can create elongated air structures that penetrate significantly

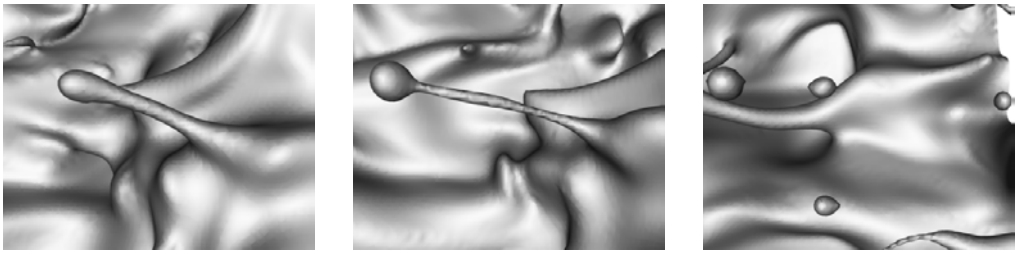

(a) Rayleigh breakup of a ligament. Note that on the rightmost picture, the bottom droplet is not associated with the breakup of the ligament followed here.

(b) Breakup of a ligament misaligned with the flow.

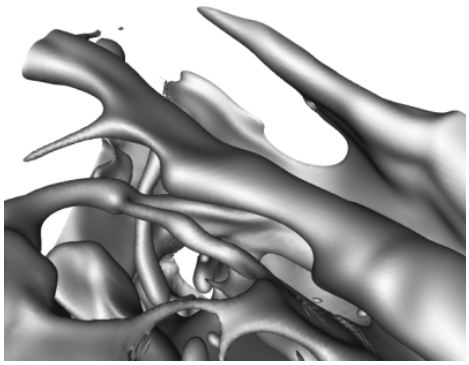

(c) Aerodynamic stripping of a ligament. On the large ligament extending from the top left corner of the picture to the bottom right corner, secondary ligaments can be seen developing.

Figure 5.19: Sample ligament breakup events for case $TPb1$.

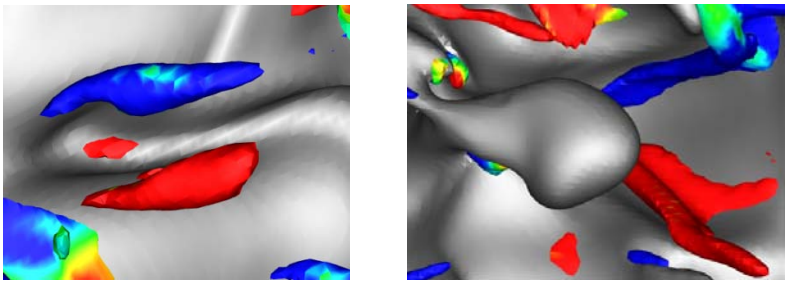

(a) Pinching of the interface between two counter-rotating vortices.

(b) Engulfment of air through local ejection.

Figure 5.20: Engulfment of air bubbles in the liquid by local ejection. Interface viewed from the liquid side, and iso-surface of Q-criterion colored by the axial vorticity.

inside the liquid. When these structures eventually break, air bubbles remain in the liquid jet.

- *Bubble bursting.* The air bubbles that have been entrapped in the liquid are found to occasionally break the liquid surface. When this occurs, the interface first bulges because of the rising bubble, which is shown in Fig 5.21. Then, the thin liquid layer ruptures, and a crater is formed. As the remaining liquid lip recedes, a vortex is formed that leads to the generation of a central jet. The event shown in Fig. 5.21 does not have any lasting consequence on the interface evolution. However, it contributes to the overall destabilization of the jet. In other cases, events of the same nature were found to have a significant influence on the evolution of the jet. In the case where the air bubble engulfed in the liquid has an elongated shape, the crater that is formed when the bubble breaks the liquid surface has a very high curvature. Such a high local curvature induces a strong acceleration, which can lead to the formation of a very intense liquid jet. If the jet is strong enough, a ligament is formed, and shear will contribute to its elongation, eventually leading to its rupture and to the formation of liquid droplets. This mechanism of ligament formation has been observed several times in these simulations, and such an event is shown in Fig. 5.22. While it is accepted that bubble bursting can lead to droplet formation [21, 40], this is the first

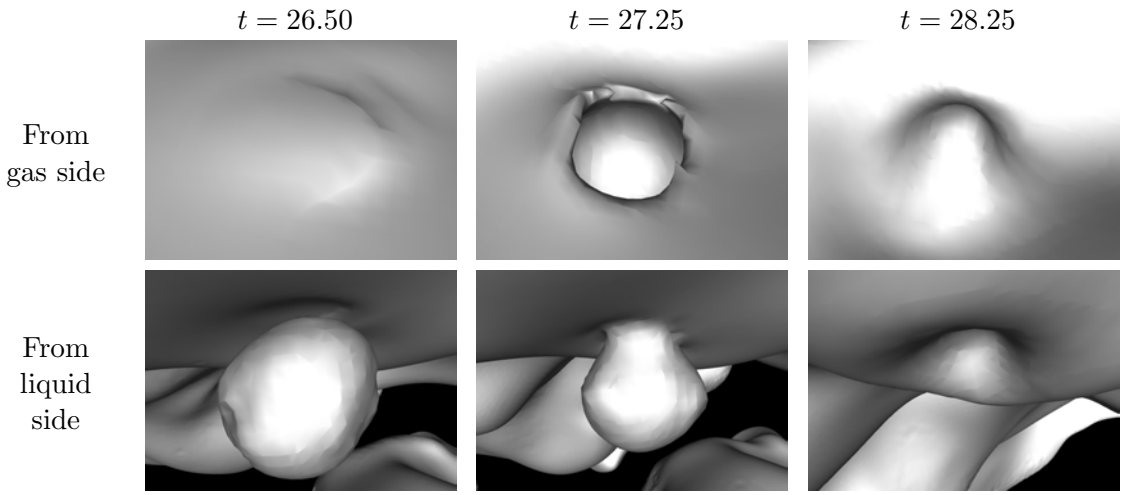

Figure 5.21: Example of bubble bursting with limited consequences on the interface.

time this mechanism is identified as a droplet generation mechanism in the turbulent atomization of liquid jets.

- *Ligament–ligament collision.* While droplet collisions have been extensively studied both experimentally and numerically [3, 107], and are expected to take place frequently provided the droplet number density is high, the simulations conducted in this work also display frequent ligament collisions. Indeed, the intense fingering of the liquid for the high Weber cases lead to a high density of ligaments at the jet surface. As stated earlier, the aerodynamic forces on these ligaments can be significant, and they can be affected by surrounding turbulence. These ligaments are therefore likely to interact and collide, leading to various outcomes as in the case of binary droplet collisions. An example is shown in Fig. 5.23, where two ligaments rupture during their collision, leading to the formation of several droplets. Another possible outcome of ligament collisions is the formation of liquid bridges. Two examples of such liquid bridges are shown in Fig. 5.24, where both bridges parallel to the flow and bridges perpendicular to the flow are observed.

- *Droplet splashing.* Finally, frequent occurrences of the splashing of a detached droplet

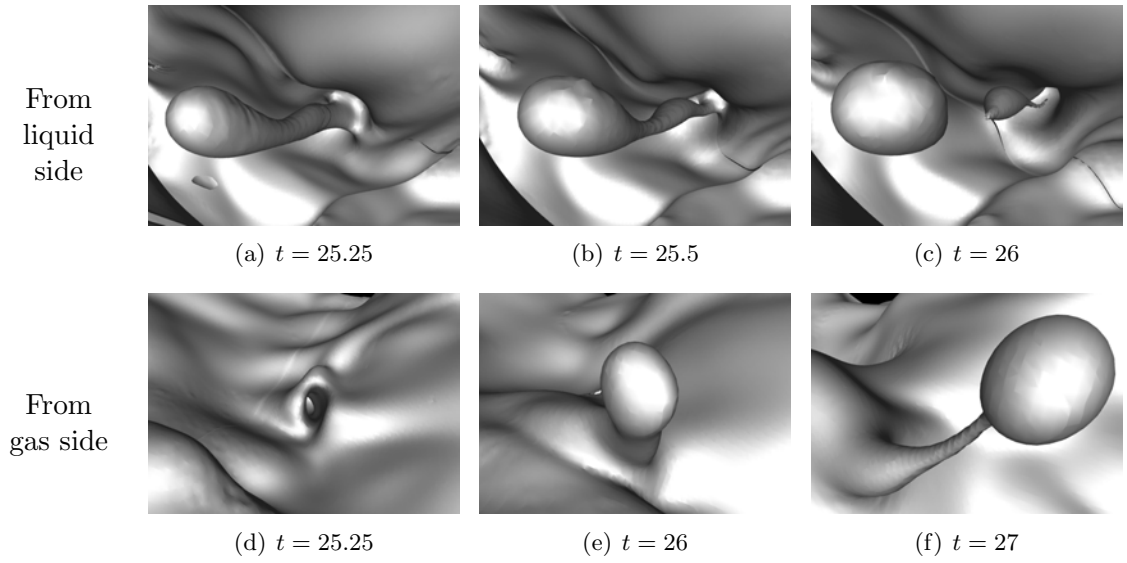

(a) $t = 25.25$ (b) $t = 25.5$ (c) $t = 26$

(d) $t = 25.25$ (e) $t = 26$ (f) $t = 27$

Figure 5.22: Example of bubble bursting with ligament generation.

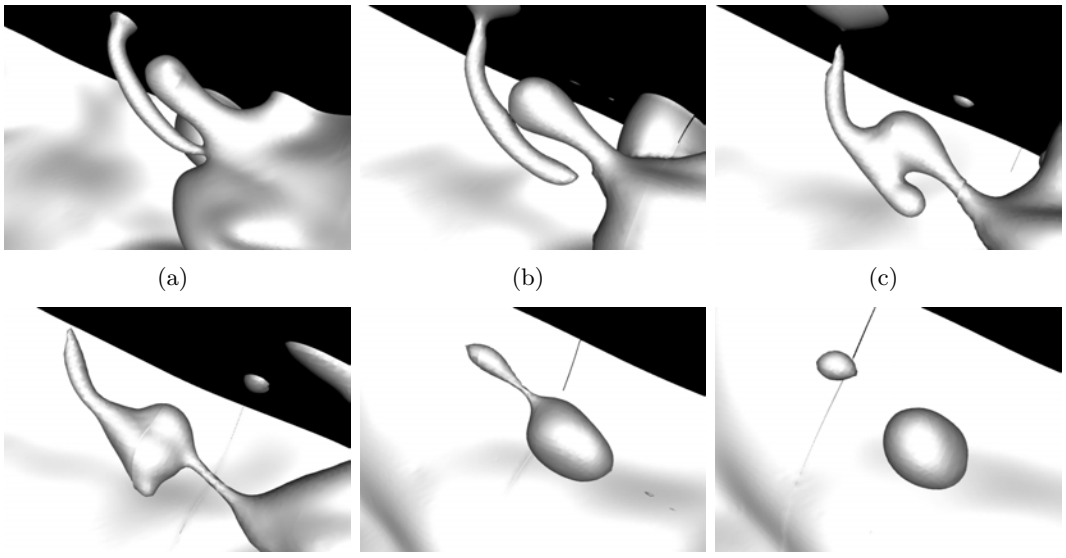

(a) (b) (c)

(d) (e) (f)

Figure 5.23: Ligament collision leading to breakup, viewed from the gas side.

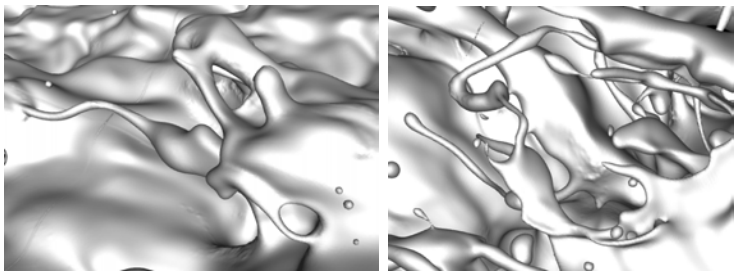

(a) We = 500 (b) We = 2000

Figure 5.24: Example of bridges formed by way of ligament collision for various Weber numbers, viewed from the gas side.

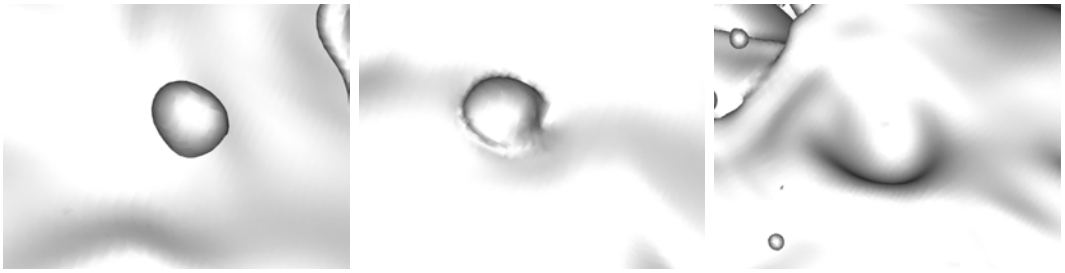

(a) (b) (c)

Figure 5.25: Example of droplet splashing with limited consequences on the interface, viewed from the gas side.

onto the inner liquid core are observed. These events follow the classical droplet splashing, described extensively in the review by Yarin [119]. Figure 5.25 shows an example of splashing, with the expected formation of a crater. In this case, little consequence on the interface shape was observed. However, in several instances, drop splashing was found to initiate the formation of ligaments, such as shown in Fig. 5.26.

This list of detailed interface behaviors suggests that when aerodynamic forces play a role, the combined effect of turbulence, ligament generation and collision, and bubble entrapment leads to a very complex atomization process. While ligament formation followed by Rayleigh breakup seems to be the major path through which droplets are generated,

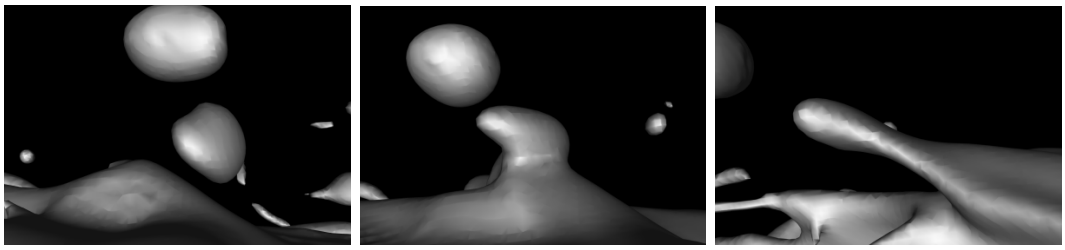

(a) (b) (c)

Figure 5.26: Example of droplet splashing with ligament generation, viewed from the gas side.

it clearly appears that highly complex ligament interactions might lead to early ligament rupture, and therefore might significantly affect drop size distribution. Note that the simulation results identified bubble bursting and droplet splashing as possible, although potentially marginal, mechanisms through which ligaments can be created.

5.5 Towards spatially evolving round liquid jets

In order to alleviate the potential confinement issue in the simulations presented above, and because of their relevance for technical systems, spatially evolving round liquid jets have also been computed. The computational cost for this problem increases significantly: for a jet of diameter D, the $20D \times 5D \times 5D$ computational domain is resolved by a $1048 \times 256 \times 256$ mesh. Compared to the previous temporal simulations, the effective resolution is decreased from $\Delta x = D/64$ to $\Delta x \approx D/50$. First, two cases are computed, both at a jet Reynolds number of $\mathrm{Re} = 3000$, but for two different Weber numbers of $\mathrm{We} = 1000$ and $\mathrm{We} = 2000$. A first simulation of a turbulent pipe at $\mathrm{Re} = 3000$ is conducted to provide inflow conditions for the jet simulations. Figure 5.27 shows the temporal evolution of the low Weber jet, while Fig. 5.28 shows the jet at the higher Weber number. Clearly, features very similar to those observed in the planar jet simulations are recovered, including the stabilizing effect of surface tension forces, the presence of liquid protrusions early in the development of the jet, and the appearance of ligaments that rupture and lead to the formation of droplets.

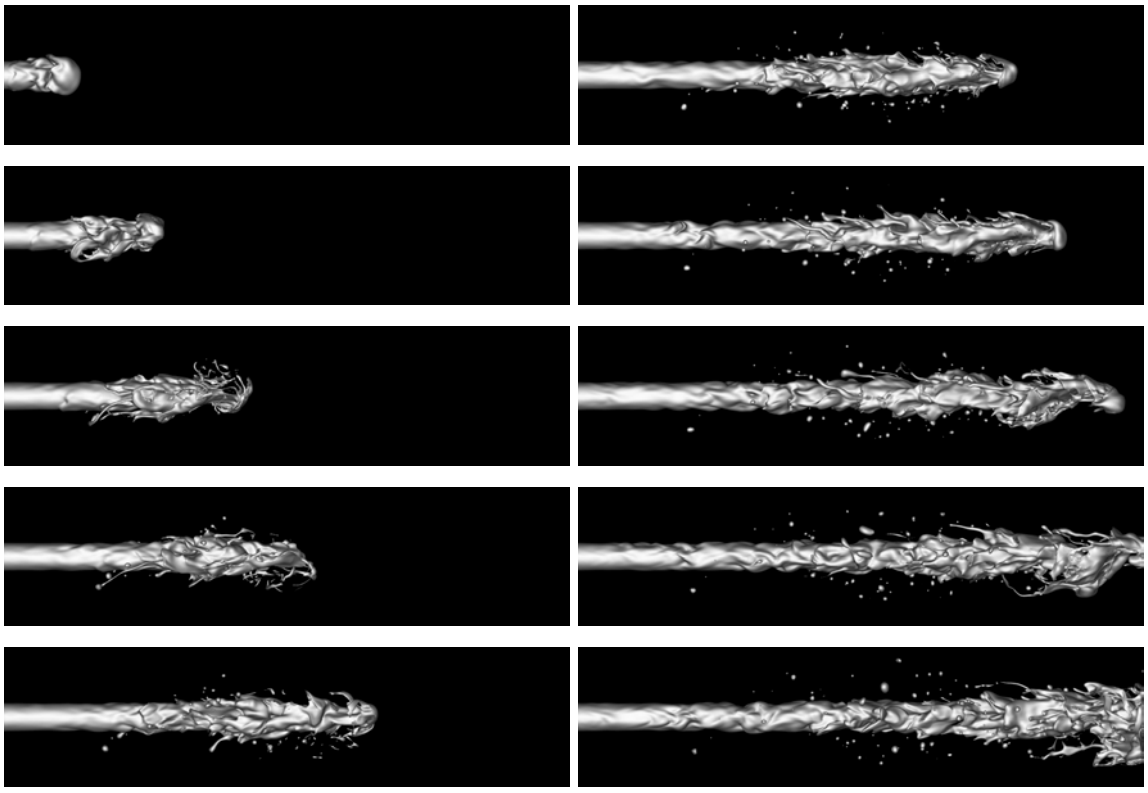

Figure 5.27: Snapshot every $\Delta t = 2.5$ of the liquid-gas interface for Re = 3000 and We = 1000.

Note that in contrast to the temporal jets, these spatially evolving jets have a liquid tip that forms a mushroom shape. Thin sheets are formed from the tips of the jets. Eventually the jet tips destabilize and move off-center for the high Weber number case.

For these two cases, Fig. 5.29 shows the ratio of the liquid mass in the domain to the exact mass that has been injected as a function of time. Most of the mass conservation errors are due to the initial disruption of the liquid jet tip that tends to form thin sheets which quickly become under-resolved. This leads to about 5% mass loss for the low Weber number case, while it leads to about 10% mass loss for the high Weber number case. In comparison, for the temporal planar jet simulations, where there was no jet tip leading to the formation of liquid sheets, mass loss remained below 2% even for the highest Weber number case. Note that despite the complexity of the topology, less than 15% mass loss is

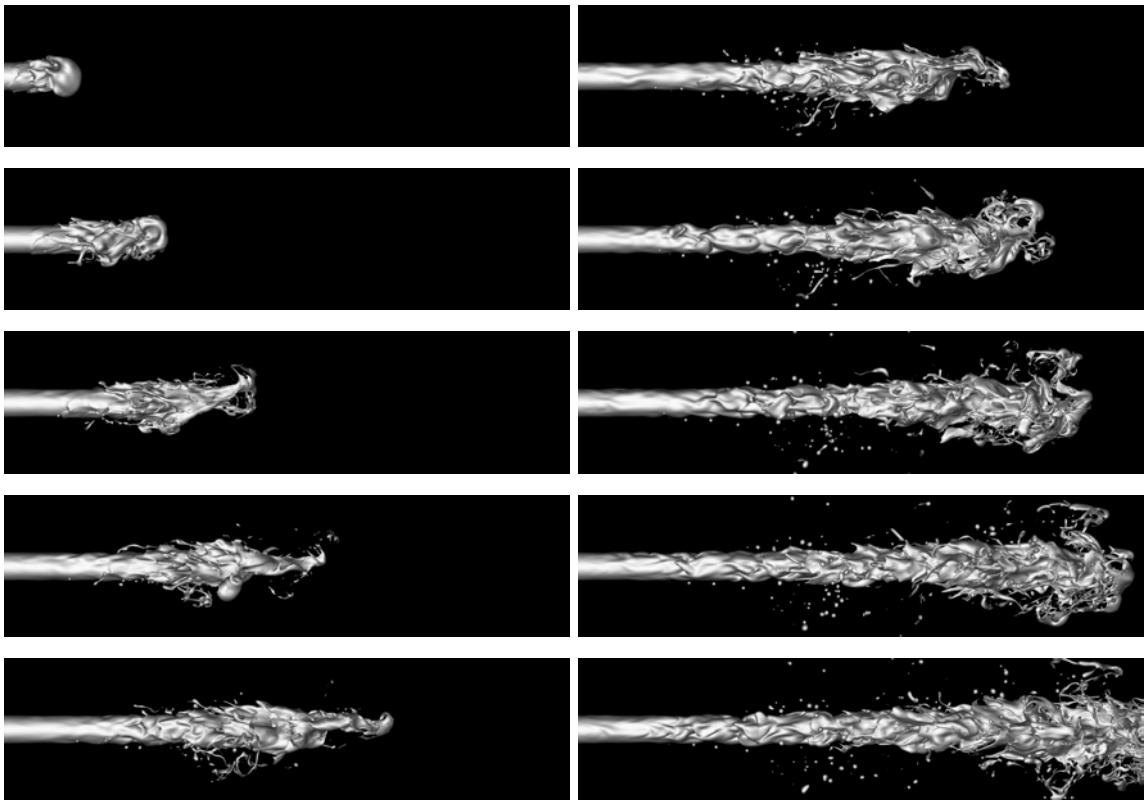

Figure 5.28: Snapshot every $\Delta t = 2.5$ of the liquid-gas interface for Re = 3000 and We = 2000.

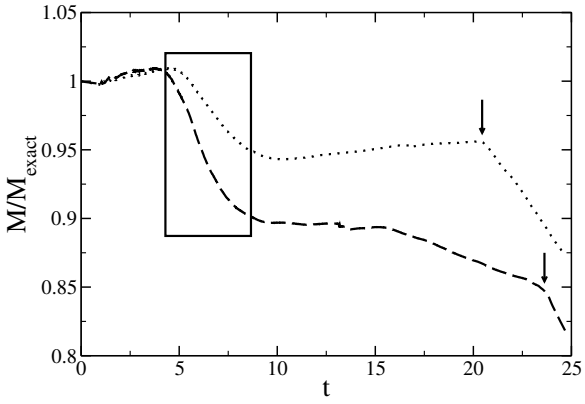

Figure 5.29: Temporal evolution of the liquid mass normalized by the exact liquid mass in the domain: We = 1000 (dotted line) and We = 2000 (dash line). The rectangle region corresponds to the rupture of the mushroom tip by means of sheets. The arrows indicate when the jets start to exit the domain, at which time M_{exact} becomes unknown.

observed with the high Weber number case, which is excellent in comparison to standard level set methods. Some time after $t = 20$, both jets start to exit the computational domain, and the measure of mass conservation error becomes unknown.

Finally, the recent work of Wang *et al.* [116], where realistic Gasoline Direct Injected (GDI) injection was visualized with the help of ultra-fast X-ray technique, is used for qualitative comparison. In their paper, Wang *et al.* [116] show a few images, and provide some estimate of the local velocity. Figure 5.30 shows one of these images, where the complex interface shape can be observed. For this experimental case, using the velocity given at the tip of the jet $U_{\text{est}} \approx 40\,\text{m/s}$, the jet diameter $D_{\text{est}} \approx 5 \times 10^{-4}\,\text{m}$, and using gasoline material properties, we can estimate the Reynolds and the Weber number to be approximately in the range 10,000 – 20,000. In an attempt to represent these realistic properties more closely in the simulations, a jet with Re = We = 5000 is simulated. A separate turbulent pipe DNS is performed at Re = 5000 in order to provide the velocity boundary conditions for the jet simulation. Following the grid Weber number analysis presented earlier, some of the smaller liquid structures will become under-resolved, and should disappear from the mesh. However, we assume here that these have a somewhat limited influence on the overall development of the jet, and that the global features of the computed jet remain physically

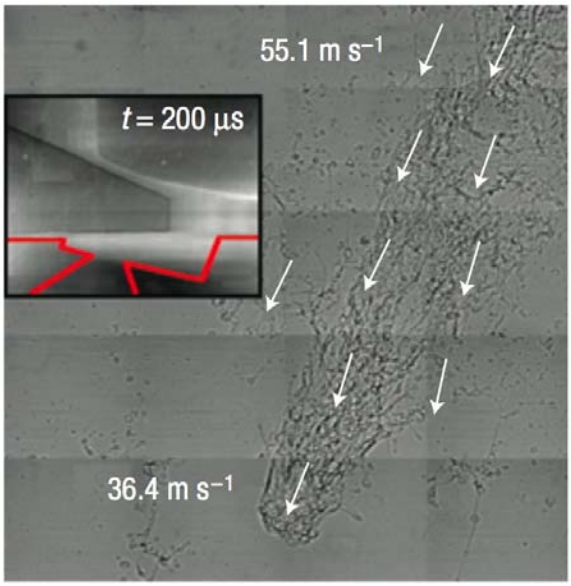

Figure 5.30: Ultra-fast X-ray visualization of the GDI injection, from Wang *et al.* [116].

correct. The liquid-gas interface is shown at two different times in Fig. 5.31. While a direct comparison remains difficult, it can be argued that many similarities exist between Fig. 5.30 and Fig. 5.31, such as the presence of numerous ligaments and drops, and the existence of a coherent liquid core. In both the experiment and the simulation, merged primary and secondary breakup can be seen, in the form of multiple ligaments being stretched out from larger ligaments.

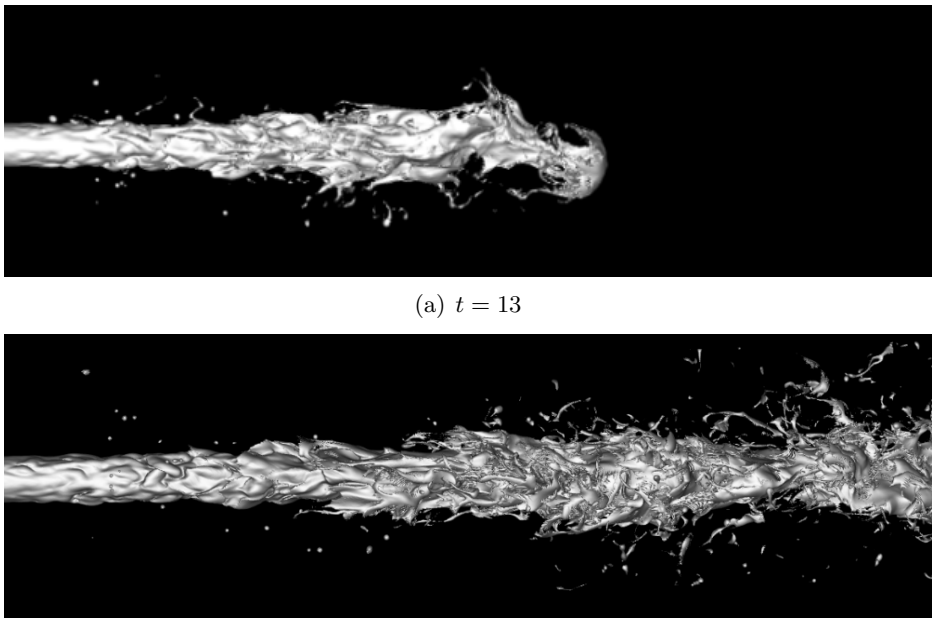

(a) $t = 13$

(b) $t = 22$

Figure 5.31: Snapshot of the liquid-gas interface for Re = 5000 and We = 5000.

Chapter 6

Conclusions and perspectives

Substantial advances have been made in computational methods both for accurate and robust simulations of turbulence, and for numerical simulations of multiphase flows. An arbitrarily high order conservative scheme has been developed for variable density, low Mach number turbulent flows, and adequate boundary conditions have been devised. Detailed numerical tests indicate that increasing the order of accuracy can be more efficient than refining the mesh to achieve a given error. Specifically, fourth order discretization provides an interesting trade-off between improved accuracy and increased computational cost. For a similar level of error, the computation of a turbulent pipe using fourth order discretization was found to be significantly cheaper than with a second order scheme.

On the topic of multiphase flows, the second order version of the aforementioned scheme was modified using the Ghost Fluid Method (GFM) to handle the discontinuous density and the surface tension force in a sharp manner, and the Continuum Surface Force (CSF) method was used to account for the jump in the viscous stresses within an semi-implicit formulation. Such a methodology provides a fast, robust, and accurate way of handling multiphase flows. Combining methods tailored for turbulence with state-of-the-art multiphase models in the context of a fully semi-implicit time integration is a unique feature of the present work. Two new numerical schemes for interface transport and representation were designed, providing substantial improvements over existing methods in terms of mass conservation, robustness,

and accuracy.

Finally, detailed simulations of primary atomization in the context of turbulent liquid injection were performed using these new numerical techniques. Careful analysis of the results suggests that aerodynamic effects play a significant role in the turbulent atomization of liquid jets. Several detailed mechanisms have been identified, such as bubble formation through sweep-ejection events, and ligament generation due to bubble bursting or droplet collision. Spatially evolving round liquid jets have been simulated, and a qualitative comparison of the interfacial features with experimental visualizations was presented.

The continuation of this work involves gathering comprehensive statistics on droplet sizes and velocity, and developing a more quantitative understanding of the mechanisms of atomization through an energy balance approach. Eventually, this information can be used to devise models based on first principles.

Then, evaporation needs to be taken into account in the numerical methods. This step will be greatly facilitated by the numerical framework presented here, as it allows to use a conservative variable density formulation, while preserving the simplicity of accounting for discontinuous variables by using GFM. The extension including phase-change will enable the investigation of more complex aspects of evaporation, such as multi-component evaporation, and will also allow to validate Lagrangian-based spray models.

Bibliography

[1] K. Akselvoll and P. Moin. Large-eddy simulation of turbulent confined coannular jets. *J. Fluid Mech.*, 315:387–411, 1996.

[2] M. Amielh, T. Djeridane, F. Anselmet, and L. Fulachier. Velocity near-field of variable density turbulent jets. *Int. J. Heat Mass Transfer*, 39:2149–4164, 1996.

[3] N. Ashgriz and J. Y. Poo. Coalescence and separation in binary collisions of liquid drops. *J. Fluid Mech.*, 221:183–204, 1990.

[4] F. Ben Rayana. *Contribution à l'étude des instabilités interfaciales liquide-gaz en atomization assistée et tailles de gouttes.* PhD thesis, Institut National Polytechnique de Grenoble, France, 2007.

[5] G. M. Bianchi, F. Minelli, R. Scardovelli, and S. Zaleski. 3D large scale simulation of the high-speed liquid jet atomization. SAE 2007-01-0244, 2007.

[6] G. M. Bianchi, P. Pelloni, S. Toninel, R. Scardovelli, A. Leboissetier, and S. Zaleski. Improving the knowledge of high-speed liquid jets atomization by using quasi-direct 3D simulation. SAE 2005-24-089, 2005.

[7] R. W. Bilger. Turbulent flows with nonpremixed reactants. in Turbulent Reacting Flows, P. A. Libby and F. A. Williams eds., Springer-Verlag, Berlin., 1980.

[8] T. Boeck and S. Zaleski. Viscous versus inviscid instability of two-phase mixing layers with continuous velocity profile. *Phys. Fluids*, 17:032106, 2005.

[9] J. U. Brackbill, D. B. Kothe, and C. Zemach. A continuum method for modeling surface tension. *J. Comput. Phys.*, 100:335–354, 1992.

[10] C. Canuto, M. Y. Hussaini, A. Quarteroni, and T. A. Zang. *Spectral methods in fluid dynamics*. Springer-Verlag, 1988.

[11] H. Choi and P. Moin. Effects of the computational time step on numerical solutions of turbulent flow. *J. Comput. Phys.*, 113:1–4, 1994.

[12] D. L. Chopp. Computing minimal surfaces via level set curvature flow. *J. Comput. Phys.*, 106:77–91, 1993.

[13] W. H. Chou and G. M. Faeth. Temporal properties of secondary drop breakup in the bag breakup regime. *International Journal of Multiphase Flow*, 24(6):889–912, 1998.

[14] F. K. Chow and P. Moin. A further study of numerical errors in large-eddy simulations. *J. Comput. Phys.*, 184:366–380, 2003.

[15] G. Comte-Bellot and S. Corrsin. Simple Eulerian time correlation in full and narrow band velocity signals in grid generated, isotropic turbulence. *J. Fluid Mech.*, 48:273–337, 1971.

[16] G. S. Constantinescu and S. K. Lele. A highly accurate technique for the treatment of flow equations at the polar axis in cylindrical coordinates using series expansions. *J. Comput. Phys.*, 183:165–186, 2002.

[17] C. B. da Silva and J. C. F. Pereira. The effect of subgrid-scale models on the vortices computed from large-eddy simulations. *Phys. Fluids*, 16:4506–4534, 2004.

[18] E. De Villiers and D. Gosman. Large eddy simulation of primary Diesel spray atomization. SAE 2004-01-0100, 2004.

[19] T. Djeridane, M. Amielh, F. Anselmet, and L. Fulachier. Velocity turbulence properties in the near-field region of axisymmetric variable density jets. *Phys. Fluids*, 6:1614–1630, 1996.

[20] Y. Dubief and F. Delcayre. On coherent-vortex identification in turbulence. *Journal of Turbulence*, 1:1–22, 2000.

[21] L. Duchemin, S. Popinet, C. Josserand, and S. Zaleski. Jet formation in bubbles bursting at a free surface. *Physics of Fluids*, 14(9):3000–3008, 2002.

[22] J. G. M. Eggels, F. Unger, M. H. Weiss, J. Westerweel, R. J. Adrian, R. Friedrich, and F. T. M. Nieuwstadt. Fully developed turbulent pipe flow: a comparison between direct numerical simulation and experiment. *J. Fluid Mech.*, 268:175–209, 1994.

[23] D. Enright, R. Fedkiw, J. Ferziger, and I. Mitchell. A hybrid particle level set method for improved interface capturing. *J. Comput. Phys.*, 183:83–116, 2002.

[24] V. Eswaran and S. B. Pope. Direct numerical simulations of the turbulent mixing of a passive scalar. *Phys. Fluids*, 31:506–520, 1988.

[25] G. M. Faeth, L. P. Hsiang, and P. K. Wu. Structure and breakup properties of sprays. *International Journal of Multiphase Flow*, 21:99–127, 1995.

[26] R. D. Falgout and U. M. Yang. HYPRE: a library of high performance preconditioners. In P. M. A. Sloot, C. J. K. Tan, J. J. Dongara, and A. G. Hoekstra, editors, *Computational Science - ICCS 2002 Part III*, volume 2331, pages 632–641, Berlin, 2002. Springer-Verlag.

[27] R. Fedkiw, T. Aslam, B. Merriman, and S. Osher. A non-oscillatory Eulerian approach to interfaces in multimaterial flows (the ghost fluid method). *J. Comput. Phys.*, 152:457–492, 1999.

[28] J. H. Ferziger and M. Peric. *Computational Methods for Fluid Dynamics*. Springer, Berlin, third edition, 2002.

[29] M. M. Francois, S. J. Cummins, E. D. Dendy, D. B. Kothe, J. M. Sicilian, and M. W. Williams. A balanced-force algorithm for continuous and sharp interfacial surface tension models within a volume tracking framework. *J. Comput. Phys.*, 213:141–173, 2006.

[30] K. Fukagata and N. Kasagi. Highly energy-conservative finite difference method for the cylindrical coordinate system. *J. Comput. Phys.*, 181:478–498, 2002.

[31] M. Germano, U. Piomelli, P. Moin, and W. H. Cabot. A dynamic subgrid-scale eddy viscosity model. *Phys. Fluids A*, 3:1760–1765, 1991.

[32] S. Ghosal. An analysis of numerical errors in large-eddy simulations of turbulence. *J. Comput. Phys.*, 125:187–206, 1996.

[33] P. Gomez, J. Hernandez, and J. Lopez. On the reinitialization procedure in a narrow-band locally refined level set method for interfacial flows. *Int. J. Numer. Meth. Eng.*, 63(10):1478–1512, 2005.

[34] M. Gorokhovski. The stochastic sub-grid-scale approach for spray atomization. *Atomization and Sprays*, 11:505–519, 2001.

[35] M. Gorokhovski and M. Herrmann. Modeling primary atomization. *Ann. Rev. Fluid Mech.*, 40:343–366, 2008.

[36] P. M. Gresho. Incompressible fluid dynamics: some fundamental formulation issues. *Ann. Rev. Fluid Mech.*, 23:413–453, 1991.

[37] F. E. Ham, F. S. Lien, and A. B. Strong. A fully conservative second-order finite different scheme for incompressible flow on nonuniform grids. *J. Comput. Phys.*, 177:117–133, 2002.

[38] F. H. Harlow and J. E. Welch. Numerical calculation of time-dependent viscous incompressible flow of fluid with free surface. *Phys. Fluids*, 8:2182–2189, 1965.

[39] M. Herrmann. A domain decomposition parallelization of the fast marching method. in Annual Research Briefs (Center for Turbulence Research, Stanford, CA), 2005.

[40] M. Herrmann. Refined level set grid method for tracking interfaces. in Annual Research Briefs (Center for Turbulence Research, Stanford, CA), 2005.

[41] M. Herrmann. A balanced force refined level set grid method for two-phase flows on unstructured flow solver grids. *J. Comput. Phys.*, 227(4):2674–2706, 2008.

[42] L. P. Hsiang and G. M. Faeth. Near-limit drop deformation and secondary breakup. *International Journal of Multiphase Flow*, 18(5):635–652, 1992.

[43] P. G. Huang, Z. J. Wang, and Y. Liu. An implicit space-time spectral difference method for discontinuity capturing using adaptive polynomials. AIAA Computational Fluid Dynamics Conference, 2005.

[44] J. C. R. Hunt, A. A. Wray, and P. Moin. Eddies, streams and convergence zones in turbulent flows. Technical Report CTR-S88, Center for Turbulence Research, 1988.

[45] G. S. Jiang and C. W. Shu. Efficient implementation of weighted ENO schemes. *J. Comput. Phys.*, 126:202–228, 1996.

[46] M. Kang, R. Fedkiw, and X. D. Liu. A boundary condition capturing method for multiphase incompressible flow. *J. Sci. Comput.*, 15:323–360, 2000.

[47] J. Kim. On the structure of wall-bounded turbulent flows. *Phys. Fluids*, 26:2088–2097, 1983.

[48] J. Kim and P. Moin. Application of a fractional-step method to incompressible Navier-Stokes equations. *J. Comput. Phys.*, 59:308–323, 1985.

[49] J. Kim and P. Moin. The structure of the vorticity field in turbulent channel flow. II. Study of ensemble-averaged fields. *J. Fluid Mech.*, 162:339–363, 1986.

[50] J. Kim, P. Moin, and R. Moser. Turbulence statistics in fully developed channel flow at low Reynolds number. *J. Fluid Mech.*, 177:133–166, 1987.

[51] S. C. Kong, P. K. Senecal, and R. D. Reitz. Developments in spray modelling in Diesel and direct-injection gasoline engines. *Oil Gas Sci. Tech. Rev. IFP*, 54:197–204, 1999.

[52] A. G. Kravchenko and P. Moin. On the effect of numerical errors in large eddy simulations of turbulent flows. *J. Comput. Phys.*, 131:310–322, 1997.

[53] J. C. Lasheras and E. J. Hopfinger. Liquid jet instability and atomization in a coaxial gas stream. *Ann. Rev. Fluid. Mech.*, 32:275–308, 2000.

[54] A. H. Lefebvre. *Atomization and spray.* Taylor and Francis, 1989.

[55] S. K. Lele. Compact finite-difference schemes with spectral-like resolution. *J. Comput. Phys.*, 103:16–42, 1992.

[56] B. P. Leonard. A stable and accurate convective modelling procedure based on quadratic upstream interpolation. *Comput. Methods Appl. Mech. Engrg.*, 19:59–98, 1979.

[57] R. J. LeVeque. High-resolution conservative algorithms for advection in incompressible flow. *SIAM Journal on Numerical Analysis*, 33(2):627–665, 1996.

[58] V. G. Levich. *Physico-chemical hydrodynamics.* Prentice-Hall, 1992.

[59] D. K. Lilly. A proposed modification of the Germano subgrid-scale closure method. *Phys. Fluids A*, 4:633–635, 1992.

[60] X. D. Liu, R. Fedkiw, and M. Kang. Boundary condition capturing method for poisson equation on irregular domains. *J. Sci. Comput.*, pages 151–178, 2000.

[61] X. D. Liu, S. Osher, and T. Chan. Weighted essentially non-oscillatory schemes. *J. Comput. Phys.*, 115:200–212, 1994.

[62] Y. Liu, M. Vinokur, and Z. J. Wang. Spectral difference method for unstructured grids I: Basic formulation. *Journal of Computational Physics*, 216(2):780–801, 2006.

[63] T. S. Lund and P. Moin. Large-eddy simulation of a concave wall boundary layer. *Int. J. Heat and Fluid Flow*, 17:290–295, 1996.

[64] T. S. Lundgren. Linearly forced isotropic turbulence. in Annual Research Briefs (Center for Turbulence Research, Stanford), 2003.

[65] E. Marchandise, P. Geuzaine, N. Chevaugeon, and J. F. Remacle. A stabilized finite element method using a discontinuous level set approach for the computation of bubble dynamics. *J. Comput. Phys.*, 225(1):949–974, 2007.

[66] P. Marmottant and E. Villermaux. On spray formation. *J. Fluid Mech.*, 498:73–112, 2004.

[67] V. V. Meleshko and G. J. F. Heijst. On Chaplygin's investigations of two-dimensional vortex structures in an inviscid fluid. *J. Fluid Mech.*, 272:157–182, 1994.

[68] T. Ménard, S. Tanguy, and A. Berlemont. Coupling level set/VOF/ghost fluid methods: Validation and application to 3D simulation of the primary break-up of a liquid jet. *Int. J. Multiphase Flow*, 33:510–524, 2007.

[69] C. Meneveau, T. S. Lund, and W. H. Cabot. A Lagrangian dynamic subgrid-scale model of turbulence. *J. Fluid Mech.*, 319:353–385, 2000.

[70] C. C. Miesse. Correlation of experimental data on the disintegration of liquid jets. *Ind. Eng. Chem.*, 47:1690–1701, 1955.

[71] R. Mittal and P. Moin. Suitability of upwind-biased finite difference schemes for large-eddy simulation of turbulent flows. *AIAA Journal*, 35:1415–1417, 1997.

[72] Y. Morinishi, T. S. Lund, O. V. Vasilyev, and P. Moin. Fully conservative higher order finite difference schemes for incompressible flow. *J. Comput. Phys.*, 143:90–124, 1998.

[73] Y Morinishi, O. V. Vasilyev, and T. Ogi. Fully conservative finite difference scheme in cylindrical coordinates for incompressible flow simulations. *J. Comput. Phys.*, 197:686–710, 2004.

[74] S. Nagarajan, S. K. Lele, and Ferziger J. H. A robust high-order compact method for large eddy simulation. *J. Comput. Phys.*, 191:392–419, 2003.

[75] F. Nicoud. Conservative high-order finite difference schemes for low-mach number flows. *J. Comput. Phys.*, 158:71–97, 2000.

[76] R. R. Nourgaliev and T. G. Theofanous. High-fidelity interface tracking in compressible flows: Unlimited anchored adaptive level set. *J. Comput. Phys.*, 224:836–866, 2007.

[77] W. Ohnesorge. Formation of drops by nozzles and the breakup of liquid jets. *Z. Angew. Math. Mech.*, 16:355–358, 1936.

[78] E. Olsson and G. Kreiss. A conservative level set method for two phase flow. *J. Comput. Phys.*, 210:225–246, 2005.

[79] E. Olsson, G. Kreiss, and S. Zahedi. A conservative level set method for two phase flow ii. *J. Comput. Phys.*, 225:785–807, 2007.

[80] I. Orlanski. A simple boundary condition for unbounded hyperbolic flows. *J. Comput. Phys.*, 21:251–269, 1976.

[81] S. A. Orszag. On the elimination of aliasing in finite-difference schemes by filtering high-wavenumber components. *J. Atmosph. Sci.*, 28:1074–1074, 1971.

[82] S. Osher and R. Fedkiw. *Level set methods and dynamic implicit interfaces.* Springer, New York, 2003.

[83] Y. Pan and K. Suga. A numerical study on the breakup process of laminar liquid jets into a gas. *Phys. Fluids*, 18, 2006.

[84] R. Paoli, T. Poinsot, and K. Shariff. Testing semi-Lagrangian schemes for two-phase flow applications. In *Proceedings of the 2006 Summer Program.* Center for Turbulence Research, Stanford, CA, 2006.

[85] M. Park, J. Y. Yoo, and H. Choi. Discretization errors in large eddy simulation: on the suitability of centered and upwind-biased compact difference schemes. *J. Comput. Phys.*, 198:580–616, 2004.

[86] G. S. Patterson and S. A. Orszag. Spectral calculations of isotropic turbulence: Efficient removal of aliasing interactions. *Phys. Fluids*, 14:2538–2541, 1971.

[87] M. A. Patterson and R. D. Reitz. Modeling the effects of fuel spray characteristics on Diesel engine combustion and emissions. SAE Tech. Pap. 980131, 1998.

[88] D. Peng, B. Merriman, S. Osher, H. Zhao, and M. Kang. A pde-based fast local level set method. *J. Comput. Phys.*, 155:410–438, 1999.

[89] C. D. Pierce and P. Moin. Progress-variable approach for large eddy simulation of turbulent combustion. Technical Report TF80, Flow Physics and Computation Division, Dept. Mech. Eng., Stanford University, 2001.

[90] S. Popinet and S. Zaleski. A front-tracking algorithm for accurate representation of surface tension. *Int. J. Numer. Meth. Fluids*, 30:775–793, 1999.

[91] A. Prosperetti. Motion of two superposed viscous fluids. *Phys. Fluids*, 24:1217–1223, 1981.

[92] A. A. Ranger and J. A. Nicholls. Aerodynamic shattering of liquid drops. *AIAA*, 7:285–290, 1969.

[93] R. D. Reitz. *Atomization and other breakup regimes of a liquid jet.* PhD thesis, Princeton University, 1978.

[94] J. Réveillon and L. Vervisch. Response of the dynamic LES model to heat release induced effects. *Phys. Fluids*, 8:2248–2250, 1996.

[95] C. Rosales and C. Meneveau. Linear forcing in numerical simulations of isotropic turbulence: Physical space implementations and convergence properties. *Phys. Fluids*, 17:095106–1–095106–8, 2005.

[96] K. A. Sallam, Z. Dai, and G. M. Faeth. Drop formation at the surface of plane turbulent liquid jets in still gases. *International Journal of Multiphase Flow*, 25(6):1161–1180, 1999.

[97] K. A. Sallam, Z. Dai, and G. M. Faeth. Liquid breakup at the surface of turbulent round liquid jets in still gases. *International Journal of Multiphase Flow*, 28(3):427–449, 2002.

[98] R. L. Sani, J. Shen, O. Pironneau, and P. M. Gresho. Pressure boundary condition for the time-dependent incompressible Navier-Stokes equations. *Int. J. Num. Methods Fluids*, 50:673–682, 2006.

[99] R. Scardovelli and S. Zaleski. Direct numerical simulation of free-surface and interfacial flow. *Ann. Rev. Fluid Mech.*, 31:567–603, 1999.

[100] J. A. Sethian. *Level set methods and fast marching methods.* Cambridge University Press, Cambridge, UK, second edition, 1999.

[101] G. Smallwood and Ö. Gülder. Views on the structure of transient Diesel spray. *Atomization and Sprays*, 10:355–386, 2000.

[102] S. A. Stanley, S. Sarkar, and J. P. Mellado. A study of the flow-field evolution and mixing in a planar turbulent jet using direct numerical simulation. *J. Fluid. Mech.*, 450:377–407, 2002.

[103] M. Sussman and M. Y. Hussaini. A discontinuous spectral element method for the level set equation. *Journal of Scientific Computing*, 19(1):479–500, 2003.

[104] M. Sussman and E. G. Puckett. A coupled level set and volume of fluid method for computing 3D and axisymmetric incompressible two-phase flows. *J. Comput. Phys.*, 162:301–337, 2000.

[105] M. Sussman, P. Smereka, and S. Osher. A level set method for computing solutions to incompressible two-phase flow. *J. Comput. Phys.*, 114:146–159, 1994.

[106] M. Sussman, K. M. Smith, M. Y. Hussaini, M. Ohta, and R. Zhi-Wei. A sharp interface method for incompressible two-phase flows. *J. Comput. Phys.*, 221:469–505, 2007.

[107] S. Tanguy and A. Berlemont. Application of a level set method for simulation of droplet collisions. *Int. J. Multiphase Flow*, 31:1015–1035, 2005.

[108] G. I. Taylor. Cavitation of viscous fluid in narrow passages. *J. Fluid Mech.*, 16:595–619, 1963.

[109] T. C. Treurniet, F. T. M. Nieuwstadt, and B. J. Boersma. Direct numerical simulation of homogeneous turbulence in combination with premixed combustion at low Mach number modelled by the G-equation. *J. Fluid Mech.*, 565:25–62, 2006.

[110] S. Unverdi and G. Tryggvason. A front-tracking method for viscous, incompressible, multi-fluid flows. *J. Comput. Phys.*, 100:25–37, 1992.

[111] A. Vallet, A. Burluka, and R. Borghi. Development of an Eulerian model for the atomization of a liquid jet. *Atomization and Sprays*, 11:619–642, 2001.

[112] H. A. van der Vorst. *Iterative Krylov methods for large linear systems.* Cambridge University Press, Cambridge, first edition, 2003.

[113] O. V. Vasilyev. High order finite difference schemes on non-uniform meshes with good conservation properties. *J. Comput. Phys.*, 157:746–761, 2000.

[114] R. Verzicco and P. Orlandi. A finite-difference scheme for three-dimensional incompressible flows in cylindrical coordinates. *J. Comput. Phys.*, 123:402–414, 1996.

[115] E. Villermaux. Fragmentation. *Ann. Rev. Fluid. Mech.*, 39:419–446, 2007.

[116] Y. Wang, X. Liu, K.-S. Im, W.-K. Lee, J. Wang, K. Fezzaa, D. L. S. Hung, and J. R. Winkelman. Ultrafast X-ray study of dense-liquid-jet flow dynamics using structure-tracking velocimetry. *Nature Physics*, 4:305–309, 2008.

[117] C. Weber. Disintegration of liquid jets. *Z. Angrew. Math. Mech.*, 11:136, 1931.

[118] P. K. Wu and G. M. Faeth. Aerodynamic effects on primary breakup of turbulent liquids. *Atomization and Sprays*, 3(3):265–289, 1993.

[119] A. L. Yarin. Drop impact dynamics: Splashing, spreading, receding, bouncing... *Ann. Rev. Fluid. Mech.*, 38:159–192, 2006.

[120] P. Yecko, S. Zaleski, and J.-M. Fullana. Viscous modes in two-phase mixing layers. *Phys. Fluids*, 14:4115–4122, 2002.

[121] P. K. Yeung and S. B. Pope. Lagrangian statistics from direct numerical simulations of isotropic turbulence. *J. Fluid Mech.*, 207:531–586, 1989.

[122] Y. Yi and R. D. Reitz. Modeling the primary break-up of high-speed jets. *Atomization and Sprays*, 14:53–80, 2004.

[123] S. T. Zalesak. Fully multidimensional flux-corrected transport algorithms for fluids. *J. Comput. Phys.*, 31:335–362, 1979.